Universität Rostock

Traditio et Innovatio

Selective Synthesis of 1,5-Pentanediol from Furfural Derivatives over Stable Nickel-Based Catalysts

Dissertation

zur

Erlangung des akademischen Grades

doctor rerum naturalium (Dr. rer. nat.)

der Mathematisch Naturwissenschaftlichen Fakultät

der Universität Rostock

angefertigt am Leibniz-Institut für Katalyse e.V.

an der Universität Rostock

vorgelegt von

Mohammed Al-Yusufi

geboren am 30.03.1991 in Sanaa, Jemen

Rostock, 12.08.2022

https://doi.org/10.18453/rosdok_id00004535

Jahr der Einreichung: 2022
Jahr der Verteidigung: 2023

Gutachter:

Prof. Thomas Werner
Leibniz-Institut für Katalyse e.V. (LIKAT Rostock)

Prof. Tapio Salmi,
Åbo Akademi University

Contents

Declaration

I declare that the work in this thesis entitled “Selective Synthesis of 1,5-Pentanediol from Furfural Derivatives over Stable Nickel-based Catalysts” is an original report of my research, and it has not been written and submitted for any previous degree. The experimental work is entirely my own and collaborative contributions have been indicated clearly and acknowledged. All supporting references have been properly cited.

_____

Mohammed Al-Yusufi

Rostock, 12.08.2022

Acknowledgment

First and foremost, I am thankful to Almighty Allah for giving me the strength, knowledge, ability, and opportunity to undertake my doctoral research and complete it satisfactorily.

I would like to express my sincerest gratitude and appreciation to my scientific supervisor Dr. Angela Köckritz who has guided me through my doctoral journey. I am deeply grateful for her patience, encouragement, and assistance at every stage of my research work even after her retirement. I would like to extend my sincere thanks to my academic supervisor Dr. Thomas Werner for invaluable supervision and Dr. Sebastian Wohlrab and Dr. Udo Armbruster for their insightful suggestions and support. I also gratefully acknowledge the “Deutscher Akademischer Austauschdienst” (DAAD) for the financial support I received during my research stay at LIKAT.

Also, I would like to offer my special thanks to all my colleagues in the Department of Heterogeneous Catalytic Processes, in particular Dr. K. Neubauer, Dr. H. Atia, Mr. R. Eckelt, Mrs. R. Bienert, Dr. T. Brunzel, Dr. A. Täufer, M.Sc. M. Vogt, Dr. H. Mena, Dr. A. AbdelMageed, Dr. E. Kraleva, Ms. J. Schröder, M.Sc. J. Mosrati, M.Sc. D. German and M.Sc. S. Löbner for their kind help and great support not only at work, but also in social life. My gratitude extends to Dr. N. Steinfeldt and Mr. M. Sebek from Department of Heterogeneous Photocatalysis for their technical support in continuous operation of a micro-reactor which took my thesis to a higher level.

I want to greatly thank Dr. D. Michalik and Mrs. H. Borgwaldt from the NMR service of the University of Rostock for their fruitful contributions which helped me to elucidate the reaction mechanism. Also, I would like to thank Dr. C. Kubis, Dr. J. Rabeah, Dr. X. Dai and Mrs. C. Rautenberg from Department of Catalytic in-situ Studies for their cooperation with spectroscopic measurements, as well as to all colleagues of the Analytics, especially Dr. N. Rockstroh, Dr. C. Kreyenschulte, Dr. S. Bartling, Dr. H. Lund, Mrs. A. Simmula, Mrs. A. Lehmann, Dr. C. Fischer, and Mrs. K. Schubert.

Lastly but most importantly, I am extremely grateful to my dear mother, Fairoz, my beloved wife, Shaima, and my sweetheart son, Yamann, for everything that they have done to help me reach the peak of my profession. I also want to have mercy on my father, Abdullah, and grandparents, who have passed away during my studies abroad. They have unwaveringly supported me and believed in me from childhood. Also, I am so thankful to all my brothers, sisters, friends, and relatives. I feel so blessed to have wonderful people like them in my life.

Again, many thanks to ALL of you and everyone who positively impacted my life and contributed to my success….

Zusammenfassung

Ni(0) auf basischen, hydroxidischen Lanthanoid-Trägern (wt% Ni-Ln(R), Ln = La-, Pr-, Sm-Hydroxid/(Oxy)hydroxid, (R) = reduzierter Katalysator) in Isopropanol (2-PrOH) erwies sich als effizienter Katalysator und als wirtschaftlich tragfähige Alternative zu modifizierten Edelmetallkatalysatoren für die direkte Hydrogenolyse von Tetrahydrofurfurylalkohol (THFA) und Furfural (FUR) zu 1,5-Pentandiol (1,5-PeD). Die katalytische Aktivität von Ni auf verschiedenen Seltenerdträgern wurde im Batch- und kontinuierlichen Reaktor untersucht. Die höchste Ausbeute an 1,5-PeD unter Batchbedingungen lag bei 88 % mit 40Ni-La(R) und 37Ni-Pr(R) als Katalysatoren, ausgehend von THFA, und bei 80 % THFA+1,5-PeD, wenn FUR als Substrat und 38Ni-Sm(R) als Katalysator verwendet wurden. Die katalytische Wirkung war optimal, wenn der Katalysator durch Kopräzipitation und anschließende Reduktion über längere Zeit bei niedriger Temperatur (250 °C) hergestellt wurde, um die vollständige Reduktion der NiO-Phase zu Ni(0) sicherzustellen, aber die Struktur der stark basischen Hydroxidspezies unverändert zu lassen. Der Umsatz von THFA war in sekundären Alkoholen (Wasserstoffdonatoren) als Lösungsmittel höher, welche teilweise zu den korrespondierenden Ketonen dehydriert wurden, wobei sogar in Gegenwart von H_2-Gas zusätzlicher Wasserstoff entstand. Die Verwendung von 2-PrOH als einzige Wasserstoffquelle im Sinne einer katalytischen Transfer-Hydrogenolyse (CTH) unter Batch-Bedingungen führte jedoch zu einem Absinken der Katalysatorselektivität zu 1,5-PeD aufgrund der konkurrierenden Belegung der Katalysatoroberfläche mit dem Lösungsmittel, das zu Aceton und Wasserstoff dehydriert wurde. Interessanterweise war die Wasserstoffkonzentration unter kontinuierlichen CTH-Bedingungen ausreichend, so dass ein zusätzlicher Einsatz von gasförmigem Wasserstoff keine Auswirkungen auf die Katalysatoraktivität und -selektivität hatte. Somit wurde zum ersten Mal ein kontinuierlicher CTH-Prozess für die selektive Hydrogenolyse von THFA zu 1,5-PeD unter Verwendung von Ni-La(R) in 2-PrOH entwickelt. Unter kontinuierlichen CTH-Bedingungen wurde eine maximale 1,5-PeD-Ausbeute von 73 % und eine Produktivität pro Stunde von 1,4 mmol $g(cat)^{-1}$ h^{-1} erreicht. Bemerkenswerterweise zeigten 40Ni-La(R) und 38Ni-Sm(R) eine hohe Langzeitstabilität unter kontinuierlichen Bedingungen (bis zu 386 h TOS), wohingegen 37Ni-Pr(R) bereits am ersten Tag deaktiviert wurde. Die Deaktivierung wurde auf die starke Ablagerung von kohlenstoffhaltigem Material auf der Nickeloberfläche zurückgeführt, die bei 37Ni-Pr(R) auf stärker dispergiertem Ni deutlich größer war als auf weniger dispergiertem Ni im Fall der langzeitstabilen Katalysatoren 40Ni-La(R) und 38Ni-Sm(R). Nach Auswertung experimenteller und spektroskopischer Ergebnisse wurde angenommen, dass die Ni-Träger-Grenzfläche, die sich durch intensive Durchmischung von sehr fein verteilten metallischen Ni-Partikeln und Lanthanoid-Spezies gebildet hatte, für die hohe katalytische Aktivität von Ni-Ln(R) verantwortlich ist, bei der die basischen Zentren die Hydroxylgruppe von THFA deprotonieren und metallische Ni-Spezies Wasserstoffgas

(und/oder ein Wasserstoff-Donor-Lösungsmittel) aktivieren. Auf der Grundlage von Isotopenmarkierungsexperimenten wurde als entscheidender Schritt im Mechanismus dieser Reaktion ein direkter Hydridangriff oder eine ringöffnende Tautomerisierung (über 2-Hydroxytetrahydropyran) vorgeschlagen.

Abstract

Reduced Ni on highly basic lanthanide supports (wt% Ni-Ln(R), Ln= La, Pr, Sm hydroxides/oxyhydroxides, (R) = reduced catalyst) in isopropanol (2-PrOH) was proved to be an efficient catalyst and an economically viable alternative to modified noble metal catalytic systems for the direct hydrogenolysis of tetrahydrofurfuryl alcohol (THFA) and furfural (FUR) to 1,5-pentanediol (1,5-PeD). The conversion of THFA over Ni on several rare-earth supports was investigated under batch and continuous conditions. The highest yield of 1,5-PeD under batch conditions was 88% on 40Ni-La(R) and 37Ni-Pr(R) starting from THFA, and 80% of THFA+1,5-PeD on 38Ni-Sm(R) starting from FUR. The conversion was significantly increased when the catalyst was prepared by co-precipitation followed by a long-term reduction at low temperature (250 °C), in order to ensure the complete reduction of the NiO phase and also to maintain strongly basic hydroxide sites. The conversion of THFA was higher in secondary alcohols (hydrogen donors) which were partially dehydrogenated to the corresponding ketones producing additional hydrogen even in the presence of gaseous hydrogen. However, the use of 2-PrOH as single hydrogen source in the sense of a catalytic transfer hydrogenolysis (CTH) led to a decrease of the catalyst selectivity to 1,5-PeD under batch conditions due to the competitive occupation of the catalyst surface with the dehydrogenation of the solvent to acetone and hydrogen. Interestingly, the hydrogen concentration was sufficient under continuous CTH conditions, so that additional use of gaseous hydrogen had no impact on the yield of target 1,5-PeD. For the first time, a continuous CTH process for the selective hydrogenolysis of THFA to 1,5-PeD was developed using Ni-La(R) in 2-PrOH. A maximum 1,5-PeD yield of 73% with an hourly productivity of 1.4 mmol $g(cat)^{-1}$ h^{-1} was achieved under continuous CTH conditions. Remarkably, 40Ni-La(R) and 38Ni-Sm(R) demonstrated high stability in long continuous runs (up to 386 h TOS) compared to 37Ni-Pr(R) which was already deactivated within the first day. The deactivation of the Ni catalyst was attributed to the high deposition of the carbonaceous material on the nickel surface which was significantly larger on more dispersed Ni in the case of 37Ni-Pr(R) than on less dispersed Ni in the case of highly stable 40Ni-La(R) and 38Ni-Sm(R). After evaluation of experimental and spectroscopic results, it was assumed that the Ni-basic support interface, which was formed due to the intensive entanglement of metallic Ni particles and lanthanide species, was responsible for the high yield of 1,5-PeD over Ni-Ln(R) where the strong basic sites deprotonate the hydroxyl group of THFA and metallic Ni species activate hydrogen gas (and/or hydrogen-donor solvent). Based on isotopic labeling experiments, a direct hydride attack or ring-opening tautomerization (via 2-hydroxytetrahydropyran) was proposed as a decisive step in the mechanism of the hydrogenolysis of the C–O bond of THFA.

List of abbreviations and name index

Chemical nomenclatures

1,4-BDO	1,4-butanediol
1-BuOH	1-butanol
2-BuOH	2-butanol
3,4-DHP	3,4-dihydropyran
ETHFE	ethyl tetrahydrofurfuryl ether
EtOH	ethanol
FUR	furfural
FOL	furfuryl alcohol
GHB	γ-hydroxybutyric acid
1,6-HDO	1,6-hexanediol
HMF	hydroxymethylfurfural
2-HY-THF	2-hydroxytetrahydrofuran
5-HY-PAL	5-hydroxypentanal
2-HY-THP	2-hydroxytetrahydropyran
2-MF	2-methylfuran
2-MTHF	2-methyltetrahydrofuran
2-MTHP	2-methyltetrahydropyran
PBT	polybutylene terephthalate
PBS	polybutylene succinate
1,3-PDO	1,3-propanediol
1-PeOH	1-pentanol
2-PeOH	2-pentanol
PeDs	pentanediols
1,5-PeD	1,5-pentanediol

1,2,5-PTO	1,2,5-pentanetriol
THF	tetrahydrofuran
THFA	tetrahydrofurfuryl alcohol
THFAL	tetrahydrofurfural
THP	tetrahydropyran
THP-2M	tetrahydropyran-2-methanol

Other abbreviations

ABF-STEM	annular bright-field scanning transmission electron microscopy
BET	Brunauer–Emmett–Teller
CN	coordination number
Cat	catalyst
CTH	catalytic transfer hydrogenolysis
DFT	density functional theory
DWF	Debye−Waller factor
EDX	energy dispersive X-ray analysis
EELS	electron energy loss spectroscopy
EXAFS	extended X-ray absorption fine structure
FTIR	fourier transform infrared spectroscopy
GC-MS	gas chromatography-mass spectrometry
HAADF-STEM	high-angle annular dark field scanning transmission electron microscopy
ICP-OES	inductively coupled plasma optical emission spectroscopy
ICDD	International Centre for Diffraction Data
IWI	incipient wetness impregnation
LCA	linear combination analysis

LHSV	liquid hourly space velocity
MPV	Meerwein−Ponndorf−Verley
mri	materials research instruments
NMR	nuclear magnetic resonance spectroscopy
Q	liquid flow
R.T.	room temperature
Sub	substrate
STEM	scanning transmission electron microscopy
TOF	turnover frequency
TOS	time-on-stream
TPD	temperature-programmed desorption
TPR	temperature-programmed reduction
XANES	X-ray absorption near edge structure
XAS	X-ray absorption spectroscopy
XRD	X-ray powder diffraction
XPS	X-ray photoelectron spectroscopy
WI	wet impregnation

1. State of the art

1.1. α,ω-Diols as high-value added chemicals

1.1.1. Production of C_4-C_6 α,ω-diols

α,ω-Diols ($C_XH_{(2X+2)}O_2$) are organic compounds which contain two hydroxyl groups (-OH) at both terminal positions. The following, industrially important compounds belong to this group of diols: 1,3-Propanediol (1,3-PDO), 1,4-butanediol (1,4-BDO), 1,5-pentanediol (1,5-PeD) and 1,6-hexanediol (1,6-HDO). They are largely used in plastic, coatings and paint industries [1-3]. Due to their good flexibility and adhesive properties, they are considered as intermediates and monomers in production of polyester and polyurethane resins, acrylates, adhesives, solvents, electronic chemicals and elastic fibers [4]. In 2020, C_4-C_6 α,ω-diols represented an annual market over 10 billion $ with an annual growth rate of nearly 7% [5-7]. As shown in Figure 1.1, 97% of the C_4-C_6 α,ω-diols market belongs to 1,4-BDO which is mostly produced from petrochemical feedstocks (acetylene, butadiene, allyl acetate, etc.), and almost half of it is dehydrated to THF for fiber production [8]. However, the production of 1,5-PeD is significantly lower and its price is quite higher than that of 1,4-BDO. Compared to 1,6-HDO, the 1,5-PeD market is remarkably lower (over 30 times more) with two times higher costs (Figure 1.1) because C5 petroleum feedstocks are not readily available in large scale [9, 10].

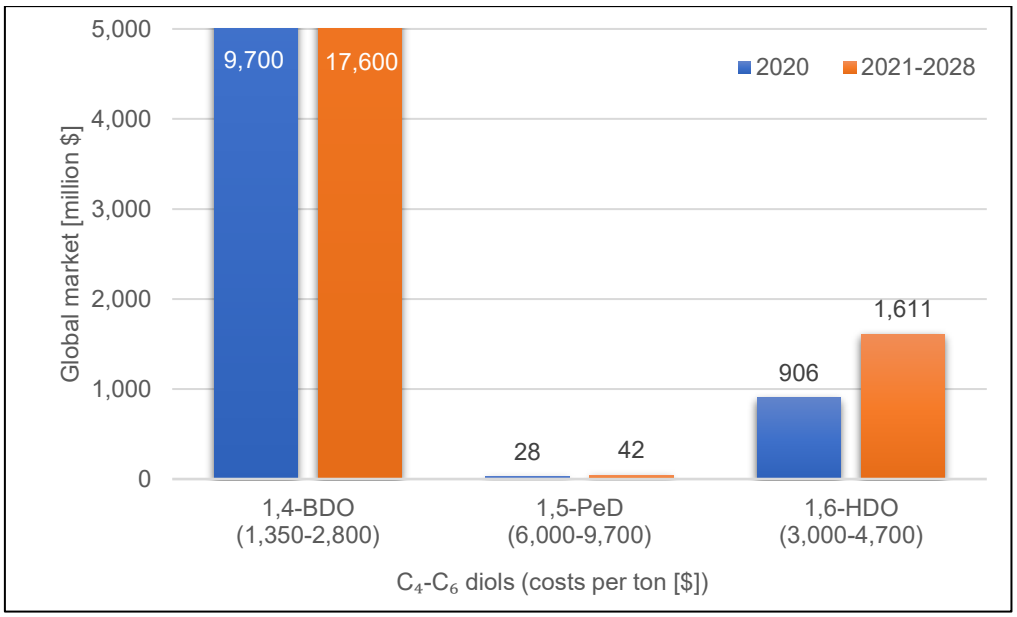

Figure 1.1. Global market of C4-C6 α,ω-diols in 2020 and its expected growth in the next years [5-7].

Scheme 1.1 demonstrates the mainly used C5-feedstocks for production of 1,5-PeD. 1,5-PeD is produced industrially by catalytic hydrogenation of glutaric acid and its esters [1]. Also, dicarboxylic acid mixtures containing glutaric acid can be used [1]. Similarly, 1,6-HDO is produced industrially by reduction of C6-petrochemical feedstocks, such as adipic acid and its esters, ε-caprolactam or 6-hydroxycaproic acid, on Cu-, Co- or Mn catalysts at temperatures

between 170-240 °C and pressures of 150-300 bar [1]. The small scale of C5 petroleum feedstocks versus the increased global demand for polyurethanes, polyesters, plasticizers, and other manufacturing segments should be covered by renewable resources such as bio-based C5 lignocellulose feedstocks. 1,5-PeD could also be obtained by hydrogenolysis of furfural (FUR) and tetrahydrofurfuryl alcohol (THFA) at temperatures between 250–300 °C and pressures of 230–430 bar on copper chromite [11] (Scheme 1.1). Although this pathway might be preferable due to the negative environmental impact of petroleum-based chemicals, the use of toxic copper chromite as a catalyst is not favorable. Moreover, due to the harsh reaction conditions that are industrially applied to obtain 1,5-PeD and 1,6-HDO, it is essential to develop active, stable and environmentally friendly catalysts for processes under continuous conditions.

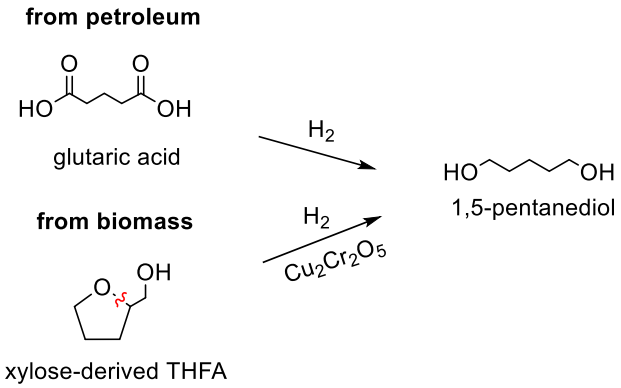

Scheme 1.1. C5-feedstocks for production of 1,5-PeD.

1.1.2. Properties of C_4-C_6 α,ω-diols

Table 1.1 compares the physical properties of C_4-C_6 α,ω-diols and polyester-polyols based on them [12-15]. Generally, the physical properties of this group of diols are similar, however, 1,5-PeD has a remarkable lower melting point resulting in different physical properties of 1,5-PeD-based polyesters. For instance, the melting transition temperature of C5 polyesters is lower than that of polybutylene terephthalate (PBT), and the biodegradability of C5 polyesters is worse than that of C4 polyesters (polybutylene succinate PBS) [9]. Consequently, polyesters made from 1,5-PDO are considered as safer polymers than polyesters made from 1,4-BDO, for example used for children's toys, since 1,4-BDO is rapidly absorbed from skin and metabolized into g-hydroxybutyric acid (GHB) which is considered as a drug to be controlled because of its ability to stimulate a deep sleep [16]. Such polymers should have a low viscosity, low glass transition temperature, and good flexibility (Table 1.1). 1,5-PeD-based polyesters and polyurethanes provide a good balance between hardness and flexibility, adhesion, weatherability or hydrolysis resistance [17]. Thus, they could be a better alternative to other diols (1,6-HDO or 1,4-BDO) in several applications [2, 9, 10]. Thus, it is necessary and highly desirable to develop efficient catalytic systems for production of 1,5-PeD from bio-based feedstocks, particularly from FUR and its alcoholic derivatives.

Table 1.1. Physical properties of C_4-C_6 α,ω-diols and polyester polyols based on them (adapted from ref. [12-15]).

α,ω-diol [CAS no.]	Molar weight [g mol^{-1}]	Boiling point [°C]	Melting point [°C]	Density (25°C) [g cm^{-3}]	Solubilty in water [vol.%]	Properties of polyester polyols (α,ω-diols + adipic acid)			
						Molar weight [g mol^{-1}]	Viscosity [mPa s]	$T_{glass\ transition}$ [°C]	$T_{melting\ transition}$ [°C]
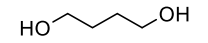 1,4-BDO [110-63-4]	90.1	235	20	1.017	Miscible	2110	1482	-53.7	53.3
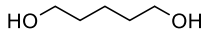 1,5-PeD [111-29-5]	104.1	242	-18	0.994	Miscible	2188	1316	-61.8	38.6
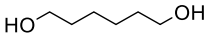 1,6-HDO [629-11-8]	118.2	250	42	0.967	-	1961	1100	-	51.8

1.2. Furfural and its alcoholic derivatives

Furfural (FUR) ($C_5H_4O_2$) is a heterocyclic organic compound with an aldehyde group attached to the 2-position of the furan aromatic ring. It is considered as one of the top value-added building blocks due to its high production flexibility derived from lignocellulosic biomass [18, 19]. It is directly produced from non-food feedstocks of crops residues, such as corncobs or sugar cane bagasse and wood wastes. As shown in Scheme 1.2, FUR is produced by acid-catalyzed dehydration of xylose after acid-catalyzed hydrolysis reaction of hemicellulose [20]. Depending on the type of the feedstock, up to 10% of feedstocks from crop residues can be recovered as FUR [21]. FUR alcoholic derivatives, furfuryl alcohol (FOL) and tetrahydrofurfuryl alcohol (THFA), can be obtained by hydrogenation of the aldehyde group, or in the case of THFA, also of the furan ring (Scheme 1.2).

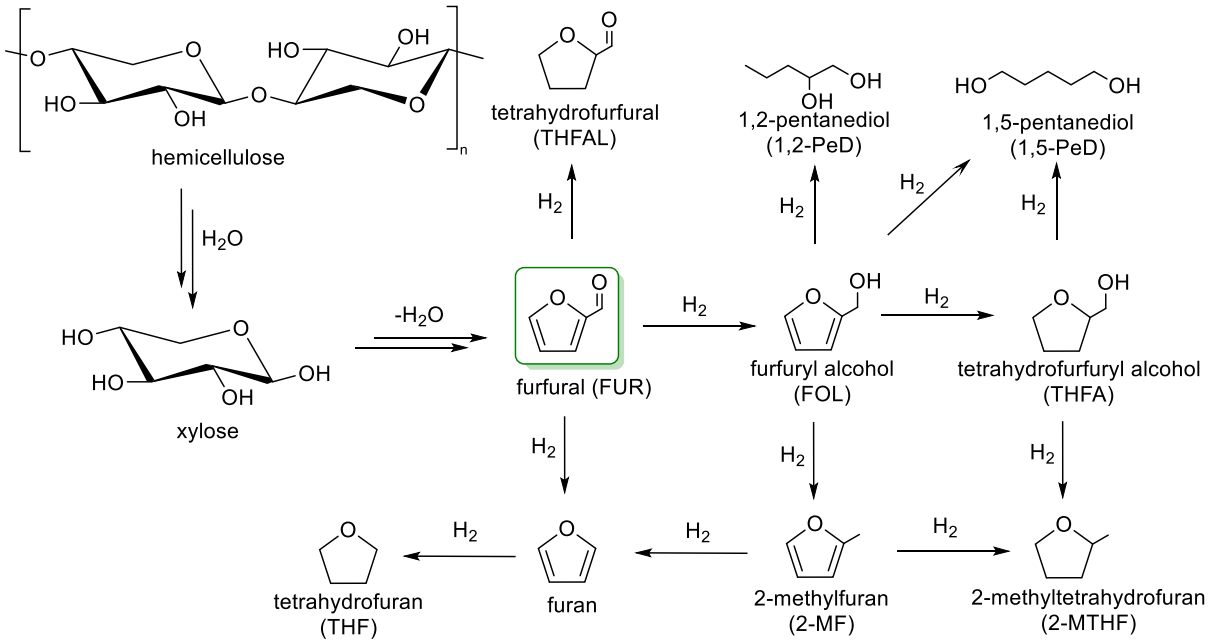

Scheme 1.2. Production of furfural and its derivatives from lignocellulosic biomass (adapted from [18, 22]).

On the other hand, further hydrogenolysis of FOL and THFA may lead to formation of pentanediols due to C–O bond cleavage (ring-opening reaction). The C–O bond hydrogenolysis reaction might be accompanied by other reactions such as hydrogenation and decarbonylation which results in various side products, such as 2-methylfuran (2-MF), 2-methyltetrahydrofuran (2-MTHF) and tetrahydrofuran (THF) (Scheme 1.2) [19]. Since desired products can be obtained after hydrogenation of FUR, it is essential to develop selective catalysts for conversion of FUR to specific products, especially to FOL and THFA, which are highly demanded in industry. FOL and THFA have been used as fuel additives and precursors of biofuel, because of their comparable physicochemical properties to kerosene (octane number of THFA = 83) [4, 5]. In general, FUR derivatives are widely used as monomers and solvents in plastics, resins, food and pharmaceutical industries and as intermediates in fragrances and detergents production [18, 19]. Table 1.2 shows the physical properties of FUR, FOL and THFA at room temperature.

Table 1.2. Physical properties of furfural and alcoholic derivatives (adapted from ref. [19, 23]).

Compound [CAS no.]	Molar weight [g mol^{-1}]	Melting point [°C]	Boiling point [°C]	Density[a] [g cm^{-3}]	Vapor pressure[a] [kPa]	Viscosity[b] [mPa s]	Solubility in water[b] [vol.%]
Furfural (FUR) [98-01-1]	96.08	-36.5	161	1.160	0.27	1.49	8.3
Furfuryl alcohol (FOL) [98-00-0]	98.10	-14.6	170	1.129	0.05	4.62	Miscible
Tetrahydrofurfuryl alcohol (T2HFA) [97-99-4]	102.13	-80.0	178	1.051	0.03	5.49	Miscible

[a] at 20°C, [b] at 25°C.

1.2.1. Selective hydrogenation of FUR to FOL

FOL is industrially produced by catalytic hydrogenation of FUR in liquid or gas phase. The first patented works were published in 1929 and 1931 using asbestos-supported copper and Ni/MgO in liquid and gas phase, respectively [24, 25]. Over-hydrogenation of FOL to THFA was also observed and could not be avoided using these catalysts [25]. Also, reduced copper chromite as a conventional catalyst was widely applied for liquid phase hydrogenation of FUR at high H_2 pressure (230–430 bar) yielding ≥90 of FOL [25]. Moreover, the addition of CaO to copper chromite increased the catalyst selectivity to FOL achieving 98% yield of FOL [26, 27]. Nevertheless, the catalyst deactivation and the fact that chromite-based materials are toxic and carcinogenic increased the interest to replace copper chromite by other environmentally friendly catalysts [25]. Thus, several catalytic systems were reported to be efficient alternatives in liquid hydrogenation of FUR. For instance, almost total yields of FOL were obtained in ethanol (EtOH) and isopropanol (2-PrOH) using the following systems: Ni-alloy [27], Mo-doped Co-B alloy [28], $Ni_{34.1}Fe_{36.0}B_{29.9}$ [29], $Cu_{3/2}PMo_{12}O_{40}$/Raney Ni [30], Pt–$Sn_{0.3}/SiO_2$ [31], $Zr(OH)_4$

[32]. Also, high yields were achieved in aqueous solution by bimetallic catalysts (Ir–ReO_x/SiO_2 [33], Pd–Cu/MgO [34]) and MOF-based catalysts (Ru/Zr-MOF [35], Pd/H-UiO-66 [36]). Concerning the gas phase, FOL yields between 86-97% were achieved over Cu on several supports: SiO_2 [37], SiO_2 (SBA-15) [38], MgO [39], ZnO [40]. However, many catalysts were highly active, but not selective to FOL and underwent further hydrogenation to THFA.

1.2.2. Selective hydrogenation of FUR to THFA

In industry, THFA is produced by hydrogenation of FOL over supported Ni catalysts both in gas and liquid phase [41]. However, many reported works have been focused on direct conversion of FUR into THFA using various catalytic systems. Nakagawa *et. al.* the reported the gas-phase hydrogenation of FUR using Ni/SiO_2 with a yield of 94% of THFA after 60 min time-on-stream (TOS) (turnover frequency (TOF) = 130 h^{-1}) [42]. Based on kinetic studies, it was found that total hydrogenation of FUR took place via two separate steps: initially hydrogenation of FUR to FOL and then to THFA [42, 43]. On the other hand, liquid-phase conversion of FUR to THFA was extensively investigated in the recent years. Table 1.3 shows the best results reported for the selective hydrogenation of FUR to THFA in liquid phase. Complete conversion of FUR was achieved and yields of THFA between 92-100% were obtained in aqueous solution on supported Ni, NiPt, Pd, and Rh catalysts (entries 4, 5, 11, 16, 17). Likewise, complete conversion of FUR was achieved in organic solvents, particularly in EtOH and 2-PrOH. For instance, up to 99% yields of THFA were obtained using non-noble bimetallic Ni-Co and Ni-Cu catalysts in EtOH and supported Ni and Pd catalysts in 2-PrOH (entries 2, 3, 6-10, 12, 14). These catalysts generated excellent selectivity to THFA under mild to moderate conditions. Briefly, the hydrogenation of FUR to FOL and THFA was extensively explored using several non-noble and noble metal catalysts. However, the selective ring-opening of FUR and its alcoholic derivatives, FOL and THFA, to 1,5-PeD is still challenging due to the by-product formation of 1,2-PeD. Therefore, it is necessary to study the catalytic behavior of hydrogenolysis of these feedstocks to pentanediols (PeDs) in different solvents.

Table 1.3. Best reported yields of THFA by liquid phase hydrogenation of FUR under batch conditions.

Entry	Catalyst	Solvent	Reaction conditions				Conv. [%]	Yield [%]	Ref
			Catalyst:Substrate (Cat:Sub) (g:g)	T [°C]	p(H_2) [MPa]	t [h]			
1	Supported Ni/Cu	-	0.03	130	4	3	100	97	[44]
2	CuNi/CNT	EtOH	0.17	130	4	10	100	90	[45]
3	CuNi/MgAlO	EtOH	0.10	150	4	3	100	95	[46]
4	Ni/Ba–Al_2O_3	H_2O	0.4	140	4	4	99	99	[47]
5	Ni-LN650	H_2O	0.31	120	4	3	100	100	[48]

6	RANEY® Ni–Al(OH)$_3$	2-PrOH	0.52	110	3	1.25	100	99	[49]
7	Ni@C	2-PrOH	0.1	120	3	3	100	90	[50]
8	Ni-Co/SBA-15	EtOH	0.14	130	4.5	3	100	92	[51]
9	NiCo/SiO$_2$-MOF	EtOH	0.13	80	3	8	100	99	[52]
10	NiCo/SBA-15	2-PrOH	0.10	200	8	8	100	93	[53]
11	Pd/UiO-66	H_2O	0.5	60	1	4	100	100	[54]
12	Pd-HAP	2-PrOH	0.3	40	1	4	100	100	[55]
13	Pd–Pt/TiO$_2$	-	0.002[a]	30	0.3	4	100	95	[56]
14	PdCo$_3$O$_4$@NC	2-PrOH	0.73	150	2	6	100	95	[57]
16	PtNi/C	H_2O	0.5	35	2	12	99	93	[58]
17	Rh/C	H_2O	0.42	30	1	12	100	92	[59]
18	Ru−MoO$_x$/CN	H_2O	0.42	100	2	1	92	91	[60]

[a] molar ratio.

1.3. Hydrogenolysis of FUR and FOL to PeDs in liquid phase

Historically, the first reported syntheses of PeDs from FUR and its derivatives was published in 1923 using platinum oxide [61]. In 1931, copper chromite was reported as an active catalyst for direct hydrogenolysis of FOL to 1,2-PeD and 1,5-PeD with a total yield of 70% [62]. Table 1.4 lists the reported results of hydrogenolysis of FUR and FOL in organic solvents, mainly EtOH, using several catalytic systems. Concerning non-noble metal catalysts, although Cu and Co metals are active catalysts for this reaction, they are not selective to one type of PeDs. Consequently, both 1,2- and 1,5-PeD were obtained under batch conditions in different yields (Table 1.4). In the case of conversion of FUR in EtOH, the maximum yield of 1,5-PeD was 49% with the lowest formation of 1,2-PeD (9%) over Co-Mg−Al oxides (entry 7). In contrast, the maximum yield of 1,2-PeD was 46% (with a 1,5-PeD yield of 24%) over CuMgAlO-S3 (entry 4). This implies that the Co-based catalyst is more selective to 1,5-PeD and Cu more to 1,2-PeD on Mg-Al oxides. This was proven also by other works on hydrogenolysis of FOL on mixed 0.25Cu-2.5Co-Al oxides which showed a higher formation of 1,5-PeD (41%) compared to 1,2-PeD (16%) probably due to the higher molar ratio of Co to Al than Cu to Al (5 times more) (entry 6), and the lowest reported yield of 1,5-PeD was 19% using Cu-Al_2O_3 (entry 1). Moreover, the formation of THFA was significantly higher in the case of Co-containing catalysts compared to Cu catalyst (Table 1.4). Using Cu catalysts, only traces of THFA were detected, however, a higher formation of THFA was observed with Co and Co-Cu mixed catalysts (compare entries 1-4 and 5-7). It is most likely that a Co catalyst tends more to hydrogenate

FUR or FOL to THFA where the 1,2-C–O bond of THFA is easier to cleave, while a Cu catalyst more tends to cleave first the 4,5-C–O bond of FOL and then to hydrogenate the resulting double bonds forming 1,2-PeD via the intermediate 2-oxopentanol. But the possibility of cleaving also the 1,2-C–O of THFA forming 1,5-PeD is not excluded.

Table 1.4. Reported yields of PeDs in liquid-phase hydrogenolysis of FUR and FOL.

Entry	Catalyst	Metal loading [wt%] (molar ratio)	Sub	Solvent	Reaction conditions				X [%]	Yield [%]		Ref
					Cat: Sub (g:g)	T [°C]	p(H_2) [MPa]	t [h]		FOL + THFA	1,2- + 1,5- PeD	
1	Cu-Al_2O_3	10 Cu	FOL	EtOH	0.1	140	6	8	86	0+2	41+19	[63]
2	CuMg	39.6 Cu	FOL	2-PrOH	0.2	140	6	10	90	0+4	45+22	[64]
3	Cu–$Mg_3AlO_{4.5}$	10 Cu	FOL	EtOH	0.1	140	6	24	99	0+2	51+29	[65]
4	CuMgAlO-S3	4.9Cu (Mg:Al=3.2)	FUR	EtOH	-	150	6	6	84	5+0	46+24	[66]
5	Cu-$LaCoO_3$	10 Cu	FOL	EtOH	0.1	140	6	2	100	0+29	15+40	[67]
6	Cu-Co-Al oxides	(0.25 Cu, 2.75Co)	FOL	EtOH	-	160	4	2	99	0+15	16+41	[68]
7	Co-Mg−Al oxides	(1.5Co, 1.5Mg)	FUR	EtOH	0.5	170	5	4	100	0+12	9+49	[69]
8	NiFeMgAl	(1.6Ni, 0.4Fe)	FUR	EtOH	0.25	170	4	3	100	0+29	22+27	[70]
9	Li-Pt/Co_2AlO_4	1.9 Pt, 1.4 Li	FUR	-	-	140	1.5	24	100	20+30	15+34	[71]
10[a]	Pt/Mg(Al)O@ Al_2O_3	0.08% Pt	FOL	EtOH	-	200	3	-	41	0+14	17+6	[72]
11	Pt/CeO_2-C	4.5Pt	FOL	EtOH	0.5	165	2	8	50	0+7	37+4	[73]
12	Pt/hydrotalcite	1mol% Pt	FOL	2-PrOH	-	60	3	4	99	0+50	16+28	[74]
13	Rh/OMS-2	1 Rh	FUR	toluene	0.34	160	3	8	92	30+40	8+22	[75]

[a] WHSV= 0.12 h^{-1}.

Regarding noble metal catalysts, several Pt and Rh catalysts were active, but not selective to one specific PeD (Table 1.4). In the case of hydrogenolysis of FOL by Pt catalysts, the formation of both 1,2- or 1,5-PeD was influenced remarkably by the support and the solvent. For instance, higher formation of 1,2-PeD was reported using Pt on Mg(Al)O@Al_2O_3 and CeO_2-C in ethanol while higher yields of THFA and 1,5-PeD resulted in the case of Pt/hydrotalcite in

2-PrOH (entries 10-13). Similarly, Rh on manganese oxide octahedral molecular sieves (Rh/OMS-2) was found to be selective in conversion of FUR to 1,2-PeD in MeOH, EtOH and PrOH (no formation of 1,5-PeD or THFA), but both 1,2- and 1,5-PeD were obtained in 1,4-dioxane and toluene with higher proportions of 1,5-PeD and THFA (entry 13) [75]. Another mixed metal systems reported were NiFeMgAl and Li-Pt/Co_2AlO_4 which were also active, but not selective to one product (entries 8,9). In summary, all previous works in liquid phase hydrogenolysis of FUR and FOL showed a significant impact of the metal and the type and morphology of the support as well as of the solvent and reaction conditions on the reaction pathway. It also implies that the best selective catalyst to 1,5-PeD tends to directly hydrogenate FUR (or FOL) to THFA whose 1,2-C–O bond is easier to cleave to form 1,5-PeD

1.4. Selective conversion of FUR and THFA into 1,5-PeD in liquid phase

1.4.1. Indirect conversion of THFA into 1,5-PeD

The first approach to obtain selectively 1,5-PeD was the indirect conversion of THFA via a multi-step reaction route using several cost-efficient catalysts. This approach was first described in 1946 and contains the following steps (Scheme 1.3) [76]:

1. Dehydration of THFA to 3,4-dihydropyran (3,4-DHP) in vapor phase over ɣ-Al_2O_3.
2. Hydration of 3,4-DHP to 2-hydroxytetrahydropyran (2-HY-THP) using HCl.
3. Hydrogenolysis of 2-HY-THP to 1,5-PeD over copper chromite as catalyst.

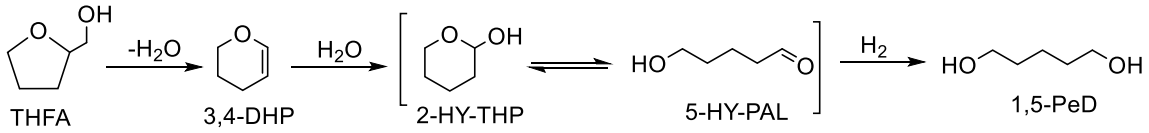

Scheme 1.3. Indirect conversion of THFA to 1,5-PeD (adapted from [2, 76]).

Applying this multistep approach, the maximum total yield of 1,5-PeD from THFA was 70% [77]. However, the increased number of reaction steps, including the separation step of HCl, and purification of the target diol from intermediary products makes this process economically inefficient. On the other hand, the use of a toxic chromite-containing catalyst makes the hydrogenolysis step environmentally undesirable. Therefore, this approach was further developed in 2017 by using more selective catalysts which increased the yields of 1,5-PeD to 85-90% [2, 9, 10]. The second hydration step was carried out without a catalyst instead of using HCl, and Ru/C was used instead of copper chromite in the third step of hydrogenolysis of 2-HY-THP to 1,5-PeD. Moreover, it was proposed to add an initial step for the hydrogenation of FUR to THFA using Ni/SiO_2, and the overall yield of 1,5-PeD following this redesigned multistep reaction sequence was found to be 80% [10]. According to a pilot plant analysis, the calculated minimum selling price per ton of 1,5-PeD was close to 2000 $ compared to 6000$ (1,5-PeD market price) [10]. The purpose behind developing the multistep approach was to

use cheap catalysts which could be applied for large-scale processes without limitation for selective synthesis of 1,5-PeD. Nevertheless, the use of precious Ru/C besides the increased process costs did not serve this purpose. Thus, alternatively to multistep approach, single-step approaches for selective C–O bond hydrogenolysis of THFA to 1,5-PeD were also developed in the recent years using different noble metal catalytic systems as discussed in the following paragraph.

1.4.2. Direct hydrogenolysis of THFA to 1,5-PeD

The first successful ring-opening reaction of THFA was reported in 1948 using copper chromite with yields of 1,5-PeD between 40-47% [11]. However, the selectivity of 1,5-PeD from THFA was further improved using modified noble metal catalysts in 2009 [78, 79]. Scheme 1.4 shows four main pathways for hydrogenolysis of THFA. 2-MTHF and THF were obtained by cleaving off the hydroxymethyl group of THFA (pathways 1 and 4). The hydrogenolysis of THFA led to a cleavage of the C–O bond of the tetrahydrofuran ring from both sides resulting in 1,2- and 1,5-PeD (pathways 2 and 3), respectively. The over-hydrogenation of PeDs or furfural derivatives resulted in the formation of primary alcohols, particularly of 1-PeOH, 2-PeOH and 1-BuOH. Due to these different possible pathways, it is necessary to choose a selective catalyst which undergoes pathway 3 under appropriate conditions to achieve the highest possible yield of 1,5-PeD.

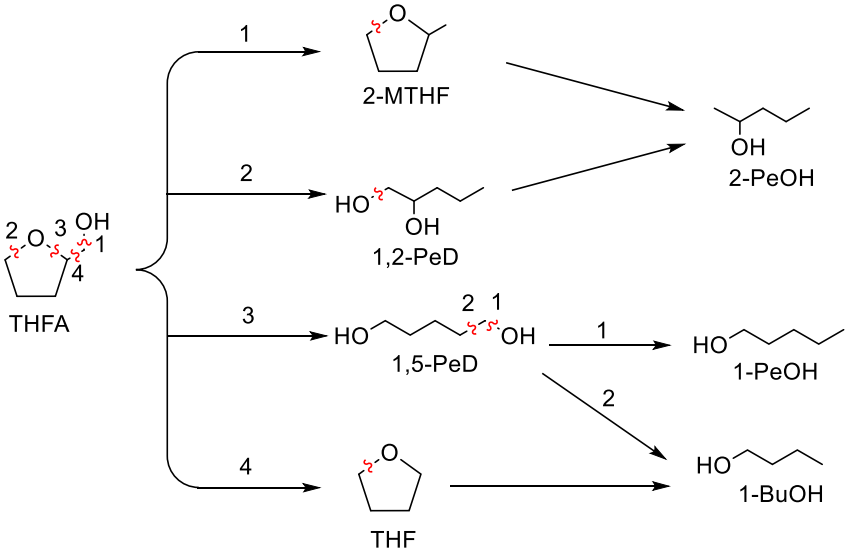

Scheme 1.4. Reaction pathways for direct hydrogenolysis of THFA (adapted from [79]).

Table 1.5 shows the best catalysts for selective hydrogenolysis of THFA to 1,5-PeD. This reaction was extensively investigated using noble metals (Rh, Ir) modified by ReO_x, MoO_x on SiO_2 and active carbon. These systems achieved a high selectivity to 1,5-PeD up to 98% under the following batch conditions: 100-120°C, 3.4-8 MPa (entries 1, 14-21). The best yields of 1,5-PeD ranged from 77 to 94% after 24 h (entry 15, 17, 19, 20). The main reported by-products were 1-PeOH and 1-BuOH [78, 79].

Table 1.5. Selective hydrogenolysis of THFA to 1,5-PeD in liquid phase.

Entry	Catalyst	Metal loading [wt%] (molar ratio)	Solvent	Reaction conditions				X [%]	1,5-PeD		Ref.
				Cat:Sub (g:g)	T [°C]	p (H_2) [MPa]	t [h]		Y [%]	S [%]	
1	Ir–ReO_x/SiO_2	4 Ir (Re:Ir=2)	H_2O	0.2	100	8	2	60	57	94	[80]
2[a]	Ir-MoO_x/SiO_2	4 Ir (Mo:Ir=0.13)	H_2O	-	120	6	Flow	70	52	74	[81]
3[a]	Ir–VO_x/SiO_2	4 Ir (V:Ir=0.1)	H_2O	-	80	6	Flow	85	57	67	[82]
4	Ni/Al_2O_3	20 Ni	H_2O	-	250	-	Flow	17	10	59	[83]
5	Ni–$La(OH)_3$	(Ni:La=2.5)	2-PrOH	0.5	150	2	84	99	92	93	[84]
6	Ni–Y_2O_3	(Ni:Y=2.5)	2-PrOH	0.5	150	2	72	80	78	97	[84]
7	Ru/Ni-Y_2O_3	1 Ru, (Ni:Y=2.5)	2-PrOH	0.5	150	2	40	93	86	93	[85]
8	Ni-WO_x	10 Ni, 15 W	H_2O	0.1	250	3.4	4	36	15	41	[86]
9	Ni/ZSM–5	10.3 Ni	H_2O	0.1	250	3.4	4	36	12	33	[87]
10	Pt/WO_3@SiO_2	3 Pt, (W:SiO_2=0.8)	H_2O	0.25	200	6	12	83	60	73	[88]
11[b]	Pt/WO_3@SiO_2	10 Pt (W:Pt= 0.5)	H_2O	-	200	3.6	Flow	20	16	78	[89]
12	Pt-WO_3/ZrO_2	3 Pt, 5 W	2-PrOH	0.33	150	5	15	100	43	43	[90]
13[c]	Rh/MCM-41	1 Rh	H_2O	0.25	80	4 + 14	24	81	73	91	[91]
14	Rh-MoO_x/C	4 Rh (Mo:Rh= 0.13)	H_2O	0.1	120	3.4	4	52	47	91	[92]
15	Rh-MoO_x/SiO_2	4 Rh (Mo:Rh= 0.13)	H_2O	0.1	100	8	24	94	85	90	[79]
16	Rh/SiO_2+MoO_3	4 Rh	H_2O	0.1	120	6	20	33	26	78	[93]
17	Rh-ReO_x/C	4 Rh (Re:Rh=0.25)	H_2O	0.1	100	8	24	99	94	95	[94]
18	Rh-ReO_x/C	4 Rh (Re:Rh=0.5)	H_2O	0.1	120	3.4	4	47	46	97	[92]
19	Rh–ReO_x/SiO_2	4 Rh (Re:Rh=0.5)	H_2O	0.1	120	8	24	96	77	80	[78]

20	Rh-ReO_x/SiO_2	4 Rh (Re:Rh=0.5)	H_2O	0.1	100	8	24	90	82	92	[79]
21	Rh-ReO_x/SiO_2	4 Rh (Re:Rh=0.5)	H_2O	0.2	100	8	2	54	52	97	[80]

[a] Q= 0.04 mL min^{-1}, [a] Q(H_2)= 60 mL min^{-1}, [b] space time= 1.67 min g mL^{-1}, [c] in supercritical CO_2 (p= 14 MPa).

Based on EXAFS analysis, the presence of a bond between Re (or Mo) and Re was as an evidence for a direct interaction between Rh metal and ReO_x (or MoO_x) species in the interface area [78, 79, 95-97]. This interface was proposed as the catalytically active site in C–O bond hydrogenolysis [78, 79, 95-97]. However, different model structures for Rh modified by ReO_x and MoO_x were illustrated, suggesting that three ReO_x atoms adsorbed on the Rh metal site, whereas only one isolated MoO_x atom adsorbed on Rh (Figure 1.2) [96, 98]. In addition, an Ir catalyst modified by MoO_x and VO_x was active, but not stable under flow conditions due to leaching of the modifiers in aqueous solution (entries 2, 3). Another modified system was Pt-WO_x/SiO_2 which showed lower conversion of 83% and 20% in aqueous solution under batch and flow conditions, respectively (entries 10, 11). Rh-MCM-41 was the only non-modified Rh catalyst with high selectivity to 1,5-PeD due to the applied supercritical conditions (additional p(CO_2)=14 MPa) (entry 13). Nevertheless, the high costs of applied modified noble catalysts (7-10 wt% total loading of precious metals) versus the low stability of them due to the leaching of the modifying metals (Re, Mo, V, W) limited the possibility of applying these systems in industrial scale. Also, the leak of studies under flow conditions obstructed their consideration for such continuous processes.

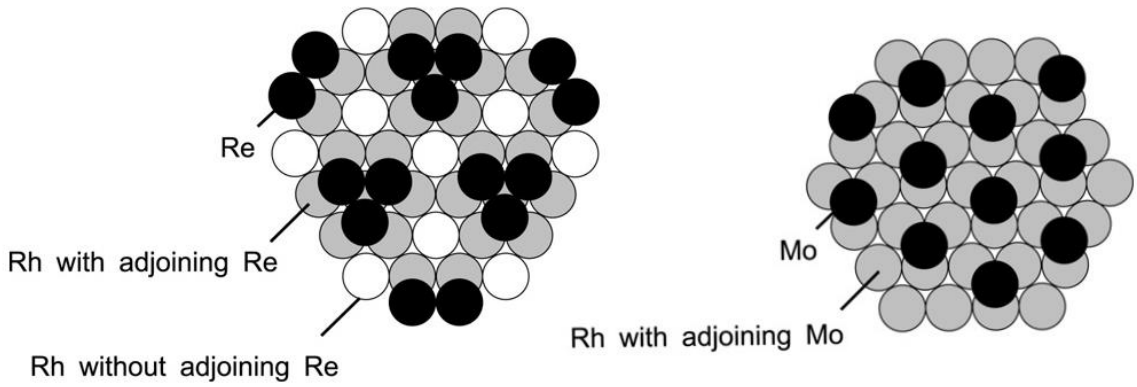

Figure 1.2. A model structure of Rh-ReO_x (left) and Rh-MoO_x (right) on SiO_2 (4wt Rh; M:Rh= 0.13, M= Re, Mo) [96].

Thus, in the recent years, the focus turned to noble metal-free catalysts, particularly to nickel, cobalt, and copper catalysts. However, most reported Cu or/and Co-based catalysts were not selective to 1,5-PeD, consequently 1,2-PeD was obtained as a by-product in different yields (Table 1.4, entries 1-7). The reported studies on Ni catalysts showed higher selectivity to 1,5-PeD (entries 4, 8, 9). However, the by-products formed such as 1,3,5-pentanetriol, 1-BuOH, THF and THP, on Ni/Al_2O_3, Ni-WO_x and Ni/ZSM–5 Significantly decreased the selectivity to

1,5-PeD under batch and flow conditions [83, 86, 87]. Interestingly, the works by *Wijaya et al.* on Ni-Y_2O_3 and Ni-$La(OH)_3$ in 2-propanol (2-PrOH) reported a high selectivity to 1,5-PeD up to 97% after 72-84 h (entries 5, 6). It was assumed that the interaction between Ni and Y_2O_3 species at the phase boundary is responsible for conversion of THFA and selectivity to 1,5-PeD [99]. This is consistent with the conclusion of the Tomishige group that the formed interface between Rh and Re species plays a key role in the ring-opening reaction of THFA [78, 79, 95-97]. Based on that, the formation of an active interface caused by strong interaction between active species seems to be extremely important in order to achieve high yields of 1,5-PeD. Nevertheless, the conversion of THFA over Ni catalysts was lower than that of noble metal catalysts previously investigated. Complete conversion of THFA could not be achieved within 24 h (99% after 84 h) (entries 5, 6). Even after adding 1 wt% of Ru on Ni-Y_2O_3, a complete conversion was not achieved within 40 h (entry 7). Also, 1-BuOH was the main side product over Ni-Y_2O_3 catalysts in 2-PrOH [84], and no formations of 1-PeOH was observed as in the case of modified noble metal catalysts [79]. Although nickel is an economically feasible metal and it is widely applied in industry without limitation, the stability of reported selective catalysts has not yet been investigated in a continuous flow reactor. To understand the reason behind the low conversion and the high selectivity of nickel as well as the role of the rare-earth metal support, it is essential to reveal the structure-activity relationships. It is more important to elucidate the mechanism of the ring-opening reaction of THFA using Ni catalysts which has not been discussed before.

1.4.3. One-pot selective conversion of FUR to 1,5-PeD

As discussed before, the selective ring opening of THFA to 1,5-PeD using noble metal catalysts in aqueous solution was extensively investigated (Table 1.5). As shown in Table 1.6, a lower number of studies was carried out on direct conversion of FUR to 1,5-PeD since this reaction was more challenging for several reasons. i) FUR is known for its low stability and the tendency to polymerization at high temperatures [100-102]. ii) The furan ring can be attacked by an electrophile via an electrophilic substitution, while iii) the existence of the aldehyde group makes the molecule also reactive in aldol condensation reactions [101, 102]. More important, iv) the opening of the furan ring using acidic catalysts at higher temperatures can produce some even more reactive sites for polymerization [33, 102, 103]. *Liu et al.* reported that the color of the reaction mixture intended to yellow color at 100 °C, while it was almost colorless at 40 °C, at complete conversion of FUR hinting to formation of FUR-based oligomers and polymers [103]. Therefore, it was suggested to carry out the hydrogenolysis of FUR in two-step reactions under different temperature regimes [33, 103]. For instance, Ir–ReO_x/SiO_2 was a highly selective catalyst in ring-opening of THFA to 1,5-PeD [80]. However, it was not active in the hydrogenation of aldehyde group and furan ring [33, 103].

Table 1.6. One-pot selective conversion of FUR to 1,5-PeD in batch reactor.

Entry	Catalyst	Metal loading [wt%] (molar ratio)	Solvent	Reaction conditions				X [%]	Yield [%]		Ref.
				Cat:Sub (g:g)	T [°C]	p (H_2) [MPa]	t [h]		THFA	1,5-PeD	
1	CoAl-spinel	20 Co	2-PrOH	-	150	4	8	100	69	24	[104]
2	Ni–$La(OH)_3$	(Ni:La=2.5)	2-PrOH	0.5	150	2	72	100	32	56	[84]
3	Ni–Y_2O_3	(Ni:Y=2.5)	2-PrOH	0.5	150	2	72	100	38	46	[84]
4[a]	Ni–Y_2O_3	(Ni:Y=2.5)	2-PrOH	0.5	150	2	24	100	30	42	[99]
5[b]	Pd–Ir–ReO_x/SiO_2	0.66 Pd, 4 Ir (Re:Ir=2)	H_2O	0.1	40 - 100	6	8 - 48	100	6	71	[33]
6[b]	Rh–Ir–ReO_x/SiO_2	0.66 Rh, 4 Ir (Re:Ir=2)	H_2O	0.1	40 - 100	6	8 - 48	100	4	78	[103]
7[c]	Pt@Al_2O_3+$NaBH_4$	11.8 Pt	H_2O	0.3	45	0.45	8	100	25	75	[105]

[a] from FOL; [b] two-step reaction, [c] FUR:$NaBH_4$= 0.33.

Thus, metallic Pd and Rh were additionally added to improve the catalytic activity (entries 5, 6). The first step was to convert FUR to THFA at low temperature (40 °C) to avoid FUR polymerization for 8 h, and in the second step, the reaction mixture was heated up to 100 °C for 48 h to cleave the tetrahydrofuran ring at the same pressure (6 MPa) [33, 103]. The total yields of 1,5-PeD were between 71-78% (entries 5,6). Similar yields were obtained over highly loaded Pt/Al_2O_3 at near-ambient temperature with the aid of $NaBH_4$ (entry 7). Regarding non-noble metal catalysts, Ni on Y_2O_3 and $La(OH)_3$ in 2-PrOH showed yields between 46-56% after 72 h (entries 2-3), and Ni on CoAl-spinel yielded 24% of 1,5-PeD after 8 h (entry 1). Nevertheless, traces of 1,2-PeD (≤2) were observed almost in all reported studies on direct conversion of FUR, but not in the hydrogenolysis of THFA. The formation of 1,2-PeD might result from FOL, a small quantity of which was probably catalytically hydrogenolyzed at the 4,5-C–O bond before hydrogenation of the furan ring. Generally, complete hydrogenation of FUR or FOL to THFA was achieved in the first hours but cleaving the tetrahydrofuran ring took several days. That might be caused by catalyst poisoning in the beginning due to the FUR polymerization which blocks the active sites, at least partially, on the catalyst surface. For instance, FOL was totally converted to THFA over Ni-Y_2O_3 within 1.5 h [99]. Then, THFA was converted to 1,5-PeD obtaining a yield of 42% in 24 h (Table 1.5, entry 4). However, the yield of THFA did not change significantly after the first day and remained similar with 30% and 25% after 24 and 48 h [99]. The activity drop was attributed to the polymerization of FOL where FOL-based polymers were detected on the used Ni-Y_2O_3 catalyst surface by FTIR

measurements [99]. Thus, it is important to improve the catalyst stability to obtain higher yields of target diol in a shorter time span. Also, the best reported catalysts for selective conversion of FUR to 1,5-PeD were precious metals which are not preferable for industrial applications. Moreover, the reported results were obtained under batch conditions which could not be applied for continuous processes without further investigations in flow systems. Therefore, it is important to develop highly selective catalysts under batch conditions and to test them afterwards in a continuous reactor set-up for stability and selectivity.

1.5. Reported mechanisms of ring-opening reaction of THFA

In the recent ten years, the mechanism of C–O bond hydrogenolysis of THFA to 1,5-PeD was a subject of debate [106]. Two methods were applied to elucidate the mechanism, particularly density functional theory (DFT) and isotope labelling technique. Based on the catalytically active species and products distribution, three mechanisms were proposed for the ring-opening reaction on modified Rh catalysts in aqueous solution [80, 92, 93] (see paragraph 4.4 for more detailed description of mechanisms). Briefly, the formation of metal hydrides on the Rh metal surface which directly attack the C–O bond in β-position of the formed alkoxide was suggested for the first regioselective mechanism called “hydride mechanism” (adsorbed THFA on ReO_x species) resulting in ring cleavage (Scheme 1.5a) [80, 95, 98, 107]. Regarding the second “carbenium ion” mechanism, the formation of a carbenium ion was assumed as an intermediate formed by proton transfer to THFA and causing a concerted hydrogen shift from the α-position to the β-position, resulting in C–O dissociation (Scheme 1.5b) [92]. The third mechanism, “hydrogen-transfer ring-opening”, shows the same concerted hydrogen shift after chemisorption of THFA to MoOH to form a stable intermediate (5-HY-PeAL) that is hydrogenated by metallic species to 1,5-PeD (Scheme 1.5c) [93]. On the other hand, an indirect muti-step reaction route using different catalysts was reported as an alternative approach for the selective conversion of THFA to 1,5-PeD through sequential dehydration-hydration-hydrogenolysis steps leading to 3,4-DHP and 2-HY-THP (or 5-HY-PeAL), respectively, as possible intermediates (see Scheme 1.3) [2, 9, 76]. Nevertheless, all reported studies deal with rhodium-catalyzed hydrogenolysis in presence of acidic modifiers in aqueous solution for which the mechanism was extensively discussed in previous works [80, 92, 93] (see paragraph 4.4 for more detailed description of mechanisms). However, a mechanistic study of nickel-catalyzed hydrogenolysis of THFA on basic supports, which were found to be highly selective to 1,5-PeD in 2-PrOH, has not yet been explored [84, 85, 99].

a) hydride attack

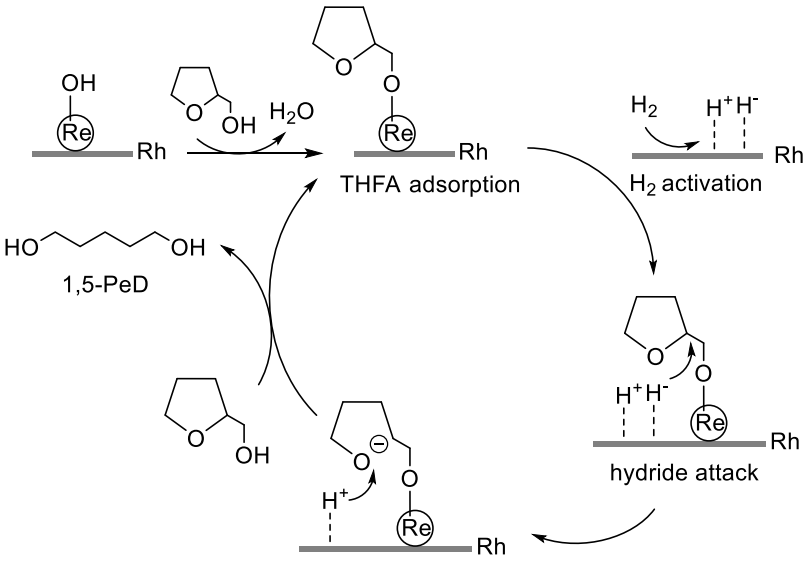

b) carbenium ion

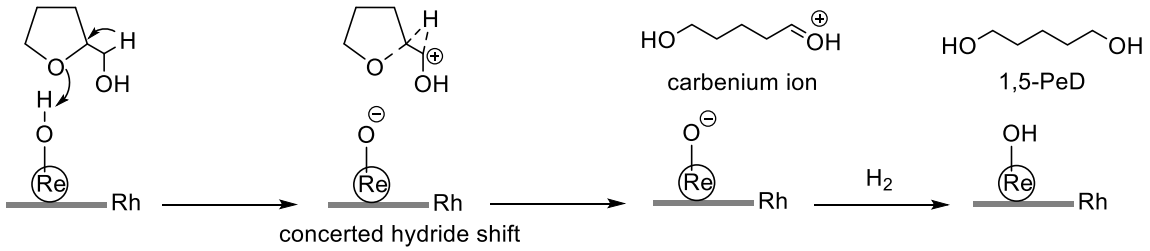

c) hydrogen transfer

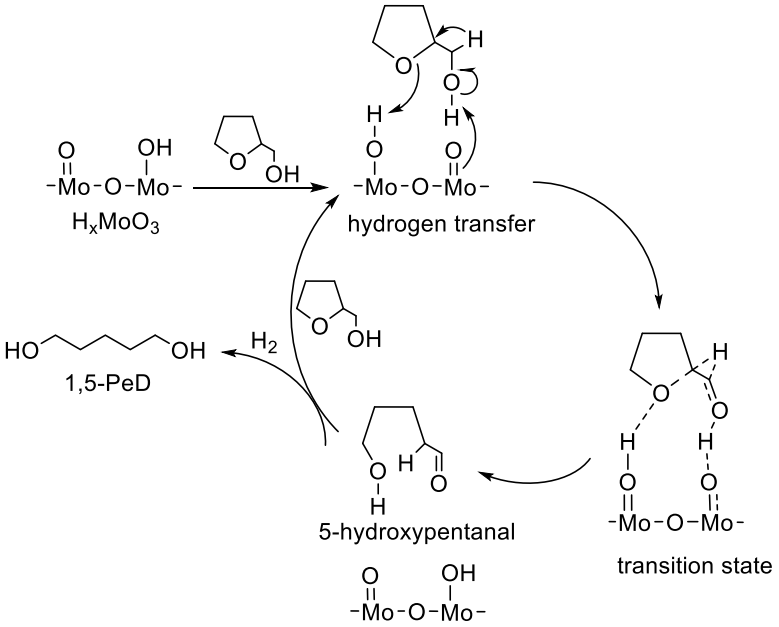

Scheme 1.5. Proposed mechanisms for hydrogenolysis of THFA over acid-modified Rh catalysts in aqueous solution (a-c) (adapted from [106]).

2. Motivation and Objective

As mentioned in Chapter 1, due to negative environmental impact of petroleum-based polymers and plastics and the increased global demand for polyurethanes, polyesters and plasticizers, it is highly desired to develop alternative reaction routes to get these polymers based on renewable resources and especially on lignocellulose feedstocks. For this purpose, FUR and its derivative THFA are promising and well available C5 building blocks. They can be selectively converted to 1,5-PeD indirectly via multi-step reactions using different catalysts, mainly non-environmentally friendly copper chromite, or directly, using precious expensive noble metals, such as Rh and Ir catalytic systems (see paragraph 1.4). However, the high costs of these modified noble metal catalysts versus their low stability in continuous reaction due to leaching of the modifying metals (Re, Mo, V, W) limited the possibility of applying these systems in an industrial scale. In contrast, non-noble metal catalysts in hydrogenolysis of FUR and THFA were mostly not selective enough to either 1,5- or 1,2-PeD, preventing their industrial application. Moreover, the low number of studies on this reaction under flow conditions makes investigations in continuous reactors even more valuable for practical aspects. Therefore, the continuous synthesis of bio-based 1,5-PeD over stable catalyst is necessary to optimize the selectivity to the target diol and the productivity of the process.

Considering theoretical aspects, the development of highly selective and stable catalysts requires a deep understanding of the effective parameters on the catalyst preparation procedures and catalytic investigations by revealing structure-activity relationships using advanced characterization techniques, including *in situ* methods. More importantly, the elucidation of the mechanism of hydrogenolysis of C–O bonds using noble metal-free catalysts in non-aqueous solution has not yet been explored. In particular, the mechanism of the selective C–O bond hydrogenolysis of THFA to 1,5-PeD using nickel catalysts on basic rare-earth metal-containing supports is not known in contrast to the above mechanism using Rh and Ir catalytic systems modified with acidic metal oxides in water [80, 92, 93, 95, 98, 107]. Therefore, the aim of this doctoral thesis is to replace the conventional noble metal catalysts by Ni catalysts for selective hydrogenolysis of THFA to 1,5-PeD in a continuous process in liquid-phase. To achieve the objectives of this study, the following tasks must be fulfilled:

1. Synthesis of several active noble metal (benchmark) and non-noble metal catalysts.
2. Investigation of the catalytic behavior and exploration of the structure-reactivity relationships.
3. Optimization of reaction conditions in batch and flow reactors to achieve the highest 1,5-PeD yields.
4. Testing the stability of most active catalysts in long-term continuous runs.
5. Elucidation of the mechanism of C–O bond hydrogenolysis of THFA to 1,5-PeD.

3. Experimental Section

3.1. Catalyst preparation

3.1.1. Preparation of Rh catalysts

As a benchmark, rhodium catalysts were prepared by an impregnation method with several modifiers (ReO_x, MoO_x, WO_x, NbO_x, TaO_x) and supports (SiO_2, TiO_2, Al_2O_3, ZrO_2 and activated carbon) applying similar procedures to ref. [78, 79, 92]). The following materials were purchased and used without further purification: $RhCl_3 \cdot xH_2O$ (38-40%Rh), NH_4ReO_4 (≥99%), $(NH_4)_2RuCl_6$, $(NH_4)_6Mo_7O_{24} \cdot 4H_2O$ (81-83.0% MoO_3), $(NH_4)_{10}H_2(W_2O_7)_6$ (99.9%), $NbCl_5$ (99.9%), $TaCl_5$ (99.9%), TiO_2 (anatase) (99.7%), TiO_2 (rutile) (99.5%), TiO_2 (brookite) (99.9%) (Sigma-Aldrich); TiO_2 (P25) (VP AEROPERL® P 25/20) (Evonik); ZrO_2 (Alfa Asear); activated carbon (Vulcan XC72) (Fuel Cell Store). Both SiO_2 (Gel X) and (SBA-15) were prepared in the laboratory from tetraethoxysilane (TEOS) (98%) (Alfa Aesar) and γ-Al_2O_3 support from Disperal P2 (AlOOH, boehmite 75% Al_2O_3) (Sasol) (see Appendix for synthesis procedure).

In the case of wet impregnation (WI) to obtain a Rh catalyst loaded with approx. 2.7 wt%, 8 mL of 0.5 M aqueous solution of $RhCl_3$ (50 mL) was added to 1 g of the support and diluted with 10 mL of distilled water. The mixture was stirred for 30 min without heating. Then, water was evaporated at 60 °C for 1 h. The residue was dried overnight at 120°C in a drying oven. Next day, the modifier was added, for example to obtain approx. 3.0 wt% of Re content: 4 mL of 0.5 M aqueous solution of NH_4ReO_4 (50 mL) was impregnated to the dried supported 2.7wt% Rh (Re:Rh=0.6) precursor. The same drying procedure was repeated. In the case of incipient wetness impregnation (IWI), the same preparation method was repeated step by step without adding 10 mL of distilled water in the beginning. However, both aqueous solutions of $RhCl_3$ and NH_4ReO_4 were added together in one step in the case of co-impregnation. The other preparation steps were the same as described for WI. After drying, the fresh catalyst was crushed and sieved to fine powder (≤ 100 µm). Then, it was calcined in a furnace to 500 °C with a heating rate of 2 K min^{-1}, and held at this temperature for 4 hours. After calcination, the catalyst was reduced in a H_2 flow of 30 mL min^{-1} in a tube furnace at 300 °C (heating rate 1 K min^{-1}) overnight.

3.1.2. Preparation of Ni catalysts

A series of Ni catalysts on lanthanide supports (designation as Ni-Ln, Ln: La, Ce, Pr, Nd and Sm hydroxides or/and oxyhydroxides or/and oxides) (13-41 wt% Ni, Ni:Ln=0.5-2.8), including further rare-earth metal supports (Sc and Y) were prepared by a co-precipitation method [108]. All materials for nickel catalyst preparation were purchased and used without further purification: $Ni(NO_3)_2 \cdot 6\ H_2O$ (≥97%), $Ce(NO_3)_3 \cdot 6\ H_2O$ (99.9%), $Pr(NO_3)_3 \cdot 6\ H_2O$ (99.9%), $Nd(NO_3)_3 \cdot 6\ H_2O$ (99.9%), $Sm(NO_3)_3 \cdot 6\ H_2O$ (99.9%) (Sigma-Aldrich); $Y(NO_3)_3 \cdot 6\ H_2O$ (99.9%)

(Acros organics), $La(NO_3)_3 \cdot 6\ H_2O$ (99.9%) (abcr), NaOH (99.6%) (AlfaAesar). For instance, to prepare 3 g of 40 wt% of Ni on $La(OH)_3$, an aqueous solution of 0.46 M $Ni(NO_3)_2 \cdot 6\ H_2O$ (50 mL) was mixed with an aqueous solution of 0.46 M $La(NO_3)_3 \cdot 6\ H_2O$ (25 mL) at room temperature. The solution was acidic (pH= 3.5-4.0). 2 M NaOH aqueous solution (10 mL) was added dropwise to the acidic solution until pH≈14. The resulting mixture was stirred at R.T., for 1 hour. Then, the strongly basic solution was aged in a hydrothermal autoclave at 150 °C for 1-3 days. The resulting slurry was light green in various shades. The slurry was filtered under vacuum and the filtered gel was washed several times with hot water until pH≈7. It was stored in the fume hood for some days until it was totally dried. The dried gel was crushed and sieved to fine powder (grains ≤ 100 µm). These fresh catalysts were mixtures of nickel hydroxide and lanthanide hydroxide gels (denoted as Ni-Ln(F)) which were pretreated before the reaction. In addition, other preparation methods were applied, particularly ball-milling and wet impregnation. In the case of ball-milling, nickel hydroxide and lanthanide hydroxide were prepared separately applying the previous co-precipitation method. After obtaining dried powders of both components separately, they were ground into extremely fine powders using a ball mill for 3 h. Also, Ni on $La(OH)_3$ (Ni/La) was also prepared by wet impregnation. First, 0.4 M $La(NO_3)_3 \cdot 6\ H_2O$ (25 mL) was prepared alone as described above, only without adding an aqueous solution of $Ni(NO_3)_2 \cdot 6\ H_2O$ in the beginning. So, the same precipitation procedure was repeated until a fine white powder of $La(OH)_3$ was obtained. Then, the aqueous solution of 0.5 M $Ni(NO_3)_2 \cdot 6\ H_2O$ (50 mL) was added to $La(OH)_3$, and water was evaporated under vacuum for 1 h. After that, the resulting gel was dried in a drying oven at 120 °C overnight. Furthermore, all fresh catalysts were pretreated before the reaction. The calcination step was performed in a furnace with a heating rate of 3 K min^{-1} from R.T. to 350 °C, and then this temperature was maintained for 4 hours. The calcined catalyst was abbreviated as Ni-Ln(C) (Table 3.1). Then, the reduction step was carried out in a tubular furnace. The catalyst precursor was heated up in a gentle H_2 flow (30 mL min^{-1}) with a heating rate of 1 K min^{-1} to 250 °C with a holding time at 250 °C of 8 hours. The calcined catalyst was abbreviated as Ni-Ln(R) (Table 3.1). After reduction, the support nature was different depending on the lanthanide species lanthanum hydroxide, praseodymium mixed hydroxide-oxyhydroxide or samarium oxyhydroxide were formed (see Table 3.1). After reaction, the spent catalyst was abbreviated as Ni-Ln(S) (Table 3.1).

Table 3.1. Abbreviation of the Ni catalyst name after pretreatment and the reaction.

Examples for catalyst name	Ni content (wt%)	lanthanide support	After pretreatment	After reaction
40Ni-Ln(F)	40	$Ln(OH)_3$, Ln=La, Pr, Sm	-	-
40Ni-La(C)	40	$La(OH)_3$	Calcined	-
37Ni-Pr(R)	37	$Pr(OH)_3$+ PrO(OH)	Reduced	-
38Ni-Sm(S)	38	SmO(OH)	-	Spent

3.2. Catalyst characterization

The catalysts were characterized by ICP-OES, BET, XRD (including *in situ XRD)*, XPS (including pseudo *in situ* XPS), XAS (XANES and EXAFS), H_2-pulse chemisorption, TPR, TPD and (ABF-) HAADF-STEM with EDX elemental mapping techniques [108].

First, *inductively coupled plasma optical emission spectroscopy* (ICP-OES) was performed using a 715-ES ICP emission spectrometer (Varian, Palo Alto, CA, USA) to determine the metal contents in the prepared samples. For preparation procedure, each sample was digested in a mixture of hydrofluoric acid and a mixture of nitric acid and hydrochloric acid (1:3) (*Aqua regia*). Then, it was treated in a microwave-assisted apparatus at 200 °C and 60 bar.

For *Brunauer–Emmett–Teller* (BET) method, BET surface area and pore volume was calculated based on the measured N_2 adsorption isotherms (at -195°C) using a Micromeritics ASAP 2010 device. Before starting the measurement, the degasification of the samples was carried out at 200 °C for 4 h. The average pore diameters were calculated using the BJH method from the desorption branch of the isotherm.

X-ray powder diffractions (XRD) were recorded on a Panalytical X'Pert θ/2θ-diffractometer equipped with X'Celerator detector using automatic divergence slits and Cu $k\alpha_1/\alpha_2$ radiation (40 kV, 40 mA; λ= 0.15406 nm, 0.154443 nm). Cu beta-radiation was eliminated using a nickel filter foil. The measurements were carried out with 0.021°s^{-1}. Samples were fastened on silicon zero background holders. For further analysis, recorded intensities were converted from automatic to fixed divergence slits (0.25°). By using Pseudo-Voigt function of the HighScore Plus software package (Panalytical), peak positions and profiles were fitted. The phase was identified by International Center for Diffraction Data (ICDD), using PDF2 Database. Crystallite sizes were calculated based on the Scherrer-equation assuming the spherically shaped crystallites and using the integrated breadth [109]. K was set to 1.0747.

In situ XRD experiments have been conducted on a Panalytical Empyrean X'Pert θ/2θ - diffractometer equipped with a PIXcel 3D detector system using automatic divergence slits and Cu $k\alpha_1/\alpha_2$ radiation (40 kV, 40 mA; λ= 0.15406 nm, 0.154443 nm). Diffraction data of samples to be investigated under *in situ* conditions were recorded primarily to gain position references. For non-ambient measurements a mri TG-basic equipped with a Pt sample holder was used. Investigated samples were suspended in distilled water or ethanol, and the suspension was dropped on the Pt sample holder. The correct height of the sample was manually adjusted until the diffraction data matched the obtained reference dataset. Before starting the measurement program, the oven was flushed with He (40 mL min^{-1}) for 60 minutes. Gas feed was changed to 10% O_2 in He for calcination or 10% H_2 in He for reduction monitoring, respectively. The specimen was either heated to the desired temperature in 100 °C steps or continuously to the

desired temperature with a heating rate of 5 °C min^{-1}. The sample was allowed to equilibrate for 5 minutes before collecting the data at the desired temperature.

The XPS (*X-ray Photoelectron Spectroscopy*) data were obtained using an ESCALAB 220iXL (Thermo Fisher Scientific) with monochromatic Al Kα radiation (E = 1486.6 eV). Sample preparation was done on a stainless-steel holder with conductive double-sided adhesive carbon tape. The electron binding energies were acquired with charge compensation using a flood electron source and referenced to the C 1s core level of carbon at 284.8 eV (C–C and C–H bonds). For quantitative analysis, the peak fitting was deconvoluted with Gaussian-Lorentzian functions using the software Unifit 2021. The peak areas were normalized by the transmission function of the spectrometer and the element specific sensitivity factor of Scofield [110].

For pseudo *in situ* XPS, a laboratory based Near Ambient Pressure X-ray photoelectron spectroscopy system (NAP-XPS, SPECS Surface Nano Analysis GmbH, Germany) was used. The setup was equipped with a differentially pumped Phoibos 150 electron energy analyzer, a nozzle of 500 µm (allowing a maximum pressure of 10 mbar in the analysis chamber) and a monochromatic Al Kα radiation source (E = 1486.6 eV, operated at 70 W, spot size ~300 µm). The system was connected to a separate high-pressure cell (HPC 20, SPECS Surface Nano Analysis GmbH, Germany) which could be operated at gas pressures of up to 20 bar. The catalyst powder was pressed on a stainless-steel sample plate using a press with 5 mm diameter and a load of about 0.5 t to obtain a flat solid surface. For temperature monitoring, a thermocouple was attached to the sample plate and pressed on the sample surface (SPECS type SH 2/12). After the first XPS measurements, the sample was transferred to the high-pressure cell, the cell was closed and filled with H_2 until atmospheric pressure was reached. During the reduction, a constant flow of 30 mL min^{-1} H_2 was maintained by a Bronkhorst mass flow controller. The sample was heated from the back side to 250 °C for 3 hours using a halogen lamp. After the reductive gas treatment, the sample was transferred under vacuum back to the measurement chamber with a base pressure of $2 \cdot 10^{-9}$ mbar. The XPS measurements of the calcined and reduced samples were performed in a N_2 atmosphere at a pressure of 2 mbar.

X-ray Absorption spectroscopy (XAS) measurements were carried out to investigate the electronic properties and local geometric environment of Ni active species. The measurements were done in the *X-ray absorption near edge structure* (XANES) and *extended X-ray absorption fine structure* (EXAFS) Ni K-edge (8332.8 eV) at Spring8 storage ring (Japan). Experiments of the calcined, reduced and spent catalysts were done in transmission mode, and NiO and Ni foil were used as references for the evaluation of XANES and EXAFS data. Briefly, the samples were transferred from the autoclaves into a glass reactor in a glovebox to

avoid effects from atmospheric oxygen and moisture. The powderous sample was delimited in the middle of the measurement cell by small pieces of filter papers. The evaluation of XANES spectra was carried out using the Athena software package from the IFEFFIT program package [111]. This includes the removal of background spectra and the normalization as well as the linear combination analysis (LCA) of the fraction of different contribution of Ni species. Based on the linear combination analysis of the XANES spectra, the fraction of oxidized/reduced Ni nanoparticles was obtained as partial contribution of the reference spectra (i.e. Ni foil and NiO). to the catalyst/reaction spectra. For the analysis of EXAFS, XDAP software package for the data reduction and fits according to a standard procedures was used, as described elsewhere [112]. For data fits, theoretical references were calculated by FEFF 8.0 code and were subsequently calibrated with experimental EXAFS reference spectra of Ni foil and NiO powder [113, 114]. The EXAFS data were evaluated in the R-space (R: 0.0−4.5 Å), using the k-range from 3.2 to 11.0 $Å^{-1}$. In the EXAFS data fit, the coordination number (CN), the Debye−Waller factor (DWF), the Ni−Ni or Ni-O bond length (R), and the energy shift (E_0) were allowed to change freely.

H_2-Pulse chemisorption experiments were conducted on a 3-Flex Micromeritics instrument. 100 mg of each catalyst was loaded into a U-shaped quartz reactor and pretreated in a flow of 50 mL min^{-1} (5% H_2:Ar) at a heating rate of 10 K min^{-1} to the corresponding reduction temperature for 2 h. Then, the sample was flushed with pure Ar at the same flow rate for 1 h before it cooled down to RT. After that, the sample loop was filled with 5% H_2/95% Ar and further H_2 pulses were introduced to the sample using Ar as a carrier gas (50 mL min^{-1}). A TCD detector was used to record and integrate the peaks obtained.

Temperature-programmed reduction (TPR) experiments were carried out using an Autochem II 2920 instrument (Micromeritics, Aachen, Germany). To remove any adsorbed species, the sample was heated up to 400 °C with a heating rate of 10 K min^{-1} in a flow of 5% O_2:He (50 mL min^{-1}) and was held at this temperature for 30 min before it was cooled down to R.T. TPR experiments were conducted from RT to 900 °C in a 5% H_2/95% Ar flow (50 mL min^{-1}) with a heating rate of 10 K min^{-1}. The H_2 consumption was recorded and quantified by a thermal conductivity detector.

Temperature-programmed desorption (TPD) experiments were conducted using a Micromeritics Autochem II 2910 instrument. A 100-150 mg of each catalyst was loaded into a U-shaped quartz reactor and pretreated in a flow of 50 mL min^{-1} (5% H_2/95% Ar) with a heating rate 10 K min^{-1} to the corresponding reduction temperature for 2 h. Then, the sample was cooled down to 100 °C in a flow of He (50 mL min^{-1}). A He flow (50 mL min^{-1}) containing 1% CO_2 (for basicity) or 1% NH_3 (for acidity) was introduced to the sample at 100°C for 2 h, before it was flushed with pure He (50 mL min^{-1}) for 1 h. After that, the sample was ramped to 900°C for TPD-CO_2 or 700°C for TPD-NH_3 with a heating rate of 10 K min^{-1} in a flow of He

(50 mL min^{-1}). The maximum temperature was held for further 1 h. A quadrupol mass spectrometer (Balzers Omnistar) was used for analysis of desorbed gases.

Scanning transmission electron microscopy (STEM): micrographs were taken by 200 kV with an aberration corrected transmission electron microscope (JEM-ARM200F, JEOL Ltd.). The microscope was further equipped with a JED-2300 energy dispersive X-ray spectrometer (JEOL) with a silicon drift detector (dry SD60GV). For better differentiation between particles, both high-angle annular dark field (HAADF) and annular bright field (ABF) detectors were applied. For EELS acquisition, the annular dark field (ADF) detector was used for position control. EELS was done at a camera length of 4 cm, an illumination semi-angle of 27.8 mrad and a filter entrance aperture semi-angle of 41.3 mrad using the low loss region for compensation of energy shifts during acquisition. Sample preparation was done using dry deposition of the catalyst powder on a Cu grid (mesh 300) covered by a holey carbon film, before it was transferred into the microscope.

3.3. Experiments for mechanistic studies

The mechanism of the hydrogenolysis reaction of THFA in organic solvents, mainly 2-PrOH, was elucidated using isotopic labelling. For that, a series of reactions were carried out with the hydrogen isotope deuterium (D_2) and/or in deuterated isopropanol (C_3D_8O) (99.5%) (Sigma-Aldrich). After the reactions, the solvents were evaporated, and the samples were dissolved in $CDCl_3$ for *nuclear magnetic resonance spectroscopy* (NMR) analysis. ^{1}H NMR (500.13) and ^{13}C-NMR (125.8) spectra were recorded on a *Bruker AVANCE Neo 500* spectrometer. The chemical shifts are referenced to $CDCl_3$ signals: $\delta(^1H) = 7.27$, $\delta(^{13}C) = 77.0$. The assignment of NMR signals was supported by DEPT and two-dimensional correlation spectra (^{1}H,^{1}H-COSY, ^{1}H,^{1}H-NOESY, ^{1}H,^{13}C- (HSQC, HMBC)) using standard pulse sequences (standard *Bruker* software). The deuterium exchange rates were determined based on ^{13}C IG NMR spectra (30-degree pulse, 20 sec relaxation delay). Moreover, the transfer hydrogenolysis of THFA or/and the dehydrogenation reactions of 2-PrOH have been monitored by *in situ Fourier Transform Infrared Spectroscopy (In situ* FTIR). These experiments were carried out in a 45 mL Parr autoclave coupled with a fiber optical AgX ATR-probe (Mettler Toledo) with a silicon reflection element at the bottom. This immersion ATR-probe was connected to a ReactIR 15 spectrometer system from Mettler Toledo controlled by the iCIR proprietary software. The IR spectra were recorded in the spectral range from 650 – 3000 cm^{-1} with a setting resolution of 4 cm^{-1}. The *Happ-Genzel* algorithm was used as the apodization method. The entire reaction time was set to 4 h and IR-spectra were registered in time intervals of 1 min. Before starting the experiment, a background spectrum of the reaction mixture was collected after pressurizing with H_2 or Ar and heating up to the desired temperature. The subtraction of the background spectrum was done after the reaction using iCIR proprietary software.

3.4. Catalytic test

3.4.1. Experiments in the batch reactor

Catalytic reactions with Rh catalysts were carried out in 300 mL Parr stainless steel autoclaves equipped with a sample holder for seven 4 mL inserts, all with small magnetic stirrers. Each insert was charged with 1 mmol of THFA dissolved in 2 mL of water. The catalytic reactions on nickel catalysts were performed in 45 mL Parr stainless steel autoclaves equipped with magnetic stirrers, glass inserts, and small tubes for sampling. Each autoclave was charged with 1 mmol THFA dissolved in 5 mL of solvent. Prior to the reaction, the autoclave was flushed three times with argon and pressurized to the desired pressure with hydrogen (in some cases with argon or deuterium), before heating was started. Then, it was heated to the appropriate temperature with slow stirring (100 rpm). The reaction time started when the reaction temperature was reached. The stirring speed of the reaction was increased to 1500 rpm. After the reaction, the catalyst was washed, the reaction mixture was filtered and diluted to 10 mL in a volumetric flask with ethanol. For gas chromatography-mass spectrometry (GC-MS) analysis, 1 mL of 0.1 M standard solution (diethylene glycol dibutyl ether) was added to 4 mL of the diluted reaction mixture. Then 1 µL of the sample was injected into a Shimadzu GC-MS model GCMS-QP2010 Ultra equipped with a GC column OPTIMA® 5MS (50 m×0.32 mm×0.50 µm). For the nickel catalyst, the turnover frequency (TOF) was calculated by the following equation:

$$TOF\ (h^{-1}) = \frac{moles\ of\ converted\ substrate}{moles\ of\ active\ superficial\ Ni(0) * reaction\ time}$$

Since one molecule of H_2 can be chemisorbed on two atoms of superficial nickel, and a stoichiometry factor of 2 can be assumed (H_2:Ni= 1:2) for H_2-pulse chemisorption experiments [115], the formula can be expressed as

$$TOF\ (h^{-1}) = \frac{moles\ of\ converted\ substrate}{moles\ of\ adsorbed\ H_2\ on\ superficial\ Ni(0) * reaction\ time}$$

3.4.2. Experiments in the continuous flow reactor

Continuous flow reactions (gas:liquid:solid or liquid:solid) were carried out in a modular micro-reaction system (Ehrfeld) equipped with a cartridge reactor XL (Figure 3.1, Figure 3.2) [116]. This set-up was recently described in detail [108, 117]. The catalyst powder was pressed, the solid formed was granulated, and the grains were sieved to a fraction of 300-500 µm and loaded into a 5 mL reactor (d_{inner} = 1 cm). The catalyst bed was packed between two thin layers of quartz wool. The flow of H_2 (NmL: normalized at 0 °C and 1,013 bar) was regulated with a mass flow controller (Bronkhorst). The liquid flow (Q) (THFA in 2-PrOH solution) was pumped by a Knauer K-501 HPLC pump. Both H_2 and liquid phase were mixed in a slit-plate micro

mixer (model LH2). They were heated to the desired temperature before being introduced into the reactor (from bottom to top). Samples were collected directly behind the back pressure regulator. In the catalytic transfer hydrogenolysis (CTH) without hydrogen flow, the reaction pressure was adjusted by means of a small N_2 flow which was stopped after reaching the desired pressure. The reaction was carried out only in the presence of the liquid flow. For GC-MS analysis, 1 mL of reaction mixture was collected, 0.5 mL of 0.1 M standard solution (diethylene glycol dibutyl ether) was added, and the mixture was diluted with 0.5 mL EtOH. The liquid hourly space velocity (LHSV) was calculated by the following equation:

$$LHSV\ (h^{-1}) = \frac{liquid\ phase\ flow\ rate\ (mL \cdot h^{-1})}{volume\ of\ catalyst\ bed\ (mL)}$$

In addition, the nickel-based catalyst productivity in flow and batch reactor was calculated and compared using the following equation:

$$Productivity\ (mmol\ g(cat)^{-1}\ h^{-1}) = \frac{molar\ mass\ of\ 1{,}5-PeD\ per\ hour\ (mmol * h^{-1})}{mass\ of\ catalyst\ (g)}$$

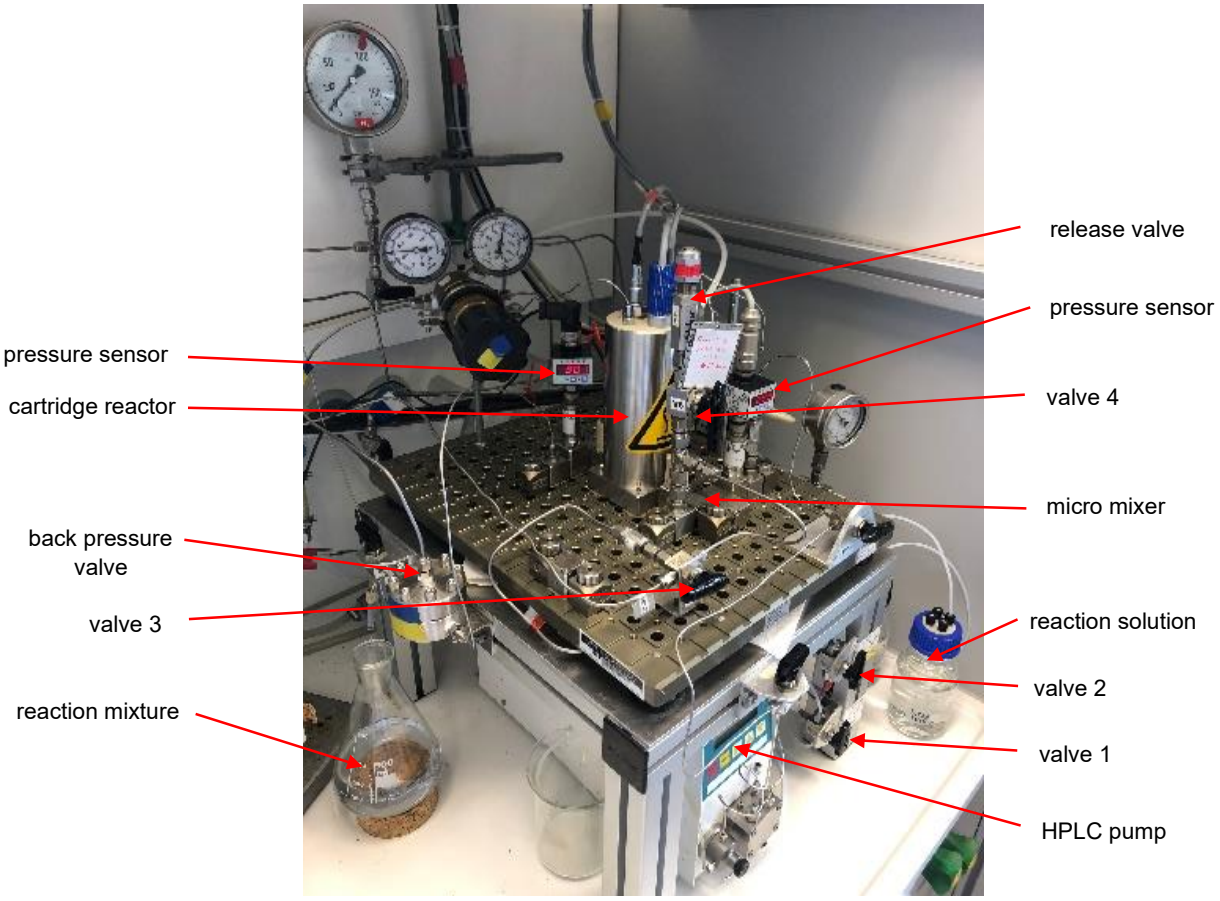

Figure 3.1. Liquid-phase flow set-up equipped with a cartridge reactor.

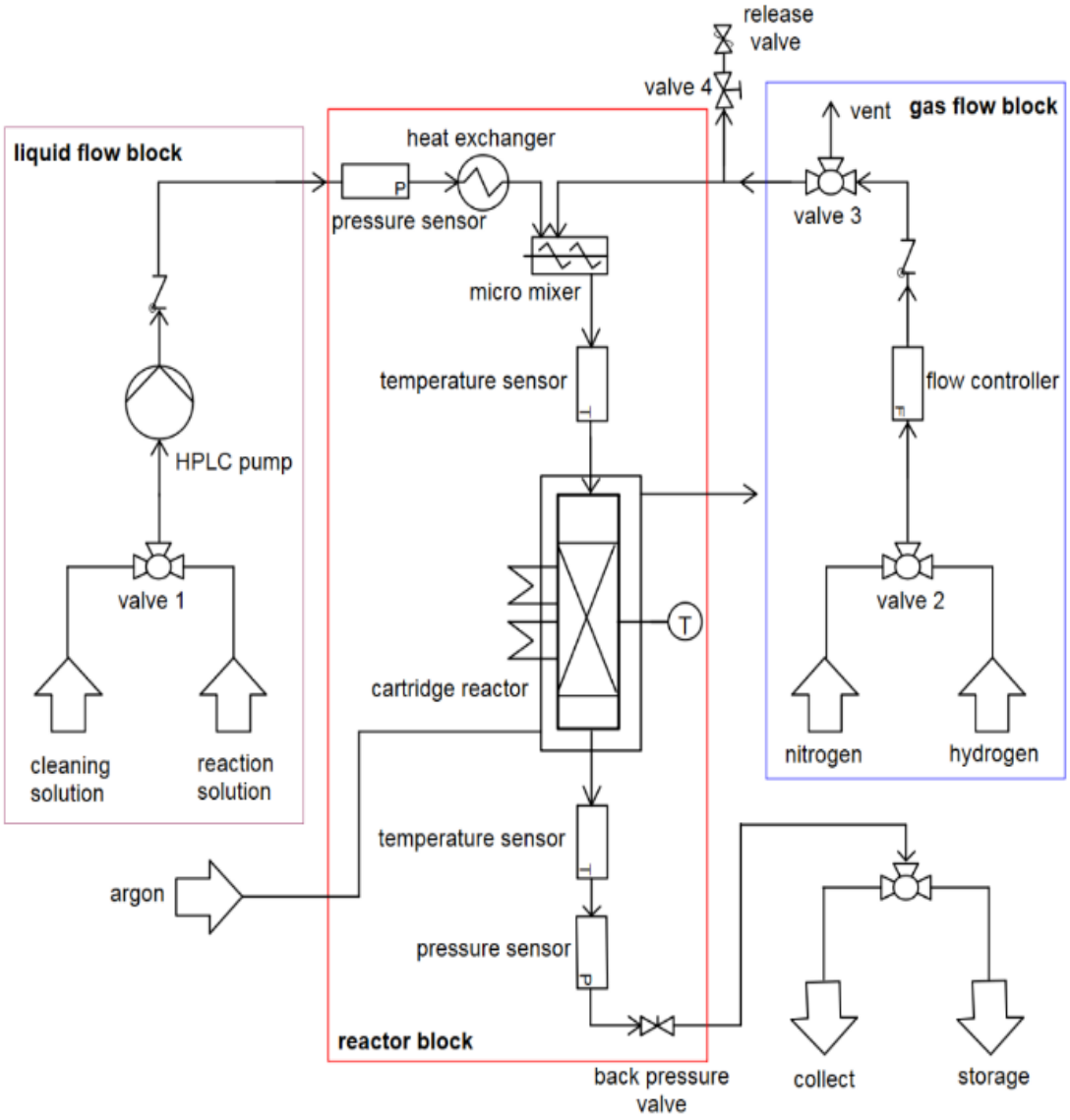

Figure 3.2. Scheme of liquid-phase flow set-up for continuous flow operation (adapted from [117]).

4. Results and Discussion

4.1. Hydrogenolysis of THFA over noble modified rhodium metal catalyst under batch conditions

As mentioned in paragraph 1.4.2, the best reported catalysts for hydrogenolysis of THFA to 1,5-PeD have been modified Rh catalysts on SiO_2 and carbon supports. Thus, modified Re-ReO_x catalysts were considered as a benchmark for this study. They were prepared on several supports, examined for this purpose for the first time, by an impregnation method before subsequent pretreatment (for preparation details see paragraph 3.1.1). Since the characterization and the catalytic studies on modified Rh-ReO_x catalysts in direct hydrogenolysis of THFA to 1,5-PeD have been intensively investigated in the recent years [78-80, 92, 94-97], the characterization and catalytic performance of Rh-based catalytic systems was briefly investigated in this thesis to establish basic methods for characterization of very active catalysts and their catalytic testing. Subsequently, the obtained results using the benchmark catalyst (Re-ReO_x) were compared with nickel on lanthanide supports as noticeable alternative catalysts.

4.1.1. Catalyst characterization

Rh-ReO_x catalysts were characterized using BET, XRD, TPR, XPS and STEM techniques (for experimental details see paragraph 3.2). Table 4.1 shows the surface area and pore volume of Rh-ReO_x catalysts on different supports. Depending on the support surface, the highest BET surface area of a Rh catalyst was on SiO_2 (SBA-15) with 656 $m^2\ g^{-1}$, and the lowest surface area was on TiO_2 (rutile) (30 $m^2\ g^{-1}$) (N_2 adsorption-desorption isotherms see Figure A1).

Table 4.1. BET surface area of Rh-ReO_x on several supports.

Entry	Catalyst (wt%Rh-ReO_x/support)	Molar ratio (Re:Rh)	S_{BET} [$m^2\ g^{-1}$]	V_p [mL g^{-1}]
1	2.7Rh-ReO_x/SiO_2 (SBA-15)	0.62	656	0.89
2	2.6Rh-ReO_x/SiO_2 (Gel X)	0.45	314	0.74
3	2.6Rh-ReO_x/C (Vulcan XC72)	0.37	164	0.27
4	2.7Rh-ReO_x/TiO_2 (anatase)	0.67	72	0.23
5	2.7Rh-ReO_x/TiO_2 (rutile)	0.63	30	0.27
6	2.7Rh-ReO_x/TiO_2 (brookite)	0.64	71	0.34
7	2.7Rh-ReO_x/TiO_2 (P25)	0.58	76	0.32
8	2.7Rh-ReO_x/ZrO	0.70	86	0.25
9	3.4Rh-ReO_x/ γ-Al_2O_3	0.55	286	0.79

Next, XRD measurements were implemented for Rh-ReO_x on selected supports (see their diffractograms in Figure 4.1). In the case of carbon support, the main peaks were found at 2θ= 41.1°, 47.8°, 69.9° corresponding to the (111), (200) and (220) lattice planes of metallic rhodium (ICDD 00-005-0685). In addition, two small peaks at 2θ= 16.6, 25.4 were detected in SiO_2-supported catalysts which can be attributed to the (101), (112) lattice planes of remaining traces of ammonium perrhenate (NH_4ReO_4) (ICDD 01-085-0347). ReO_x was not detected probably due to the high dispersion of ReO_x species after reduction. This assumption was supported by the model structure of Rh-ReO_x/SiO_2 according to reported *in situ* EXAFS analysis which demonstrated that Re oxidic species were highly dispersed on Rh metallic surface after reduction at lower temperatures (<322 °C) (see model structure in Figure 1.2) [97]. These findings could be also applied to present catalysts since they were prepared in the same manner as the benchmark catalyst (Rh-ReO_x/SiO_2) [78, 79, 92] (for preparation details see paragraph 3.1.1). In the case of TiO_2 supports, the dominating characteristic X-ray diffraction peaks of TiO_2 were exclusively observed. These were anatase (ICDD 01-075-2547), rutile (ICDD 00-021-1276), brookite (ICDD 01-076-1934) and P25 type (combination of anatase and rutile) (ICDD 00-021-1272 and 01-079-6031), respectively. This might be due to the low metal loading and the overlap between the little intensive Rh and very intensive TiO_2 support reflexes.

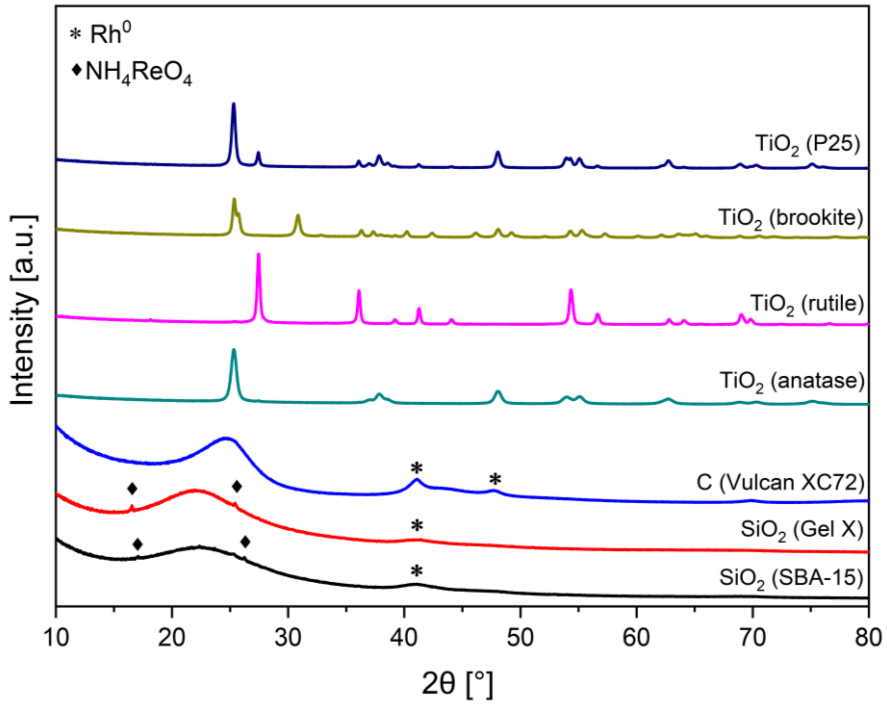

Figure 4.1. Powder diffractograms of 2.6/2.7Rh-ReO_x on different supports.

Next, a TPR analysis of both 5.2Rh/TiO_2 (P25) and the ReO_x-modified Rh catalyst (2.7Rh-ReO_x/TiO_2 (P25); Re:Rh=0.58) was carried out to determine the influence of ReO_x on the reducibility of Rh. As shown in Figure 4.2, the reduction peaks of 5.2Rh/TiO_2 (P25) were very broad starting from 120 °C with two optimums at 205 and 244 °C. These combined peaks could

be assigned to the reduction of differently sized Rh_2O_3 particles on the TiO_2 surface. The hydrogen consumption during the TPR measurement was 549 µmol/g which was close to the calculated value for reduction of 5.2wt% Rh (505 µmol/g). This slight increase might indicate the reduction of the interfacial TiO_2 support. On the other hand, the reduction peak of 2.7Rh-ReO_x/TiO_2 (P25) was very sharp with an optimum at 73 °C corresponding to first reduction peak of Rh_2O_3 which was indicated at 205 °C for 5.2Rh/TiO_2 (P25) (see Figure 4.2). These results match well references [92, 96] showing that the reducibility of Rh was significantly improved after the addition of ReO_x. Interestingly, a small peak was attached to the main sharp peak at 90 °C which may correspond to the partially reduced Re species on the Rh metal surface hinting to an interaction between both species (see Figure 4.2). These findings are in good agreement with TPR for Rh-ReO_x/SiO_2 which suggested that reduced Re species at 92 °C interacts with metallic Rh without interacting with other Re species [96]. That is why, the hydrogen consumption was 491 µmol/g which was significantly higher than the calculated value for reduction of 2.7wt% Rh (262 µmol/g), suggesting that interfacial Ti^{4+} and initial Re^{7+} may partially be reduced to lower low-valent oxidized species (Re^{x+}, x<7). Low valent Re cation species with higher dispersion were formed during reduction in the case of Rh-ReO_x/SiO_2 [92, 96]. This suggests that the enhancement of reducibility of Rh species is caused by a close interaction with ReO_x species in the interfacial areas. Such interface assumption was proved using *in situ* EXAFS analysis which verified a presence of Re-Rh bonds for reduced Rh-ReO_x/SiO_2 [97].

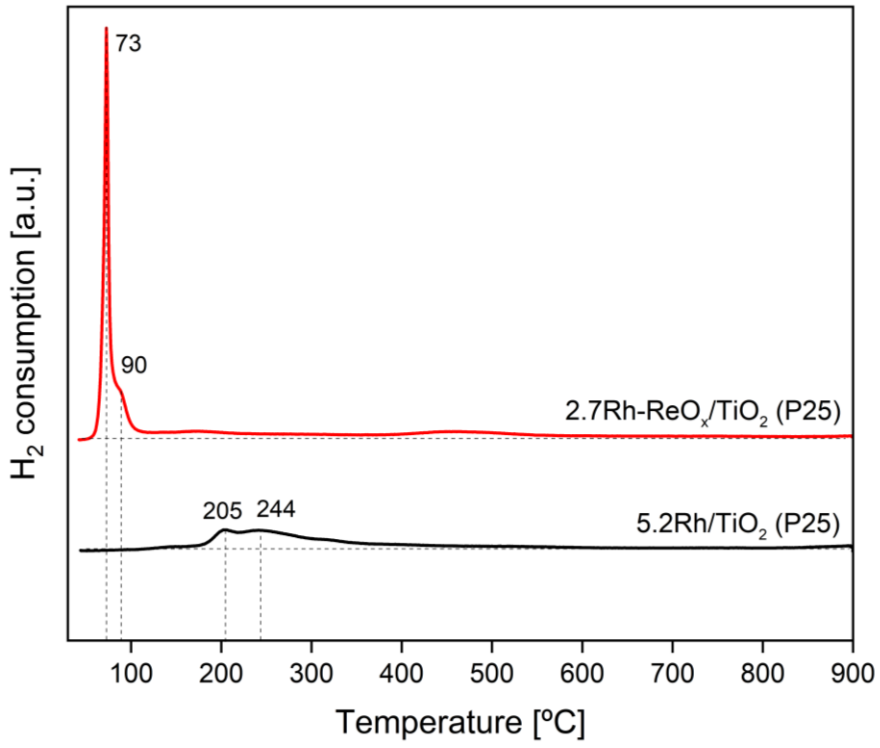

Figure 4.2. TPR profiles of calcined 5.2Rh/TiO_2 (P25) and modified 2.7Rh-ReO_x/TiO_2 (P25).

In addition, XPS spectra were recorded to identify the surface composition of Rh and the low-valent ReO_x species after reduction. Figure 4.3 shows the Rh3d spectra (a) and Re4f spectra (b) of Rh-ReO_x/TiO_2 (P25). The main peaks in the Rh3d spectrum at binding energies of 309.1 eV and 313.8 eV could be identified as Rh $3d_{5/2}$ and Rh $3d_{3/2}$ peaks of Rh_2O_3, respectively. Peaks for Rh(0) only appeared as shoulders in the Rh 3d bands probably due to the oxidization of superficial Rh species after exposure to air before measurement. Regarding the ReO_x modifier, the dominating peaks detected at 46.3 eV and 48.5 eV could be allocated to Re $4f_{7/2}$ and Re $4f_{5/2}$ bands of Re^{7+}, respectively (Figure 4.3b). Also, a small peak observed at 44.1 eV was assigned to a $4f_{7/2}$ signal of Re^{6+} species. This observation confirms the TPR results which showed that Re^{7+} was partially reduced to lower valent species (see Figure 4.2).

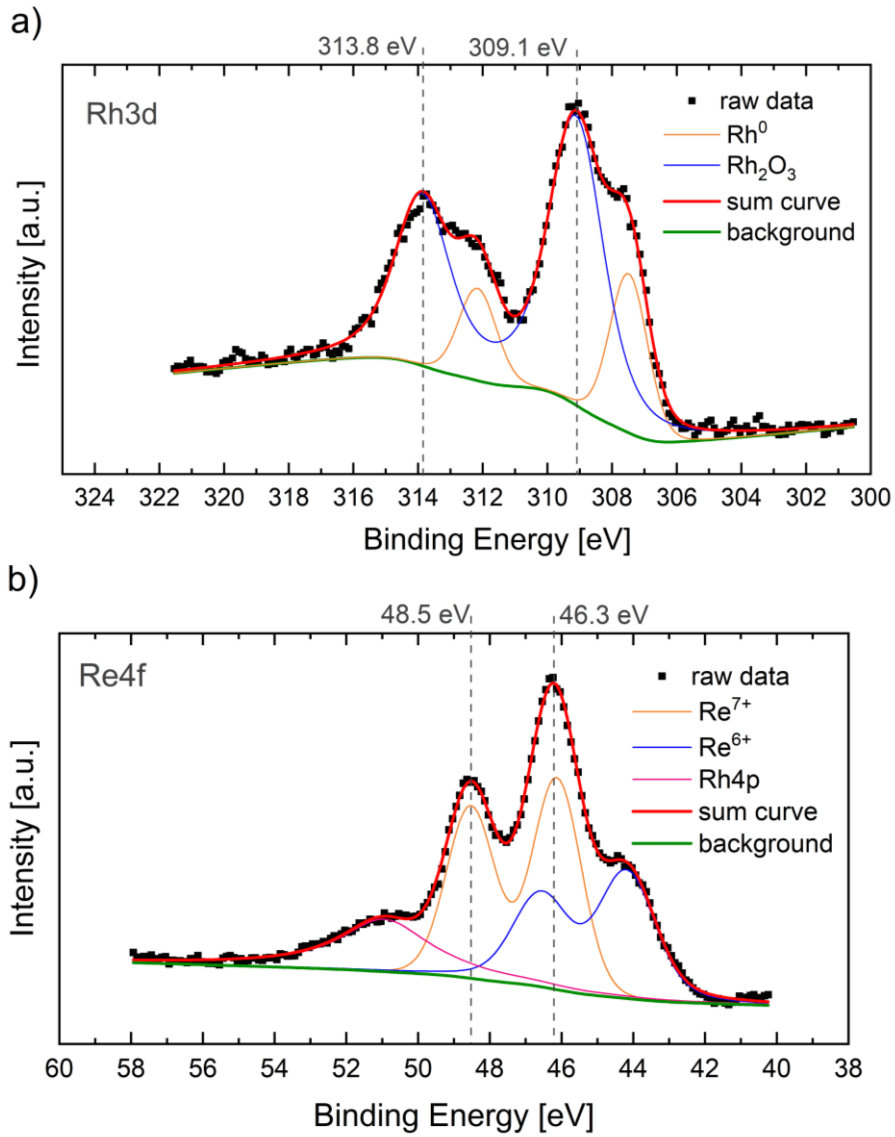

Figure 4.3. XPS spectra for 2.7Rh-ReO_x/TiO_2 (P25) a) Rh3d; b) Re4f.

Moreover, the high-angle annular dark field (HAADF)-STEM technique was applied to investigate the morphology of Rh-ReO_x/TiO_2 (P25). As shown in Figure 4.4, Rh exists as small particles, clusters, and singular atoms with rather probable Re content (with brighter contrast)

on the TiO_2 surface (a-c). In order to identify the atomic composition, the EELS method was applied which showed that a parallel observation of Rh and Re was not possible due to the large differences in ionization edge energies, overlapping edges and limited energy ranges of the spectrometer (see Figure A2). On the other hand, the presence of a Re phase attached to TiO_2 was unambiguously, which was also been verified by EELS (Figure 4.4, d-f) (for EELS, see Figure A2). The contrast difference in the HAADF image clearly indicated that Rh was also quite evenly contained in the Re-phase as Rh populated the support (d, e). The Rh-Re phase appeared amorphous and conformed to the support surface, covering certain areas (d-e). This implies that the Re species were in contact with Rh metallic particles hinting to direct interaction between both species. These observations are in line with reported EDX results for Rh-ReO_x/C which found that dispersed nanoparticles contained both Rh and Re in different ratios [92].

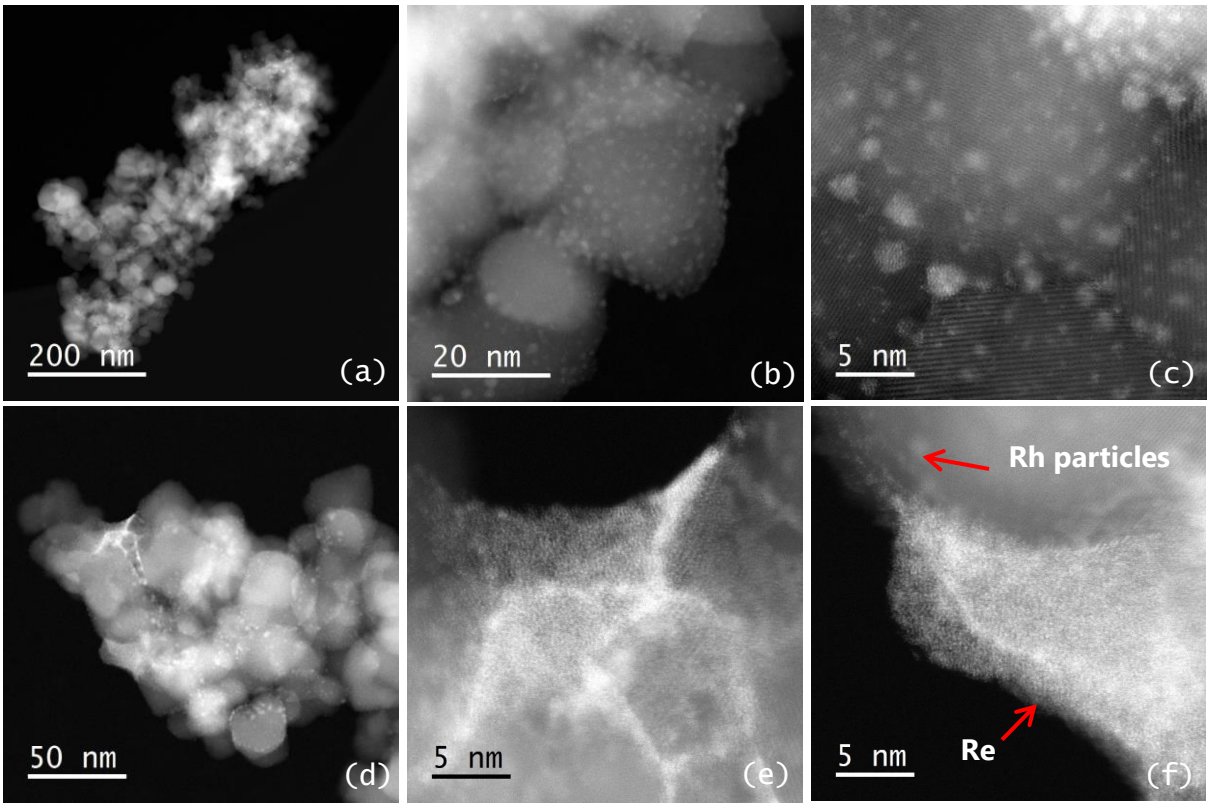

Figure 4.4. HAADF-STEM images of 2.7Rh-ReO_x/TiO_2(P25) (a-f).

4.1.2. Influence of the impregnation and pretreatment procedure

Initially, the influence of the impregnation methods on the conversion and 1,5-PeD yield using noble metal catalytic systems was investigated. Rh-ReO_x supported on TiO_2 (P25) was selected as low-surface support compared to reported SiO_2 and activated carbon and was described as an inactive support for selective hydrogenolysis of THFA to 1,5-PeD [98]. Thus, different impregnation methods for the preparation of this catalyst were applied as follows: incipient wetness impregnation (IWI), wet impregnation (IW) and co-impregnation (for preparation details see paragraph 3.1.1). Also, the effect of pretreatment, calcination, and

reduction for each method was investigated. The hydrogenolysis reaction of THFA was conducted in a batch reactor over differently prepared Rh-ReO_x/TiO_2 (P25) for 24 hours. As demonstrated in Figure 4.5, the various techniques of impregnation applied had no significant impact on the conversion of THFA, and almost complete conversion was achieved in the case of all calcined samples (≈ 99%). Regarding reduced catalysts, the conversion was lower and ranged between 91-96% and the best yield of 1,5-PeD was 82% for samples prepared by IWI and co-impregnation. Interestingly, the selectivity to 1,5-PeD was comparable (76-77%) in the case of WI for calcined and reduced catalysts at similar conversions (96-99%). As shown in TPR profile (Figure 4.2), ReO_x-modified Rh was totally reduced at temperatures less than 120 °C. That appears to indicate that Rh_2O_3 was completely reduced at 120 °C under 8 MPa hydrogen pressure, so that Rh(0) was available for interaction with ReO_x. *Koso et al.* reported that non-modified Rh/SiO_2 as well as ReO_x/SiO_2 showed low activity in the hydrogenolysis of the C–O bond of THFA [78, 79]. They proposed that the interface areas between Rh and ReO_x formed due to their strong interaction were the catalytically active sites for the hydrogenolysis [95-97]. This implies that the presence of metallic Rh was important for the formation of an active interface with ReO_x to achieve high yields of 1,5-PeD. Therefore, a reduction step was indispensable for all noble metal catalysts before the reaction.

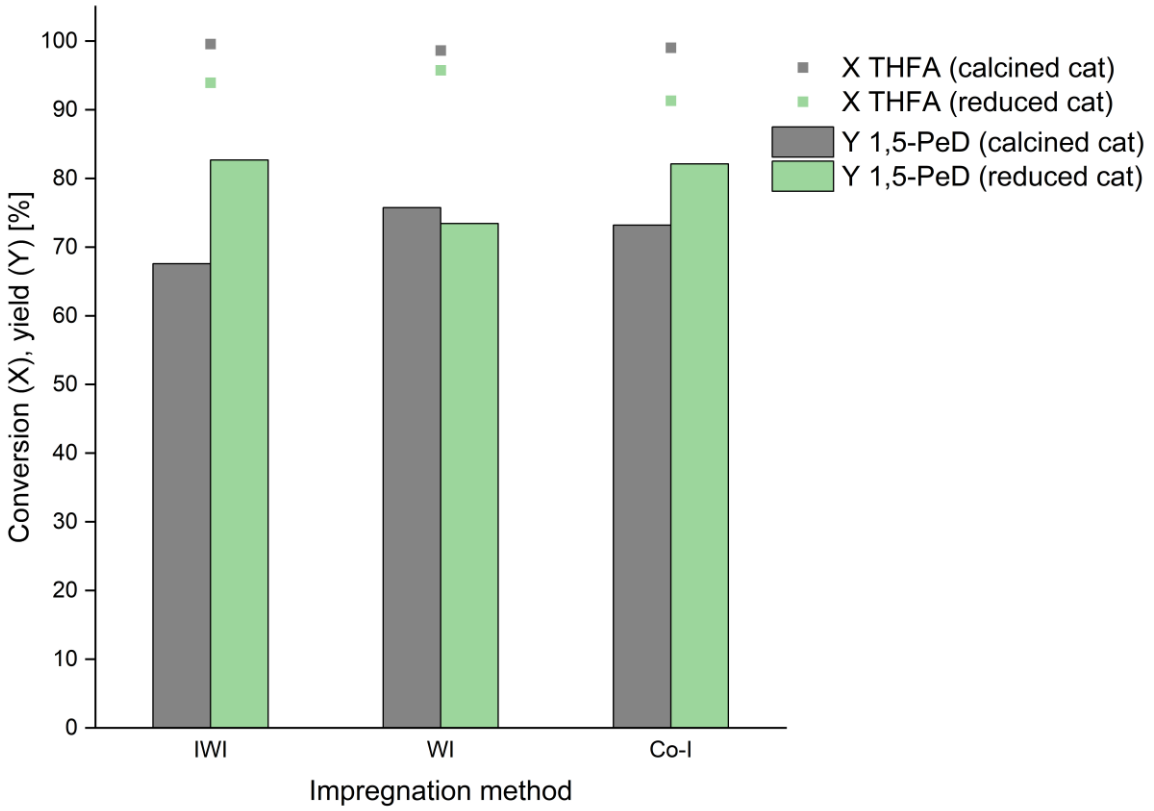

Figure 4.5. The influence of the impregnation procedures and pretreatment on conversion and 1,5-PeD yield in hydrogenolysis of THFA over 3.5Rh-ReO_x/TiO_2 (P25) (molar ratio (Re:Rh)= 0.5). Reaction conditions: 5 wt% THFA aqueous solution (2 mL), m(cat)= 20 mg, mass ratio (cat:THFA)= 1:5, T= 120 °C, p(H_2)= 8 MPa, t= 24 h. IWI: incipient wetness impregnation; WI: wet impregnation; Co-I: co-impregnation.

4.1.3. The effect of the metal and metal oxide modifier

After selecting the best preparation procedure, series of ReO_x modified metal (Rh, Ir, Ni) catalysts on TiO_2 (P25) were prepared by the IWI method and subsequently calcined and reduced before the reaction started (for preparation and pretreatment details see paragraph 3.1.1). As demonstrated in Figure 4.6a, the impact of metal on the catalytic performance of catalysts modified with ReO_x was remarkable. The highest yield of 1,5-PeD at 94% conversion was 83% using Rh-ReO_x/TiO_2 (P25). After replacing Rh by Ir with similar content of Re (~4 wt%), the conversion was significantly decreased to 65%, and 45% yield of 1,5-PeD resulted. Moreover, ReO_x-modified Ni was hardly active on TiO_2 (P25) support (Figure 4.6a). It seems likely that the metallic oxidation state zero plays a key role in activation of hydride species on the catalyst surface and in the interaction of the metal with ReO_x which was optimal in the case of Rh surface whereas Ni was obviously present as Ni^{2+} in aqueous solution. In addition, the effect of the ratio of active Rh-ReO_x/TiO_2 to the substrate was investigated (Figure 4.6b). The conversion was decreased when the catalyst amount was lowered, and the best yields of 1,5-PeD were 83 and 72% at a mass ratio (cat:THFA) of 1:5 and 1:10, respectively (Figure 4.6b). However, the yield of 1,5-PeD was significantly decreased at mass ratios lower than 1:15. Therefore, the presence of an optimal number of active sites was important to achieve a high yield of 1,5-PeD. Also, Rh was active and selective to 1,5-PeD due to the direct interaction with the ReO_x modifier forming an active interface which was proposed as the catalytically active site for C–O bond hydrogenolysis [78, 79, 95-97] (see paragraph 1.4.2).

To understand the specific role of the modifier in the formed interface, ReO_x and other modifiers such as MoO_x, WO_x, NbO_x and TaO_x were impregnated on Rh/TiO_2 (P25) and tested under batch conditions. Table 4.2 details the product distribution after hydrogenolysis of THFA over non-modified and modified Rh catalysts on TiO_2 (P25). 5.2Rh/TiO_2 (P25) (entry 1) was not active in cleaving the tetrahydrofuran ring and significant formation of THF was observed (entry 1). However, Rh modified by Re, Mo and W oxides was selective to 1,5-PeD, and no formation of 1,2-PeD was observed (entries 2-4). The maximum yield of 1,5-PeD was 82% at almost total conversion on Rh-ReO_x/TiO_2 (P25). These results are in line with previous studies [78, 79] which showed that unlike Rh/SiO_2, modified Rh catalysts were selective to 1,5-PeD. In addition, Rh modified with NbO_x and TaO_x (entries 5-7) were found to be not selective to 1,5-PeD and some formation (up to 9%) of 1,2-PeD was detected (entries 5,6). So, the yield of 1,5-PeD on Rh catalysts decreased depending on the modifier in the following order: ReO_x > MoO_x > WO_x > NbO_x > TaO_x.

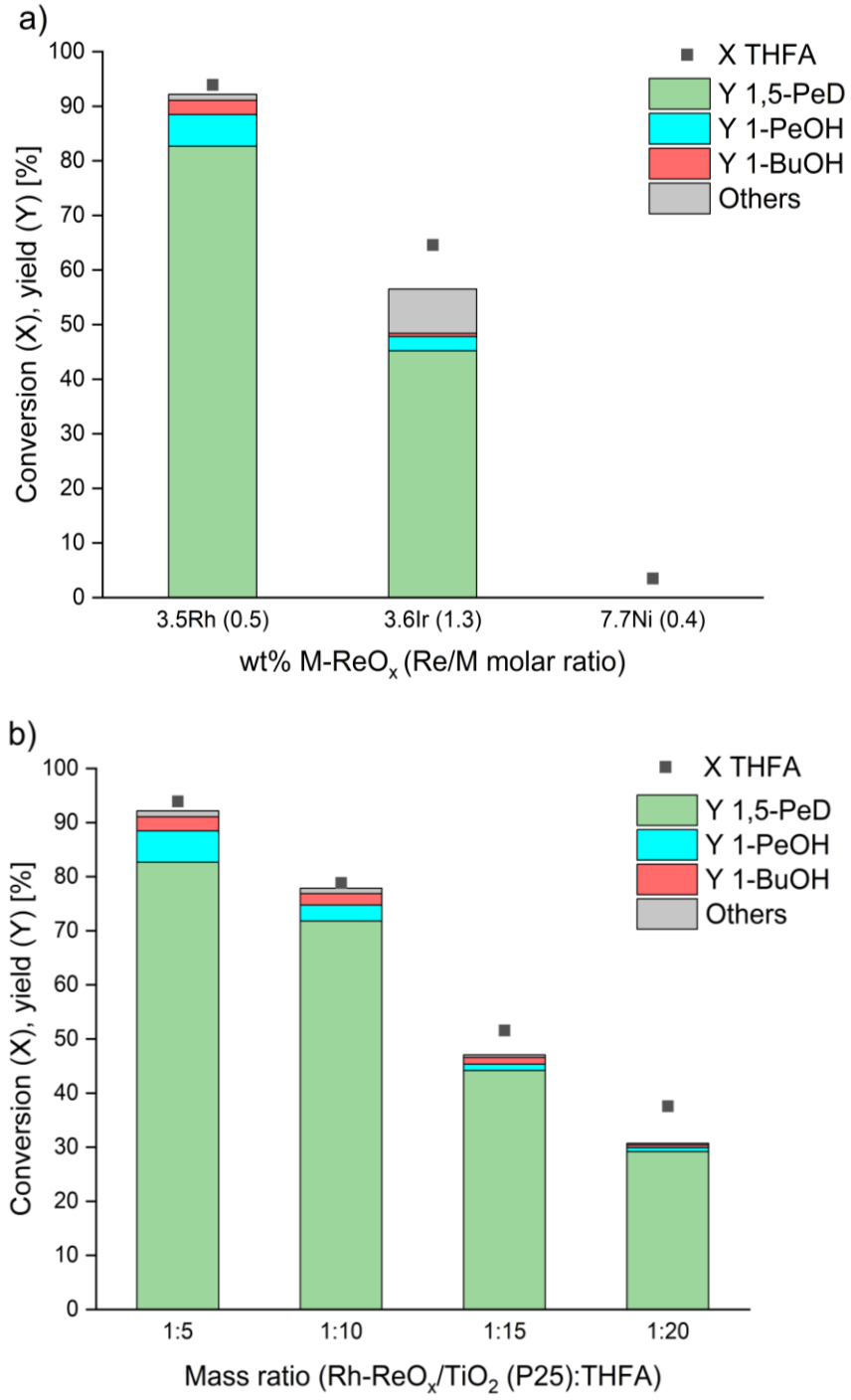

Figure 4.6. The effect of catalyst metal (a) and catalyst ratio (b) on conversion and yields in hydrogenolysis of THFA on TiO_2 (P25). Reaction conditions: 5 wt% THFA aqueous solution (2 mL), [a]m(cat)= 20 mg, [a]mass ratio (cat:THFA)= 1:5, T= 120 °C, p = 8 MPa, t= 24 h. Others: estimated value of by-products based on an average GC response factor of known products.

Furthermore, the active modifiers (Re, Mo, W and Nb oxides) were also impregnated to Ir/TiO_2 catalysts to investigate with a less active metal to perhaps better track variations in conversion and yields in the hydrogenolysis of THFA. As shown in Table A1, $Ir\text{-}ReO_x/TiO_2$ generated the highest yield of 1,5-PeD (45%) and other modified Ir catalysts were less active. Moreover, Ni catalysts with different modifiers were not active (see Table A1). As reported previously, the synergistic effect caused by interaction between metal and acidic modifier species was responsible for a high yield of 1,5-PeD [78, 79, 95-97].

Table 4.2. The influence of metal oxide modifiers on conversion and yields in Rh-catalyzed hydrogenolysis of THFA.

Entry	Cat on TiO_2 (P25)	Molar ratio (M:Rh)	Conversion [%]	Yield [%]					Others [%]
				1,5-PeD	1,2-PeD	1-PeOH	1-BuOH	THF	
1	5.2Rh	-	18	0	0	0	0	15	3
2	2.7Rh-ReO_x	0.58	99	82	0	7	3	0	4
3	2.4Rh-MoO_x	0.14	81	77	0	3	1	0	0
4	5.0Rh-WO_x	0.67	51	41	0	1	1	0	4
5[a]	3.2Rh-NbO_x	0.65	59	28	9	7	5	0	6
6[a]	3.2Rh-TaO_x	1.11	28	6	5	1	1	0	8

Reaction conditions: 5 wt% THFA aqueous solution (2 mL), m(cat)= 20 mg, mass ratio (cat:THFA)= 1:5, T= 120 °C, p= 8 MPa, t= 24 h. [a] m(cat)= 50 mg, mass ratio (cat:THFA)= 1:2. Others: estimated value of by-products based on an average GC response factor of known products.

One reason for the difference in the conversion of THFA was the molar ratio of metal modifier to Rh since the optimal ratio varied depending on the modifier. For instance, the optimal molar ratio for Re:Rh was found to be 0.5, but 0.13 for Mo:Rh [79]. Even at similar ratios, the local structure of the metal and oxidic modifier in the interface might also influence the reactivity of the catalytic system. For instance, the local structure of ReO_x- and MoO_x- modified Rh catalysts was found to be different by EXAFS analysis [96]. Briefly, it was suggested that clusters consisting of three ReO_x units were attached to the Rh (111) surface in the case of Rh–ReO_x/SiO_2 (Re/Rh = 0.13) while isolated MoO_x species Rh–MoO_x/SiO_2 (Mo/Rh = 0.13) were located on this Rh surface (see Figure 1.2) [96]. Furthermore, Rh modified by ReO_x, MoO_x and WO_x was active and selective to 1,5-PeD, and no formation of 1,2-PeD was observed. In contrast, NbO_x- and TaO_x-modified Rh catalysts were less active and not selective to 1,5-PeD (entries 5-6), and 1,2-PeD was formed in different ratios (see Table 4.2). This might be probably due to the low redox activity of NbO_x- and TaO_x which affect the ability of interexchange of electrons with metallic Rh species. According to the proposed hydride mechanism (see paragraph 1.5), the formation of hydride species may be enhanced due to the presence of redox-active oxides, e.g. ReO_x, to cleave hydrogen to two hydrogen atoms which are converted to a proton in the aqueous solution and a hydride adsorbed on a Rh atom at the interface of Rh and ReO_x [95]. Therefore, Rh-ReO_x was found to be the best system for the selective hydrogenolysis of THFA to 1,5-PeD, so it was further prepared on different supports.

4.1.4. Effect of the support

As mentioned before, the best catalyst for direct hydrogenolysis of THFA to 1,5-PeD was Rh-ReO_x on SiO_2 and C [78, 79, 92]. However, it was reported that Rh-ReO_x on other supports, particularly on Al_2O_3 and TiO_2, showed a very low activity because of a stronger interaction between MO_x (M=Re, Mo, etc.) and the supports than with Rh metal species [98]. Thus, it was essential to reveal the role of the support sites in the catalytic hydrogenolysis of THFA.

Therefore, a series of Rh-ReO_x catalysts was prepared by co-impregnation on active supports, SiO_2 and C, and compared with γ-Al_2O_3, ZrO_2 and different types of TiO_2 (anatase, rutile, brookite and P25). Table 4.3 compares the conversion and 1,5-PeD yield of these catalysts under batch conditions. Obviously, Rh-ReO_x was highly active on SiO_2 (Gel X and SBA-15), carbon (Vulcan XC72) and all types of TiO_2. The surface area of the supports had no noticeable impact on the conversion of THFA (see Table 4.1 and Table 4.3). The conversion was ≥ 92% for all catalysts, and the yield of 1,5-PeD ranged from 82 to 88%. However, the conversion and yields of 1,5-PeD were significantly lower than 55% in the case of catalysts supported by ZrO_2 and Al_2O_3. It seems likely that the metallic rhodium and acidic ReO_x were not only the exclusively responsible species for the high yield of 1,5-PeD, but also the nature of the support. Unlike the reported findings of the low activity of Rh-ReO_x on TiO_2 support, it was proved that the yields of 1,5-PeD over Rh-ReO_x were similar on all types of TiO_2 as on SiO_2 and C, even if surface areas of TiO_2 were significantly lower (Table 4.1). This shows clearly that the surface area has no impact on the catalyst performance. It would appear to indicate that the strong interaction between the amphoteric supports (Al_2O_3 or ZrO_2) and ReO_x may lead to a decrease of the acidity of ReO_x which could weaken the interaction between Rh and ReO_x in the interface resulting in low conversion. However, the conversion did not decrease using Rh-ReO_x on acidic TiO_2 even when acidic ReO_x was clearly attached to TiO_2 support (see HAADF-STEM images Figure 4.4). This indicates that the nature of the support influenced the activity of the Re-ReO_X interface in the hydrogenolysis of THFA to 1,5-PeD.

Table 4.3. The effect of the support on conversion and yields in the hydrogenolysis of THFA over Rh-ReO_x catalysts.

Entry	Support	Rh loading [%]	Molar ratio (Re:Rh)	Conversion [%]	Yield [%]			Others [%]
					1,5-PeD	1-PeOH	1-BuOH	
1	SiO_2 (Gel X)	2.6	0.45	98	86	8	1	4
2	SiO_2 (SBA-15)	2.7	0.62	97	84	7	1	6
3	C (Vulcan XC72)	2.6	0.37	92	88	3	1	1
4	TiO_2 (P25)	2.7	0.58	99	82	7	3	4
5	TiO_2 (anatase)	2.7	0.67	96	84	6	3	3
6	TiO_2 (rutile)	2.7	0.63	95	87	5	2	0
7	TiO_2 (brookite)	2.6	0.64	97	85	7	3	2
8	ZrO_2	2.7	0.70	54	50	1	1	2
9	γ-Al_2O_3	3.4	0.55	34	29	0	0	4

Reaction conditions: 5 wt% THFA aqueous solution (2 mL), m(cat)= 20 mg, mass ratio (cat:THFA)= 1:5, T= 120 °C, p= 8 MPa, t= 24 h. Others: estimated value of by-products based on an average GC response factor of known products.

4.1.5. Effect of hydrogen pressure

The reaction rate of hydrogenolysis of THFA over modified noble metal catalysts in aqueous solution is highly influenced by the hydrogen pressure [80, 95]. The reaction is estimated to be first order with respect to H_2 pressure [80, 95]. 8 MPa was found to be the optimal pressure applied at 120 °C using Rh-ReO_x/SiO_2 in aqueous solution [78-80, 92]. One of the goals of this study was to investigate this reaction over Rh-ReO_x on different active supports at milder hydrogen pressure. Therefore, the effect of pressure on the conversion of THFA over Rh-ReO_x on SiO_2 (Gel X and SBA-15), C (Vulcan XC72) and different types of TiO_2 (anatase, rutile, brookite and P25) was investigated (Figure 4.7). In general, the conversion decreased progressively with lowering H_2 pressure. Also, a slight change in yields was observed with catalysts on different supports at high pressures. The yield of 1,5-PeD ranged from 82 to 88% at pressures between 6-8 MPa. However, when the pressure was decreased to 2 MPa, the conversion of THFA dropped, however, this decline in the conversion varied depending on the support. For instance, the highest yield was 73% with TiO_2 (brookite) while the lowest yield was 54-55% with TiO_2 (rutile) and activated carbon (Vulcan XC72) (Figure 4.7). The conversion of THFA decreased at 2 MPa in the following order: TiO_2 (brookite) > TiO_2 (anatase) > SiO_2 (SBA-15) ≈ SiO_2 (Gel X) ≈ TiO_2 (P25) > TiO_2 (rutile) ≈ C (Vulcan XC72). Interestingly, the pressure did not significantly affect the selectivity of the catalyst for 1,5-PeD, as it ranged from 87 to 94% using catalysts on all selected supports at all applied pressures. The decrease in conversion could be due to the solubility of hydrogen in water which decreases almost three times when decreasing the pressure from 8 MPa to 2 MPa at 120 °C [118]. Another reason could be the delay in adsorption of the substrate at lower pressures which varied depending on the support. Therefore, these results demonstrate that the hydrogen pressure had a significant effect on the yield of 1,5-PeD in aqueous solution and the highest 1,5-PeD yield (74%) at low pressure (2 MPa) was achieved over Rh-ReO_x/TiO_2 (brookite).

In summary, the research part on modified noble metal catalytic systems showed that the best combination of active species for aqueous hydrogenolysis of THFA to 1,5-PeD was Rh-ReO_x on all types of low-surface TiO_2 (anatase, rutile, brookite and P25) supports, as well as on already-known SiO_2 and C (Vulcan XC72) supports [78-80, 92]. There was no remarkable influence of the support on conversion of THFA over ReO_x modified Rh catalysts at reaction pressure (8 MPa). However, when the hydrogen pressure was significantly reduced to 2 MPa, it became clear that TiO_2 (brookite) was the best support for this system due to the high conversion of THFA (X= 80%) even at p= 2 MPa. Moreover, the loading of precious Rh metal was also reduced to 2.7 wt% achieving almost complete conversion as with the reported 4 wt% Rh-ReO_x/SiO_2 under the same batch conditions after 24 h [78-80, 92]. At this lower Rh loading, up to 88% yield of 1,5-PeD was achieved over all selected supports. In addition, non-reported

acidic modifiers, particularly NbO_x and TaO_x, were investigated for this catalytic system showing that they are not selective to 1,5-PeD as ReO_x and MoO_x on TiO_2 support.

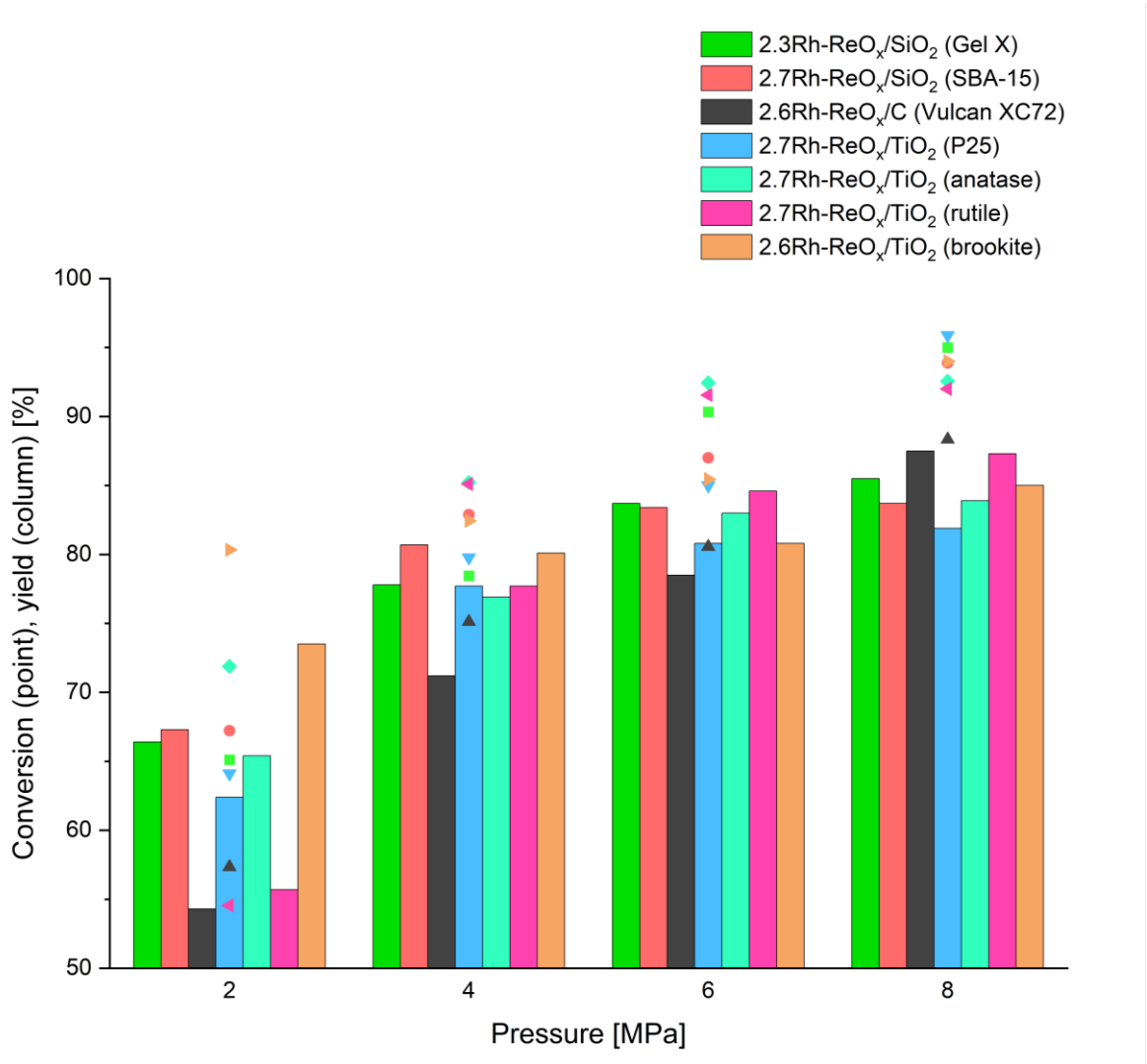

Figure 4.7. The influence of the hydrogen pressure on conversion and yields in hydrogenolysis of THFA over Rh-ReO_x on various supports. Reaction conditions: 5 wt% THFA aqueous solution, m(cat)= 20 mg, mass ratio (cat:THFA)= 1:5, T= 120 °C, p= 8 MPa, t= 24 h.

Nevertheless, ReO_x and MoO_x were found to be unstable due to their leaching in water [81, 82] and therefore they are not suitable for a continuous synthesis of 1,5-PeD from THFA. Moreover, these noble metal catalytic systems are not cost-efficient, so they are not considered for industrial applications. Therefore, the main aim of this study was to replace the benchmark Rh-ReO_x catalyst by economically efficient non-modified Ni catalysts for continuous operation. For that, accessible organic solvents such as 2-PrOH were selected instead of water since modified nickel was found to be unactive in water. In the following paragraph, the hydrogenolysis of THFA and furfural over lanthanide supported nickel catalysts will be discussed under batch and continuous conditions.

4.2. Hydrogenolysis of THFA and FUR over nickel catalyst supported by hydroxidic lanthanide species under batch conditions

As discussed in paragraph 1.4, the direct conversion of THFA and FUR to 1,5-PeD is challenging due to the low selectivity of non-noble metal catalysts to 1,5-PeD (see Table 1.4) and the low stability of expensive modified noble metal catalytic systems in aqueous flow reactions [81, 82]. Thus, it was essential to develop a selective and highly stable noble metal-free catalyst to obtain 1,5-PeD by processing in a continuous reactor. Nickel on lanthanide supports was selected as an alternative for the hydrogenolysis of THFA due to the high selectivity to 1,5-PeD reported for Ni-$La(OH)_3$ and Ni-Y_2O_3 in the batch mode [84, 85, 99]. In this doctoral thesis, the catalytic behavior of Ni on several rare-earth supports was studied in batch experiments, and the most active catalysts were selected for flow investigations and stability tests.

4.2.1. Catalyst characterization

The Ni content and the surface area of all catalysts on rare-earth supports were determined by ICP-OES and BET methods. However, only the best active Ni catalysts on lanthanide supports (wt% Ni-Ln, Ln: La, Pr, Sm hydroxides/oxyhydroxides) were extensively characterized using XRD, XPS, H_2 chemisorption, TPR, TPD-CO_2, and TPD-NH_3. Moreover, XAS and STEM methods with EDX element mapping technique were applied to identify the structural and electronic features and the morphology of Ni-La catalysts before and after reduction and reaction (for experimental details see paragraph 3.2). In the beginning, 40Ni-La(F) was calcined during an *in situ* XRD experiment to explore the possible phase formation and transition. As shown in Figure 4.8, the fresh sample was a mixture of both hexagonal crystallites of $Ni(OH)_2$ (2θ= 19.2°, 33.0°, 38.5°, 52,0° and 58.9°) and $La(OH)_3$ (ICDD 00-059-0462 and 00-036-1481), respectively. The main diffraction peaks of the NiO phase appeared at around 37° and 43° (2θ) at calcination temperatures ≥ 300 °C, corresponding to the (111) and (200) planes (ICDD 01-089-7130) (see Figure 4.8). Regarding the La support, it existed mostly as $La(OH)_3$ at 300 °C and was totally transformed to cubic La_2O_3 up to 500 °C (ICDD 03-065-3185). Based on that, 350 °C was chosen as a calcination temperature for fresh Ni catalysts on all selected lanthanide supports. After calcination, the BET surface areas of NiO, $La(OH)_3$ and NiO on several rare-earth supports were measured (Table 4.4). The surface area of all highly loaded Ni catalysts on rare-earth supports ranged from 82 to 177 $m^2\ g^{-1}$ (entries 3-9) (for N_2 adsorption-desorption isotherms see Figure A3). The surface area of the pure $La(OH)_3$ was 59 $m^2\ g^{-1}$ (entry 2), while that of 40Ni-La(C) increased to 82 $m^2\ g^{-1}$ probably due to the contribution of NiO which had similar surface as the support $La(OH)_3$ (entry 1). To get more information about the influence of the NiO phase on the textural properties of Ni-La(C), the Ni content was varied from 13 wt% to 41 wt% (Table 4.4) (for N_2 adsorption-desorption

isotherms see Figure A4). When the loading of Ni was reduced to 13 wt%, the BET surface area significantly decreased to 46 $m^2 g^{-1}$ (entry 10). However, it increased again at Ni loadings ≥21 wt% (entries 7,8). This seems to indicate that finely dispersed NiO covered the smaller $La(OH)_3$ surface at low Ni content. However, when the content increased to more than 13 wt%, NiO formed a separate phase which was not attached to the support surface resulting in a higher surface area.

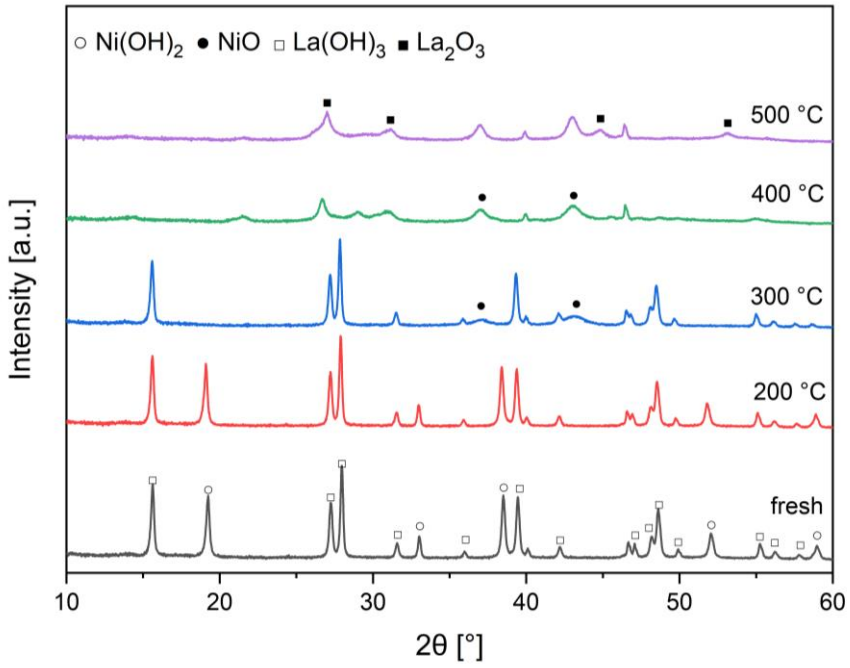

Figure 4.8. Powder diffractograms of 40Ni-La(F) calcined *in situ* under a flow of 10% O_2/Ar (20 mL min^{-1}).

Table 4.4. BET surface area of NiO, $La(OH)_3$ and Ni-Ln(C) catalysts.

Entry	Catalyst	Molar ratio (Ni:Ln)	BET surface area [$m^2 g^{-1}$]	Pore volume [$cm^3 g^{-1}$]
1	NiO	-	62	0.39
2	$La(OH)_3$	-	59	0.24
3	42Ni-Sc(C)	1.8	177	0.43
4	48Ni-Y(C)	2.9	98	0.30
5	40Ni-La(C)	2.5	82	0.21
6	41Ni-Ce(C)	2.7	146	0.31
7	41Ni-Pr(C)	2.7	93	0.40
8	42Ni-Nd(C)	2.8	106	0.37
9	40Ni-Sm(C)	2.8	99	0.18
10	13Ni-La(C)	0.5	46	0.14
11	21Ni-La(C)	0.9	99	0.25
12	28Ni-La(C)	1.3	90	0.31

To confirm the observations of BET measurements, the ABF-STEM method was applied to 40Ni-La(C). As shown in Figure 4.9, $La(OH)_3$ had a columnar compact structure with small pores while NiO had a more porous structure (a-b). Obviously, NiO was well separated from

the $La(OH)_3$ support and they formed a conglomerate of rather independent particles. This finding is in a good agreement with the conclusion of previous BET measurements.

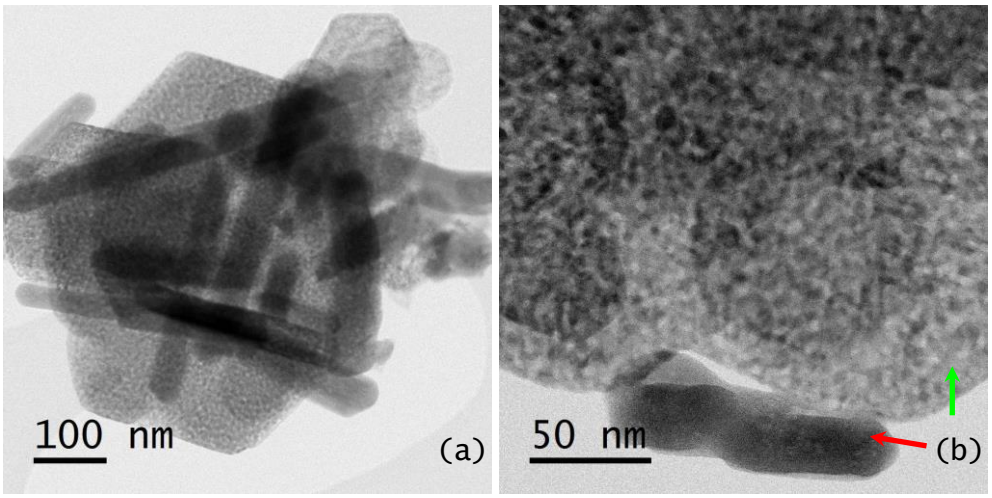

Figure 4.9. ABF-STEM images of 40Ni-La(C) (a, b) (green arrows for NiO phase and red for $La(OH)_3$ phase).

To determine the reduction temperature of NiO and to compare its reducibility on different lanthanide supports, TPR measurements were performed of selected calcined Ni catalysts (Ni-Ln(C), Ln: La, Pr, Sm hydroxides and oxyhydroxides) (Figure 4.10). The reduction profile of NiO consisted of one reduction peak which was found to be at 314 °C. However, two reduction peaks were observed in the case of all Ni-Ln(C) materials (Figure 4.10). The main reduction peak was shifted to 342 °C for NiO on lanthanide supports. This could be explained by the different type of Ni-support interaction which might lead to a formation of interface zones between two phases on the catalyst surface. This hypothesis is similar to previous findings assuming that an interaction between Ni^0 and Y_2O_3 might occur at the phase boundary of both species [99]. Moreover, the shape of the NiO reduction peak was different compared to calcined Ni catalysts confirming that the reducibility of bulk NiO was influenced by the lanthanide supports (Figure 4.10). Regardless of the type of lanthanide species, the reduction temperature of bulk NiO was almost the same for each selected calcined catalyst. On the other hand, small reduction peaks for 40Ni-La(C), 41Ni-Pr(C) and 40Ni-Sm(C) were observed at 178, 205 and 183 °C, respectively (see Figure 4.10). Such a low-temperature peak was not found in the case of NiO, and it could be assigned to the reduction of slightly smaller NiO particles and/or superficially amorphous NiO. Also, the slight change of the peak area at 205 °C in the case of Ni-Pr(C) might be due to the different size of NiO particles on the catalyst surface.

Interestingly, a small tail of the 40Ni-La(C) reduction peak showed that some material was not reduced before 700 °C (see Figure 4.10). This observation was synchronized with the increase of the actual hydrogen consumption calculated with 12% which was unusual since the considered error in hydrogen consumption calculations was around 6% for other catalysts (see Table A2). This increase can be justified by the fact that lanthanum hydroxide species are

reactive under ambient atmosphere and can adsorb some H_2O and CO_2 on its surface forming lanthanum carbonate and oxycarbonate ($La_2O_2CO_3$) which is decomposed again at higher temperature during TPR measurement forming CO_2 affecting a higher hydrogen consumption. This observation could be proved with other methods such as XRD. Nevertheless, these findings appear to be well substantiated by previous studies [36, 37].

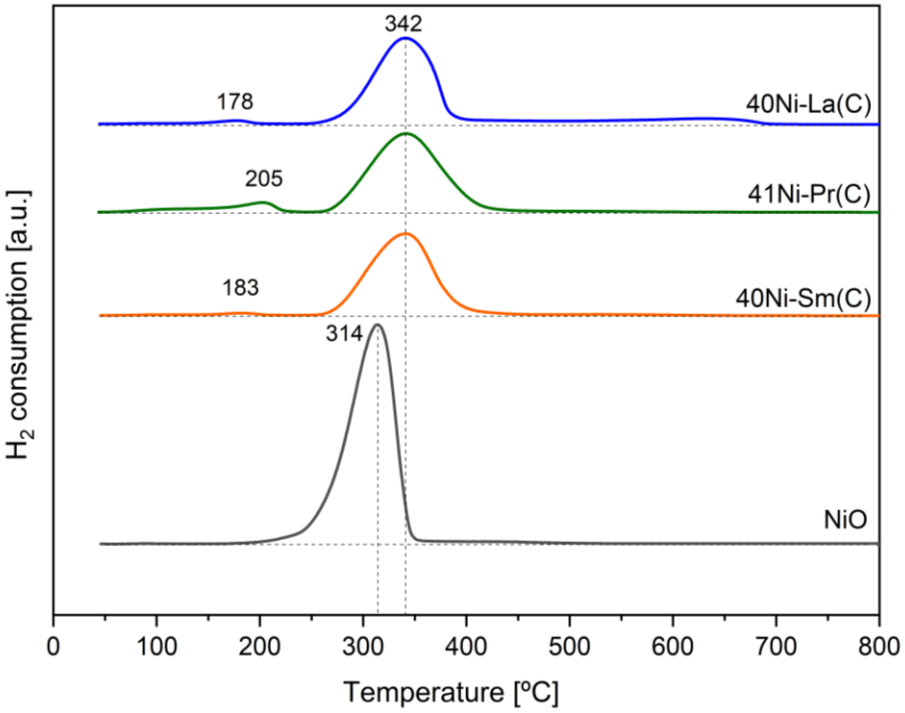

Figure 4.10. TPR profiles of NiO and Ni-Ln(C) (Ln= La, Pr, Sm hydroxides/oxyhydroxides).

Furthermore, XRD measurements were conducted for reduced Ni catalysts (Ni-Ln(R), Ln= La, Pr, Sm hydroxides/oxyhydroxides) before the reaction. Additionally, their diffractograms were compared with the spent catalyst 40Ni-La(S) obtained after a continuous flow reaction for 386 hours (for more details about reaction conditions see paragraph 4.3.4). Concerning the Ni-Ln(R) catalysts, the reduction was carried out *ex situ* at 250°C for 8 h followed directly by XRD analysis. As shown in Figure 4.11, the reflections at 2θ= 44.5°, 51.9° and 76.4° appeared as the dominating signals for the nickel phase corresponding to the (111), (200) and (220) lattice planes of metallic nickel (ICDD 00-004-0850). To prove the complete reduction of NiO to metallic Ni, the TPR method was used, The TPR profile of 40Ni-La(R) was compared with that of 40Ni-La(C) showing that most of NiO (~94%) was reduced to metallic Ni (see Figure A5). In contrast, 40Ni-La(S) showed small traces of NiO which might be probably due to partial oxidation of Ni^0 in interface zones with $La(OH)_3$ during the reaction. In addition, some traces of $La_2O_2CO_3$ were detected in both reduced and spent samples of 40Ni-La due to the high reactivity of $La(OH)_3$ with H_2O and CO_2 [36, 37]. The possible contamination with $La_2O_2CO_3$ was also confirmed by the TPR profile of 40Ni-La(C) (see Figure 4.10). As mentioned in paragraph 3.1.2, the lanthanide supports had a slightly different composition even when the same reduction conditions were applied. For the La support, the dominating peaks were

characteristic for $La(OH)_3$ (ICDD 01-079-5398) with some traces of LaO(OH), in contrast to the Pr support which mostly consisted of PrO(OH) (ICDD 00-027-0478). However, the dominating phase exclusively corresponded to SmO(OH) in the case of 38Ni-Sm(R) (ICDD 01-083-2504). Obviously, after long reduction time, the composition of the hydroxidic support was influenced by the lanthanide metal. However, there was no effect of the lanthanide support on the reducibility of the bulk nickel phase. This finding supported the previous TPR results which showed similar reduction peaks for bulk NiO on different lanthanide supports.

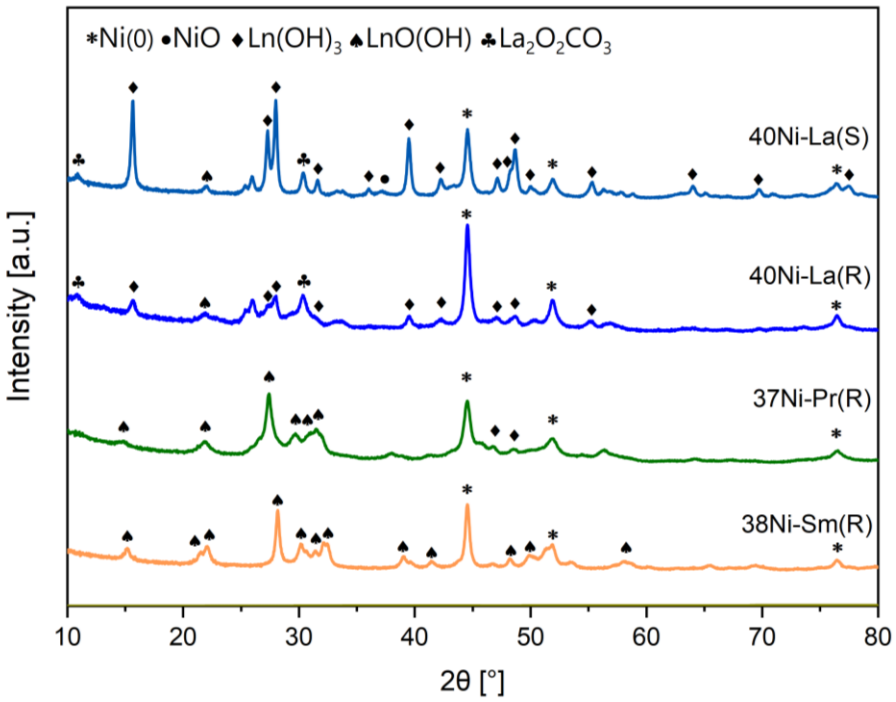

Figure 4.11. XRD patterns of Ni-Ln(R) (Ln= La, Pr, Sm hydroxide/oxyhydroxide) and Ni-La(S) (after 386 h TOS).

To quantify the amount and the strength of the basic sites of the lanthanide supports after reduction, CO_2-temperature-programmed desorption measurements (TPD-CO_2) were performed (Figure 4.12). Depending on the CO_2 desorption temperature, the strength of basic centers was identified, where the desorption of CO_2 (breaking CO_2 bonds) occured at temperatures between 100-230 °C for weak, 230-500 °C for moderate and higher than 500 °C for strong centers [119-121]. As shown in Figure 4.12a, both 40Ni-La(R) and 37Ni-Pr(R) possessed the highest amount of strong basic centers >500 °C (see Figure 4.12). In the case of 40Ni-La(R), the dominating peak indicating the desorbed CO_2 concentration was found at 741°C as a main sharp band while a broader peak at 643°C was observed in the case of 37Ni-Pr(R). In contrast, the basicity of 40Ni-Sm(R) ranged from weak to strong with a declined desorption band (see Figure 4.12). The difference in the basicity could be explained by the various composition of lanthanide supports which appeared in the XRD diffractions patterns (see Figure 4.11). For instance, the La support in 40Ni-La(R) consisted mostly of hydroxidic species (3 per La center) which are more basic than (oxy)hydroxidic species in SmO(OH) (Figure 4.1) [108]. In the case of 37Ni-Pr(R), $Pr(OH)_3$ was not fully transformed to PrO(OH)

after calcination and reduction as in 40Ni-Sm(R), thus its basicity was comparable to 40Ni-La(R) (Figure 4.1). Moreover, the different basicity could also be attributed to the variation in ionic radii and the size of lanthanide cations according to Fajans' rule (lanthanide contraction) [122]. The decrease in the size of Ln^{3+} ions from La^{3+} to Sm^{3+} increases the covalent character whereby the basicity of Ln^{3+} hydroxides diminishes [122]. So, the basicity of Ni-Ln(R) decreased depending on the lanthanide supports in the order: La ≥ Pr > Sm supports (see Table 4.6).

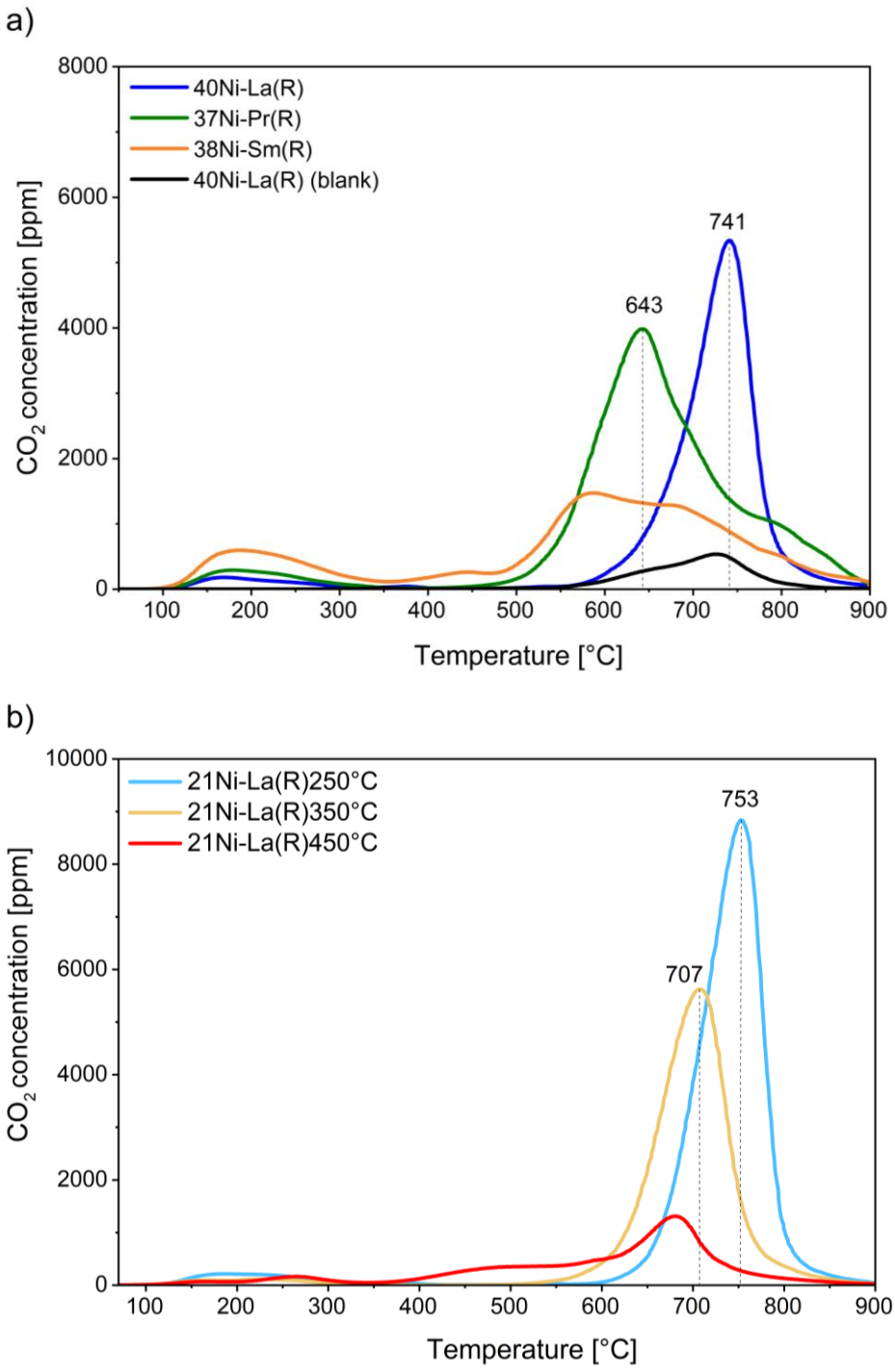

Figure 4.12. TPD-CO_2 profiles of Ni catalysts a) on different supports Ni-Ln(R) (Ln= La, Pr, Sm hydroxides/oxyhydroxides); b) on $La(OH)_3$ at different reduction temperatures.

To ensure that the high basicity of 40Ni-La(R) was not caused by the decomposition of lanthanum oxycarbonates (see reflections of $La_2O_2CO_3$ in the powder diffractogram of 40Ni-La(R) (Figure 4.11)) a blank experiment in helium (without preliminary adsorption of CO_2) was additionally conducted (see 40Ni-La(R) (blank) in Figure 4.12a). Predictably, a small peak appeared at a temperature range from 550 to 850°C which might indicate the decomposition of $La_2O_2CO_3$. However, this peak presents only ≈10% of the actual CO_2 desorbed from 40Ni-La(R). This clearly shows that the strong basicity of 40Ni-La(R) originated from the $La(OH)_3$ support. Additionally, NH_3-TPD measurements of Ni-Ln(R) catalysts were also performed and showed only small traces of acidic sites, (see Figure A6 and Table 4.6). Figure 4.12b shows the effect of reduction temperature on the amount of strong basic sites of 21Ni-La(R) (compare 21Ni-La(R)250°C and 21Ni-La(R)450°C). Due to the gradual transformation of $La(OH)_3$ to La_2O_3 via LaO(OH) at higher reduction temperatures, the basicity of 21Ni-La(R) dropped from 1875 to 951 µmol g^{-1} of adsorbed CO_2 (Table 4.6). in Figure 4.12b). In summary, the reduction temperature had a remarkable impact on the number of strong basic sites of the support. Also, the basicity strength depended on the type of lanthanide metal due to the lanthanide contraction and on the consumption of CO_2 since hydroxides are naturally more basic than oxyhydroxide species.

Next, pseudo *in situ* XPS was conducted for these catalysts after a short reduction time to identify this influence of the lanthanide support on the reducibility of surface NiO. Figure 4.13 shows the Ni 2p spectra of Ni-Ln catalysts before reduction (calcined samples) and after reduction in a high-pressure cell at 250 °C for 3 h (for experimental details see paragraph 3.2) (for values of binding energies and Ni surface concentrations see Table A3). In the case of calcined catalysts, the Ni $2p_{3/2}$ peak was observed at a binding energy of 853.7 eV together with the typical multiple splitting as well as pronounced satellite features characteristic for NiO (see Figure 4.13) [123]. After 3 hours of reduction in atmospheric pressure of H_2 at 250°C, new peaks at 852.6 eV and 870.0 eV could be observed in all samples assigned to Ni $2p_{3/2}$ and Ni $2p_{1/2}$ energy levels of metallic Ni, respectively [123, 124]. However, the used fit (Ni^0 + NiO) does not perfectly describe all peaks in the spectra, for example the deviation at about 867 eV, thus hinting to an interaction of Ni with the lanthanide support species. This matches well with the previous TPR assumption (see discussion of Figure 4.10). Briefly, the maximum degree of reduction was around 97% for 38Ni-Sm(R) followed by 81% in the case of 37Ni-Pr(R) (for details see Table A3). In the case of 40Ni-La, the detailed analysis of the spectra was more complicated due to the strong overlap of La 3d and Ni 2p bands, but even in this case, a reduction degree of 79% could be estimated. It seems likely that the reduction time was not enough to reduce all the NiO species on the surface. However, it is worth to mention that the deconvolution is complex considering all NiO components (5 doublets) and Ni^0 (4 doublets) leading to a big uncertainty in the calculated Ni^0:NiO ratio, especially in the case of 40Ni-La.

Moreover, the spent catalysts Ni-Ln(R) were also measured after a long continuous flow reaction (50-384 h TOS) (for XPS Ni 2p spectra of spent catalysts see Figure A8). The main Ni $2p_{3/2}$ peak was observed at a binding energy of around 855.0 eV which is identical to $Ni(OH)_2$, and metallic Ni could not be detected anymore in all spent catalysts (Figure A8).

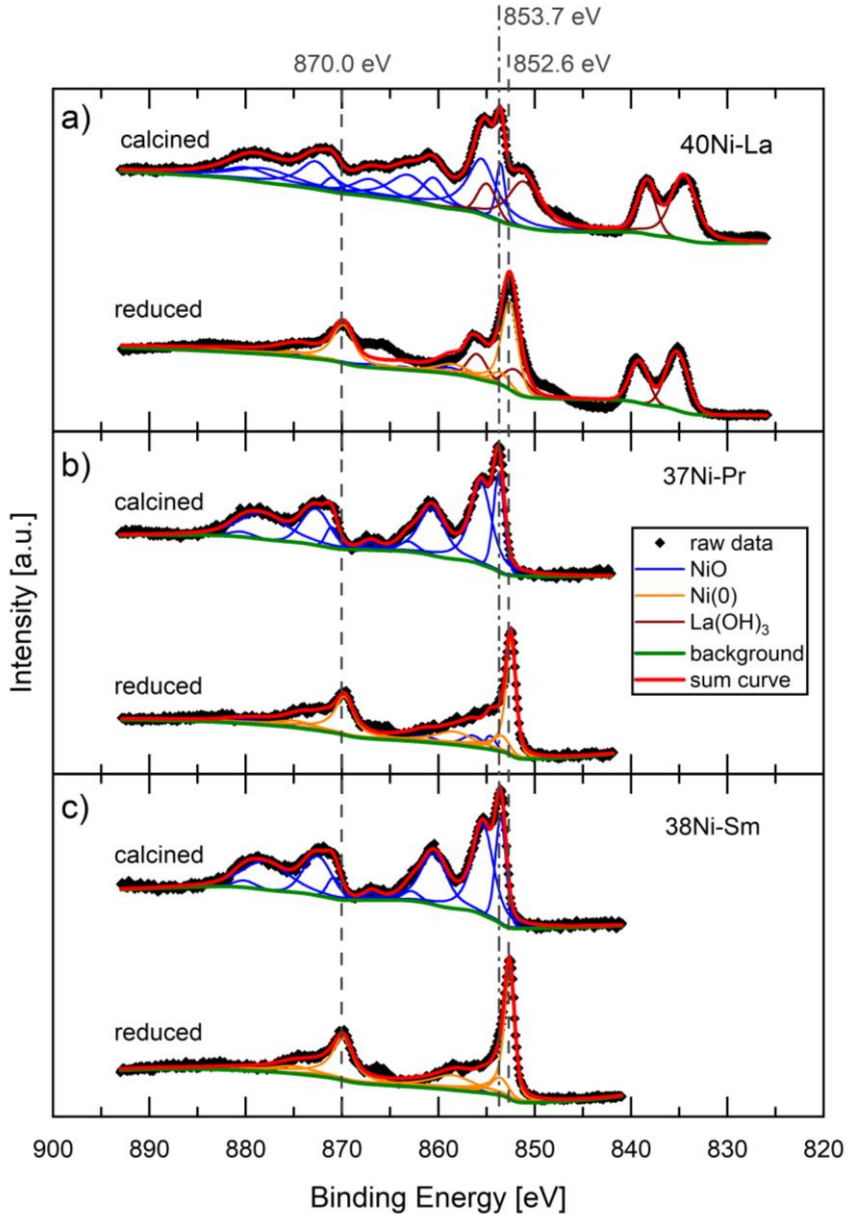

Figure 4.13. Pseudo *in situ* XPS Ni 2p spectra of calcined (top) and reduced (bottom) 40Ni-La (a), 37Ni-Pr (b) and 38Ni-Sm (c) (for experimental details see paragraph 3.2, and for details of the applied fitting model see Figure A7).

Table 4.5 summarizes the detected atomic concentration on the surface of all samples (before reduction: Ni-Ln(C); after reduction: Ni-Ln(R); after flow reaction: Ni-Ln(S)). Obviously, a significant increase of the carbon concentration accompanied by a decrease in nickel concentration was observed. This change in concentration was more remarkable in the case of 37Ni-Pr after 50 h TOS where 30.8 at.% C and 8.7 at.% Ni were determined for 37Ni-Pr(S) compared to 4.9 at.% C and 29.1 at.% Ni for 37Ni-Pr(R). That implies the deposition of the carbonaceous material probably by decomposition of organic species on the catalyst surface

was higher in the case of dispersed Ni on PrO(OH) support after only 50 h TOS which could block the active sites of the catalyst. However, the increase of carbon concentration at the surface was not significant in the case of 40Ni-La(S) and 38Ni-Sm(S) even after long continuous run (up to 386 h TOS).

Table 4.5. The atomic concentrations on the surface for catalysts before/after reduction and after reaction.[a]

Entry	Catalyst	The surface concentration [at.%]					
		C	O	Ni	La	Pr	Sm
1	40Ni-La(C)	6.5	50.2	34.3	9.0	-	-
2	40Ni-La(R)	10.8	37.9	40.6	10.7	-	-
3	40Ni-La(S) after 386 h TOS	19.1	47.0	20.6	13.3	-	-
4	37Ni-Pr(C)	6.3	62.2	26.8	-	4.7	-
5	37Ni-Pr(R)	4.9	52.5	29.1	-	13.5	-
6	37Ni-Pr(S) after 50 h TOS	30.8	50.9	8.7	-	9.6	-
7	38Ni-Sm(C)	7.2	65.3	26.1	-	-	1.4
8	38Ni-Sm(R)	12.0	46.3	37.0	-	-	4.7
9	38Ni-Sm(S) after 192 h TOS	19.2	56.1	19.1	-	-	5.6

[a] for flow reaction conditions see Figure 4.24 and Figure 4.25 in paragraph 4.3.4.

Furthermore, to understand the effect of the lanthanide support on the active Ni surface and the dispersion of Ni particles, H_2 chemisorption was conducted for Ni catalysts on selected supports with a similar Ni loading after catalyst reduction (Table 4.6). Systematically, the Ni loading as well as reduction temperature were varied for Ni-La(R) catalysts. The Ni surface area and its dispersion was significantly lower in the case of 40Ni-La(R) and 38Ni-Sm(R) than for 37Ni-Pr(R) (4.4, 5.8 and 9.5 $m^2\ g^{-1}$, respectively) (entries 1-3). Thus, the particle size of metallic Ni was much lower in the case of 37Ni-Pr(R) compared to others. Regarding 40Ni-La(S), its particle size had changed significantly after 386 h TOS (for see paragraph 4.3.4 for more details), compared to 40Ni-La(R) (entry 4). Briefly, the dispersion of Ni on different lanthanide supports varied in the order: 37Ni-Pr(R) >> 37Ni-Sm(R) > 40Ni-La(R) ~ 40Ni-La(S) (see Table 4.6). Regarding particle and crystallite size of metallic Ni, the highest average particle size (determined by chemisorption) and crystallite size (determined by XRD) of Ni was found on $La(OH)_3$ (entry 1). This finding supports the previous TPR results for calcined catalysts which showed that the reduction temperatures of superficially amorphous NiO was lower on La and Sm supports than on Pr support (see Figure 4.10). Table 4.6 also presents the active nickel surface area for Ni-La(R) with lower Ni contents (13 and 21 wt%) and at different reduction temperatures (250 °C- 450 °C). As expected, the decrease in Ni content to 13% significantly enhanced the Ni dispersion (compare entries 1 and 5). However, the nickel surface area did not change in the same manner because of the formation of larger particles (60.6 nm for 40Ni-La(R) vs 25.1 nm for 13Ni-La(R) (Table 4.6). On the other hand, the increase of the reduction temperature had only a low impact on Ni dispersion (compare entries 6-8). In

summary, the nickel dispersion is influenced by the support and significantly enhanced by decreasing the nickel content, but not by the thermal pretreatment.

Table 4.6. Structural properties of Ni-Ln(R) at different nickel loading and reduction temperature.

Entry	Catalyst (wt% Ni-Ln)	Crystallite size of Ni^{0} [c]	H_2 Pulse chemisorption			CO_2 ←TPD→ NH_3	
			Ni surface area [m^2 g^{-1}]	Ni dispersion [%]	Ni particle diameter [nm]	Basicity [µmol g^{-1}]	Acidity [µmol g^{-1}]
1	40Ni-La(R)	16	4.4	1.7	60.6	1324	8
2	37Ni-Pr(R)	12	9.5	3.9	26.2	1370	10
3	38Ni-Sm(R)	12	5.8	2.3	43.7	1144	14
4	40Ni-La(S)	14	4.8	1.8	55.8	-	-
5	13Ni-La(R)	-	3.5	4.0	25.1	-	-
6	21Ni-La(R)	-	4.0	2.9	35.4	1875	-
7[a]	21Ni-La(R)	-	3.5	2.5	40.2	1369	-
8[b]	21Ni-La(R)	-	3.8	2.7	36.8	951	-

All catalysts were reduced at 250°C, except [a] at 350°C and [b] at 450°C. The increase of temperatures leads to gradually transformation of $La(OH)_3$ to LaO(OH) and further to La_2O_3. [c] calculation by Scherrer equation based on XRD peak of Ni^0 (111).

In addition, XAS measurements in near (XANES) and extended (EXAFS) Ni K-edge regions were carried out to evaluate the electronic and structural features of the catalysts. For that, 21Ni-La(F), 21Ni-La(C) and 21Ni-La(S) (after 120 h TOS) were selected. First, the electronic properties of the catalysts were studied by evaluating the XANES region (see Figure 4.14a). The comparison of the spectra of the catalyst together with the reference spectra of NiO and the Ni foil shows in the first glance a strong influence of the pretreatment used on the electronic properties of the catalyst. First, a strong white line for the fresh (21Ni-La(F)) and calcined samples (21Ni-La(C)) can be seen which is characteristic for Ni^{2+} ions [125]. There is, however, a clear difference between 21Ni-La(F) and the 21Ni-La(C) in the shape of the white line. For 21Ni-La(F), the peak is broader, with an apparent shoulder at 8343 eV (peak X in Figure 4.14a). This can be assigned to the presence of Ni^{2+} as $Ni(OH)_2$ species [126, 127]. A pre-edge feature at 8329 eV for both samples is characteristic for 1s-3d transition in the Ni^{2+} ions [125, 128]. Regarding the spectrum of 21Ni-La(R), a strong decay of the white line and a concomitant appearance of pre-edge features at 8329 eV characteristic for the 1s-4p transition were observed. The appearance of these features is typical for the change of the symmetry of Ni^{2+} as a result of dehydration. This observation indicates the strong reduction of Ni^{2+} ions to Ni^0. For the spent catalyst (21Ni-La(S)), exposed to reaction at 150 °C and 30 bar directly after reductive pretreatment, a higher intensity in the white line is clearly seen, which refers to a less reduced state of nickel in 21Ni-La(S) compared to 21Ni-La(R). The peak shape at the energy position X (8343 eV) here indicates the possibility of the presence of $Ni(OH)_2$ species.

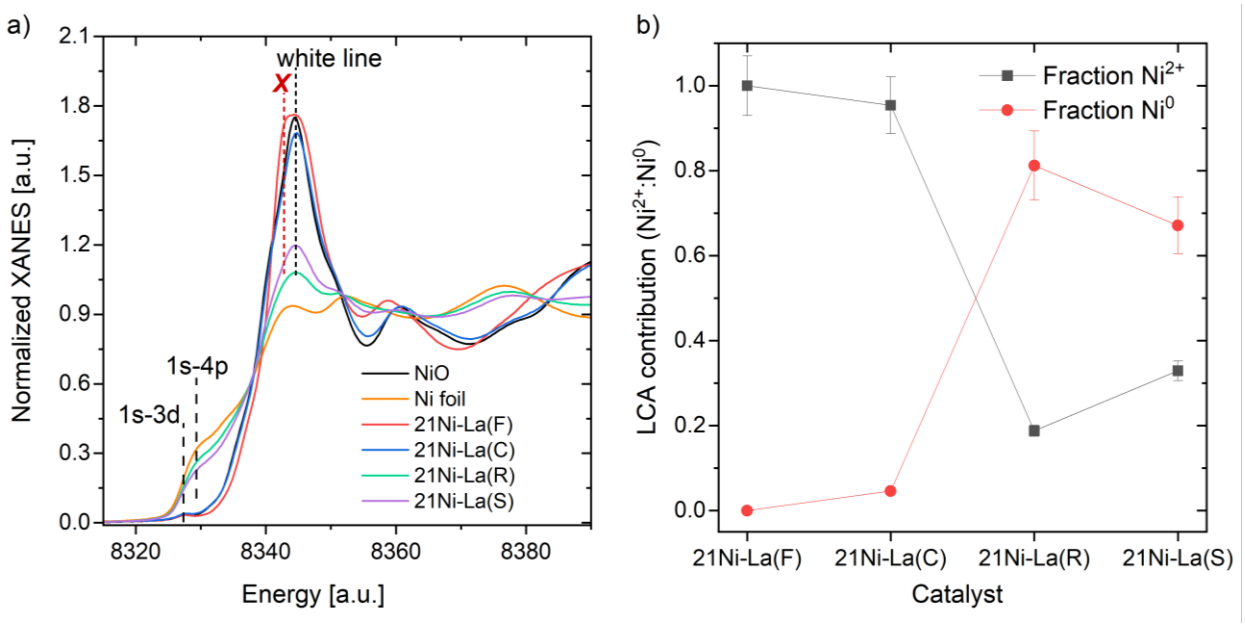

Figure 4.14. (a) Normalized XANES spectra at the Ni K-edge for 21Ni-La(C), 21Ni-La(R) and 21Ni-La(S) (120 h TOS) in addition to spectra of 21Ni-La(F), NiO and Ni foil references. (b) Linear combination analysis (LCA) of different 21Ni-La samples using NiO and Ni foil as analytical standards.

To get more quantitative information on the state of reduction of 21Ni-La catalysts during preparation, pretreatment and after reaction, a linear combination analysis (LCA) of the pretreated and reaction spectra was applied using NiO and Ni foil spectra as reference (see Figure 4.14b and data analysis in Figure A9). The analysis of the data indicates that 21Ni-La(F) essentially consisted of Ni^{2+}. After calcination, the LCA result confirms a high contribution of NiO (95%) with a limited amount of Ni^0, which is in the range of error. However, after reduction, the Ni species were mainly reduced, the Ni^{2+} contribution decreased to 18% and Ni^0 increased to 82% (see Figure 4.14b). The resistance of this fraction of Ni^{2+} ions under reducing conditions can be explained by a strong interaction of the $La(OH)_3$ support and the Ni species resulting in the presence of oxidized Ni at the Ni-La interface. Interestingly, an increase of the fraction of Ni^{2+} to about 32% and a decrease of the fraction of Ni^0 to 68% was observed after the reaction. This was also confirmed by XPS measurements which showed that only Ni^{2+}, mainly $Ni(OH)_2$, was detected on the catalyst surface of 21Ni-La(S). Considering, that the catalyst was not exposed to air after the reaction, this oxidation can be attributed to interaction with the substrate or reaction by-products (e.g. water). Further, the EXAFS data were evaluated for 21Ni-La(R) and 21Ni-La(S). FT-evaluated EXAFS spectra indicated the presence of back-scattering at distances of 2.092 ± 0.011 and 2.55 ± 0.007 Å *characteristic* for O *a*nd Ni respectively with average coordination numbers of 2.14± 0.5 and 7.9 ±1, respectively (see Figure A10, Figure A11 and Table A4). Essentially no change occurred after exposure to the reaction gas mixture. Note that the small coordination number (CN) for the Ni-O shell indicated in both cases that NiO or $Ni(OH)_2$ existed as very small particles which may possibly represent the Ni-La interface region. To prove the assumption of an interface between Ni and La species, 40Ni-La(C), 40Ni-La(R) and 40Ni-La(S) catalysts were compared using ABF- and HAADF-STEM methods and

EDX elemental mapping techniques. As discussed before, 40Ni-La(C) consisted of well separated NiO and $La(OH)_3$ whereby both phases were not homogeneously mixed but formed a conglomerate of rather independent particles (see Figure 4.9, a-b and HAADF-STEM images in Appendix, Figure A12, a-c). Some tiny $La(OH)_3$ clusters seemed to be placed on NiO (Figure A12, c). This observation was further confirmed by the EDX elemental map showing both the presence of Ni and La in the material, but just as separate entities (see Figure A13). However, after reductive pretreatment at 250 °C for 8 h (40Ni-La(R)), NiO was reduced to metallic nickel, while $La(OH)_3$ remained in its structure (Figure 4.15, a, b; Figure A12, d-f; Figure A14). In the case of Ni, the porous structure of NiO vanished after reduction forming a rather compact Ni phase (Figure A12, e) and more fragmented nickel particles developed (Figure 4.15, a and Figure A12, d).

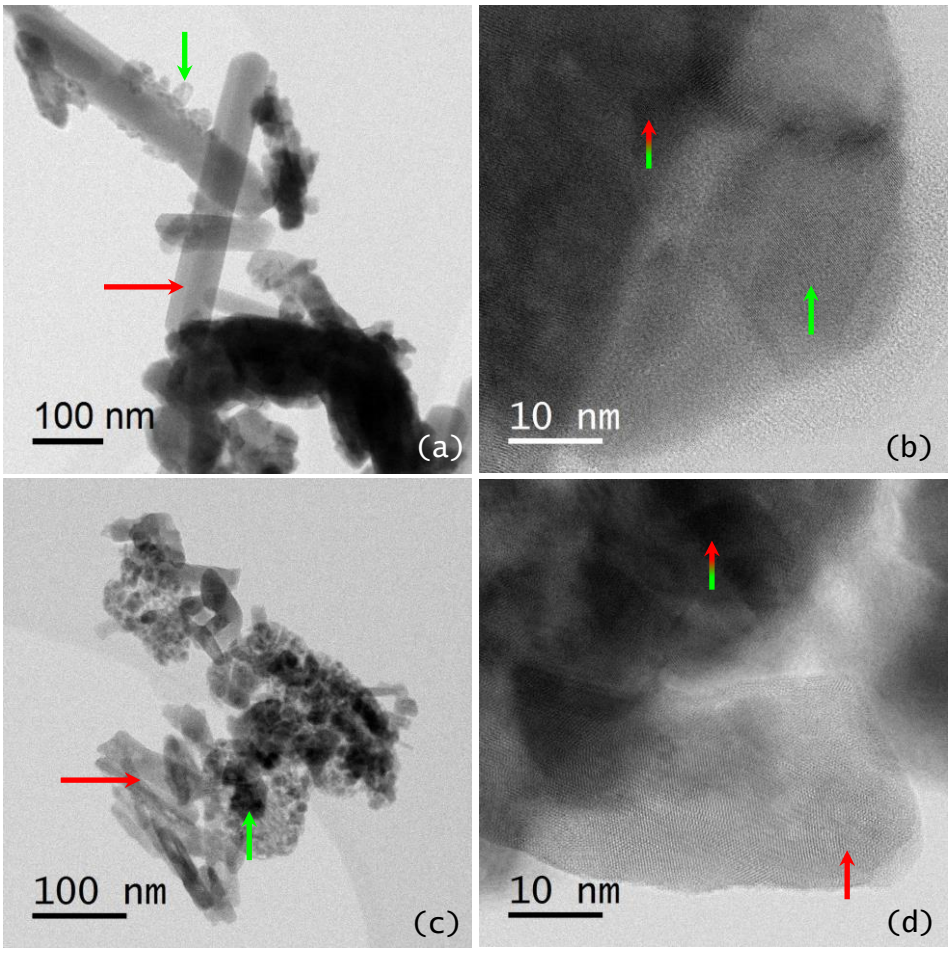

Figure 4.15. ABF-STEM images of 40Ni-La(R) (a, b) and 40Ni-La(S) after 386 h TOS (c, d). The Ni phase is marked with green arrows, while the La phase is indicated by red arrows and interface regions with both colors.

In contrast to NiO, metallic nickel species were more in direct contact with $La(OH)_3$ (columnar particles) (Figure 4.15, b and Figure A12, e). That was more apparent in the EDX elemental map which showed a better distribution of Ni and La with an overlay of Ni on the support indicating that the contact area between both species increased (see Figure 4.16, a-b, and middle of c). This close contact between these Ni and La species may enhance their interaction leading to a joint interface (Ni-La interface). The hypothesis of a strong interaction between Ni^0

and the support was supported by TPR, XPS and XANES results and in line with previous findings for the similar catalytic system of Ni^0 on Y_2O_3 [99]. Regarding the spent catalyst 40Ni-La(S), all previous observations for 40Ni-La(R) did also apply for 40Ni-La(S) (Figure 4.15, c,d; Figure A12, g-l; Figure 4.16, d-f). However, traces of oxygen could be detected close to Ni species (see Figure 4.16, d), which can be either attributed to oxidation of metallic nickel during the reaction or during the transport of the sample to the microscope which could not be completely carried out under inert conditions. The partial oxidation of metallic Ni surface was confirmed for Ni-La(S) by XRD, XPS and XANES results. Nevertheless, the NiO porous structure in 40Ni-La(S) was not completely restored as in 40Ni-La(C), and most important, the interface regions between Ni and La still existed even after a long-term reaction run (386 h TOS) (compare Figure 4.15, c-d and Figure 4.9, a-b; see Figure 4.16).

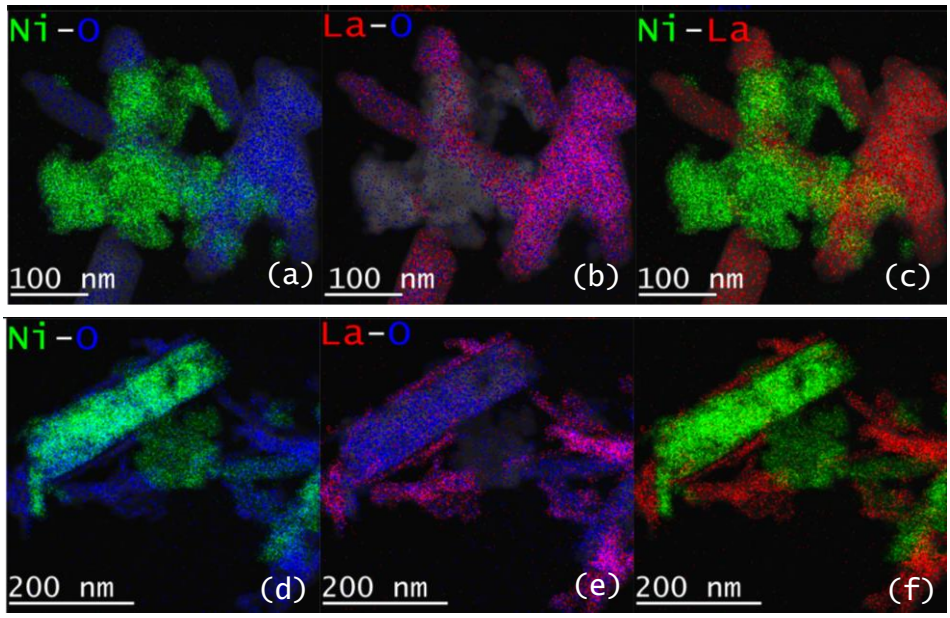

Figure 4.16. EDX elemental mapping of 40Ni-La(R) before the reaction (a-c) and 40Ni-La(S) (d-f) after a continuous run (386 h TOS).

4.2.2. Effect of the preparation method

In order to select the most efficient preparation procedure, several methods such as wet-impregnation, co-precipitation, ball-milling and physical mixing were applied to prepare Ni catalysts on $La(OH)_3$ (for preparation details see paragraph 3.1.1). Table 4.7 compares the conversion of THFA and 1,5-PeD yield using differently prepared 40Ni-La catalysts and the initial compounds. NiO and $La(OH)_3$ as well as metallic nickel, which is known for its activity in hydrogenation reactions, were not active in hydrogenolysis of THFA (entries 1-3). This implies that the catalytic activity was not a result of only one component, but both participated in the reaction to cleave the THFA ring. However, after mixing both components by solid-state methods, physical mixing and ball milling for 2 hours, only low conversion of the resulting catalysts was observed (X= 22-35%) (entries 4,5). Also, wet impregnation was applied, and it did not show any significant impact on the conversion (entry 6). Remarkably, 40Ni-La(R)

obtained after reduction showed almost total conversion with a 1,5-PeD yield of 88%. This yield was up to five times higher than yields obtained with reduced catalysts prepared by other methods (compare entries 7 with 4-6). EDX elemental maps of active 40Ni-La(R) prepared by co-precipitation showed a dispersed distribution of Ni and La with an increasing contact area hinting to a better interaction between these two species causing an enhanced synergetic effect after reduction (Figure 4.16a). This clearly shows that the direct entanglement of metallic Ni particles and lanthanum species after reduction led to a drastic increase of the conversion of THFA. It is likely that the increase in the conversion depended on the interaction between metallic Ni and La species, not only on the surface, but also in catalyst bulk which was achieved by co-precipitation. Thus, the catalyst should be prepared by co-precipitation and pre-reduced before the reaction since the calcined sample (40Ni-Ln(C)) was not active (entry 9) due to the absence of Ni metal particles which were necessary for the interaction with basic $La(OH)_3$ support. This interface concertedly contributed to the reaction whereby metallic Ni activated hydrogen and basic sites deprotonated the substrate (e.g. THFA) resulting in the formation of 1,5-PeD. This interface assumption for Ni-La(R) catalysts was supported by previous conclusions of TPR, XPS, XAS and EDX methods and it was consistent with previous findings about the proposed interface of Rh-ReO_x [78, 79, 95-97] (for more details see paragraph 4.1). Based on that, the formation of a Ni-La phase interface is assumed to be essential to cleave the C–O bond of THFA achieving high yields of 1,5-PeD.

Table 4.7. The effect of preparation method for Ni on $La(OH)_3$ and of its separate components on THFA conversion and product yields.

Entry	Catalyst	Preparation method	Conversion [%]	Yield [%]		Others
				1,5-PeD	1-BuOH	[%]
1	Ni^0	-	3	0	0.4	0.2
2	NiO	-	4	0.4	0.5	0
3	$La(OH)_3$	-	3	0	0.3	1
4	$40Ni^0$+$La(OH)_3$(R)	Physical mixing	22	19	1	2
5	$40Ni^0$+$La(OH)_3$(R)	Ball milling	35	30	1	1
6	40Ni/La(R)	Wet impregnation	25	18	1	4
7	40Ni-La(R)	Co-precipitation	98	88	5	5
8	40Ni-La(C)	Co-precipitation	5	0	0.3	4

Reaction conditions: 2.5 wt% THFA (1 mmol) in 2-propanol (5 mL), m(cat)= 100 mg, mass ratio (cat:THFA)= 1:1, T= 150 °C, $p(H_2)$= 3 MPa, t= 24 h. Others: estimated value of by-products based on an average GC response factor of known products.

4.2.3. Effect of the support

As mentioned before, the most active Ni catalyst was prepared by co-precipitation followed by calcination and reduction. To select the best support for such Ni catalysts, series of nickel on rare earth metal hydroxides/oxyhydroxides/oxides containing Sc and Y, but also La, Ce, Pr, Nd and Sm, were prepared by co-precipitation with Ni contents from 37 to 48% (determined by ICP-OES). Figure 4.17 demonstrates the catalytic performance of reduced Ni catalysts on

selected rare earth supports. Almost complete conversion (98%) was achieved over 40Ni-La(R) and 37Ni-Pr(R) in batch reactors after 24 h. However, 40Ni-La(R) was more selective than 37Ni-Pr(R) to the target 1,5-PeD resulting in a slightly higher yield of 88%. Interestingly, a significant drop in the yield of 1,5-PeD (84%) using 38Ni-Sm(R) was not observed due to the higher selectivity (96%) even if the conversion decreased to 87%. Also, the conversion diminished to 81% for both 48Ni-Y(R) and 37Ni-Nd(R), but the yield of 1,5-PeD was much higher for 37Ni-Nd(R) than for 48Ni-Y(R) due to the subsequent hydrogenolysis of 1,5-PeD to 1-BuOH (highest yield of 1-BuOH = 21%). The lowest conversion (10%, 30%) was found with 42Ni-Sc(R) and 41Ni-Ce(R), respectively.

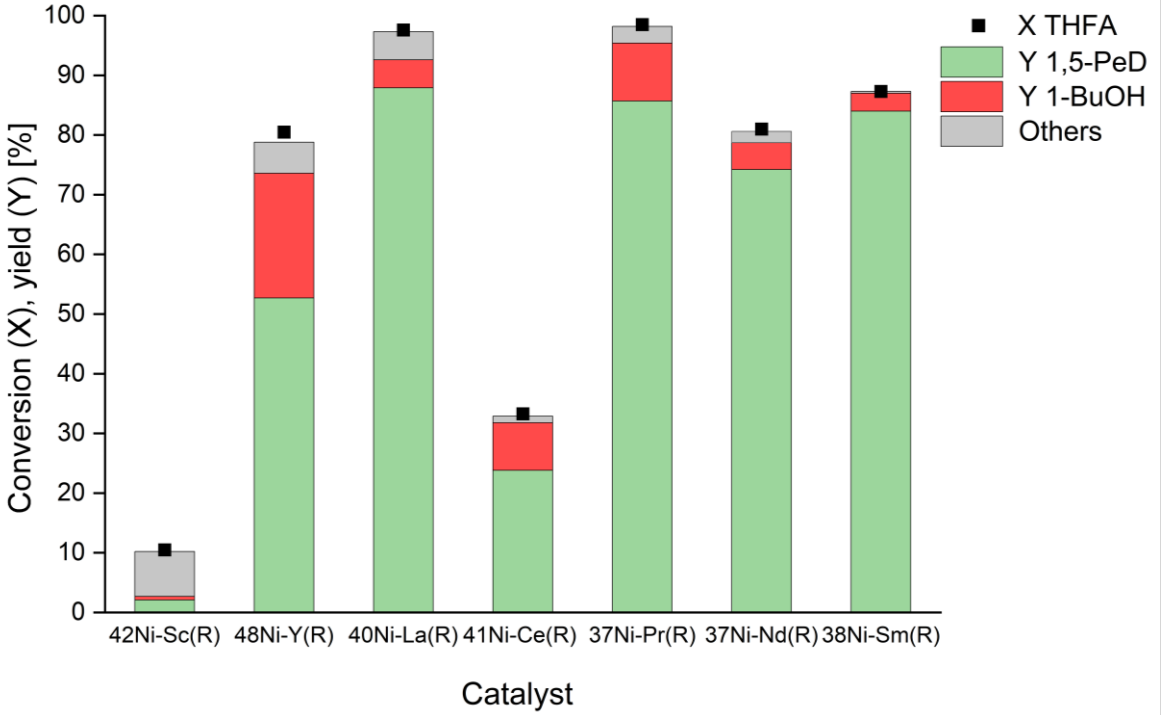

Figure 4.17. The effect of rare-earth supports on conversion and yields in Ni-catalyzed hydrogenolysis of THFA. Reaction conditions: 2.5 wt% THFA (1 mmol) in 2-propanol (5 mL), m(cat)= 100 mg, mass ratio cat:THFA = 1:1, T= 150 °C, p(H_2) = 3 MPa, t = 24 h. Others: estimated value of by-products based on an average GC response factor of known products.

Furthermore, the structural properties of reduced Ni catalysts on the best active supports were extensively studied using H_2-chemisorption and TPD techniques (see Table 4.6). The decrease in the conversion over similarly loaded Ni catalysts (see 38Ni-Sm(R) compared to 40Ni-La(R) and 37Ni-Pr(R)) could be explained by the decrease of the number of basic sites in the metal-support interface which influenced the ability of the catalyst to deprotonate THFA in the initial reaction stage (see TPD-CO_2 profiles in Figure 4.12). Regarding the selectivity to 1,5-PeD, 40Ni-La(R) was more selective than 37Ni-Pr(R) probably due to the difference in the active nickel surface area. At similar Ni contents, it was found that the dispersion of nickel was significantly higher in the case of Pr- compared to the La-based support (3.9 and 1.7%, respectively) (see Table 4.6). In other words, the selectivity to 1,5-PeD was inversely

proportional to the active nickel surface which was 9.5 m^2 g^{-1} on the Pr-based support. Briefly, to achieve high yields of 1,5-PeD, it was essential that the Ni catalysts contained a larger number of strong basic sites, and the active Ni surface area should be less than 9.5 m^2 g^{-1}.

4.2.4. Effect of the solvent

After selecting co-precipitation as the best preparation method and La, Pr and Sm hydroxides and oxyhydroxide as the best active lanthanide supports, it was essential to investigate the effect of the solvent on the catalytic performance in the hydrogenolysis of THFA. As mentioned in the introduction, the choice of the solvent is important in hydrogenolysis of THFA since it could change the reaction pathway and products distribution [86]. Thus, to evaluate the role of the solvent, 40Ni-La(R) was tested in different solvents under the same batch conditions (Figure 4.18). Figure 4.18a compares the catalytic performance of 40Ni-La(R) in aqueous solution and in various organic solvents under hydrogen pressure. 40Ni-La(R) was inactive in aqueous solution in contrast to acid-modified Rh catalysts which were highly active in water [78, 79, 92, 107]. This might be probably explained by the rapid deactivation of nickel surface due to the superficial conversion of Ni^0 to $Ni(OH)_2$ in water which does not participate in the hydrogenolysis reaction [129]. Regarding the other solvents, 40Ni-La(R) was active in several organic solvents, and the highest yields of 1,5-PeD (70-80% after 15 h) were obtained in secondary alcohols (2-PrOH, 2-BuOH and 2-PeOH). Although the conversion of THFA over 40Ni-La(R) in toluene was comparable to secondary alcohols, it was not selective to the target diol. The yield was comparable to that obtained in 1-PrOH and 1,4-dioxane (48-54%). 40Ni-La(R) showed the lowest conversion in ethanol with conversion of 32%. In short, the obtained yields of 1,5-PeD varied depending on the solvents and increased in the following order: H_2O < EtOH < 1,4-dioxane ≈ 1-PrOH ≈ toluene << 2-PeOH < 2-BuOH ≈ 2-PrOH.

The big difference in the conversion of THFA over 40Ni-La(R) in secondary alcohols and other organic solvents gave rise to carry out further experiments under inert conditions to identify the role of the solvents. During the reaction, an exclusive formation of ketones in secondary alcohols was observed which were detected by GC-MS. This finding could be an evidence for dehydrogenation of the solvent on the nickel surface forming internal hydrogen gas and/or for direct transfer of hydrogen from solvent to the substrate in the sense of CTH [130]. Consequently, the above experiments were repeated under the same conditions, but under argon instead of gaseous hydrogen (Figure 4.18b). As expected, 40Ni-La(R) was hardly active without hydrogen except in secondary alcohols, and the highest yields of 1,5-PeD were obtained in 2-PrOH and 2-BuOH (27-30%). The lower yield of 1,5-PeD in this group of solvents indicated that additionally generated hydrogen together with the external gaseous hydrogen contributed to an increase in the ring opening reaction rate as seen in Figure 4.18a.

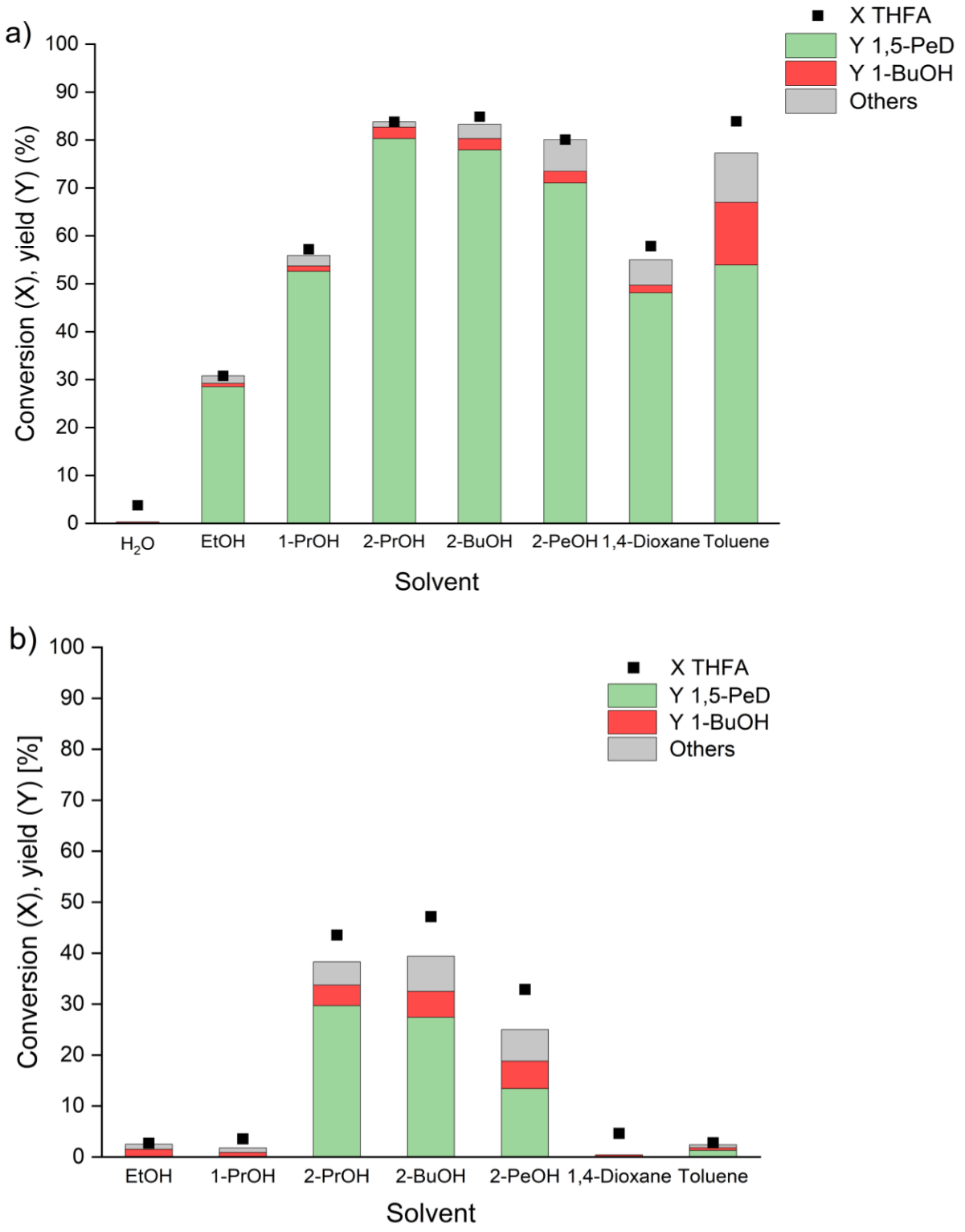

Figure 4.18. Effect of the solvent on conversion and yields in hydrogenolysis of THFA over 40Ni-La(R) under H_2 (a) and Ar pressure (b). Reaction conditions: 2.5 wt% THFA (1 mmol) in solvent (5 mL), m(cat)= 100 mg, mass ratio (cat:THFA)= 1:1, T= 150 °C, p= 3 MPa, t= 15 h. Others: estimated value of by-products based on an average GC response factor of known products.

In contrast, the use of secondary alcohols (volume of 5 mL) as single hydrogen source instead of external gaseous hydrogen was not sufficient to obtain high yields of 1,5-PeD due to the significantly lower conversion of THFA under batch conditions. The reason for that might be due to the preferable occupation of the active Ni surface by the adsorbed solvent, e.g. 2-PrOH,

which represent 97.5% of the reaction mixture under these “inert” conditions. This assumption was confirmed when the formation of acetone caused by dehydrogenation of 2-PrOH was compared under both H_2 and Ar pressure. The results showed that the acetone formation was 10 times higher under Ar pressure. This implies that the dehydrogenation of 2-PrOH became the preferred reaction and not the hydrogenolysis of THFA to target 1,5-PeD in absence of gaseous hydrogen.

4.2.5. Effect of the nickel loading and reduction conditions

To investigate the effect of Ni content on the conversion of THFA, a series of Ni-La(R) and Ni-Pr(R) with different Ni loadings (13-40 wt%) and molar Ni:Ln ratios (0.5-2.5) were tested after reduction under the same conditions (Table 4.8). In the case of Ni-La(R), the highest yield of 1,5-PeD was 88% over 40Ni-La(R) with almost complete conversion (entry 3). Interestingly, a slight decrease in the yield and conversion (X= 89%) was observed over 21Ni-La(R) with half of the Ni content (compare entries 2 and 3). However, the conversion was further dropped to 79% over 13Ni-La (entry 1). The decrease in the conversion could be attributed to the slight decrease in the active nickel surface area (from 4.4 to 3.5 $m^2 g^{-1}$) due to the lower Ni content (Table 4.6). Although the nickel dispersion was significantly improved (from 1.7 to 4%) at lower Ni contents, it had no remarkable impact on the catalytic performance of Ni-La(R) in this reaction (Table 4.6).

Table 4.8. The effect of Ni content and the molar Ni:Ln ratio on conversion and yields in hydrogenolysis of THFA over Ni-Ln(R), Ln= La, Pr.

Entry	Catalyst	Ni content [wt%]		Molar ratio	Conversion	Yield [%]		Others
		Calculated	Found[a]	(Ni:Ln)[a]	[%]	1,5-PeD	1-BuOH	[%]
1	13Ni-La(R)	10	13.0	0.5	79	70	4	5
2	21Ni-La(R)	20	21.1	0.9	89	81	4	4
3	40Ni-La(R)	40	40.4	2.5	98	88	5	5
4	21Ni-Pr(R)	20	21.1	0.9	63	60	3	0
5	34Ni-Pr(R)	30	33.9	1.8	95	83	6	5
6	37Ni-Pr(R)	40	37.5	2.2	99	87	10	2

[a] data based on ICP-OES. Reaction conditions: 2.5 wt% THFA (1 mmol) in 2-propanol (5 mL), m(cat)= 100 mg, mass ratio (cat:THFA)= 1:1, T= 150 °C, $p(H_2)$= 3 MPa, t= 24 h. Others: estimated value of by-products based on an average GC response factor of known products.

Beside the basicity of the support, the active nickel surface area played an important role in enhancing the yield of 1,5-PeD on the same lanthanide support. This conclusion was supported by the catalytic results of Ni-Pr(R) with different Ni contents (Table 4.8). 21Ni-Pr(R) was remarkably less active than other 34Ni-Pr(R) and 37Ni-Pr(R) (compare entries 4-6). Also, the formation of the over-hydrogenolysis product 1-BuOH was much higher than in the case of Ni-La(R). It may be assumed that better dispersed Ni species which were not in contact with Pr-based support were more active in the hydrogenation of the product 1,5-PeD to 1-BuOH than in the cleavage of the C–O bond of THFA. Generally, the conversion of THFA was higher over

Ni-La(R) than over Ni-Pr(R) at a lower Ni content (21wt% Ni) (compare entries 2 and 4) while it was almost complete at higher loading (37/40%) (compare 3 and 6). This clearly shows that at lower nickel loading, the impact of the lanthanide support on the yield of 1,5-PeD over a Ni-Ln interfacial phase is more significant. Briefly, in order to achieve conversion ≥ 90%, it is recommended to prepare catalysts with a Ni loading higher than 21 wt% on $La(OH)_3$ and 30 wt% on Pr(O)OH (see Table 4.8). Thus, 21Ni-La was selected to investigate the influence of the reduction conditions and for their further optimization.

Furthermore, the effect of the pretreatment was the most remarkable since the catalyst containing NiO after calcination (40Ni-La(C)) was not active in contrast to the reduced sample (40Ni-La(R)) (Table 4.7). Therefore, the reduction temperature and time was varied to improve the catalytic performance of 21Ni-La(R) without raising the nickel loading. Table 4.9 compares the catalytic results of 21Ni-La(R) prepared at different reduction temperatures (250, 350 and 450 °C) and at reduction periods between 2 h to 12 h. Remarkably, the conversion dropped from 89% to 25% when the temperature was increased from 250 to 450 °C at the same reduction time (8 h) (entries 1-3). The active nickel surface area and dispersion was hardly influenced by the reduction temperature as they remained in the same range (Ni surface= 3.5-4.0 $m^2\ g^{-1}$ and Ni dispersion= 2.5-2.9%) after reduction (Table 4.6). In contrast, the drop in the conversion of 21Ni-La(R) due to the increased reduction temperature was accompanied by a significant decrease in the basicity from 1875 to 951 µmol g^{-1} (Table 4.6). Figure 4.12 showed clearly that the significant drop in the intensity of the CO_2 desorption curve at temperatures higher than 500 °C was related to a decline of the strong basic centers. That was due to the transformation of strong basic $La(OH)_3$ to LaO(OH) and further to low basic La_2O_3 at higher temperatures up to 500 °C (Figure 4.8). Thus, it was decided to keep the lowest reduction temperature (250 °C) to avoid the basicity loss even if it was lower than the reduction temperature for bulk nickel determined by TPR (342 °C) (see Figure 4.10). In contrast, the reduction time was varied to ensure that all the NiO phase was reduced to metallic nickel at 250 °C. As shown in Table 4.9, the conversion of THFA was 33 and 53% for 21Ni-La(R) reduced for 2 and 5 h, respectively (entries 4,5). Also, a conversion of 89% was achieved if the catalysts was pre-reduced for 8 h which was found to be sufficient to reduce the majority of NiO species (compare TPR profiles of 40Ni-La(R) before and after reduction for 8 h in Figure A5). However, the increase of the reduction time to 12 h was sufficient to achieve almost complete conversion with 21Ni-La(R) (entry 6). The increase in the conversion did not lead to a higher 1,5-PeD yield since the latter remained almost the same of about 80% (compare entries 1 and 6) because of the growing formation of 1-BuOH and other side products. Thus, a reduction temperature of 250 °C was found to be the optimal one to maintain the basic nature of the hydroxidic support, and a reduction time of 8 h was sufficient to reduce most of the NiO in 21Ni-La (see Figure A5).

Table 4.9. Effect of the reduction temperature and time on conversion and yields in hydrogenolysis of THFA over 21Ni-La(R).

Entry	Reduction conditions		Conversion	1,5-PeD selectivity	Yield [%]		Others
	T [°C]	t [h]	[%]	[%]	1,5-PeD	1- BuOH	[%]
1	250	8	89	90	81	4	4
2	350	8	41	93	34	1	1
3	450	8	26	87	22	2	1
4	250	2	33	93	30	2	0
5	250	5	54	94	50	2	2
6	250	12	99	85	80	9	8

Reaction conditions: 2.5 wt% THFA (1 mmol) in 2-propanol (5 mL), m(cat)= 100 mg, mass ratio (cat:THFA)= 1:1, T= 150 °C, p(H_2)= 3 MPa, t= 24 h. Reduction conditions: H_2 flow= 30 mL min^{-1}, heating rate= 1 K min^{-1}. Others: estimated value of by-products based on an average GC response factor of known products.

4.2.6. Influence of the catalyst ratio and reaction time

Due to the small difference in the conversion using highly loaded 40Ni-La(R) and 21Ni-La(R) with the half Ni content, 21Ni-La(R) was selected to investigate the effect of other reaction parameters (see Table 4.14 for more kinetic measurements for 40Ni-La(R)). Initially, the catalyst mass was varied to identify the sufficient ratio of catalyst to THFA to achieve high conversions. Table 4.10 demonstrates the catalytic results of hydrogenolysis of THFA over 21Ni-La(R) at different mass ratios to THFA. A reduction of the catalyst amount drastically decreased the conversion because of the lower number of active sites, mainly basic sites. As shown before in Table 4.8, the increase in Ni content from 21 wt% to 40 wt% did not have such a marked impact on the conversion since it was 89% over 21Ni-La(R) compared to 97% over 40Ni-La(R) (entries 2 and 3).

Table 4.10. The effect of the cat:THFA ratio and reaction time on conversion and yields in the hydrogenolysis of THFA over 21Ni-La(R).

Entry	m(cat)	Mass ratio	Reaction time	Conversion	Yield [%]		Others
	[mg]	(cat:THFA)	[h]	[%]	1,5-PeD	1-BuOH	
1	100	1:1	24	89	81	4	4
2	50	1:2	24	60	57	2	1
3	25	1:4	24	30	27	1	2
4	100	1:1	4	39	36	1	2
5	100	1:1	15	81	72	3	4

Reaction conditions: 2.5 wt% THFA (1 mmol) in 2-PrOH (5 mL), T= 150 °C, p(H_2)= 3 MPa, t= 24 h. Others: estimated value of by-products based on an average GC response factor of known products.

In contrast, the decrease of the ratio (cat:THFA) was found to be proportional to the conversion using 21Ni-La(R) (Table 4.10, compare 1-3). This is further evidence that not only Ni species or strongly basic sites of $La(OH)_3$, but both of them in the proposed interfacial phase influence the yield of 1,5-PeD. Thus, it is important to apply the mass ratio (cat:THFA) 1:1 to achieve high conversions and yields of 1,5-PeD in batch reactions. Moreover, the hydrogenolysis reaction of THFA was studied at several reaction times (entries 4 and 5). In the first four hours,

the conversion was already 39% while it was 81% after 15 h. However, the selectivity was high (90%) even at significantly different conversions and time. Although 21Ni-La(R) was not very active in 2-PrOH and complete conversion was not achieved at a mass ratio (cat:THFA) of 1:1, it was highly selective to 1,5-PeD and the yield of the subsequent product (1-BuOH) did not exceed 4% after 24 h (more kinetic details will be discussed in paragraph 4.4.3).

4.2.7. Influence of the temperature and hydrogen pressure

Furthermore, 21Ni-La(R) was selected to investigate the influence of different batch conditions, particularly temperature, H_2 pressure and reaction time (Figure 4.19). As illustrated in Figure 4.19a, the raise of temperature increased the conversion of which 100% was achieved at 160 °C. However, the growing formation of by-products, especially of 1-BuOH (Y= 15% at 160 °C), prevented a significant increase in the yield of 1,5-PeD. The highest yield of 1,5-PeD was 81% at 150 °C (the optimum temperature). In addition, the effect of hydrogen pressure on the composition of the reaction mixture was investigated (Figure 4.19b). According to the reported literature, 2-PrOH has a vapor pressure of 8.7 bar at 150 °C, which means that it was present even at 2 MPa in the liquid phase [131]. However, the increase in the conversion from 59% to 89% at 2 and 3 MPa, respectively, was obviously due to the better solubility which was found to be 1.5 times higher at 3 MPa than at 2 MPa in 2-PrOH at 100 °C [132]. The further increase of the pressure to 4 MPa was not productive resulting in a similar yield (83%) of 1,5-PeD as obtained at 3 MPa, probably the high concentration of adsorbed hydrogen hampered the interaction of THFA with the catalyst surface. Since the pressure was also needed to keep 2-PrOH in liquid phase avoiding any vapor formations during the reaction, a pressure of 3 MPa was sufficient.

Comparing these results with modified Rh catalysts, the best yield of 1,5-PeD ranged from 83 to 88% over Rh-ReO_x/TiO_2 with 2.7 wt% for each Rh and Re in this study (see Table 4.3), and from 77 to 94% in the reported works over Rh-ReO_x/SiO_2 with a Rh content of 4 wt% and 3.6 wt% Re under high H_2 pressure (up to 8 MPa) in water under batch conditions [78, 79, 94]. Both supported Ni and modified Rh catalysts were highly selective to the target diol. However, the high costs of precious noble metal catalysts and their low stability due to the leaching of the modifier obstruct the transfer of these systems from batch reactions to continuous processes even if they are active at high concentration of THFA in water. Only three works were reported of continuous hydrogenolysis of THFA using modified Ir and Pt catalysts over the last ten years [81, 82, 89]. On the other hand, noble-metal free catalysts Ni-Ln(R) demonstrated comparable yields of target diol (up to 88% after 24 h) at significantly lower H_2 pressure (3 MPa) in 2-PrOH as a commonly used solvent. These catalysts have more potential to be applied in industry as alternative cheap catalysts. Nevertheless, to prove the efficiency of Ni catalysts, the catalytic stability of Ni-La(R) should be tested in long continuous runs under flow conditions.

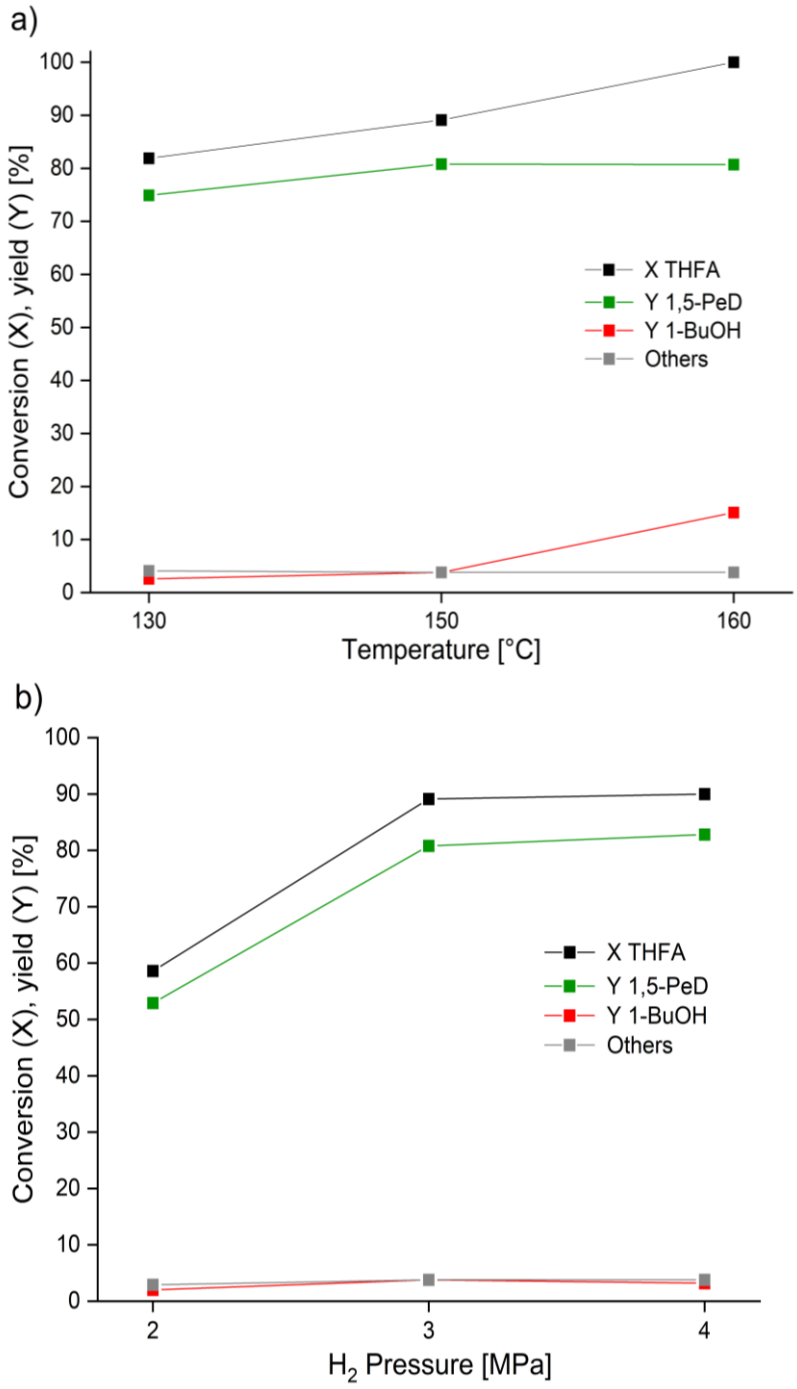

Figure 4.19. Influence of temperature (a) and hydrogen pressure (b) on conversion and yields in hydrogenolysis of THFA over 21Ni-La(R) under batch conditions. Reaction conditions: 2.5 wt% THFA (1 mmol) in solvent (5 mL), m(cat)= 100 mg, mass ratio (cat:THFA)= 1:1, [b] T= 150 °C, [a] p(H_2)= 3 MPa, t= 24 h. Others: estimated value of by-products based on an average GC response factor of known products.

4.2.8. One-pot conversion of FUR to 1,5-PeD via THFA

During the investigations to develop efficient catalysts for the hydrogenolysis of THFA to 1,5-PeD, the question arose if Ni on rare-earth metal supports might be also active in the hydrogenolysis of furfural, since the direct conversion of FUR to 1,5-PeD is one of the most challenging issues in this field so far. Noble bi- and trimetallic catalytic systems were proposed as the most selective catalysts for this purpose in a two-stage reaction sequence [33, 103].

Figure 4.20a shows the catalytic performance of various supported Ni catalysts in the one-pot conversion of FUR to 1,5-PeD under batch conditions. Almost total conversion was achieved using all catalysts, and THFA was found to be an intermediary product after complete hydrogenation of all double bonds of FUR. In contrast to other catalysts, 42Ni-Sc(R) was not active in hydrogenation of the FUR ring, and 66% of FAL was obtained. Also, 48Ni-Y(R) and 38Ni-Sm(R) were not as selective as other lanthanide supports, and 23-27% of THFA remained unconverted after 72 h. The highest yields of 1,5-PeD ranged from 55 to 65% in the case of Ni on lanthanide oxyhydroxides (Ln= La, Pr, Nd, Sm) after 72 h. Due to the long reaction time, several by-products were formed, and their yield exceeded 30%. However, 38Ni-Sm(R) was the best selective catalyst since the total yield of THFA plus 1,5-PeD was 80% compared to by-products (20%). Therefore, it was selected for further investigations at lower temperature because of the low stability of FUR at high temperatures [93-95]. Figure 4.20b shows the effect of temperature on hydrogenation/hydrogenolysis of FUR over 38Ni-Sm(R) after 4 h. FUR was completely converted even at R.T., and FAL was also formed as an intermediate after hydrogenation of the C=O bond of FUR (Y=18%) which was not detected at higher temperatures. The maximum yield of THFA was 92% at temperatures of 50 and 100 °C. Interestingly, a yield of 1,5-PeD around 19% was already obtained after 4 h which increased to 57% after 72 h on the same catalyst (compare Figure 4.20a and Figure 4.20b). This implies that the reaction rate was extremely high within the first hours. However, extending the time was not advantageous since only a low increase in the yield of 1,5-PeD was observed due to the formation of side and consecutive products. Comparing these results with previous ones obtained over 38Ni-Sm(R), 84% of 1,5-PeD was achieved starting from THFA at 150 °C after 24 h (Figure 4.20a). Although THFA and 1,5-PeD were obtained after total conversion of FUR within the first hours, this high yield of 1,5-PeD (84%) was not achieved even after 72 h (Figure 4.20a). This appears to indicate that active sites were partially blocked due to FUR polymerization at 150 °C. Thus, it is proposed to carry out the direct conversion of FUR via THFA in a two-step reaction at different temperatures. Thus, FUR could be hydrogenated to THFA at ≤ 50°C to obtain THFA, which could be further converted at 150 °C by hydrogenolysis of C–O bond of THFA. The two-step approach was previously proposed for one-pot conversion of FUR to 1,5-PeD using bimetallic catalysts (Pd (or Rh)–Ir–ReO_x/SiO_2) under batch conditions (see Table 1.6). By using precious noble catalytic systems, the initial hydrogenation step of FUR was carried out at 40 °C for 8 h to THFA which further underwent a hydrogenolysis step at 100 °C for 48 h which resulted in up to 78% yield of 1,5-PeD [33, 103]. At complete conversion of FUR, it was observed that the color of the reaction mixture turned yellow at high temperatures whereby it was almost colorless in the beginning [103]. It implies that the polymerization of FUR was influenced by the temperature under liquid-phase reaction conditions. Another feasible and industrially applied approach for production of 1,2-PeD from FAL was to process it in the gas phase to avoid FUR polymerization [133]. Also, Ni/SiO_2 was

found to be active in hydrogenation of FUR to THFA in a continuous gas-phase process [42]. Nevertheless, a Ni-based catalyst was not reported as an active and stable catalyst for hydrogenolysis of THFA to 1,5-PeD in continuous liquid-phase process before the studies described in this thesis [108].

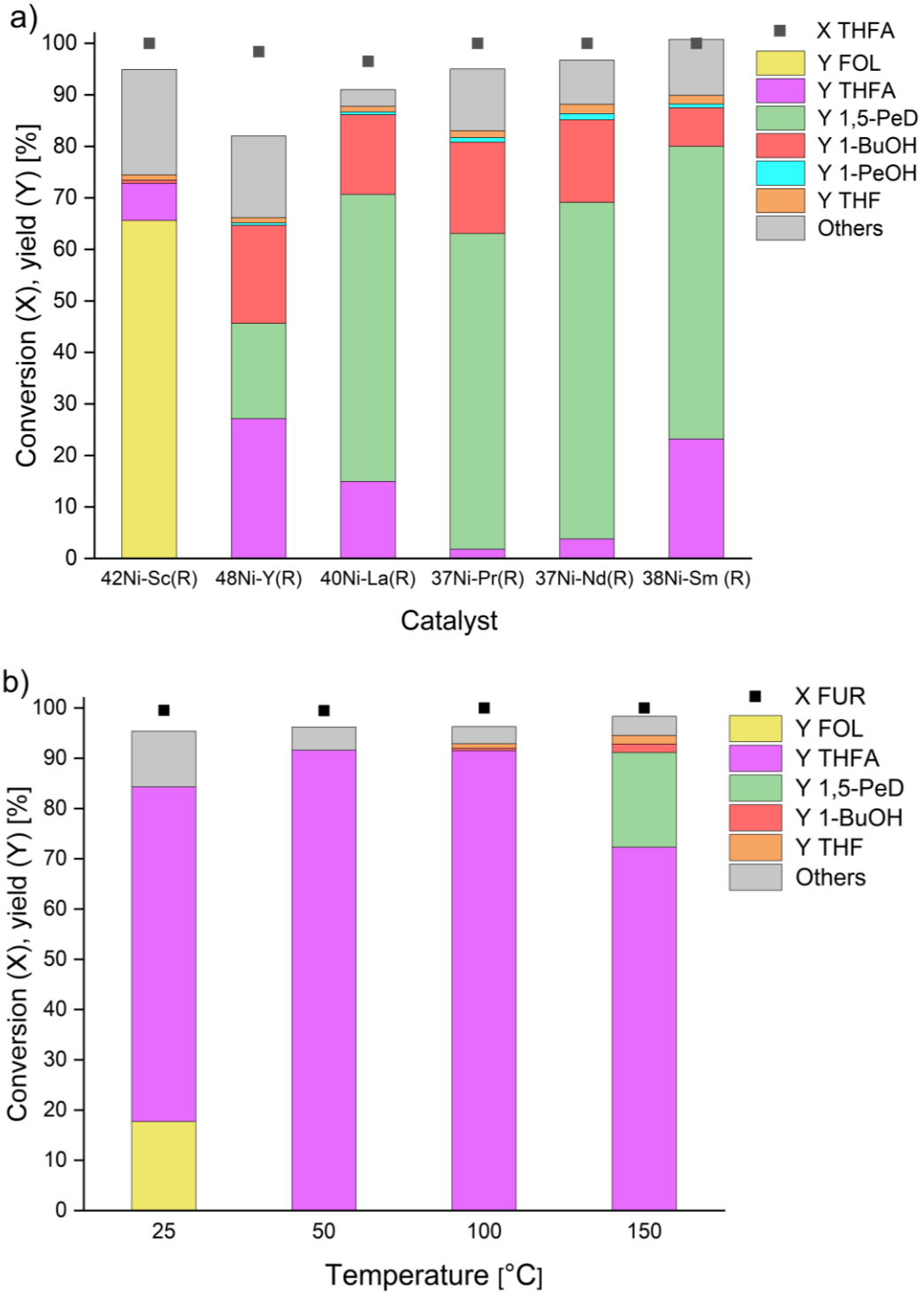

Figure 4.20. Effect of rare-earth metal-based supports of Ni-Ln(R) (a) and reaction temperature over 38Ni-Sm(R) (b) on conversion and yields in hydrogenation/hydrogenolysis of FUR. Reaction conditions: 2.5 wt% FAL (1 mmol) in 2-PrOH (5 mL), m(cat)= 100 mg, mass ratio (cat:FAL)= 1:1, T= 150 °C, p(H_2)= 3 MPa, [a] t= 72 h, [b] t= 4 h. Others: estimated value of by-products based on an average GC response factor of known products.

4.3. Catalytic transfer hydrogenolysis (CTH) of THFA over nickel supported by lanthanide species under flow conditions

As mentioned before, the aim of this work was to develop efficient noble metal-free catalysts for the direct hydrogenolysis of THFA to 1,5-PeD in a continuous process. In the previous experiments in batch reactors, Ni-Ln(R) (Ln= La, Pr, Nd, and Sm hydroxides/oxyhydroxides) showed the highest conversions and yields of 1,5-PeD in this hydrogenolysis investigated. One of the common problems that heterogeneous catalysts widely suffer from is catalyst deactivation during operation. The stability of the active catalyst in a continuous flow process is the key factor for further industrial applications. Indeed, there is a huge gap between the reported works concerning the selective hydrogenolysis of THFA to 1,5-PeD in batch and flow reactors so far. Moreover, the only reported studies on this reaction under flow conditions focused on modified noble metal catalysts in aqueous solution [81, 82, 89]. Ir-MO_X/SiO_2 (4 wt% Ir; M=V, Mo) showed the highest conversion resulting in yields of 1,5-PeD up to 57% [81, 82]. Regrettably, the conversion of THFA over reported Ir catalysts in aqueous solution dropped in the first day of stability test due to the leaching of metal modifiers (Mo, V oxides) [81, 82]. That is why, such modified noble metal catalysts cannot be considered for their large-scale industrial application in the future, even if they are active in water. Thus, to prove that non-modified, noble metal-free Ni catalysts might be an efficient alternative to these already reported catalysts, series of long-term flow experiments were conducted in a continuous microreactor system (see paragraph 3.4.2 for experimental details).

4.3.1. Effect of hydrogen flow rate

The previous batch experiments showed clearly that the conversion of THFA was higher in the case of secondary alcohols (hydrogen-donor solvents) compared to other organic solvents even in presence of a sufficient amount of gaseous hydrogen, the latter condition improved the yield of 1,5-PeD (Figure 4.18a). On the other hand, the yield of the target diol was significantly low when the reaction was carried out without gaseous hydrogen under inert conditions (Figure 4.18b). That is why, the influence of hydrogen flow was also investigated under flow conditions. Figure 4.21a demonstrates the influence of the H_2 flow rate on the catalytic performance of 21Ni-La(R) which was set to 0, 1.2 and 2.8 NmL min^{-1} (NmL: normalized flow rate at 0 °C and 1,013 bar). Obviously, the H_2 flow had almost no significant impact on the conversion of THFA since it was 78-80% in all cases (Figure 4.21a). The selectivity was 5% higher in presence of a H_2 flow, and only a slight increase in the yield of 1,5-PeD resulted (from 63% to 68%). The addition of H_2 had no beneficial effect probably due to the low liquid hourly space velocity (LHSV= 6.3 h^{-1}). Thus, the catalyst mass (40Ni-La(R)) was decreased to 1 g and the concentration of THFA was increased from 1.3 to 2.5 wt%, and the LHSV sequentially increased to 18.8 h^{-1} (Figure 4.21b). Nevertheless, even at a lower catalyst ratio and low

conversion of about 40%, a remarkable advantage due to the introduction of H_2 could not be observed. This may mean that the amount of hydrogen delivered from 2-PrOH to the substrate was already sufficient for the catalyst to selectively cleave the C–O bond of THFA. Therefore, the further investigations of other reaction parameters were conducted under transfer hydrogenolysis conditions (without hydrogen gas flow). This seems to be an advantage for industrial applications since the abandonment of high-pressure hydrogen would reduce the process costs and raise the safety.

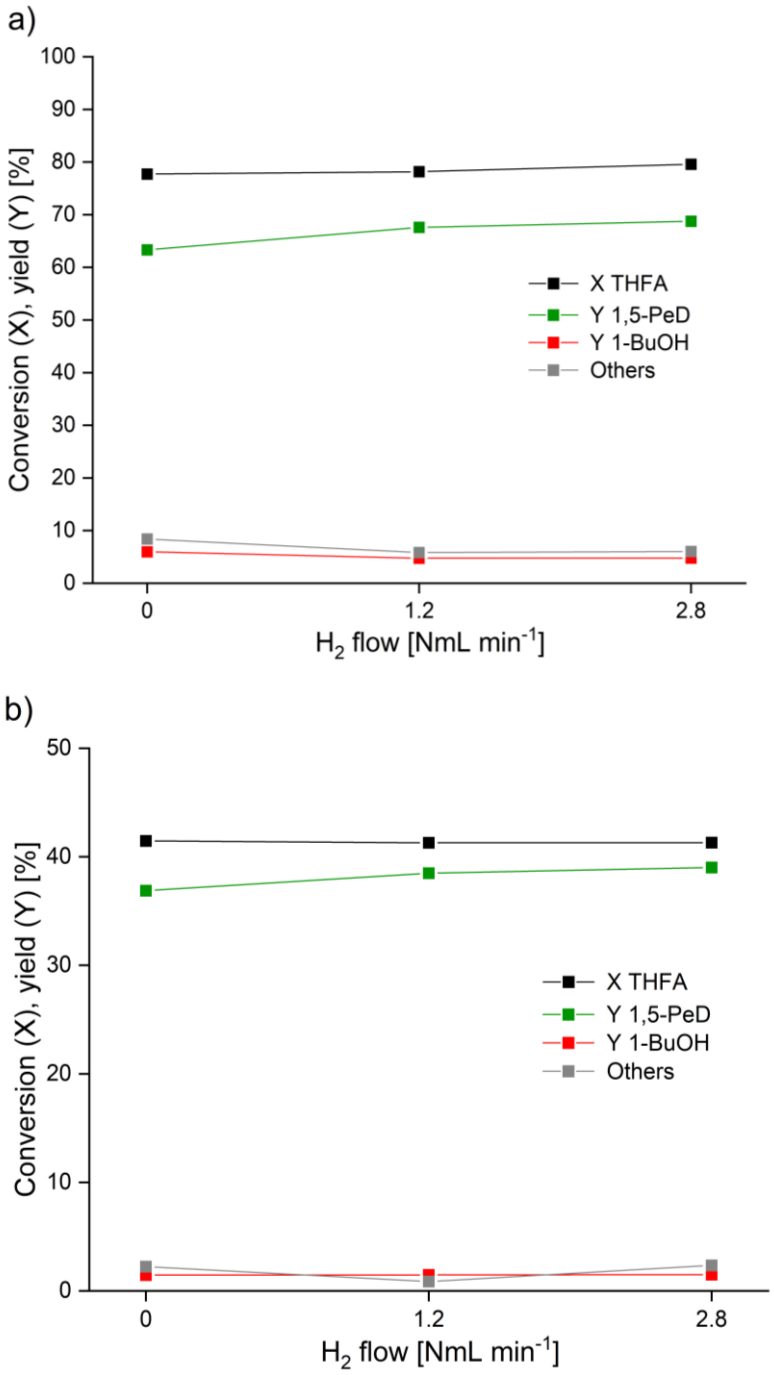

Figure 4.21. Effect of the flow rate of gaseous H_2 on conversion and yields in hydrogenolysis of THFA over Ni-La(R) under flow conditions. Reaction conditions for (a): 1.3 wt% THFA (c=100 mmol L^{-1} in 2-PrOH), m(21Ni-La(R))= 3 g (2.4 mL), T= 140 °C, p(N_2)= 3 MPa, Q= 0.25 mL min^{-1}, LHSV= 6.3 h^{-1}. Reaction conditions for (b): 2.5 wt% THFA (c=200 mmol L^{-1} in 2-PrOH), m(40Ni-La(R))= 1 g (0.8 mL), T= 150 °C, p (N_2)= 3 MPa, Q= 0.25 mL min^{-1}, LHSV= 18.8 h^{-1}. Others: estimated value of by-products based on an average GC response factor of known products.

4.3.2. Effect of liquid flow rate and THFA concentration

Furthermore, the influence of THFA concentration was studied for 21Ni-La(R) at constant LHSV (LHSV= 6.3 h^{-1}). The initial concentration was raised from 50 to 100 and then to 200 mmol L^{-1} THFA in 2-PrOH which corresponded to 0.65, 1.3 and 2.5 wt%, respectively. As shown in Figure 4.22a, the conversion gradually decreased from 90% to 66% with increasing the substrate concentration due to the short residence time. However, the yield of 1,5-PeD was not significantly different when doubling the concentration, for instance, 1,5-PeD yields were 67% at 0.65 wt% and 63% at 1.3 wt% THFA in 2-PrOH.

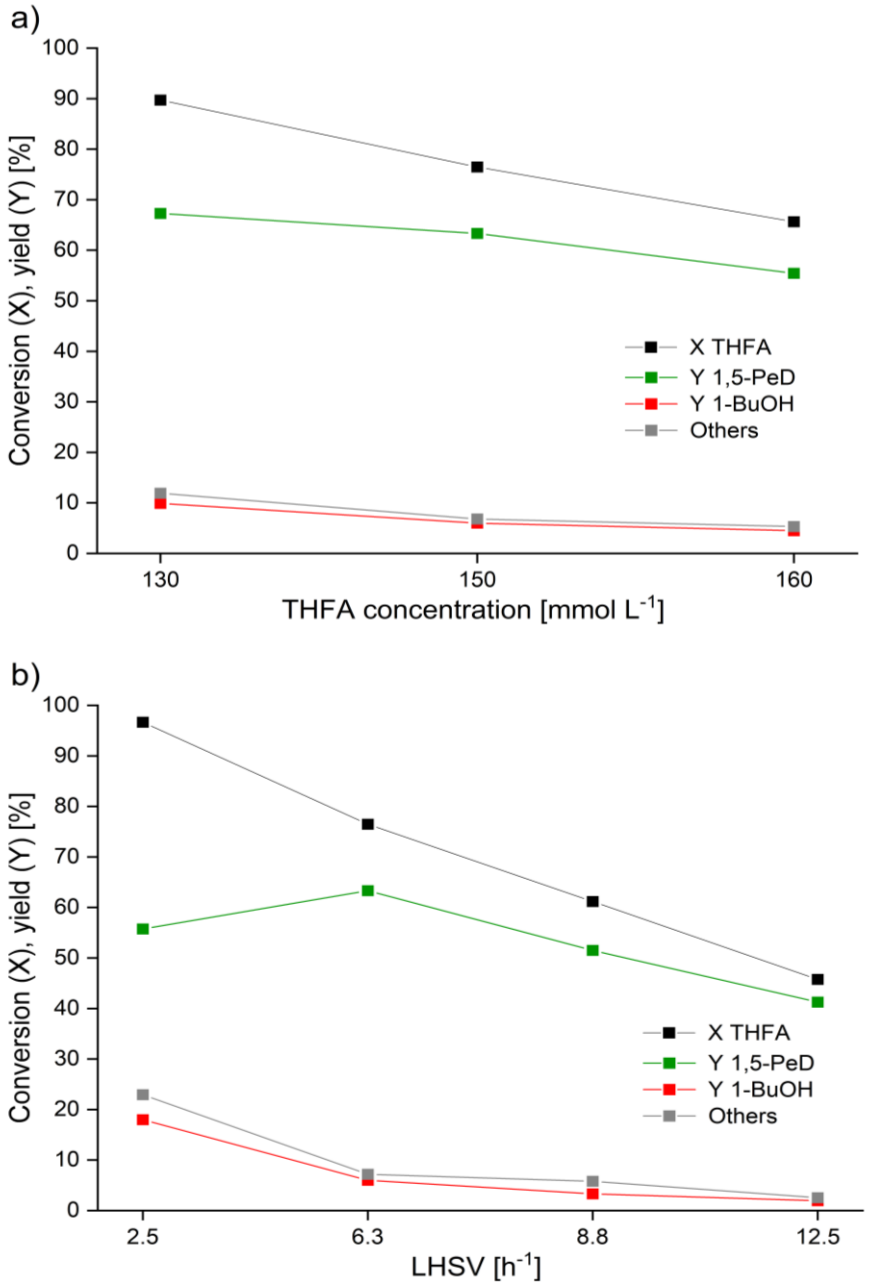

Figure 4.22. Effect of liquid flow rate and initial concentration of THFA on conversion and yields in CTH of THFA over 21Ni-La(R) under flow conditions. Reaction conditions for (a): m(cat)= 3 g (2.4 mL), T= 140 °C, p (N_2)= 3 MPa, Q= 0.25 mL min^{-1}, LHSV= 6.3 h^{-1}. Reaction conditions for (b): 1.3 wt% THFA (c= 100 mmol L^{-1} in 2-PrOH), m(cat)= 3 g (2.4 mL), T= 140 °C, p(N_2)= 3 MPa. Others: estimated value of by-products based on an average GC response factor of known products.

Thus, to investigate the influence of LHSV, 1.3 wt% of THFA in 2-PrOH was selected because the yield of 1,5-PeD decreased only slightly compared to 0.65 wt% of THFA in 2-PrOH, and both the conversion and selectivity to 1,5-PeD ranging between 76-83% were optimal for a continuous process. As mentioned before, Ni catalysts were not selective to the target diol without addition of hydrogen gas due the long reaction time in the batch reactor (15-24 h). That is why, the catalyst was mainly involved in the dehydrogenation of 2-PrOH instead of the main hydrogenolysis reaction. In contrast, the advantage of a flow system is that the residence time could be controlled by adjusting the liquid flow. Figure 4.22b compares the conversion and 1,5-PeD yields over 21Ni-La(R) at different liquid hourly space velocities (LHSV) which was calculated based on the liquid flow rate (Q) and the volume of the catalyst bed (2.4 mL) (see paragraph 3.4.2 for more details). The flow rates of 0.1, 0.25, 0.35 and 0.5 mL min^{-1} were adjusted corresponding to LHSV = 0.25, 6.3, 8.8 and 12.5 h^{-1}, respectively. Due to the reduction of the residence time with increasing the liquid flow, the conversion significantly decreased from almost complete conversion at 2.5 h^{-1} to 46% at 12.5 h^{-1}. The optimal yield of 1,5-PeD was 63% at a LHSV = 6.3 h^{-1}, so it was applied for further investigations and long-term stability tests. Thus, in contrast to the flow rate of H_2 gas, the liquid flow rate as well as the initial concentration of THFA showed a significant impact on the yield of 1,5-PeD over 21Ni-La(R) in the selective hydrogenolysis of THFA to 1,5-PeD.

4.3.3. Effect of temperature and inert pressure

In the beginning of the investigations in the continuous reactor, the optimal temperature and pressure determined in the batch reactor were applied as starting point for flow experiments (150 °C, 3 MPa) (see paragraph 4.2.7). However, the optimal conditions may differ from those in batch operation due to the significant difference in the residence time. Figure 4.23 demonstrates the catalytic behavior of 21Ni-La(R) at several temperatures and N_2 pressures at constant LHSV = 6.3 h^{-1}. Although 93% conversion was achieved at 150 °C, the yield of 1,5-PeD was only 59% which was about 20% lower than the batch yield at the same temperature (Figure 4.23a). Thus, the temperature was decreased to 140 °C and then to 130 °C to obtain higher yields of 1,5-PeD. The highest yield of 63% was achieved at 140 °C at a conversion of 76%. This temperature was the optimal one for 21Ni-La(R) and a catalyst volume of 2.4 mL. However, 140 °C might not be the optimal temperature for Ni catalysts on other lanthanide hydroxides or oxyhydroxides and for different catalyst volumes. Moreover, the effect of pressure which may influence the adsorption of substrate and desorption of products was investigated under flow conditions. Figure 4.23b compares the catalytic behavior of 21Ni-La(R) at different N_2 pressure (2, 3 and 4 MPa). Similar to observations in batch mode, pressure had no impact on the conversion of THFA and was required only to maintain the solvent in liquid phase at high temperature. In summary, it was found that temperature as well as liquid flow

rate and THFA concentration had a remarkable impact on the yield of 1,5-PeD of 21Ni-La(R) whereas hydrogen flow and pressure had no noticeable effect on that.

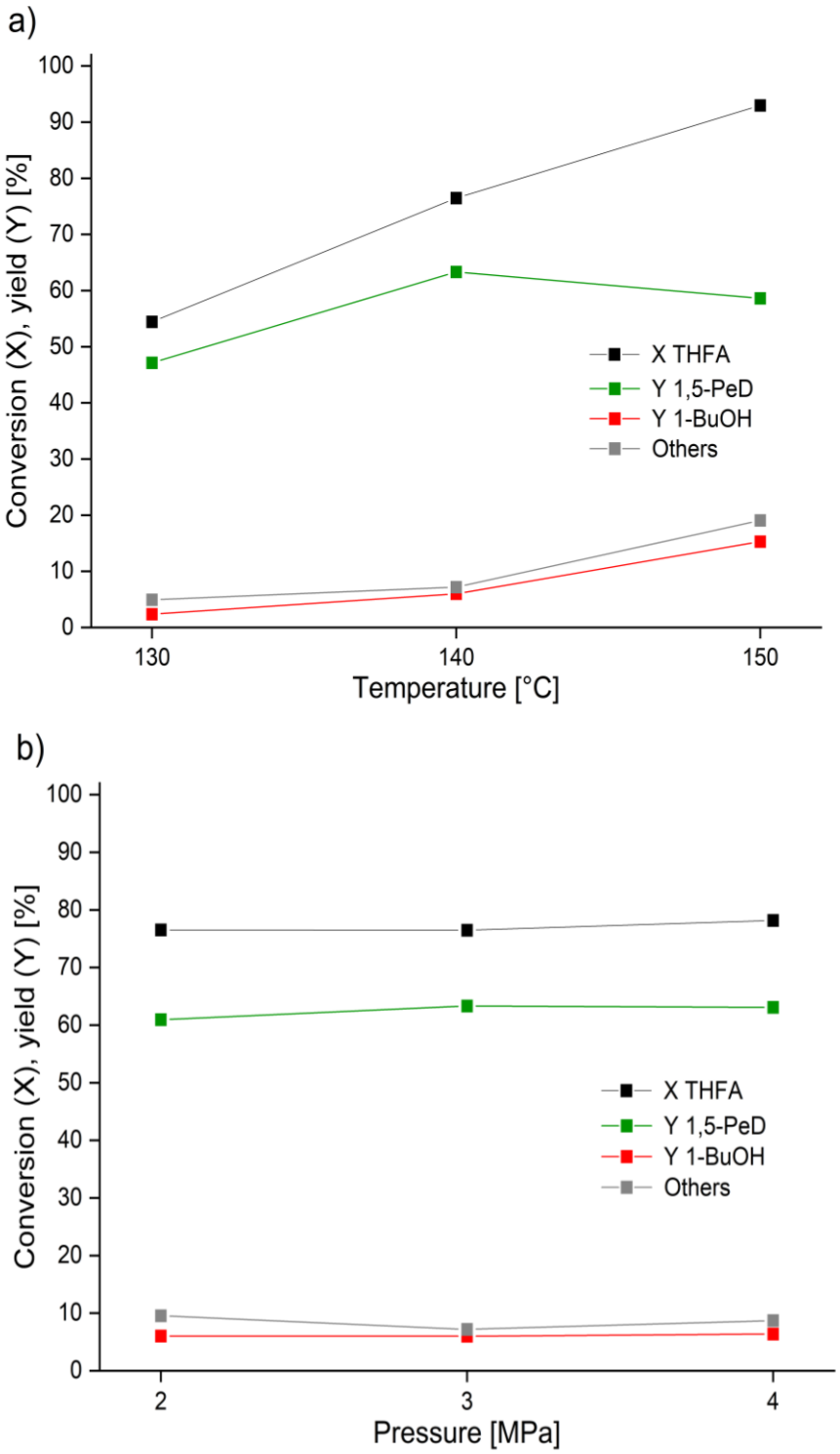

Figure 4.23. Effect of temperature and inert pressure on conversion and yields in CTH of THFA over 21Ni-La(R) under flow conditions. Reaction conditions: 1.3 wt% THFA (c= 100 mmol L^{-1} in 2-PrOH), m(cat)= 3 g (2.4 mL), [b] T= 140 °C, [a] p(N_2)= 3 MPa, Q= 0.25 mL min^{-1}, LHSV= 6.3 h^{-1}. Others: estimated value of by-products based on an average GC response factor of known products.

4.3.4. Effect of lanthanide supports on the stability of Ni catalysts

Based on the batch experiments, 40Ni-La(R) and 37Ni-Pr(R) were the most active catalysts in the hydrogenolysis of THFA with almost complete conversions, and a maximum 1,5-PeD yield of 88% after 24 h was obtained in the presence of H_2. Due to the low conversion and selectivity of the catalyst to the target diol, the yield of 1,5-PeD dropped to 30% under inert pressure compared to 71% under hydrogen pressure after 15 h (compare Figure 4.18a and Figure 4.18b). Thus, the catalytic stability of both catalysts in 2-PrOH was tested in absence of gaseous H_2 flow (CTH) at different temperatures for a long TOS (Figure 4.24) (for summarized results see Table A5). The produced hydrogen from 2-PrOH was the only resource for hydrogen delivered to THFA which was sufficient for the selective cleavage of its C–O bond (see paragraph 4.3.1). Figure 4.24a shows the catalytic behavior of 40Ni-La(R) in the transfer hydrogenolysis of THFA at different temperatures (135-150 °C) for 386 h. In the beginning of the test, the reaction temperature was adjusted to 150 °C where 40Ni-La(R) showed almost total conversion (95% after 48 h TOS). However, to observe possible changes in the catalytic behavior and to evaluate the stability under the optimal LHSV= 6.3 h^{-1}, it was essential to decrease the conversion by reducing the reaction temperature. Thus, the reaction temperature was lowered to 140 °C showing that then the best yield of 1,5-PeD was 69% (X= 85%) after 120 h TOS. To be sure that 140 °C was the optimal temperature, 135 °C was also investigated for another 48 h (168 h TOS) which resulted in a comparable yield of 1,5-PeD, but lower conversion 75%. The long-term test was therefore continued at 140 °C (X≈85%, S≈81%) for more than one week (170-360 h TOS). The catalytic behavior was stable during this time resulting in conversion of THFA between 81 to 86%. The achieved yields of 1,5-PeD were between 68-73% with yields of by-products ranging from 5 to 13%. During this period, any change in the catalytic behavior and any sign for catalyst deactivation was not observed. To compare the conversion of THFA after two weeks (360 h TOS) of continuous run to the beginning of the reaction after reaching the steady state, the temperature was increased again to 150 °C before stopping the experiment. Interestingly, the conversion as well as the selectivity to 1,5-PeD was almost the same to that after 48 h TOS. This undoubtedly led to the conclusion that 40Ni-La(R) was an efficient catalyst showing high stability in the hydrogenolysis of THFA without additional hydrogen gas in a continuous process. On the other hand, the conversion of THFA over 37Ni-Pr remarkably dropped from 64% to 32% within the first day (Figure 4.24b).

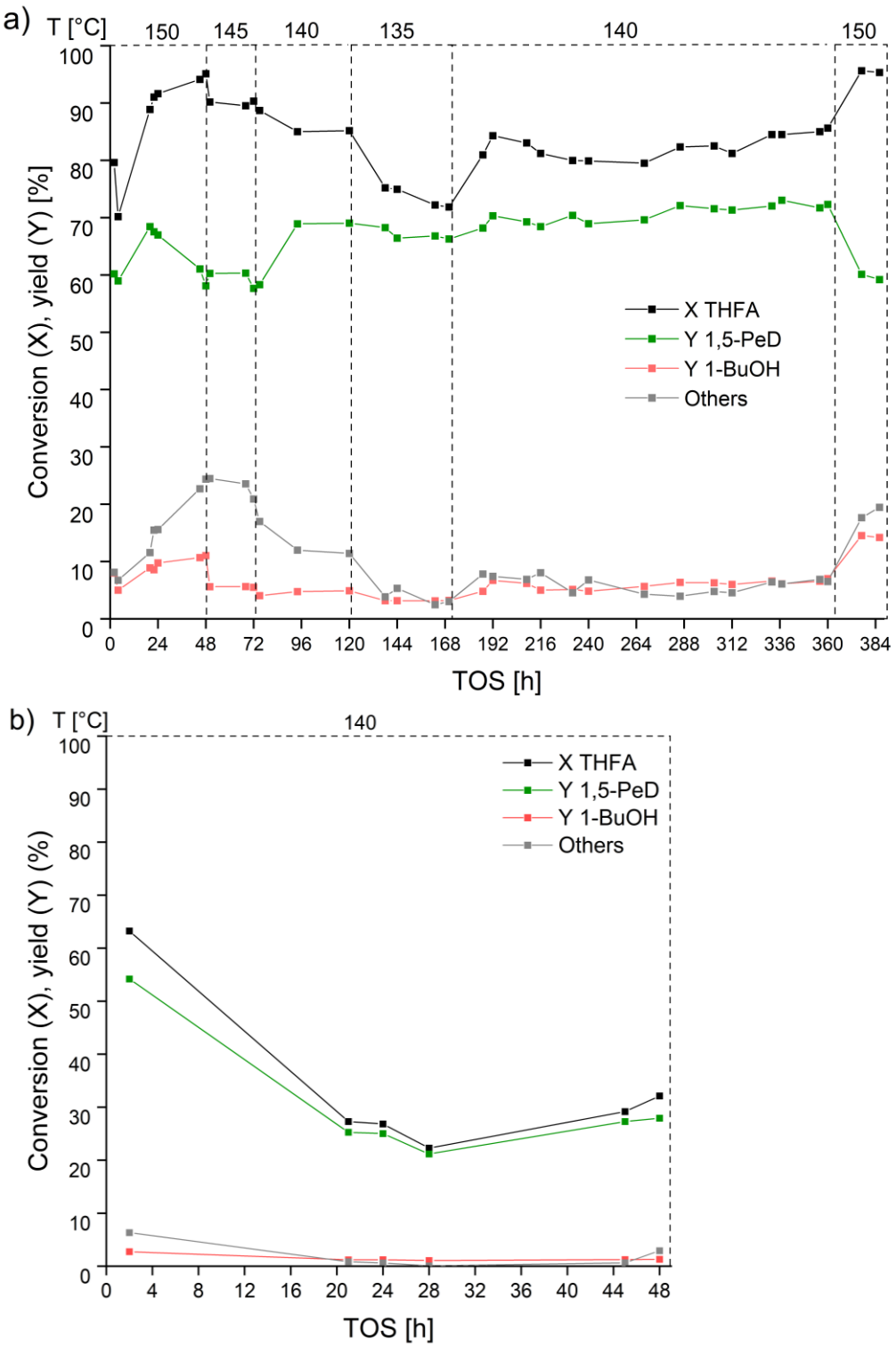

Figure 4.24. Long-term stability of a) 40Ni-La(R) and b) 37Ni-Pr(R) in CTH of THFA under flow conditions. Reaction conditions: 1.3 wt% THFA (c= 100 mmol L^{-1} 2-PrOH), m(cat)= 3 g, p(N_2)= 3 MPa, Q= 0.25 mL min^{-1}, LHSV= 6.3 h^{-1}. Others: estimated value of by-products based on an average GC response factor of known products.

As shown before, 37Ni-Pr was as highly active as 40Ni-La(R) in the batch reactor, as both had 37-40 wt% Ni loading and possessed a high number of basic sites (see Table 4.6 and Table 4.8). The deactivation of 37Ni-Pr(R) could be explained by possible oligomerization of carbon species and coverage of the active nickel surface by these oligomers. This was obvious when the atomic surface concentration of 37Ni-Pr(R) and 37Ni-Pr(S) was compared (catalysts before

and after the reaction) (see Table 4.5). The decrease of the superficial Ni concentration from 29.1 to 8.7 at.% was accompanied by a significant increase in C atomic concentration from 4.9 to 30.8 at.% after only 50 h TOS (Table 4.5, compare 37Ni-Pr(R) and 37Ni-Pr(S) after 50 h TOS). However, this increase of carbon concentration was not remarkable in the case of 40Ni-La(S) which was for both 19 at.% after long TOS compared to 10.8 at.% before the reaction (40Ni-La(R)). It seems likely that the nickel dispersion at similar Ni contents (37-40 wt%), which was higher on $Pr(OH)_3$/Pr(O)OH support than on $La(OH)_3$, played a critical role for the stability of the catalyst (see Table 4.6). It seems to indicate that the lower the dispersion of nickel (the bigger the Ni particles) was, the lower was the deposition of carbon species on the active Ni surface. That implies that the dispersion of Ni, which was influenced by the lanthanide support, was also an important parameter for the catalytic stability of the metallic nickel phase in the assumed active interface areas in continuous reactions. However, previous conclusion should be confirmed by additional stability tests for Ni on other lanthanide supports. Therefore, the catalytic stability of 37Ni-Nd(R) and 38Ni-Sm(R) was also investigated in a continuous run.

Figure 4.25 compares the stability of 37Ni-Nd(R) and 38Ni-Sm(R) in the temperature range of 140-160 °C during 192 h TOS (for summarized results see Table A6). The temperature of the stability test was set at 140 °C since it was the optimal temperature for Ni on $La(OH)_3$. However, the conversion was low (≤ 40%) in the beginning of the reaction. Then the temperature was increased to 150 °C and further to 160 °C to achieve a higher yield of 1,5-PeD. Remarkably, the highest conversion in the case of 37Ni-Nd(R) was 69% (at 160 °C and 98 h TOS), but it dropped gradually to 15% after 92 h of reaction at 160 °C (190 h TOS) (Figure 4.25a). In contrast, 38Ni-Sm(R) was stable under the same conditions, and the conversion ranged from 81 to 84% resulting in a constant yield of about 47% of 1,5-PeD over the last 113 h (75-188 h TOS). The low yield of 1,5-PeD was due to the significant formation of side and consecutive products at higher temperature (160 °C). The stability results confirmed the previous conclusions that both the active nickel surface and the atomic concentration of 38Ni-Sm(R) after and before the reaction were comparable to those of the stable 40Ni-La(R) catalyst (see Table 4.5 and Table 4.6). However, 38Ni-Sm(R) was less active due to the lower number of basic sites (see Figure 4.12a). To sum, the best active and stable catalyst was 40Ni-La(R) with a maximum yield of 73% 1,5-PeD (S ≈ 81-85%) at 140 °C.

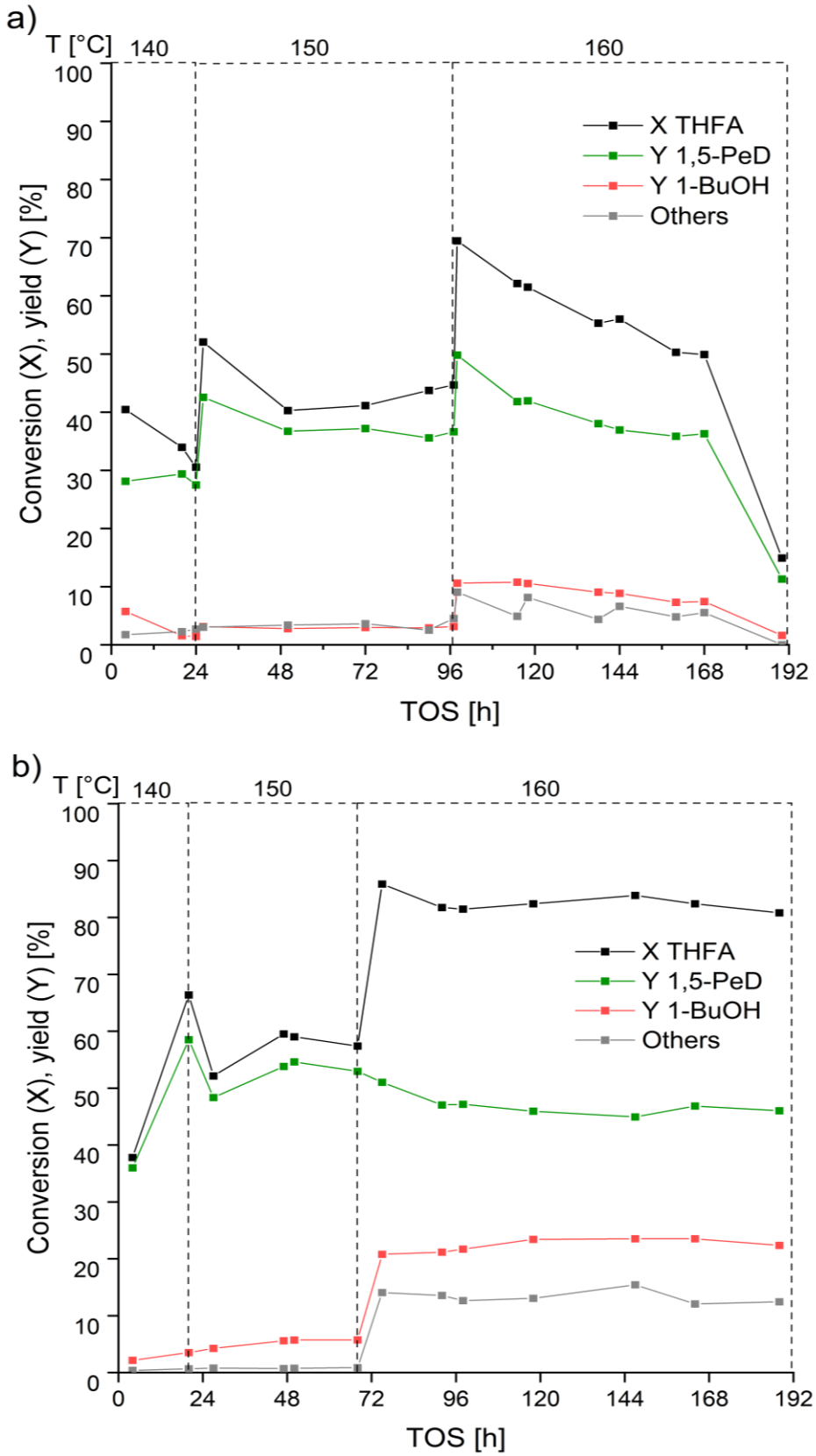

Figure 4.25. Catalytic stability of a) 37Ni-Nd(R) and b) 38Ni-Sm(R) in CTH of THFA under flow conditions. Reaction conditions: 1.3 wt% THFA (c= 100 mmol L^{-1} 2-PrOH), m(cat)= 3 g, $p(N_2)$= 3 MPa, Q= 0.25 mL min^{-1}, LHSV= 6.3 h^{-1}. Others: estimated value of by-products based on an average GC response factor of known products.

4.3.5. Productivity of the Ni-La(R) catalyst in the continuous CTH process

As mentioned earlier, the catalytic stability is considered as the main factor beside the costs for large-scale industrial applications. 40Ni-La(R) was proved to be stable in long continuous runs (up to 386 h TOS). However, in addition to the stability, the productivity of the catalyst is also important for a possible industrial production. Table 4.11 compares the productivity of Ni-La(R) and reported modified Ir and Pt catalysts under flow conditions. The productivity was calculated per mmol of 1,5-PeD per g cat per hour (mmol g^{-1} h^{-1}) (see paragraph 3.4.2 for more details). 20Ni-La(R) and 40Ni-La(R) showed a productivity of 0.5-0.7 mmol g^{-1} h^{-1} which was comparable to the calculated productivity of Pt-WO_x/C (compare entries 1,2 and 6). However, the productivity of modified Ir catalysts was higher (1.4-2.4 mmol g^{-1} h^{-1}). The productivity of 40Ni-La(R) could be optimized by reducing the volume of the catalyst bed or by increasing the concentration of the substrate or liquid flow. Therefore, an additional experiment was carried out with only 1 g catalyst and the doubled THFA concentration (2.5 wt%) at the same liquid flow rate (Q= 0.25 mL min^{-1}) (Figure 4.26) (for summarized results see Table A7). Even at this low conversion of ≥ 45%, the selectivity to 1,5-PeD was 87% and the catalytic performance was stable after 124 h TOS (Figure 4.26). The maximum yield of 1,5-PeD was 39% at 150 °C and the productivity per hour was with 1.4 mmol g^{-1} h^{-1} similar to the reported productivity of 4Ir–VO_x/SiO_2 (compare entries 3 and 4). Both Ni and Ir catalysts were highly selective to 1,5-PeD which was beneficial since it did not require additional isolation and purification steps. The main advantage of Ir catalysts is that they were active in water and that they accept high concentrations of THFA (20-40 wt%) (entries 4 and 5). However, modified Ir catalysts were reported as catalytically unstable in water in continuous runs due to the leaching of the modifiers in the first 30 h TOS which had an impact on overall productivity of the catalyst for this reaction [81, 82]. In contrast, 40Ni-La(R) was stable in 2-PrOH in long continuous runs (386 h TOS). Moreover, the gaseous hydrogen flow was omitted and replaced by a hydrogen-donating industrial solvent (2-PrOH) at a higher liquid flow rate (0.25 mL min^{-1}) than reported for Ir catalysts (0.04 mL min^{-1}) (entries 1-3 and 4-5). Besides the main advantage of replacing expensive unstable Ir catalysts with cheap stable Ni catalysts, the elimination of hazardous high-pressure hydrogen decreases the process costs and raises the level of safety. Moreover, the productivity of 1 g of 40Ni-La(R) was compared in batch and flow reactors for transfer hydrogenolysis of THFA at same conditions (see paragraph 3.4.2 for more details). The hourly productivity was 0.76 mmol g^{-1} h^{-1} in batch reactor which was almost two time less productive than in flow reactor. Also, the catalyst selectivity to the target diol significantly decreasing (form 87% to 39 over 85 h) under inert pressure in batch process (see Figure 4.29 for long-time batch reaction in paragraph 4.4.4) which was stable at 89-87% over 28-124 TOS (see Figure 4.26). Therefore, Ni on basic lanthanide hydroxide is an efficient catalyst and an alternative to

precious noble metal catalyst systems in the continuous hydrogenolysis of THFA to 1,5-PeD, and it has greater potential for application in large-scale industrial processes.

Table 4.11. The productivity of Ni-La(R) in continuous CTH of THFA to 1,5-PeD compared to reported modified noble catalytic systems.

Entry	wt% Catalyst (molar ratio)	Solvent (THFA content [wt%])	m(cat) [g]	Reaction conditions				X [%]	$Y_{1,5\text{-PeD}}$ [%]	Productivity [mmol $g(cat)^{-1}h^{-1}$]	Ref.
				Flow rate [mL min^{-1}]		T [°C]	p [MPa]				
				liquid	H_2						
1	20Ni-La (La:Ni=0.9)	2-PrOH (2.5)	3	0.25	No	140	3	66	55	0.7	Figure 4.22a
2	40Ni-La (La:Ni=2.5)	2-PrOH (1.3)	3	0.25	No	140	3	84	73	0.5	Figure 4.24a
3	40Ni-La (La:Ni=2.5)	2-PrOH (2.5)	1	0.25	No	150	3	45	39	1.4	Figure 4.26
4	4Ir–VO_x/SiO_2 (V:Ir=0.1)	H_2O (20)	2	0.04	60	80	6	85	57	1.4	[82]
5	4Ir-MoO_x/SiO_2 (Mo:Ir=0.13)	H_2O (40)	2	0.04	60	120	6	70	52	2.4	[81]
6	10Pt-WO_x/C (W:Pt= 0.5)	H_2O (1)	0.05[a]	0.03	12	200	3.6	25	20	0.7	[89]

[a] space time= 1.67 min g mL^{-1}.

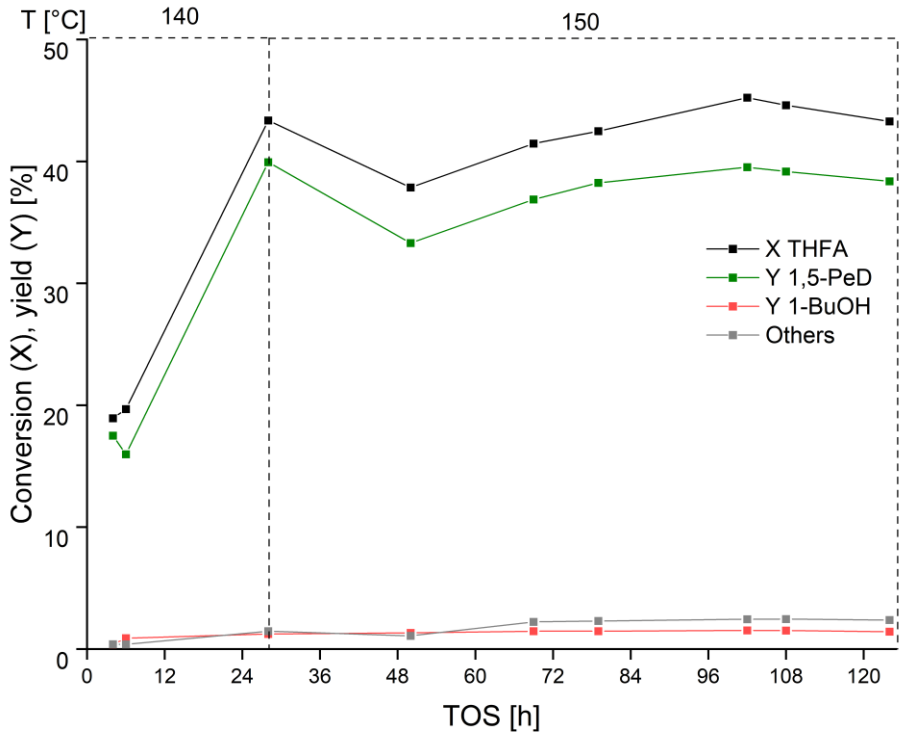

Figure 4.26. The conversion of THFA and 1,5-PeD yield over 1 g 40Ni-La(R) in CTH of THFA under flow conditions. Reaction conditions: 2.5 wt% THFA (c= 200 mmol L^{-1} in 2-PrOH), m(cat)= 1 g (0.8 mL), T= 150 °C, $p(N_2)$= 3 MPa, Q= 0.25 mL min^{-1}, LHSV= 18.8 h^{-1}. Others: estimated value of by-products based on an average GC response factor of known products.

4.4. Mechanistic study of C–O bond hydrogenolysis of heterocyclic compounds to α,ω-diols catalyzed by nickel on basic lanthanide supports

The selective C–O bond hydrogenolysis of heterocyclic compounds to value-added α,ω-diols remains one of the major challenges in biomass conversion due to a multitude of possible side reactions that reduce selectivity for target diols. For instance, direct conversion of FUR to 1,5-PeD may be accompanied by side reactions such as dehydrogenation, hydrogenation, dehydration, hydration, and decarbonylation resulting in many intermediate and by-products. Another problem is that FUR significantly tends to polymerize at higher temperatures in liquid phase blocking the active catalytic centers and leading to rapid deactivation of the catalyst [100-102]. Scheme 4.1 demonstrates the possible reaction pathways for hydrogenation of FUR and C–O hydrogenolysis of the furan and tetrahydrofuran rings. Depending on the catalyst composition and the reaction conditions, FUR could be hydrogenated to THFA via FOL by initial hydrogenation of the C=O bond or via THFAL by hydrogenation of C=C bonds in the FUR ring. In addition, both pathways could take place simultaneously.

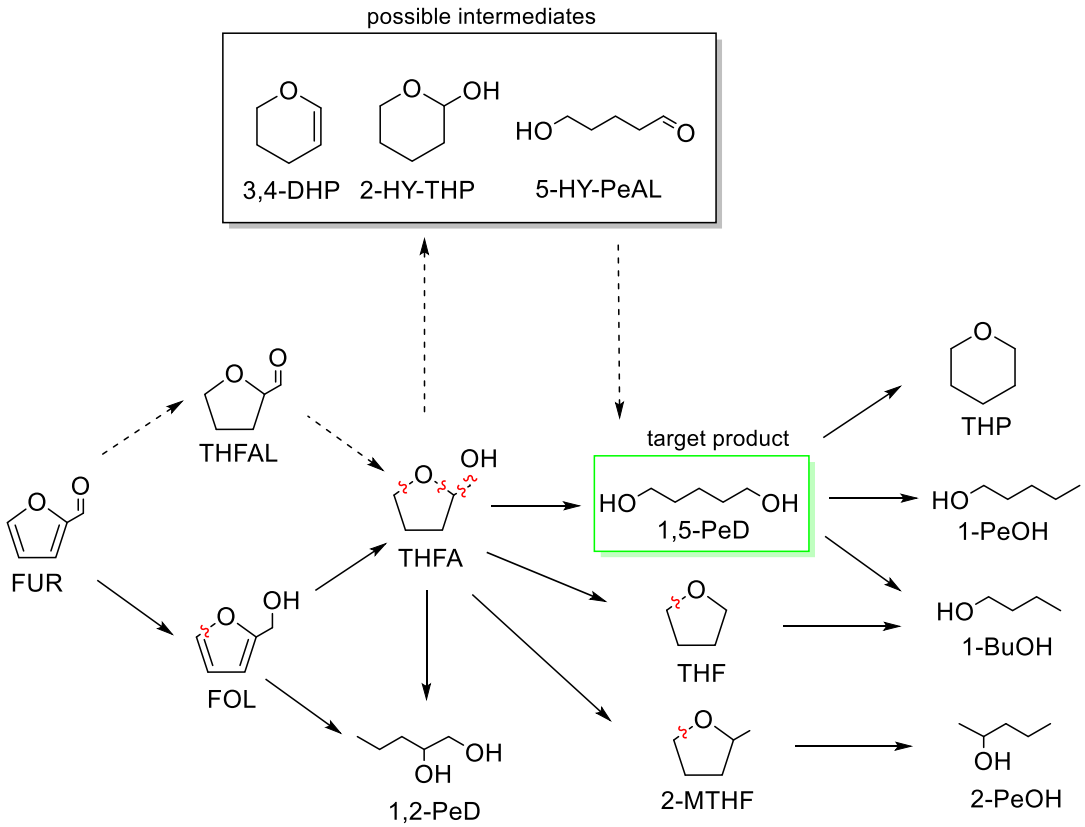

Scheme 4.1. Reaction pathways of hydrogenation/hydrogenolysis of furfural and its derivatives.

However, the initial hydrogenation of the FUR ring was proposed as a minor pathway and most of the reported studies on hydrogenation of FUR reported FOL as the main intermediate [42, 53, 54, 59]. Also, the C–O bond hydrogenolysis of FOL might mainly occur before

hydrogenation of the ring forming 1,2-PeD together with a minor amount of THFA. Several mechanisms were proposed for the selective hydrogenolysis of FUR and FOL to 1,2-PeD or accompanied by 1,5-PeD formation using Cu, Co, Pt and Rh based catalysts [48, 73, 74, 134, 135]. On the other hand, 1,5-PeD was more selectively obtained from THFA using modified noble metal catalysts (M-M'O_x/support, M= Rh, Ir, Pt; M'=Re, Mo, W, V) (see Table 1.5 for details). For this reaction, the following mechanisms were proposed for modified Rh catalysts in aqueous solution:

1. Direct hydride attack mechanism

The direct "regioselective hydride attack" mechanism was proposed for Rh-MO_x/SiO_2 (M=Re, Mo) by the Tomishige group using the isotope labeling technique [80, 95, 98]. The mechanism based on the interaction of hydride species bond to Rh and alkoxide species (Scheme 4.2). Initially, the hydroxymethyl group (–CH_2–OH) of the tetrahydrofuran ring in THFA is adsorbed on a MO_x (M= Re, Mo) cluster forming alkoxide species. The hydride is formed due to the activation of H_2 on the surface of Rh metal, and it can be stabilized by withdrawing electrons of Rh atoms after interaction with MO_x species. Then, it attacks the C–O bond at the C2 atom resulting in its cleavage. The ring-opening can be assisted by an interaction of the proton to the oxygen atom in the ring. Finally, 1,5-PeD is released by exchange of the formed alkoxide with a new THFA molecule. Concerning the reaction kinetics, it was found that THFA adsorption on ReO_x acidic sites was zero order in terms of the THFA concentration while H_2 activation on the Rh surface was first order (rate-determining step) [98].

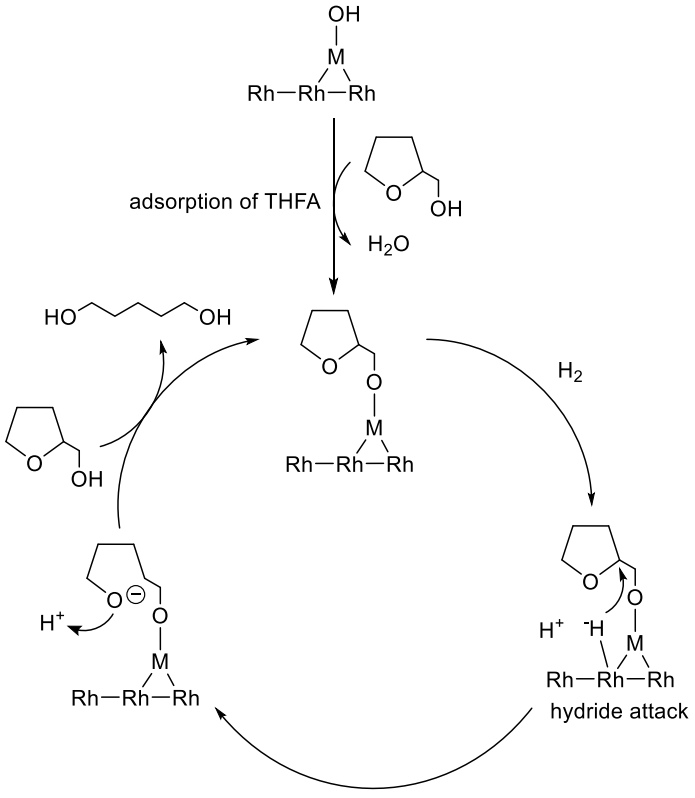

Scheme 4.2. The proposed regioselective hydride attack mechanism for ring-opening reaction of THFA over Rh-MO_x/SiO_2, M= Re, Mo (adapted from [98]).

2. Concerted carbenium ion mechanism

The concerted “carbenium ion” mechanism was proposed by *Chia et al.* based on a bifunctional metal–acid Rh-ReO_x/C catalyst that facilitates the C–O bond cleavage by acid-catalyzed ring-opening and dehydration reactions followed by metal-catalyzed hydrogenation [92]. Thus, an acidic Re–OH species associated with Rh donates a proton to the tetrahydrofuran ring of THFA (protonation step). Then, the H atom in α-position (in the CH_2–OH group) is concertedly shifted to the β-position (tetrahydrofuran ring) resulting in the formation of a highly unstable primary carbenium ion intermediate. This intermediate is then further hydrogenated by Rh metal species forming 1,5-PeD. This proposed mechanism was explored by DFT calculations showing that Rh metal also strengthens the acidity of ReOH due to the direct interaction between both species on the catalyst surface [92, 98, 136, 137]. The reaction order was found to be approximately first order (0.9) with respect to THFA concentration and hydrogen pressure.

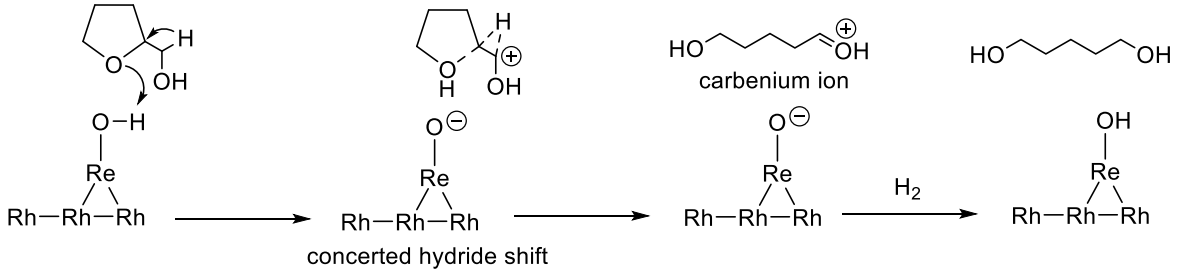

Scheme 4.3. The proposed concerted “carbenium ion” mechanism for ring-opening reaction of THFA over Rh-ReO_x/C (adapted from [98]).

3. Concerted “hydrogen-transfer ring-opening” mechanism

Another concerted mechanism called “hydrogen-transfer-ring-opening” was proposed by *Guan et al.* for binary catalyst consisting supported Rh nanoparticles and MoO_3 [93] (Scheme 4.4). MoO_3 is transformed to homogeneous hydrogen molybdenum oxide bronzes (H_xMoO_3) after dissolving in liquid phase in the presence of H_2. This mechanism consists of two consecutive reaction steps. First, THFA is adsorbed chemically on the acidic MoOH group of H_xMoO_3, followed by hydrogen shift from the α- to β-position of THFA forming 5-hydroxypentanal (5-HY-PAL) as a stable intermediate. This intermediate is quickly hydrogenated to 1,5-PeD on Rh metallic species. This mechanism is quite similar to the “carbenium ion” mechanism by assuming a hydrogen shift from the α-position to the β-position resulting in formation of an intermediate which could be detected as 5-HY-PAL in the case of “hydrogen-transfer ring-opening” mechanism. Also, both concerted mechanisms were proposed based on DFT calculations which was in line with the hypothesis of a metal-acid bifunctional nature of the modified Rh catalyst [92, 93]. However, the role of the solvent in the mechanism of C–O hydrogenolysis has not been clearly revealed. Rh catalysts showed the best catalytic performance in water compared to other organic solvents [93, 95, 96, 106]. The assumed role

of water was that it could increase the formation of the active catalytic sites and stabilize the transition state of the substrate to intermediates [93, 95, 96, 106].

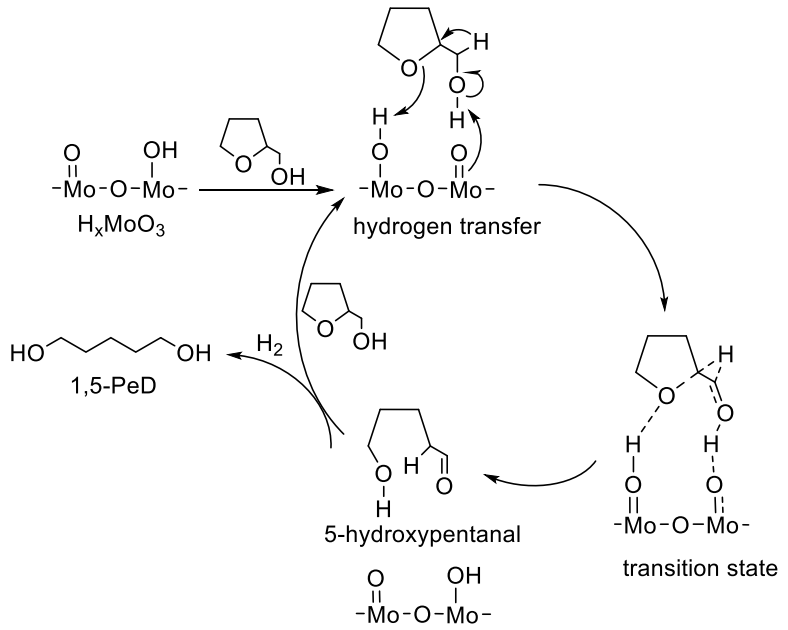

Scheme 4.4. The proposed “hydrogen-transfer ring-opening” mechanism for ring-opening reaction of THFA over Rh−H$_x$MoO$_3$ catalyst (adapted from [106]).

Interestingly, *Soghrati et al.* reported the indirect hydrogenolysis of THFA using Ni-WO$_x$ in water and 1,4-dioxane [86]. In the first minutes of reaction, a higher formation of 1,5-PeD and 1,2,5-pentanetriol (1,2,5-PTO) was observed in aqueous solution while more 1-PeOH and tetrahydropyran (THP) were formed in 1,4-dioxane [86]. That implies that the solvent plays a key role in the reaction pathway and products distribution. In addition, an indirect multi-step route was also proposed for the selective hydrogenolysis of FUR to 1,5-PeD via several intermediary reaction steps. The first pathway started with dehydration of THFA to 3,4-DHP (see Scheme 4.5). This intermediate was further hydrated to 2-HY-THP (or 5-HY-PAL) which underwent a hydrogenolysis (hydrogenation) step to form 1,5-PeD. This pathway was discussed in previous works [2, 9, 10, 76, 80]. Nevertheless, all previous mechanisms deal with the acid-catalyzed hydrogenolysis on noble metal catalysts in aqueous phase, and such mechanism transferred to other non-noble metals, particularly Ni, as catalytically active centers in various organic solvents (e.g. 2-PrOH) has not yet been elucidated. Moreover, the effect of replacement of the acidic modifier by basic lanthanide supports in the ring-opening reaction has not been investigated yet. Therefore, a detailed mechanistic study was performed for this reaction on Ni-La(R) as catalyst in the potential hydrogen-donor 2-PrOH.

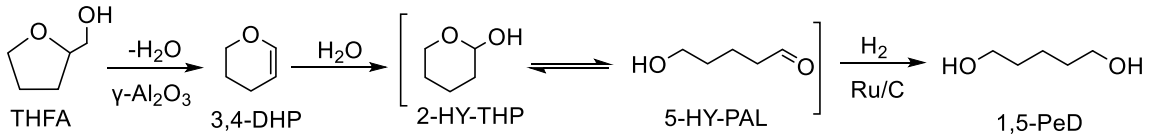

Scheme 4.5. Multi-step route of conversion of THFA to 1,5-PeD via intermediate reactions (adapted from [2, 76]).

4.4.1. Reactivity of possible intermediates

In order to elucidate the mechanism of the hydrogenolysis reaction over Ni-Ln(R), it was important to investigate possible intermediates as substrates. If they also reacted to form 1,5-PeD under the given catalytic conditions, this would indicate that they could be possible intermediates. Table 4.12 presents the results of the catalytic hydrogenation/hydrogenolysis of FUR and pyran and their derivatives over 40Ni-La(R) in 2-PrOH after 24 h. FUR was completely hydrogenated to THFA which was further hydrogenolyzed to 1,5-PeD (entry 1). No intermediary products (FOL or THFAL) could be detected at a reaction temperature of 150°C. Regardless of temperature, complete conversion of FUR was achieved over 38Ni-Sm(R) in the first hours (see Figure 4.20b). However, FOL was found to be an intermediate using 38Ni-Sm(R) at room temperature after 4 h (Figure 4.20b). This assumption was also supported by the products distribution after hydrogenation/hydrogenolysis of FOL over 40Ni-La(R) which was identical to that of FUR (compare entries 1 and 2). Inexplicably, THFAL was hydrogenated to THFA, which could be also considered as an intermediate in hydrogenation of FUR to THFA, but the catalyst was then hardly active in the subsequent cleavage of the ring to 1,5-PeD. This could mean that the catalyst was largely deactivated after the hydrogenation of the carbonyl group (–CH=O) (entry 3). To further evaluate this observation, the catalyst was added in two portions, before the reaction and after 4 h of reaction (after a high yield of THFA had already been obtained). The formation of 1,5-PeD increased from 1% to 12% after 24 h. However, it seems likely that polymers formed from THFAL in parallel with its (comparatively rapid) hydrogenation to THFA poisoned the catalytically active sites. This result explains the previous assumption of deactivation of Ni-Ln(R) in the one-pot conversion of FUR to 1,5-PeD via THFA (see paragraph 4.2.8). In view of these observations, THFAL was suggested to be a minor intermediate in the formation of THFA from FUR. In other words, it seems likely that 40Ni-La(R) was more active in the initial hydrogenation of the C=O bond then in that of the furan ring (entry 1). Also, it was assumed that an initial dehydrogenation of THFA to THFAL followed by hydrogenolysis of the cyclic C–O bond to 1,5-PeD might not be the preferred pathway for 40Ni-Ln(R).

Furthermore, 40Ni-La(R) was active in the selective hydrogenolysis of C–O bonds in THFA and 2-hydroxytetrahydrofuran (2-HY-THF) resulting in corresponding α,ω-diols (1,5-PeD and 1,4-BDO) and consecutive products (1-BuOH and 1-PrOH), respectively (entries 4, 5). Interestingly, the catalyst was not active in the hydrogenolysis of the C–O bond of other tetrahydrofuran derivatives which did not contain a hydroxy group (–OH) or carbonyl group (C=O), that could be further converted to C–OH, particularly 2-MTHF, THF and ethyl tetrahydrofurfuryl ether (ETHFE), (entries 6-8). These results are in good agreement with previous works of the Tomishige group demonstrating experimentally the importance of a $–CH_2OH$ group attached to the tetrahydrofuran ring without which the substrate could not

adsorb strongly on the catalyst surface and further react with the activated hydrogen [95, 96, 98, 107]. This also explains the necessity of the formation of an alkoxide from the substrate on the catalyst surface in the initial step of the catalytic cycle which was enabled by basic sites of $La(OH)_3$ in Ni-Ln(R).

To prove this assumption also for similar heterocycles, the investigation of catalytic hydrogenolysis was expanded to tetrahydropyran derivatives possessing different functional groups at the ring. Identically, tetrahydropyran-2-methanol (THP-2-M) and 2-HY-THP were converted selectively to 1,6-HDO and 1,5-PeD after cleaving the pyran ring, respectively (entries 9 and 10). Similarly, no hydrogenolysis or hydrogenation reactions took place in the case of other pyran derivatives without –OH groups, including 2-methyltetrahydropyran (2-MTHP), THP and 3,4-DHP (entries 12-14). Thus, the previous assumption about the initial interaction via deprotonation of the hydroxy group after adsorption of the substrate on the catalyst surface was confirmed. Inexplicably, 3,4-DHP was reported as an intermediary product after dehydration of THFA on γ-Al_2O_3 in vapor phase at 375-300 °C which could be further hydrated to intermediates (2-HY-THP and/or 5-HY-PeAL) before further hydrogenolysis/hydrogenation reactions took place (see Scheme 4.5) [2, 9, 10, 76]. In contrast, other interesting studies on vapor-phase hydrogenation of THFA over Cu-γ-Al_2O_3 and Cu-ZnO/Al_2O_3 catalysts proposed the initial formation of 2-HY-THP via rearrangement of THFA which rapidly dehydrated to 3,4-DHP [138, 139]. Surprisingly, the yield of the target 1,5-PeD was the same (88%) starting form THFA, 2-HY-THP or 5-HY-PAL, and no formation of 1,5-PeD from 3,4-DHP was observed in 2-PrOH (compare entries 4, 10, 14). This would appear to indicate that an initial rearrangement of THFA to 5-HY-THP before the ring-opening reaction to 5-HY-PAL is very likely, probably also as an equilibrium reaction.

However, it may be assumed that 3,4-DHP in 2-PrOH at 150 °C was not an intermediate as proposed in literature because it was not converted to 1,5-PeD over 40Ni-La(R) (even after addition of 1 mL of water) due to different applied active sites, solvent, or temperature (Cu/γ-Al_2O_3 in vapor-phase at 300 °C) [138]. Also, it was reported that the dehydration of 2-HY-THP to 3,4-DHP takes place over acid sites whereby $La(OH)_3$ does not contain acidic sites as γ-Al_2O_3 (see Figure A6) [139]. However, traces 2-HY-THP or 5-HY-PAL, which was not possible to differentiate between them using GC-MS technique, were observed after hydrogenolysis of THFA together with formation of 3,4-DHP probably due to the high measurement temperature of the GC device (up to 310 °C). To prove this assumption, the pure 2-HY-THP and 5-HY-PAL was injected in GC-MS and showed large formation of 3,4-DHP hinting to dehydration of these components inside the GC column. Thus, these results rule out the possibility of hydrogenolysis of THFA via 3,4-DHP in 2-PrOH at 150 °C.

Table 4.12. Hydrogenation/hydrogenolysis of various furan and pyran derivatives over 40Ni-La(R).

Entry	Substrate	Conversion [%]	Yield [%]					
1		100	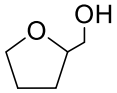	45	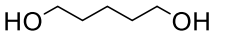	44	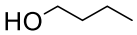	3
2	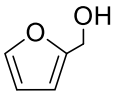	100	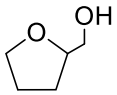	35	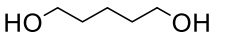	57	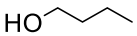	2
3		100	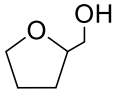	90	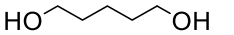	1	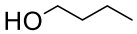	1
4	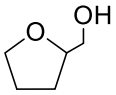	98	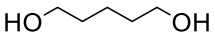	88	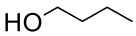	5		
5	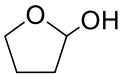	100	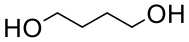	86	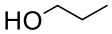	6		
6	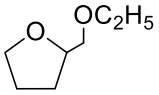	N.R.	-					
7		N.R.	-					
8		N.R.	-					
9	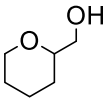	41	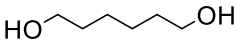	35	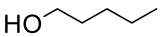	5		
10	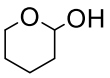	100	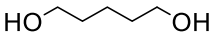	88	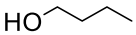	5		
11		50	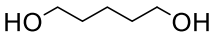	48	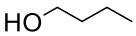	1		
12		N.R.	-					
13		N.R.	-					
14		N.R.	-					
15	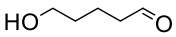	100	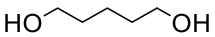	88	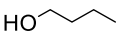	3		5
16	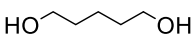	13	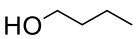	4		6		

Reaction conditions: c= 100 mg substrate in 2-PrOH (5 mL), m(cat)= 100 mg, mass ratio (cat:THFA)= 1:1, T= 150 °C, p(H_2)= 3 MPa, t= 24 h. N.R.: no reaction.

Regarding by-product distribution, 1-BuOH was observed as the main consecutive product in hydrogenolysis of THFA (entries 1-4, 10, 14). Its formation was accompanied by traces of 1-butanone which was detected by GC-MS. It seems likely that 1-BuOH was partially formed by decarbonylation of the 5-HY-PAL intermediate. That could explain the formation of 1-BuOH even at low THFA conversions in the beginning of the reaction. Another by-product was THP which was observed after the ring of THFA was cleaved. It might be formed via cyclic etherification of 1,5-PeD (entries 14-15). On the other hand, although 1-PeOH was found to be the main consecutive product in hydrogenolysis of THFA with acid-modified Rh catalysts in water, it was not observed over basic Ni catalysts on basic supports in 2-PrOH. This implies that the active sites (acidic or basic) and/or the solvent influence the product distribution, and therefore, the mechanism of hydrogenolysis on these Ni catalysts may be not identical to the reported mechanism on ReO_x-modified Rh catalysts (Scheme 4.2-Scheme 4.4). To clarify this difference, isotopic labeling experiments were carried out using D_2 and deuterated isopropanol (2-$PrOD_8$) to elucidate the mechanism of ring-opening reaction over Ni-Ln(R). It was compared with the proposed mechanisms reported.

4.4.2. Isotopic labeling experiments using D_2 and 2-$PrOD_8$

Several experiments were performed with deuterated reactants and the reaction mixtures were studied by NMR spectroscopy. D_2 or/and 2-$PrOD_8$ were used as the deuterium sources, and the hydrogen-deuterium exchange in THFA and 1,5-PeD was determined from ^{13}C NMR spectra (see paragraph 3.3 for experimental details). Table 4.13 lists the percent ratios of hydrogen and deuterium for positions C1 (α-position) and C2 (β-position) in THFA and C1,5 and C2,4 in 1,5-PeD in presence and absence of deuterium sources. Also, Figure 4.27 shows the corresponding ^{13}C NMR spectra of the resulting product mixtures calibrated to the $CDCl_3$ signal (δ = 77.0 ppm). Initially, a baseline experiment was carried out in 2-PrOH under hydrogen pressure to identify the chemical shift for each carbon atom (C1-C5) of THFA and 1,5-PeD, which was 64.40 (C1), 79.50 (C2), 27.07 (C3), 25.66 (C4) and 68.00 (C5) ppm for THFA and C1,5= 62.00, C2,4= 32.08, C3= 21.91 ppm for 1,5-PeD, respectively (Figure 4.27, entry 1). The first experiments were carried out using D_2 or 2-$PrOD_8$ (entries 2-3). A deuteration was found only in the α- and β-positions (C1 and C2) in both THFA and 1,5-PeD, with C1 and C5 as well as C2 and C4 having only one signal due to the symmetrical structure of 1,5-PeD. In addition, C3 was found to be inert to H-D exchange which is in complete agreement with previous studies which reported that C3 in 1,5-PeD was not deuterated even after a long reaction time [80, 98]. Interestingly, the deuteration in the α-position (C1) was already remarkably high in THFA using D2 or 2-$PrOD_8$ as source of deuterium (entries 2-3), whereas almost no to slight deuteration was observed in C2 (entry 2 and 3, respectively). The high level remained almost constant in C1 of 1,5-PeD, while a significant increase in the degree of deuteration was observed in position C2 of 1,5-PeD compared to the C2 position of THFA. Due

to the possible hydrogen contribution from both resources, an additional experiment using both D_2 and 2-PrOD_8 together was performed which showed that although the percentage distribution of deuterated carbon in C2 was increased, the percentage distribution in C1 was still higher but on the same level both in THFA and 1,5-PeD after 4 h (entry 4).

Table 4.13. Percentage distribution of deuterated to non-deuterated carbon atoms in the reaction mixture after hydrogenolysis of THFA to 1,5-PeD over 40Ni-La(R) in the presence of deuterated reactants.

Entry	Gas	Solvent	X[a] [%]	Proportion of deuterated and non-deuterated carbon atoms in ^{13}C NMR spectra [%]										
				Substrate (THFA)					Product (1,5-PeD)					
				C1 (α)			C2 (β)		C1,5 (α)			C2,4 (β)		
				CH_2	**C-HD**	**C-D_2**	**CH**	**C-D**	**CH_2**	**C-HD**	**C-D_2**	**CH_2**	**C-HD**	**C-D_2**
1	H_2	2-PrOH	37	100	-	-	100	-	100	-	-	100	-	-
2	D_2	2-PrOH	36	67	33	0	100	0	61	39	0	70	30	0
3	H_2	2-PrOD_8	36	25	65	10	95	5	25	60	15	60	35	5
4	D_2	2-PrOD_8	30	2	46	52	84	16	4	42	54	32	39	29
5[b]	D_2	2-PrOD_8	5	35	50	15	98	2	30	45	25	50	40	10
6[c]	Ar	2-PrOD_8	44	5	45	50	81	19	8	46	46	20	40	40

[a] based on GC; Reaction conditions: c= 1 mmol of THFA in 2-PrOH (5 mL), m(cat)= 100 mg, mass ratio (cat:THFA)= 1:1, T= 150 °C, p= 3 MPa, t= 4 h, [b] 30 min, [c] 15 h.

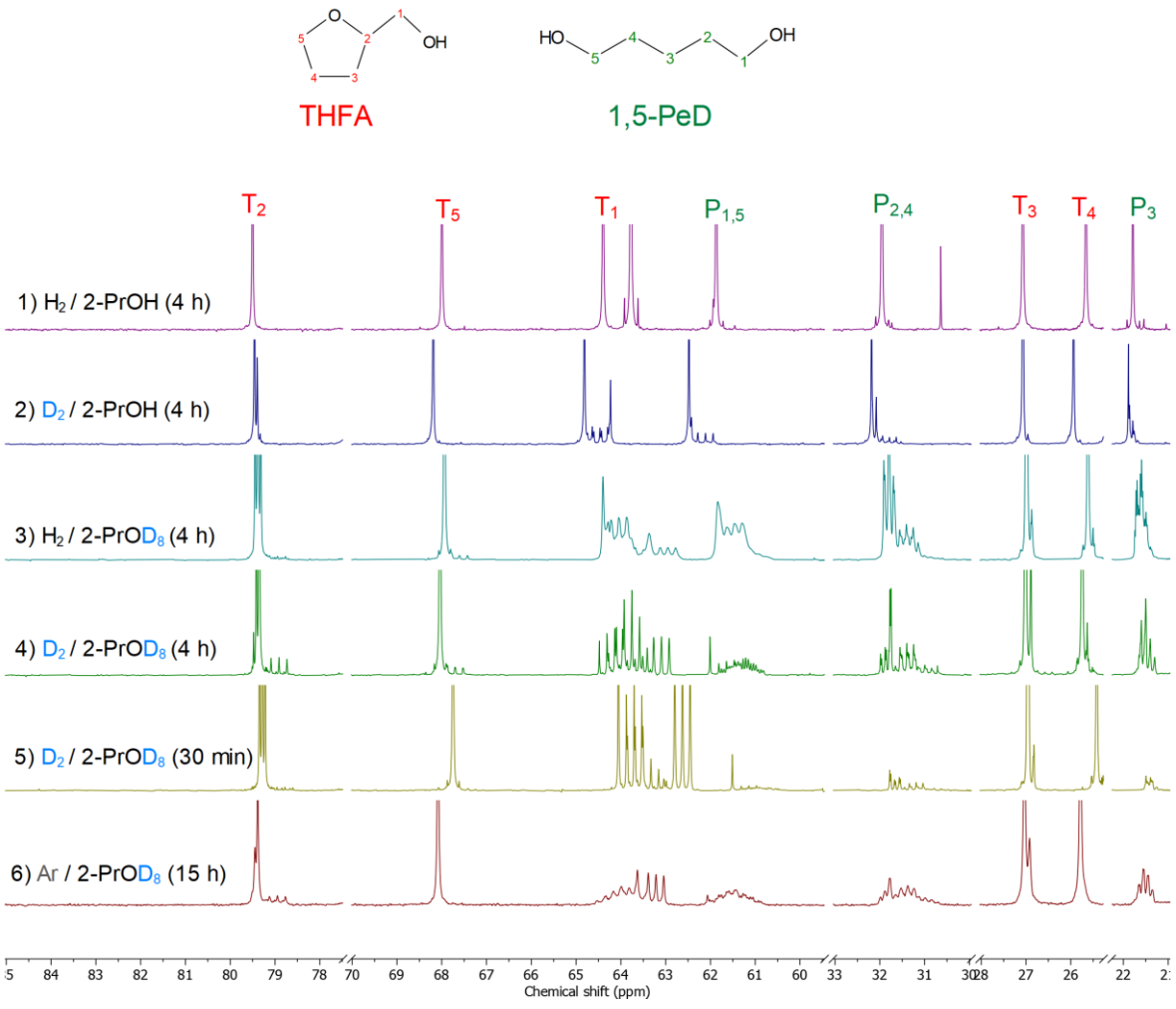

Figure 4.27. ^{13}C NMR spectra of the reaction mixture from THFA hydrogenolysis in 2-PrOH(D) over 40Ni-La(R) applying H_2 (D_2, Ar).

Therefore, the effect of the reaction time on deuteration and H-D exchange rate, which was presumably higher with extending the reaction time, was investigated. For that, an additional experiment was conducted using both D_2 and 2-PrOD$_8$ over a shorter period (30 min) (entry 5). Similarly, the deuteration in C1 was higher than in C2 from the beginning of the reaction, for both mono- and bideuteration (C-D and C-D_2), in both THFA and 1,5-PeD. The degree of deuteration in C2 of THFA was remarkably low with 2% after 30 min compared to 16% after 4 h which was clearly proportional to the high degree of deuteration in C1 (compare entries 4-5). For example, the highest degree of deuteration in C2 of THFA was 16% corresponding to the very high deuteration in C1 (C-HD plus C-D: 98%) after 4 h (entry 4), and the lowest degree of deuteration in C2 of THFA was 2% corresponding to a lower deuteration in C1 (C-HD plus C-D: 65%) after 30 min (entry 5). This implies that the deuteration in C2 in THFA was influenced by the intense deuteration in C1.

Furthermore, the percentage share of C-HD in C1 of THFA and C1,5 of 1,5-PeD remained at the same level between (65% vs. 70% for C-HD plus C-D_2) even after short time (30 min) (entry 5) whereas the degree of deuteration increased significantly in the C2,4 position of 1,5-PeD (from 2% to 50% for C-HD plus C-D_2). However, a remarkable growth of the C-D_2 proportion was observed in both positions when the reaction time was extended to 4 h (25 to 54% in C1,5 and 10 to 29% in C2,4) probably due to subsequent tautomerization reactions. This increase in the deuteration degree at position C2,4 of 1,5-PeD was not observed for the position C2 of THFA and can only be explained by the incorporation of D at C2 in the sense of a hydride attack causing the tetrahydrofuran ring cleavage as proposed by the Tomishige group as shown in Scheme 4.6 [80, 95, 98].

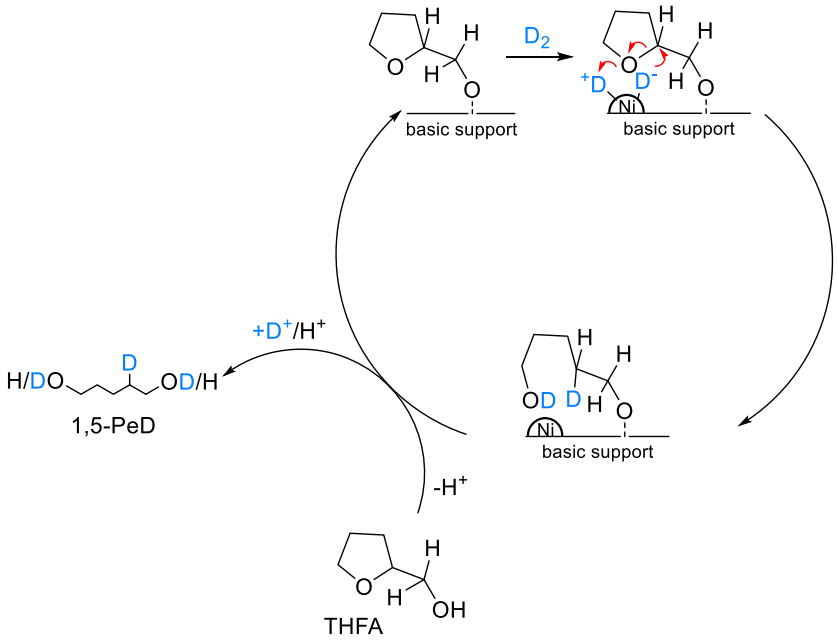

Scheme 4.6. Proposed scheme of direct hydride attack for the hydrogenolysis of THFA catalyzed by Ni-Ln(R) (adapted from *Tomishige et al.* [98]).

In order to prove the hydride mechanism, a comparison of the previous NMR results with the detailed mechanistic studies of *Chen et al.* was done where the effect of D_2 and D_2O on the hydrogenolysis of THFA using a Rh-ReO_x/SiO_2 catalyst was investigated over time. It was shown that the deuteration in C1 position of THFA was significantly higher than in C2 position even after 24 h [80]. This is in line with the previous results which showed that the deuteration in C2 of THFA was significantly lower than in C1 even after 15 h (Table 4.13, entry 6). However, *Chen et al.* reported that the deuteration in C1,5 and C2,4 of 1,5-PeD was comparable in the first 3 hours, and then the deuteration degree in C1,5 increased compared to C2,4 within 24 h [80]. More important, the degree of deuteration in C1 position of THFA was significantly lower than that in C1,5 position of 1,5-PeD which is totally inconsistent with the presented results in Table 4.13 over 40Ni-La(R). The results of the current study showed almost the same deuteration degree in the α-position in both THFA and 1,5-PeD (compare [80] with Table 4.13, entries 2-5). This appears to indicate that the exchange between the deuterium source (D_2 and/or 2-$PrOD_8$) and the α-position of THFA was higher from the beginning of the reaction and had not changed after the cleavage of the ring. Also, it seems likely that C5 was almost not deuterated before and after the ring-opening reaction due to the comparable deuteration ratio for C1 in THFA and C1,5 in 1,5-PeD. A possible explanation for this high H-D exchange at the α-position might be that THFA, after adsorption of the hydroxyl group at the basic sites of $La(OH)_3$ (deprotonation step) probably interacts with metallic Ni surface species via a dehydrogenation–hydrogenation equilibrium, forming a C=O bond in an intermediate stage [80]. This aldehyde intermediate (THFAL) might be formed considering the possible interaction between adsorbed THFA and catalytic surface species, however, it was not detected as an intermediate for the ring-opening reaction of THFA since 40Ni-La(R) was hardly active in the hydrogenolysis of THFAL to 1,5-PeD after 24 h (see Table 4.12, entry 3). Therefore, this reaction pathway was discarded.

On the other hand, the reactivity study proved that the formation of 2-HY-PAL or 5-HY-PAL intermediates was more likely since they were converted to 1,5-PeD with the same yield (88%) as from THFA (see Table 4.12, entries 4, 10, 15). This appears to indicate that the dehydrogenation–hydrogenation equilibrium might take place after the initial rearrangement of THFA to 2-HY-THP intermediate as proposed in previous studies (see Scheme 4.7) [138-140]. This intermediate proved to be 80 times more reactive than THFA in the hydrogenolysis reaction over Rh-ReO_x/C [2]. The direct hydrogenolysis of the C–O bond of 2-HY-THP could take place by metallic Ni after a dehydrogenation–hydrogenation equilibrium (Scheme 4.7, pathway A). The pathway A explains the intensive deuteration in the C1 position of THFA from the beginning of the reaction (Table 4.13, see C1 deuteration for THFA). In addition, the reported high reactivity of 2-HY-THP (at temperatures higher than R.T.) might enable an endothermic tautomerization equilibrium with 5-HY-PAL causing the ring-opening as reported

by the Huber-Dumesic group (Scheme 4.7, pathway B). So, it may be assumed that the pathway B could take place at 150 °C concomitantly with the dehydrogenation–hydrogenation equilibrium after the rearrangement resulting in 1,5-PeD after hydrogenation by metallic sites.

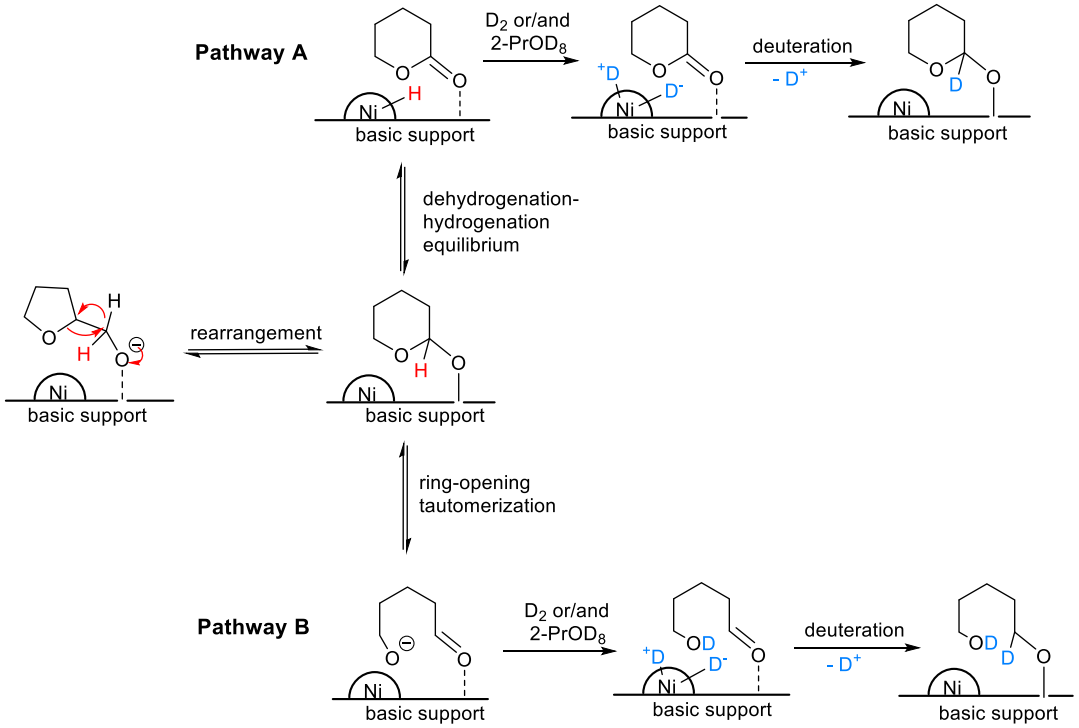

Scheme 4.7. Proposed scheme for possible intermediate reaction before obtaining 1,5-PeD over Ni-Ln(R).

Nevertheless, it may be also proposed that 5-HY-PAL was formed after cleaving of C–O bond by hydride mechanism since metallic Ni species could dehydrogenate the resulted 1,5-PeD. This probability was supported by the dehydrogenation of 2-PrOH to acetone and hydrogen (for more details see paragraph 4.4.4). In addition, the formation of 5-HY-PAL as an intermediate was also consistent with reported DFT calculations of a concerted mechanisms over acid-modified Rh catalysts [92, 93]. However, in this mechanism proposed, 5-HY-PAL was assumed to be formed due to a hydride shift from C1 to C2 after protonation of THFA by acidic sites (see Scheme 4.8). So, the D atom might be incorporated into the α-position (C1,5) of 1,5-PeD which was in contrast with the presented results in Table 4.13 for Ni-La(R) demonstrating a similar deuteration degree in the α-position in both THFA and 1,5-PeD (compare entries 2-5). This implies that 5-HY-PAL could be obtained via two routes i) from 2-HY-THP via ring-opening tautomerization (see Scheme 4.7, pathway B) or after ring-opening by “hydride attack” mechanism via dehydrogenation of 1,5-PeD over metallic Ni phase. As discussed before, the increase in the degree of mono-deuteration at the β-position in the case of 1,5-PeD (C2,4) compared to the β-position of THFA (C2) was remarkably higher in the sense of incorporation of one D atom into the β-position which could be explained by the “hydride attack” mechanism (see Scheme 4.6) [80]. The deuteration percentage of C-HD at the β-position was remarkable high (40%) after only 30 min and remained almost the same after 4 h (39%) (Table 4.13, compare entries 4 and 5).

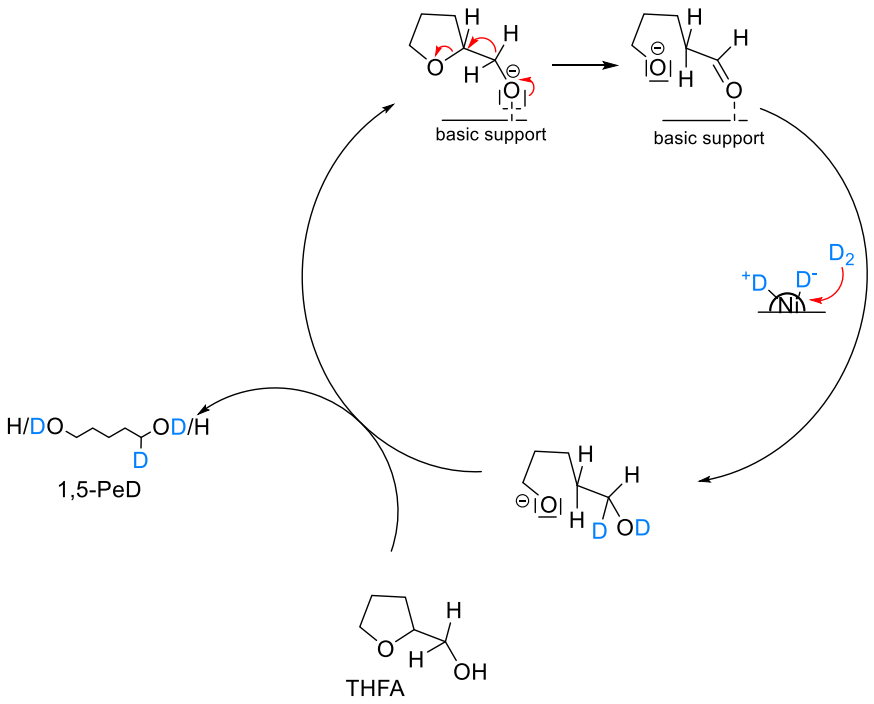

Scheme 4.8. Scheme of a hypothetical concerted hydrogen transfer for the hydrogenolysis of THFA catalyzed by Ni-Ln(R) adapted from [93, 94].

However, this assumption of a hydride attack could not explain the incorporation of the second D atom (C-D_2) at the β-position as well as at the α-position where second deuteration took place when the reaction time was extended. For instance, the deuteration proportion of C-D_2 at the α-position increased from 25% to 54% vs 10% to 29% at the β-position after 30 min and 4 h, respectively (Table 4.13, compare entries 4 and 5). This ratio was comparable (40-46%) after long reaction time (15 h) under Ar/2-PrOD_8 (Table 4.13, entry 6). This would appear to indicate that the deuteration share of C-D_2 a caused by a tautomeric keto-enol equilibrium that might require time to achieve the same degree of deuteration in both positions (Scheme 4.9). The tautomeric keto-enol equilibrium can occur in a base-catalyzed reaction where the enol form of the ketone acts as a Brønsted acid donating a proton to the strongly basic sites of $La(OH)_3$ [141]. Interestingly, this equilibrium could take place after ring-opening which might be caused directly by a hydride attack at the β-position (without formation of intermediates) or via the 2-HY-THP intermediate which could be formed after initial rearrangement of THFA followed by ring-opening tautomerization. This mechanism was confirmed based on a first-order reaction with respect to hydrogen (rate-determining step) [42, 80, 95, 98]. Thus, the reaction order over Ni-La(R) with respect to H_2 pressure and THFA concentration was determined to be compared with the mechanism previously proposed.

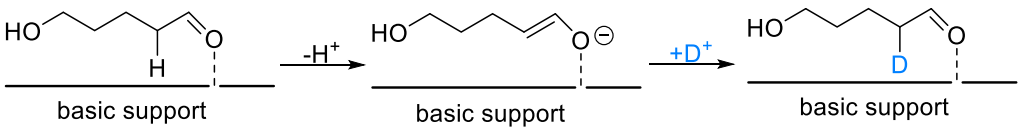

Scheme 4.9. Keto-enol tautomeric equilibrium in base-catalyzed reaction after cleaving the C–O bond of THFA (adapted from [80]).

4.4.3. Chemical reaction kinetics

Furthermore, the reaction kinetics of the hydrogenolysis of THFA over 40Ni-La(R) catalysts was studied to determine the rate-determining step in the reaction mechanism. Series of experiments over 40Ni-La(R) were carried out at different THFA concentrations between 180-1440 (mmol per liter 2-PrOH) and at different H_2 pressures (3-6 MPa) under batch conditions (Table 4.14). The turnover frequency (TOF) was calculated based on the active Ni surface area (see paragraph 3.4.1 for details). As shown in Table 4.14 (entries 1-5), the conversion gradually decreased with increasing the molar concentration of THFA. In contrast, the H_2 pressure had no remarkable impact on the conversion after 4 h (entries 6-9). These results match well with the previous findings in flow reactor (see Figure 4.21) which showed that gaseous hydrogen pressure had no significant effect on the conversion of THFA over of 40Ni-La(R). On the other hand, since the hydrogenolysis of THFA was performed in 2-PrOH which could be dehydrogenated to acetone and H_2, it was substantial to study the effect of the 2-PrOH volume as additional hydrogen source which may have an impact on the reaction rate. Therefore, the volume percent of the hydrogen-donor 2-PrOH in relation to 1-PrOH (non-hydrogen donor as solvent, see Figure 4.28) (v/v%) was varied to study the effect of hydrogen that originated from 2-PrOH, on the reaction order of hydrogenolysis (Table 4.14, entries 10-12). Surprisingly, the conversion increased with increasing volume ratio of 2-PrOH which suggested that the hydrogen from 2-PrOH as well as the THFA concentration had more influence on the reaction rate than gaseous hydrogen pressure. This was also evident in the flow experiments where no significant benefit was observed from the introduction of H_2 gas (see Figure 4.21). Accordingly, the reaction order with respect to THFA concentration and 2-PrOH volume percent over 40Ni-La(R) was found to be 0.3, but almost zero order with respect to gaseous hydrogen pressure (see Figure 4.28).

Table 4.14. Hydrogenolysis of THFA over 40Ni-La(R) at different conditions.

Entry	c(THFA) [mmol L^{-1}]	H_2 Pressure [MPa]	v/v (2-/1-PrOH)[a] [%]	Time [h]	Conversion [%]	1,5-PeD yield [%]	TOF [h^{-1}]
1	180	3	100	3	33	28	13
2	400	3	100	3	23	18	20
3	760	3	100	3	14	5	23
4	1120	3	100	3	10	2	27
5	1440	3	100	3	9	1	28
6	200	3	100	4	44	43	16
7	200	4	100	4	42	41	15
8	200	5	100	4	43	42	16
9	200	6	100	4	42	41	15
10	200	3	20	4	30	28	11
11	200	3	50	4	35	35	13
12	200	3	80	4	43	42	16

Reaction conditions: THFA in 5 mL solvent, m(cat)= 100 mg, T= 150 °C. [a] volume percent of 2-PrOH to 1-PrOH.

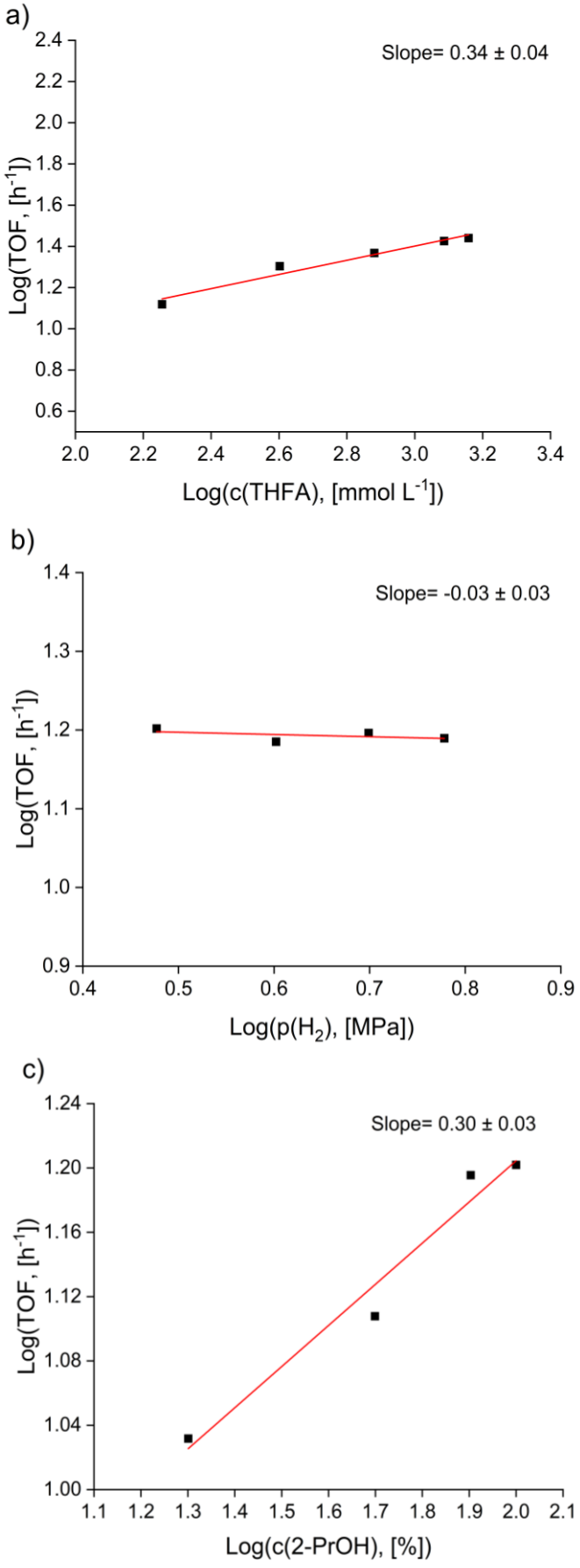

Figure 4.28. Effect of THFA concentration (a), H_2 pressure (b), volume percent of 2-PrOH in 1-PrOH (c) on hydrogenolysis reaction rate of THFA over 40Ni-La(R) (for reaction conditions see Table 4.14 above).

Concerning the reported mechanism of metal hydride attack in the hydrogenolysis of THFA on ReO_x-modified Rh and Ir catalysts in water, it was found that the reaction order ranged from 0 to 0.3 with respect to THFA concentration, but was first order with respect to H_2 pressure [42, 80, 95, 98]. The hydrogen activation step was proposed as the most important step in the hydride mechanism [80, 95, 107]. Moreover, kinetic results reported on the hydrogenolysis of THP-2-M to 1,6-HDO by the concerted carbenium ion mechanism on similar catalytic system (Rh-ReO_x/C in aqueous solution) share some similarities with the hydride mechanism. The reaction order of the hydrogenolysis was approximately first order with respect to THP-2-M concentration and H_2 pressure. Regardless the different proposed ring-opening mechanisms, the reaction order with respect to H_2 pressure was almost the same (first order) for acid-modified rhodium-catalyzed hydrogenolysis of THFA in aqueous solution. On the other hand, for the Ni-Ln-catalyzed hydrogenolysis in 2-PrOH, the reaction order with respect to hydrogen and 2-PrOH concentrations was between 0-0.3 which seems to indicate that the influence of only one parameter (deprotonation by basic sites or the activation of gaseous H_2/hydrogen-donor 2-PrOH) was not the rate-determining step. It seems likely that the step which requires a contribution of more than one parameter could be a rate-determining step. As shown in Figure 4.12, 40Ni-La(R) possesses highly basic sites generated from $La(OH)_3$ (specific base) which deprotonate the substrate before the ring is cleaved. The rate-determining step should be the following step after the fast deprotonation. This suggests that the ring cleavage is the rate-determining step that occurs at the Ni-La interface via hydride attack and/or ring-opening tautomerization of reactive 2-HY-PAL after initial dehydrogenation-hydrogenation equilibrium of THFA.

However, the contribution of transfer hydrogen from 2-PrOH over 40Ni-La(R), especially under inert conditions, and its influence on the reaction rate of hydrogenolysis have not been entirely revealed since the mechanisms reported for the C–O bond hydrogenolysis of THFA were investigated in aqueous solution which is not known as hydrogen donor under the conditions applied. Also, the effect of Ni on basic supports on the formation of hydride or intermediates in the hydrogen-donor 2-PrOH could be different from that of acid-modified Rh catalysts in water. For instance, *Gilkey et al.* reported that a direct hydrogen transfer is possible in CTH reactions from C1 of the alcoholate to C2 of the carbonyl species in a concerted step via a six-membered ring intermediate, without forming a metal hydride, according to the Meerwein−Ponndorf−Verley (MPV) mechanism, since the formation of hydrides on most acidic and basic sites is difficult [142]. It was also found that a base can accept the hydroxy proton from the hydrogen donor solvent which enhances the reactivity [142]. An interesting study with isotopic labeling experiments in 2-$PrOD_8$ for the hydrogenolysis of FUR to 2-MF was performed using Ru/RuO_x/C [143]. The authors reported that the hydrogenation of FUR catalyzed by a Lewis acid occurred via a direct hydrogen transfer mechanism (MPV). This finding based on

the result of a D atom transfer from 2-$PrOD_8$ to C1 of the formed FAL [142, 143]. Also, the authors assumed that the hydrogenolysis of FAL could take place at least in part via activation of the furan ring, where the solvent seemed to play a remarkable role in the ability to activate the ring via the Ru surface [142-144]. The solvent effect on Ni catalysts was obvious since it was active in all selected organic solvents, expect water which, in contrast, was the best solvent for reported noble metal catalysts (Rh, Ir, Pt) (Figure 4.18 and Table 1.5). The previous reported findings could also be applied for Ni-catalyzed hydrogenolysis of THFA, but the coexistence of metallic and basic active sites in the Ni-Ln(R) catalysts and the presence of 2-PrOH in addition to H_2 which could be concurrently dehydrogenated to acetone make the understanding of the role of solvent in this reaction more complicated. Thus, a series of batch experiments was carried out under H_2 and inert Ar pressure, and the acetone formation was monitored over time using GC-MS and *in situ* FTIR methods.

4.4.4. Effect of transfer hydrogenolysis via 2-PrOH

As discussed before, secondary alcohols are considered as potential hydrogen donors that can split off hydrogen and can be converted to the corresponding ketone (see paragraph 4.2.4). For instance, 2-PrOH is a hydrogen donor that can be dehydrogenated to acetone by a Ni catalyst, and the released hydrogen can then be transferred to a suitable substrate in a CTH reation (Scheme 4.10). However, the competing dehydrogenation of 2-PrOH on the heterogenous catalyst could decrease the efficiency of the catalyst in hydrogenolysis of THFA, and therefore, it is important to investigate possible side products to understand their role in the reaction network.

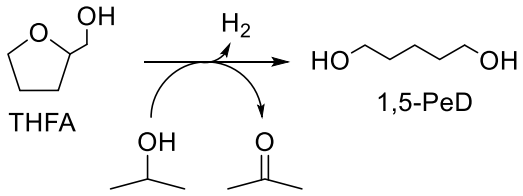

Scheme 4.10. CTH reaction of THFA in 2-PrOH over Ni-based catalyst.

Figure 4.29 compares the products formation in the hydrogenolysis of THFA over 40Ni-La(R) in 2-PrOH in a 300-mL autoclave under H_2 and Ar pressure over a long reaction time. Also, the formation of acetone at both pressures was compared based on the area shown in the gas chromatographic analysis (see GC area of acetone in Figure 4.29). As can be seen in Figure 4.29a as high in the first minutes of the hydrogenolysis reaction, but then dropped after 4 h and decreased to half of the initial formation after 84 h of reaction time. The conversion curve of THFA steadily increased during the long reaction time, and the selectivity to 1,5-PeD leveled off at ≥ 90 after the first 4 h (after stabilization of acetone formation) (Figure 4.29a). It may be assumed that the catalyst was highly active in the beginning of the reaction, and it randomly interacted with the reaction mixture, but after reaching the steady state, the catalyst surface

was mainly occupied with the hydrogenolysis of the C–O bond. This could also be due to the initial slow adsorption of H_2 gas on the catalyst surface, which was improved after some time. This could explain the reaction order of zero with respect to H_2 gas in the kinetic measurements carried out for a short time (4 h) under hydrogen pressure.

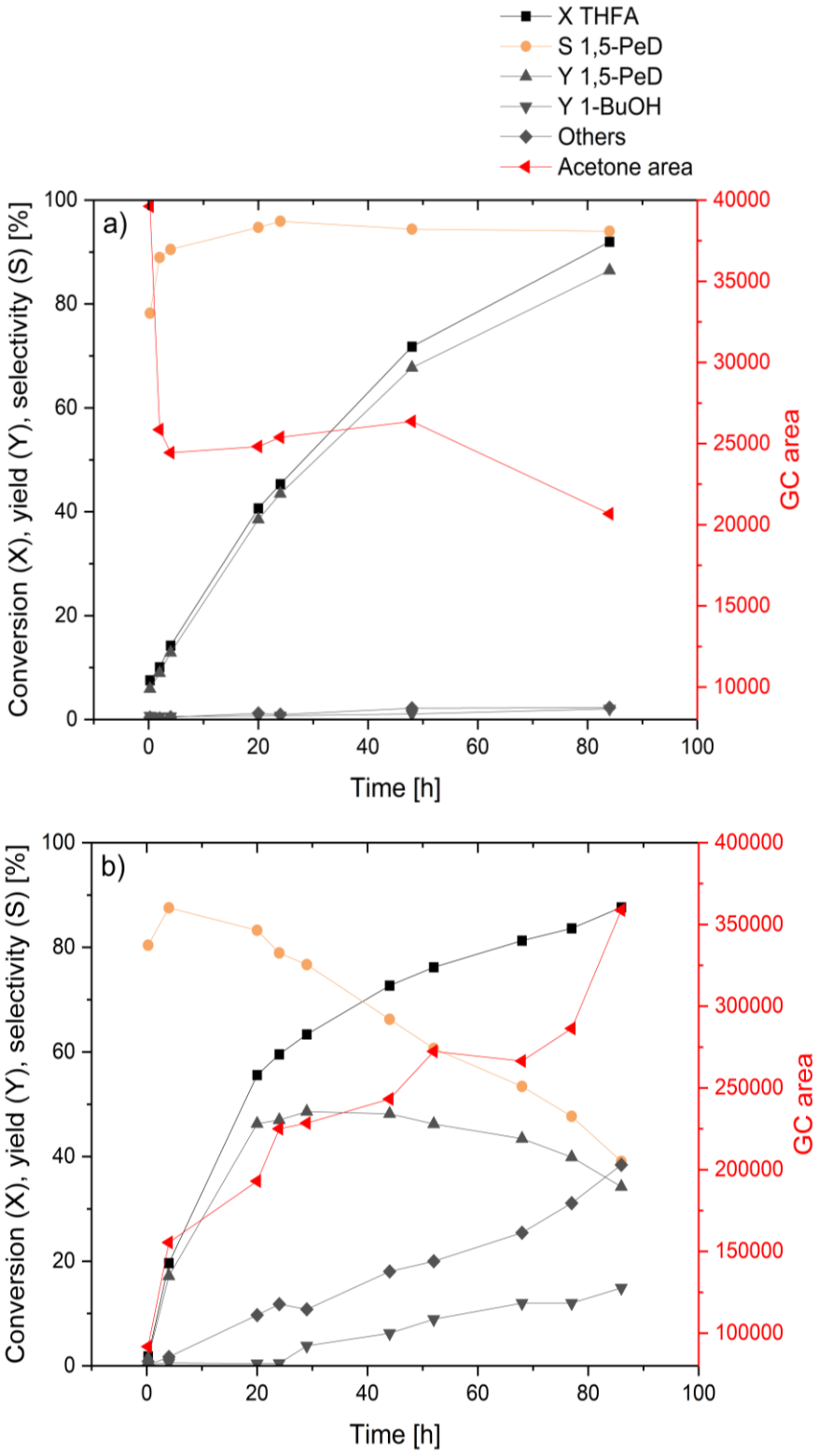

Figure 4.29. The effect of dehydrogenation of 2-PrOH on the conversion over 40Ni-La(R) in the hydrogenolysis of THFA under H_2 (a) and Ar pressure (b). Reaction conditions: 5 wt% THFA (39 mmol) in solvent (100 mL), m(cat)= 40 g, mass ratio (cat:THFA)= 1:4, T= 150 °C, p= 3 MPa. Others: estimated value of by-products based on an average GC response factor of known products.

On the other hand, acetone formation increased in parallel with the conversion of THFA (under argon), quite in contrast to the hydrogenolysis in the presence of hydrogen gas (compare Figure 4.29a and Figure 4.29b). Although the conversion was comparable in both cases, the selectivity to 1,5-PeD gradually decreased under inert conditions, resulting in a yield of ≤ 50%, as the selectivity of the catalyst for 1,5-PeD gradually decreased from about 90% (similar to the selectivity under H_2 pressure) after the first 4 h to approximately 40% after 85 h. This was due to the remarkable increase in the formation of by-products which was 10 times higher under Ar than under H_2 pressure (55% and 4.5%, respectively, after 85 h). At the same time, acetone formation increased significantly, indicating that the rate of dehydrogenation of 2-PrOH and that of the main hydrogenolysis reaction were comparable. This implies that the two reactants, THFA and 2-PrOH, compete with each other at the catalyst surface, resulting in poor selectivity for the target diol under batch conditions. The use of a large excess of the solvent in a long-term reaction in a batch reactor was not beneficial for a highly loaded nickel catalyst under transfer hydrogenolysis conditions because the nickel surface dehydrogenated the solvent to a greater extent. Therefore, the use of a flow reactor for transfer hydrogenolysis might be a better choice since a much lower amount of solvent could be introduced and the residence times could be varied by controlling the feed flow. In summary, the main advantage of adding hydrogen gas to the hydrogenolysis of THFA under batch condition in 2-PrOH was to achieve a high selectivity of the catalyst for the target diol.

Moreover, to monitor the formation of acetone per minute during the first 4 h in the batch reactor, the *in situ* FTIR technique was selected for this purpose. First, the initial pure compounds were examined, and the spectra were compared. As demonstrated in Figure 4.30, all compounds exhibited characteristic peaks at wavenumbers between 700-1500 cm^{-1}. In this range, it was not possible to detect acetone formation because the peaks of different compounds overlapped. However, at wavenumbers between 1500-2200 cm^{-1}, there was only one sharp band at 1712 cm^{-1} that could be assigned to acetone, and it was selected as the main characteristic peak for monitoring acetone formation during the hydrogenolysis reaction. Next, a series of batch experiments were monitored using an *in situ* FTIR instrument, and the reaction mixture was analyzed by GC after 4 hour (see paragraph 3.3 for experimental details). As detailed in Table 4.15, all experiments were carried out under the same conditions (H_2 or Ar) and catalysts to (40Ni-La, Ni^0 and $La(OH)_3$). Figure 4.31 shows the acetone peak at 1712 cm^{-1} corresponding to the FTIR experiments in Table 4.15. The first experiment was performed without catalyst under Ar pressure to study the temperature effect on dehydrogenation of 2-PrOH, which was ineffective, and no formation of acetone was observed (entry 1). However, a marked acetone formation was observed when 40Ni-La(R) was added, and the intensity of the acetone peak at 1712 cm^{-1} was high (entry 2). Also, the conversion of THFA was about 29% after 4 h. The intensity of the acetone peak increased continually, and this increase slowed

down with reaction time which corresponds to the GC results in Figure 4.29b (see 3D plot of FTIR spectra for more details about the formation of acetone over reaction time in Figure A15).

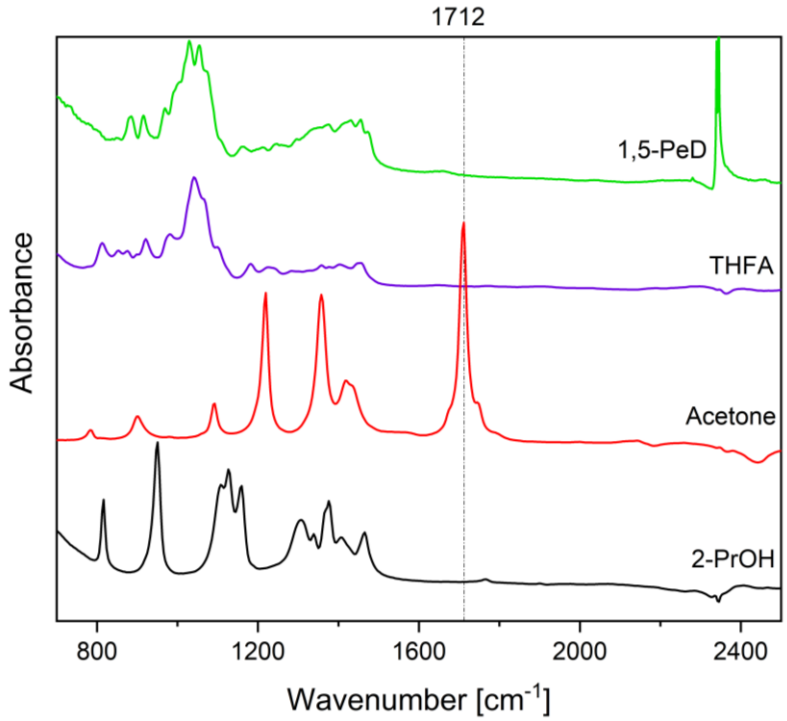

Figure 4.30. FTIR spectra of pure components at ambient conditions.

To clarify interaction of the support with the metallic Ni phase during the dehydrogenation of the solvent, the hydrogenolysis of THFA with Ni^0 and $La(OH)_3$ was carried out separately. As expected, both pure Ni^0 and $La(OH)_3$ were not active in the hydrogenolysis of the C–O bond of THFA. However, Ni^0 was active in the dehydrogenation of 2-PrOH, but the acetone peak was less intensive than that generated with 40Ni-La(R), and the GC area of acetone was consequently smaller (compare entries 2 and 3). In contrast, the peak of acetone was not detected in the case of $La(OH)_3$, but some traces of acetone were found in the respective chromatogram (entry 4). This implies that metallic Ni was mainly responsible for the dehydrogenation of the solvent, but in the presence of a strongly basic support, the rate of dehydrogenation was higher. Moreover, it seems likely that the metal-base Ni-La interface was responsible for the hydrogenolysis of THFA, whereby isolated nickel species not involved in the interface were able to dehydrogenate the solvent under Ar pressure. Regarding the dehydrogenation under H_2 pressure, the intensity of the acetone peak was low even after the amount of the catalyst was increased tenfold (from 100 mg to 1 g), and the acetone area was comparable (entries 5 and 6). The conversion of THFA was higher with increasing catalyst amount, but the selectivity was lower due to the formation of subsequent and by-products. This confirmed the previous observation that gaseous H_2 suppressed the rapid dehydrogenation of 2-PrOH, since the catalyst surface was already covered sufficiently with hydrogen, which favored the cleavage of the THFA ring. This was not the case under inert conditions [142].

Table 4.15. FTIR-tracked experiments under different batch conditions.

Entry	Gas	Catalyst	m (cat) [mg]	Conversion[a] [%]	1,5-PeD Selectivity	Acetone area[a]
1	Ar	-	-	2	0	0
2	Ar	40Ni-La(R)	100	29	83	228094
3	Ar	Ni^0	100	2	0	157482
4	Ar	$La(OH)_3$	100	2	0	3553
5	H_2	40Ni-La(R)	100	42	95	32422
6	H_2	40Ni-La(R)	1000	74	60	31421

Reaction conditions: c= 1 mmol of substrate in 2-PrOH (12 mL), T= 150 °C, p= 3 MPa, t= 4 h. [a] based on GC.

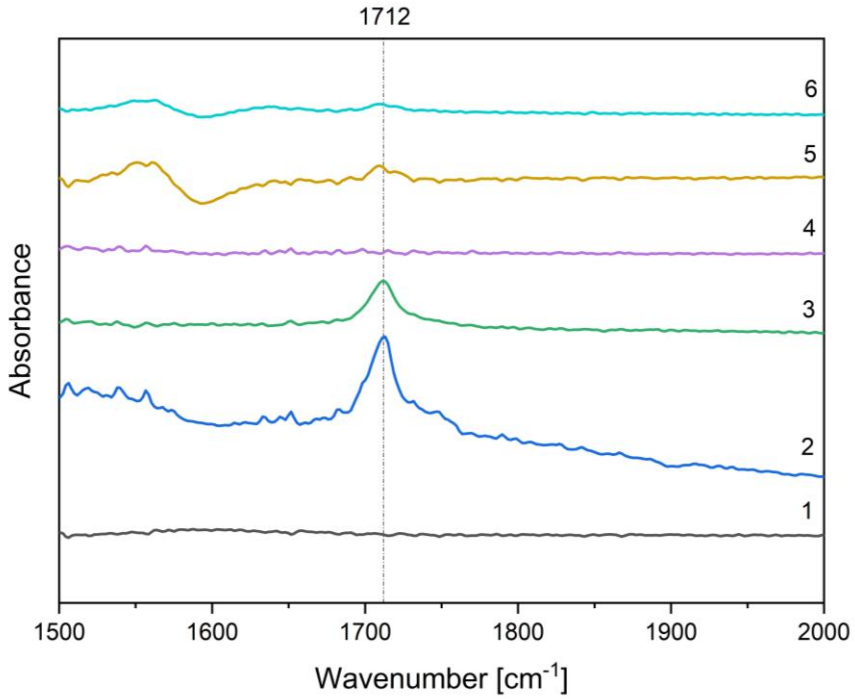

Figure 4.31. FTIR spectra detecting the acetone formation in the CTH of THFA in 2-PrOH for experiments according to the mentioned conditions in Table 4.15.

4.4.5. Proposed ring-opening reaction mechanisms of THFA

As mentioned before, the concerted hydrogen transfer mechanism via the hydride shift from C1 to C2 after protonation/deprotonation of THFA by acidic/basic sites was excluded based on the NMR results (see Table 4.13). The deuteration at C1 of THFA was high from the beginning of the reaction and did not remarkably change after ring-opening (see Table 4.13, entry 5). THFA was assumed to undergo rearrangement step to highly reactive 2-HY-THP which interacted with the surface of Ni via a dehydrogenation-hydrogenation step (see Scheme 4.7, pathway A). 5-HY-PAL was proposed to be formed from 2-HY-THP via ring-opening tautomerization (see Scheme 4.7, pathway B) or after ring-opening by “hydride attack” mechanism via dehydrogenation of 1,5-PeD over metallic Ni phase. The formation of short-lived intermediates 5-HY-PAL (or its carbenium ion) was also proposed based on DFT calculations [92, 93] and have been verified experimentally using GC-MS measurements in this study (see Table 4.12, entry 15). The formation of these intermediates after initial

interaction before the ring-opening highlighted the significance of active metal-base interfaces which were inactive in cleaving the ring of heterocyclic compounds that did not contain hydroxy groups (see Table 4.12, entries 6-8, 12-14). Reduced Ni and $La(OH)_3$ sites were inactive in the hydrogenolysis of THFA (see Table 4.7).

Concerning the hydride mechanism, the assumption of an interface between the surface of a noble metal (Rh or Ir) and that of an acidic modifier (ReO_x, MoO_x, etc.) as the catalytically active site is in complete agreement to the existence of an active Ni-$La(OH)_3$ interface. However, the reaction order with respect to hydrogen was 1 in the hydride mechanism reported where it was almost zero order in the case of 40Ni-La(R) (see Figure 4.28). The peculiarity of heterocyclic rings which could be initially rearranged to intermediates was not considered in hydride mechanism since it was proposed based on the mechanism for hydrogenolysis of glycerol to 1,3-propandiol (1,3-PDO) [98, 145]. Moreover, the interaction within the Ni-La interface before (via dehydrogenation-hydrogenation steps) and after ring-opening (via keto-enol tautomerism) was considered in the proposed mechanism based on the NMR results. Therefore, the hydride attack mechanism was proposed as the main mechanism for selective C–O bond hydrogenolysis of THFA to 1,5-PeD with a possibility of ring-opening tautomerization via 2-HY-THP and 5-HY-PAL intermediates. Scheme 4.11 demonstrates this proposed hydride mechanism. For a better understanding, the results of deuteration experiments were included, therefore deuterium is used instead of hydrogen to demonstrate the experimental results. First, the hydroxy group of THFA is chemically adsorbed on the catalyst surface where it is deprotonated by strong basic $La(OH)_3$ sites forming an alkoxide (step I). After that, THFA might rearrange to a lesser extent to the reactive intermediate 2-HY-THP which further undergoes a dehydrogenation–hydrogenation equilibrium forming a C=O bond which can be re-hydrogenated by metallic Ni (see Scheme 4.11).

The incorporation of deuterium can be explained by these upstream steps. In the catalytic cycle, the hydride (D^-) species formed by heterolytic cleavage of D_2 directly attacks the β-position (C2) of THFA while the THFA oxygen interacts with the proton (D^+) (step II). After ring cleavage, the formed 1,5-PeD could be directly exchanged with another THFA (step III) or could further undergo an additional dehydrogenation step via Ni resulting in the formation of 5-hydroxypentanal (5-HY-PAL) as intermediate (step IV). The intermediate 5-HY-PAL undergoes a tautomeric keto-enol equilibrium where the tautomeric enol acts as a Brønsted acid and transfers a proton from –OH to strong basic $La(OH)_3$ (step V). The double bonds originating from ketone and enol (C=C and C=O) are further deuterated by activated D_2 on the Ni surface and the formed deuterated 1,5-PeD is desorbed from the catalyst surface via exchange with fresh THFA (step VI).

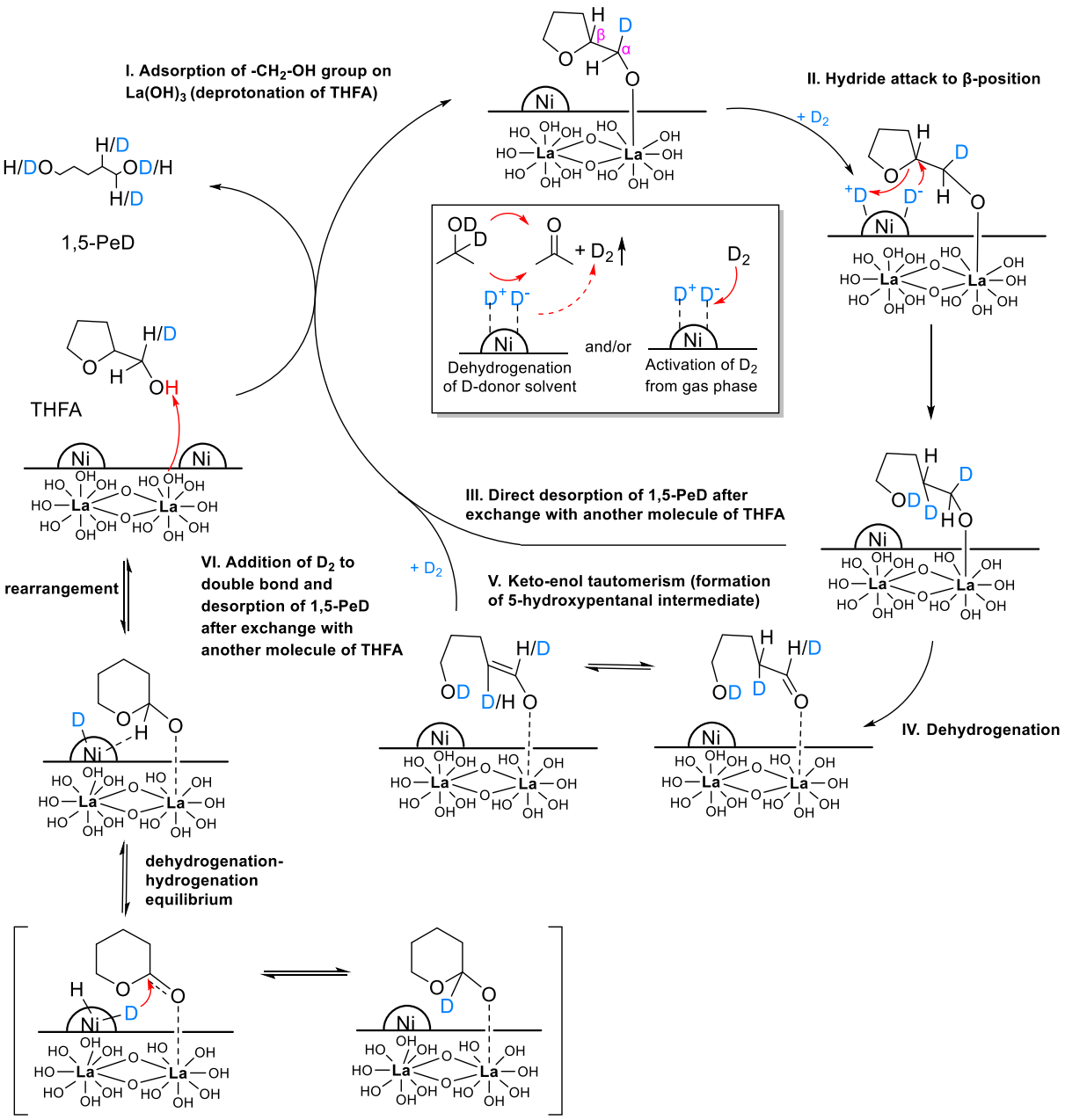

Scheme 4.11. Proposed hydride attack mechanism for hydrogenolysis of THFA over 40Ni-La(R).

On the other hand, the ring-opening tautomerization mechanism was also proposed (Scheme 4.12). First, THFA chemically is adsorbed on the catalyst surface where it is deprotonated by strong basic $La(OH)_3$ sites forming an alkoxide (step I). THFA rearranges to the reactive intermediate 2-HY-THP (step II) which further interacts with superficial Ni species via a dehydrogenation-hydrogenation step (step III). The 5-HY-PAL intermediate was formed via ring-opening tautomerization of 2-HY-THP due to its low stability at higher temperature (step IV). This intermediate undergoes a base-catalyzed keto-enol tautomeric equilibrium (deprotonation of alcoholate anion by strong basic support) (step V). Both the C=C and the C=O double bond are deuterated by activated D_2 on the Ni surface and the formed deuterated 1,5-PeD is desorbed from the catalyst surface by exchange with a fresh molecule of THFA closing the catalytic cycle (step VI).

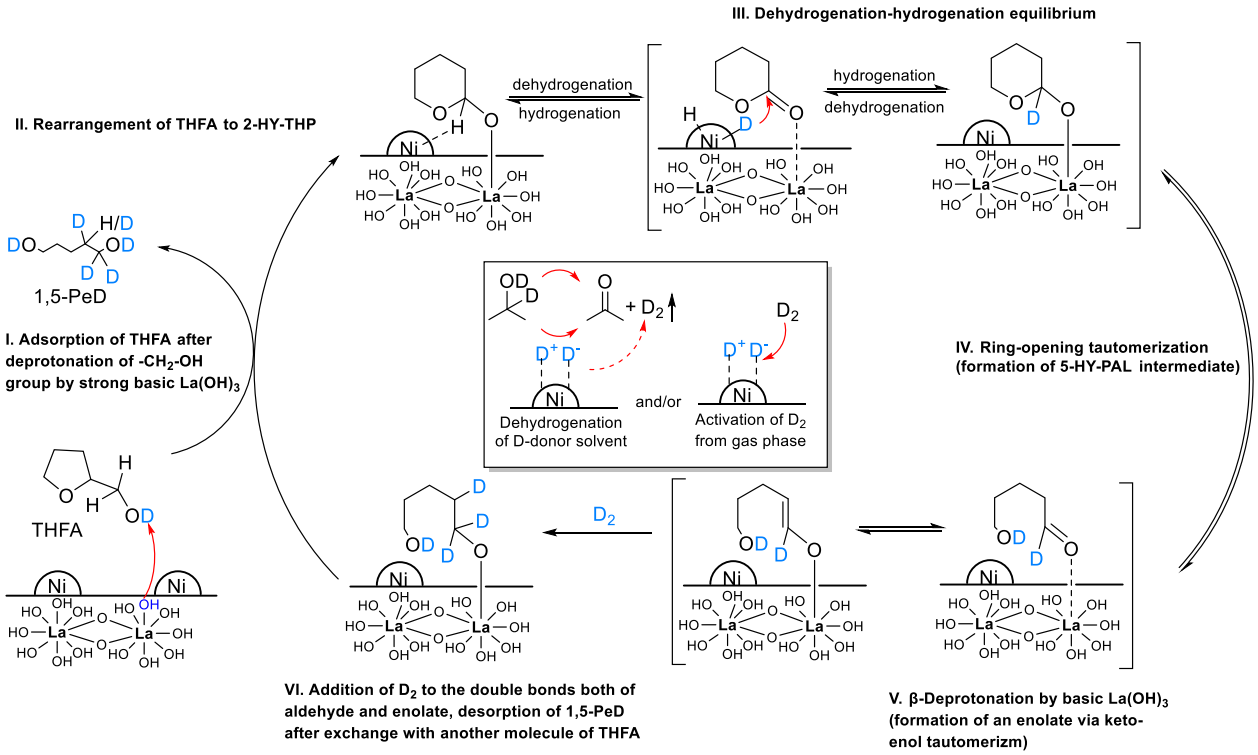

Scheme 4.12. Proposed ring-opening tautomerization mechanism for hydrogenolysis of THFA over 40Ni-La(R).

5. Conclusions and Outlook

The direct and selective hydrogenolysis of THFA, FOL and FUR to 1,5-PeD was intensively studied using heterogeneous nickel catalysts supported by basic lanthanide species under batch and flow conditions. Non-modified Ni on lanthanide supports (Ni-Ln(R), Ln= La, Pr, Nd, Sm hydroxides/oxyhydroxides) was proved to be an alternative economically efficient catalyst to modified noble metal catalysts for this reaction in non-aqueous solution. In the beginning, the effect of different preparation methods and pretreatment on the yield of 1,5-PeD over Ni on $La(OH)_3$ was studied. Reduced nickel and $La(OH)_3$ were not active in the hydrogenolysis of THFA when used individually. Also, only a low conversion of THFA (≤ 35% after 24 h) was observed over reduced Ni catalysts synthesized by solid-solid or liquid-solid preparation methods (physical mixing, ball milling and wet-impregnation). However, almost complete conversion was obtained by the reduced catalyst 40Ni-La(R) prepared by co-precipitation. It was obvious that the presence of the metallic nickel phase was essential since the calcined catalyst (40Ni-La(C)) was hardly active in the ring-opening reaction. Based on EDX elemental maps, the contact between Ni and La species was significantly increased after reduction (40Ni-La(R)) compared to 40Ni-La(C) pointing to a direct interaction between the two phases in the interface areas. The formation of a Ni-La phase interface is assumed to be responsible for the enhanced synergetic effect observed when 40Ni-La(R) was used as catalyst. This interface concertedly contributes to the hydrogenolysis of THFA, where metallic Ni species selectively activating hydrogen gas (and/or hydrogen-donor solvent) and basic sites of $La(OH)_3$ deprotonating the hydroxy group of the substrate, which subsequently leads to cleavage of the C–O bond and the formation of 1,5-PeD.

Regarding batch experiments, almost complete conversion of THFA was achieved on 40Ni-La(R) and 37Ni-Pr(R) resulting in 88% yield of 1,5-PeD. However, at similar Ni content, the selectivity to 1,5-PeD was higher on less dispersed Ni catalysts. The dispersity was different depending on the lanthanide supports in the following order: 37Ni-Pr(R) >> 38Ni-Sm(R) > 40Ni-La(R). Also, it was proved that the strength of basicity of the support played a key role in increasing 1,5-PeD yield over nickel-based catalysts. The highest conversion was obtained over Ni on strongly basic supports. The basicity decreased depending on the nature of the hydroxidic support after reduction. For instance, the La support in highly active 40Ni-La(R) maintained mostly its hydroxide nature ($La(OH)_3$), in contrast to the Sm support which was totally transformed to less basic oxyhydroxide (SmO(OH)) in 38Ni-Sm(R) after reduction at 250 °C for 8 h. However, increasing the reduction temperature to 450 °C leads to drop in the conversion due to the transformation of strongly basic hydroxide to weakly basic oxidic species. Thus, to achieve high conversion, it was suggested to reduce the Ni catalyst at lower temperature (250 °C) to avoid a loss of basicity and to extend the reduction time (up to 8 h) to

ensure complete reduction of the Ni phase. Furthermore, to maintain high 1,5-PeD yields, the Ni content was varied on the highly basic supports. The optimal loadings of Ni were ≥21 and ≥34 wt% for Ni-La(R) and Ni-Pr(R) resulting in 81 and 83% yield of 1,5-PeD, respectively.

Comparing these results with reported Ru/Ni-Y_2O_3 (1 wt% Ru, molar ratio (Ni:Y) = 2.5) which was active in hydrogenolysis of THFA resulting in a 1,5-PeD yield of 86% after 24 h [85]. 81% yield of 1,5-PeD was achieved over 21Ni-La(R) at a significantly lower molar ratio between metal and support (Ni:La = 0.9) and without addition of any noble metal to Ni-La(R) catalyst. Comparing Ni-Ln(R) with modified Rh catalysts, the best yield of 1,5-PeD ranged from 83 to 88% over Rh-ReO_x/TiO_2 with 2.7 wt% for each Rh and Re in this study (see Table 4.3), and from 77 to 94% in the reported works over Rh-ReO_x/SiO_2 with a Rh content of 4 wt% and 3.6 wt% Re under high H_2 pressure (up to 8 MPa) in water under batch conditions [78, 79, 94]. Both supported Ni and modified Rh catalysts were highly selective to the target diol. However, the high costs of precious noble metal catalysts and their low stability due to the leaching of the modifier obstruct the transfer of these systems from batch reactions to continuous processes even if they are active at high concentration of THFA in water. On the other hand, noble-metal free catalysts Ni-Ln(R) demonstrated comparable yields of target diol (up to 88% after 24 h) at significantly lower H_2 pressure (3 MPa) in 2-PrOH as a commonly used solvent. These catalysts have more potential to be applied in industry as alternative cheap catalysts.

Furthermore, Ni-La(R) was active in selective C–O bond hydrogenolysis of all selected furfural or pyran derivatives to α,ω-diols only if they are attached to a hydroxy group (–OH) which could be strongly adsorbed on the basic support. Particularly, one-pot conversion of FUR and FOL to 1,5-PeD was carried out via THFA over 40Ni-La(R) under batch conditions resulting in 44% and 57% yield of 1,5-PeD after 24 h, respectively. After extending the reaction time to 72 h, maximum 1,5-PeD yield of 65% was achieved from FUR over 37Ni-Nd(R). Due to the long reaction time, the formation of side and consecutive products was high, and the best selective catalyst was 38Ni-Sm(R) with a total yield of 80% (23% THFA+57% 1,5-PeD). The conversion of FUR over 38Ni-Sm(R) was compared at 50 °C and 150 °C after 4 h. Complete conversion of FUR was achieved at both temperatures where 92% of THFA was obtained at 50 °C compared to 19% 1,5-PeD and 72% THFA at 150 °C. This implies that a number of active sites in the beginning of the reaction was presumably poisoned due to FUR polymerization at higher temperature. Thus, it is recommended to perform the direct conversion of FUR to 1,5-PeD via THFA on Ni catalysts in a two-step reaction at different temperatures (50 °C for hydrogenation followed by 150 °C for hydrogenolysis) to avoid catalyst deactivation.

Concerning the solvent effect, the catalytic performance of nickel catalysts was compared in various solvents both for hydrogenolysis with molecular hydrogen and under inert conditions. Unlike in water, 40Ni-La(R) was active in all selected organic solvents, and the highest

conversion of THFA was observed in secondary alcohols. The obtained yields of 1,5-PeD varied depending on the solvents and increased in the following order: H_2O < EtOH < 1,4-dioxane ≈ 1-PrOH ≈ toluene << 2-PeOH < 2-BuOH ≈ 2-PrOH. However, the catalyst was not active in the hydrogenolysis of THFA under argon pressure (without hydrogen) except in the case of secondary alcohols. The increase in 1,5-PeD yield was attributed to the ability of secondary alcohols over metal catalyst to transfer hydrogen to the substrate in hydrogenation/hydrogenolysis reactions (CTH). For instance, 2-PrOH was partially dehydrogenated to acetone producing additional hydrogen even though gaseous hydrogen was abundant. It seemed that metallic Ni intended to create a hydrogen-rich environment in order to cleave the C–O bond of THFA [142]. Due to the competitive occupation of the catalyst surface with the dehydrogenation of 2-PrOH, the yield of 1,5-PeD dropped without hydrogen under batch conditions. In addition, a comparative study of the behavior of 40Ni-La(R) in the hydrogenolysis of THFA in 2-PrOH with and without gaseous hydrogen showed that the acetone formation was high in the beginning under H_2 pressure, but it decreased remarkably in the first hours, but the selectivity to 1,5-PeD remained high and stable over time. However, the selectivity to the target diol decreased significantly in absence of gaseous H_2, and the acetone formation was 10 times higher and increased continuously due to the occupation of the Ni surface with the dehydrogenation of the solvent which made up most of the reaction mixture. Therefore, it was more feasible to carry out the transfer hydrogenolysis under flow conditions since the gaseous hydrogen did not remarkably affect the selectivity of the catalyst for the target diol due to the possibility to adjust the flow rate of the liquid feed. Therefore, a CTH of THFA to 1,5-PeD was developed successfully over noble-metal free nickel catalysts at different process parameters which had not been studied before. The optimal yield was 63% with a catalyst bed volume of 2.4 mL (21Ni-La(R)) at following conditions: 1.3 wt% THFA, 140 °C, 3 MPa, LHSV= 6.3 h^{-1}.

Furthermore, the stability of the catalysts which were most active in the batch reactor, particularly 40Ni-La(R), 37Ni-Pr(R), 37Ni-Nd(R) and 38Ni-Sm(R), was tested in long continuous runs. Remarkably, 40Ni-La(R) was the most active catalyst (X= 85%), and it demonstrated high stability even after 386 h TOS. Also, 38Ni-Sm(R) was highly stable even at higher temperature (160 °C) after 188 h TOS. In contrast, the conversion of THFA over 37Ni-Pr(R) dropped within the first two days (50 h TOS) as well as that of 37Ni-Nd(R). The stability drop was accompanied by a significant increase in the C atom concentration at the catalyst surface from 4.9 to 30.8 at.% when 37Ni-Pr(R) and 37Ni-Pr(S) were compared. This increase was not significant in the case of stable 40Ni-La(R) and 38Ni-Sm(R). This implies that the high dispersion of Ni must be considered as disadvantage for stability of the catalyst in this reaction, since the deposition of the carbonaceous material was probably significant due to oligomerization of organic species on the catalyst surface in the case of better dispersed Ni on

Pr support. In addition, the productivity per hour of 40Ni-La(R) was improved by reducing the volume of the catalyst bed to 0.8 mL and increasing the THFA concentration to 2.5 wt% under continuous CTH conditions resulting in a productivity (1.4 mmol $g(cat)^{-1}h^{-1}$) which was almost two times higher than in batch reactor. Also, the catalyst productivity in flow was comparable to that of a reported modified Ir catalyst which was not stable in a short continuous run (30 h TOS) [81, 82]. So, the total productivity of the CTH process was assumed to be much higher in the case of stable 40Ni-La(R). Besides, the advantages of cheap Ni catalysts and accessible reductive organic solvents (e.g., 2-PrOH), as well as the avoidance of hazardous high-pressure hydrogen reduce the process costs and raise the level of safety in the workplace.

Finally, the reaction mechanism of hydrogenolysis of THFA to 1,5-PeD catalyzed by nickel on basic supports in 2-PrOH was elucidated for the first time using the isotopic labeling technique. For hydrogenolysis of the C–O bond at the metal-basic support interface, a hydride attack was proposed as the main mechanism with the possibility of a ring-opening tautomerization of THFA via 2-HY-THP intermediate as alternative. Both pathways could take place sharing many similarities, especially in the deprotonation of the hydroxy group of THFA which was essential for starting the reaction, but the main difference lies on formation of 5-HY-PAL which might be formed via ring-opening tautomerization of reactive 2-HY-THP or via dehydrogenation of 1,5-PeD after the ring cleavage (rate-determining step). Regarding kinetic measurements, the reaction order with respect to THFA concentration and 2-PrOH volume percent was found to be 0.3, but almost zero order with respect to gaseous hydrogen pressure. Nevertheless, various possible mechanisms reported for other modified noble metal catalysts were discussed and evaluated comprehensively based on experimental data. A combination of experimental data and theoretical DFT calculation would be beneficial to elucidate the mechanism of this reaction, but theoretical calculations were not available within the time frame of this study. Thus, it is difficult to select a single mechanism because the detection of hydrides or unstable intermediates in liquid-phase hydrogenation/hydrogenolysis reactions over heterogenous catalysts is complicated. A fundamental understanding of the C–O bond hydrogenolysis of biobased heterocyclic feedstocks will surely lead to the increase of renewable value-added α,ω-diols in the market, and this can be achieved by synthesizing efficient noble-metal free catalysts which have more potential to be applied in industry without limitations.

6. References

[1] P. Werle, M. Morawietz, S. Lundmark, K. Sörensen, E. Karvinen, J. Lehtonen, "Alcohols, Polyhydric" in: Ullmann's Encyclopedia of Industrial Chemistry, *Wiley-VCH Verlag GmbH & Co.* (**2008**) 1-18.

[2] Z.J. Brentzel, K.J. Barnett, K. Huang, C.T. Maravelias, J.A. Dumesic, G.W. Huber, *ChemSusChem* 10 (**2017**) 1351-1355.

[3] C. J. Sullivan, K. Vorlop, "Propanediols" in: Ullmann's Encyclopedia of Industrial Chemistry, *Wiley-VCH Verlag GmbH & Co.* (**2018**) 1-15.

[4] BASF, https://chemicals.basf.com/global/en/Intermediates/Product_groups/Diols_Polyols.html, accessed date 02.11.2021.

[5] Expert Market Research, https://www.expertmarketresearch.com/reports/1-6-hexanediol-market, accessed date 10.12.2021.

[6] MarketWatch, https://www.marketwatch.com/press-release/global-15-pentanediol-market-2021-industry-growth-and-key-countries-analysis-by-2027-2021-12-13, accessed date 10.12.2021.

[7] MarketWatch, https://www.marketwatch.com/press-release/14-butanediol-bdo-market-share-size-global-historical-analysisindustry-key-strategies-segmentation-application-technology-trends-and-growth-opportunities-forecasts-to-2026-2021-11-08, accessed date 10.12.2021.

[8] ECHMI, https://www.echemi.com/products/pd20160331093009182-14-butanediol.html, accessed date 02.11.2021.

[9] J.Y. He, K.F. Huang, K.J. Barnett, S.H. Krishna, D.M. Alonso, Z.J. Brentzel, S.P. Burt, T. Walker, W.F. Banholzer, C.T. Maravelias, I. Hermans, J.A. Dumesic, G.W. Huber, *Faraday Discuss.* 202 (**2017**) 247-267.

[10] K.F. Huang, Z.J. Brentzel, K.J. Barnett, J.A. Dumesic, G.W. Huber, C.T. Maravelias, *ACS Sustain. Chem. Eng.* 5 (**2017**) 4699-4706.

[11] D. Kaufman, W. Reeve, *Org. Synth.* 26 (**1946**) 83.

[12] Sigma-Aldrich, https://www.sigmaaldrich.com/DE/de/product/aldrich/p7703, accessed date 02.11.2021.

[13] Sigma-Aldrich, https://www.sigmaaldrich.com/DE/de/product/sial/493732, accessed date 02.11.2021.

[14] Sigma-Aldrich, https://www.sigmaaldrich.com/DE/de/product/aldrich/240117, accessed date 02.11.2021.

[15] PCI, https://www.pcimag.com/ext/resources/Events/CTT/2019ppt/BarnettKevin_Pyran.pdf, accessed date 31.03.2020.

[16] BASF, https://products.basf.com/global/en/ci/1_5-Pentanediol.html, accessed date 02.11.2021.

[17] USA Today, Mom: Chemical-laced toy made son 'drunk' - USATODAY.com, accessed date 31.03.2020.

[18] A. E. Eseyin, P. H. Steele, *Int. J. Chem.* 3 (**2015**) 42-47.

[19] A. M. J. Hidalgo-Carrillo, F. J. Urbano, "Chemistry of Furfural and Furanic Derivatives" in: Furfural: An Entry Point of Lignocellulose in Biorefineries to Produce Renewable Chemicals, Polymers, and Biofuels, *World Scientific* (**2018**) 1-32.

[20] C.M. Cai, T.Y. Zhang, R. Kumar, C.E. Wyman, *J. Chem. Technol. Biotechnol*. 89 (**2014**) 2-10.

[21] K. Dalvand, J. Rubin, S. Gunukula, M.C. Wheeler, G. Hunt, *Biomass Bioenergy* 115 (**2018**) 56-63.

[22] O. Aldosari, H. Alshammari, M. Alhumaimess, I. Wawata, *Turk. J. Chem.* 43 (**2019**) 24-38.

[23] N. I. Sax, W. J. Mckillip, Dangerous Properties of Industrial Materials, 6th ed., *Van Nostrand Rheinold*, (**1984**).

[24] E. Ricard, H. M. Guinot, U.S. Patent No. 1739919A (**1929**).

[25] P. Maireles-Torres, P. L. Arias, "Furfuryl Alcohol and Derivatives" in: Furfural: An Entry Point of Lignocellulose in Biorefineries to Produce Renewable Chemicals, Polymers, and Biofuels, *World Scientific* (**2018**) 55–78.

[26] H. Adkins, R. Connor, *J. Am. Chem. Soc.* 53 (**1931**) 1091−1095.

[27] L. Frainier, H. Fineberg, U.S. Patent No. 4302397A (**1981**).

[28] X.F. Chen, H.X. Li, H.S. Luo, M.H. Qiao, *Appl. Catal A: Gen.* 233 (**2002**) 13-20.

[29] H.X. Li, H.S. Luo, L. Zhuang, W.L. Dai, M.H. Qiao, *J. Mol. Catal. A: Chem.* 203 (**2003**) 267-275.

[30] B.J. Liu, L.H. Lu, B.C. Wang, T.X. Cai, K. Iwatani, *Appl. Catal., A* 171 (**1998**) 117-122.

[31] A.B. Merlo, V. Vetere, J.F. Ruggera, M.L. Casella, *Catal. Commun.* 10 (**2009**) 1665-1669.

[32] J. Zhang, K.J. Dong, W.M. Luo, H.F. Guan, *ACS Omega* 3 (**2018**) 6206-6216.

[33] S.B. Liu, Y. Amada, M. Tamura, Y. Nakagawa, K. Tomishige, *Green Chem.* 16 (**2014**) 617-626.

[34] K. Fulajtarova, T. Sotak, M. Hronec, I. Vavra, E. Dobrocka, M. Omastova, *Appl. Catal., A* 502 (**2015**) 78-85.

[35] Q.Q. Yuan, D.M. Zhang, L. van Haandel, F.Y. Ye, T. Xue, E.J.M. Hensen, Y.J. Guan, *J. Mol. Catal. A: Chem.* 406 (**2015**) 58-64.

[36] R.Q. Fang, L.Y. Chen, Z.R. Shen, Y.W. Li, *Catal. Today* 368 (**2021**) 217-223.

[37] M. Bankmann, J. Ohmer, T. Tacke, EP. Patent No. 0669163B1 (**1995**).

[38] D. Vargas-Hernandez, J.M. Rubio-Caballero, J. Santamaria-Gonzalez, R. Moreno-Tost, J.M. Merida-Robles, M.A. Perez-Cruz, A. Jimenez-Lopez, R. Hernandez-Huesca, P. Maireles-Torres, *J. Mol. Catal. A: Chem.* 383 (**2014**) 106-113.

[39] B.M. Nagaraja, V.S. Kumar, V. Shasikala, A.H. Padmasri, B. Sreedhar, B.D. Raju, K.S.R. Rao, *Catal. Commun.* 4 (**2003**) 287-293.

[40] C.P. Jimenez-Gomez, J.A. Cecilia, D. Duran-Martin, R. Moreno-Tost, J. Santamaria-Gonzalez, J. Merida-Robles, R. Mariscal, P. Maireles-Torres, *J. Catal.* 336 (**2016**) 107-115.

[41] H. E. Hoydonckx, W. M. Van Rhijn, W. Van Rhijn, D. E. De Vos, P. A. Jacobs, "Furfural and Derivatives" in: Ullmann's Encyclopedia of Industrial Chemistry, *Wiley-VCH Verlag GmbH & Co.* (**2007**).

[42] Y. Nakagawa, H. Nakazawa, H. Watanabe, K. Tomishige, *ChemCatChem* 4 (**2012**) 1791-1797.

[43] P. Maireles-Torres, P. L. Arias, "Tetrahydrofurfuryl Alcohol and Derivatives" in: Furfural: An Entry Point of Lignocellulose in Biorefineries to Produce Renewable Chemicals, Polymers, and Biofuels, *World Scientific* (**2018**), 79-89.

[44] N. Merat, C. Godawa, A. Gaset, *J. Chem. Technol. Biotech.* 48 (**1990**) 145-159.

[45] L.J. Liu, H. Lou, M. Chen, *Int. J. Hydrogen Energy* 41 (**2016**) 14721-14731.

[46] J. Wu, G. Gao, J.L. Li, P. Sun, X.D. Long, F.W. Li, *Appl. Catal., B* 203 (**2017**) 227-236.

[47] Y.L. Yang, J.P. Ma, X.Q. Jia, Z.T. Du, Y. Duan, J. Xu, *RSC Adv.* 6 (**2016**) 51221-51228.

[48] C. Chen, R.Y. Fan, W.B. Gong, H.M. Zhang, G.Z. Wang, H.J. Zhao, *Dalton Trans.* 47 (**2018**) 17276-17284.

[49] Rodiansono, M.D. Astuti, D.R. Mujiyanti, U.T. Santoso, S. Shimazu, *Mol. Catal.* 445 (**2018**) 52-60.

[50] P. Balla, P.K. Seelam, R. Balaga, R. Rajesh, V. Perupogu, T.X. Liang, *J. Environ. Chem. Eng.* 9 (**2021**).

[51] S. Li, Y. Wang, L.J. Gao, Y.F. Wu, X.H. Yang, P.X. Sheng, G.M. Xiao, *Microporous Mesoporous Mater.* 262 (**2018**) 154-165.

[52] H.J. Wang, X.D. Li, X.C. Lan, T.F. Wang, *ACS Catal.* 8 (**2018**) 2121-2128.

[53] J. Parikh, S. Srivastava, G.C. Jadeja, *Ind. Eng. Chem. Res.* 58 (**2019**) 16138-16152.

[54] C.H. Wang, A.J. Wang, Z.Q. Yu, Y. Wang, Z.C. Sun, V.M. Kogan, Y.Y. Liu, *Catal. Commun.* 148 (**2021**).

[55] C. Li, G.Y. Xu, X.H. Liu, Y. Zhang, Y. Fu, *Ind. Eng. Chem. Res.* 56 (**2017**) 8843-8849.

[56] R. Albilali, M. Douthwaite, Q. He, S.H. Taylor, *Catal. Sci. Technol.* 8 (**2018**) 252-267.

[57] S. Pendem, S.R. Bolla, D.J. Morgan, D.B. Shinde, Z.P. Lai, L. Nakka, J. Mondal, *Dalton Trans.* 48 (**2019**) 8791-8802.

[58] J.C. Wu, X.H. Zhang, Q. Chen, L.G. Chen, Q.Y. Liu, C.G. Wang, L.L. Ma, *Energy Fuels* 34 (**2020**) 2178-2184.

[59] B.M. Matsagar, C.Y. Hsu, S.S. Chen, T. Ahamad, S.M. Alshehri, D.C.W. Tsang, K.C.W. Wu, *Sustain. Energy Fuels* 4 (**2020**) 293-301.

[60] Y.L. Cao, H.P. Zhang, K.K. Liu, Q.Y. Zhang, K.J. Chen, *ACS Sustain. Chem. Eng.* 7 (**2019**) 12858-12866.

[61] W.E. Kaufmann, R. Adams, *J. Am. Chem. Soc.* 45 (**1923**) 3029-3044.

[62] H. Adkins, R. Connor, *J. Am. Chem. Soc.* 53 (**1931**) 1091-1095.

[63] H.L. Liu, Z.W. Huang, H.X. Kang, C.G. Xia, J. Chen, *Chin. J. Catal.* 37 (**2016**) 700-710.
[64] Y.W. Shao, J.Z. Wang, H.N. Du, K. Sun, Z.M. Zhang, L.J. Zhang, Q.Y. Li, S. Zhang, Q. Liu, X. Hu, *ACS Sustain. Chem. Eng.* 8 (**2020**) 5217-5228.
[65] H.L. Liu, Z.W. Huang, F. Zhao, F. Cui, X.M. Li, C.G. Xia, J. Chen, *Catal. Sci. Technol.* 6 (**2016**) 668-671.
[66] X.M. Fu, X.Q. Ren, J.C. Shen, Y. Jiang, Y.H. Wang, Y. Orooji, W.L. Xu, J.H. Liang, *Mol. Catal.* 499 (**2021**).
[67] F.F. Gao, H.L. Liu, X. Hu, J. Chen, Z.W. Huang, C.G. Xia, *Chin. J. Catal.* 39 (**2018**) 1711-1723.
[68] T.P. Sulmonetti, B. Hu, S. Lee, P.K. Agrawal, C.W. Jones, *ACS Sustain. Chem. Eng.* 5 (**2017**) 8959-8969.
[69] Y.W. Shao, M.Z. Guo, J.Z. Wang, K. Sun, L.J. Zhang, S. Zhang, G.Z. Hu, L.L. Xu, X.Z. Yuan, X. Hu, *Ind. Eng. Chem. Res.* 60 (**2021**) 10393-10406.
[70] Y.W. Shao, J.Z. Wang, K. Sun, G.M. Gao, C. Li, L.J. Zhang, S. Zhang, L.L. Xu, G.Z. Hu, X. Hu, *Renewable Energy* 170 (**2021**) 1114-1128.
[71] W.J. Xu, H.F. Wang, X.H. Liu, J.W. Ren, Y.Q. Wang, G.Z. Lu, *Chem. Commun.* 47 (**2011**) 3924-3926.
[72] Y.R. Zhu, W.F. Zhao, J. Zhang, Z. An, X.D. Ma, Z.J. Zhang, Y.T. Jiang, L.R. Zheng, X. Shu, H.Y. Song, X. Xiang, J. He, *ACS Catal.* 10 (**2020**) 8032-8041.
[73] T. Tong, X.H. Liu, Y. Guo, M.N. Banis, Y.F. Hu, Y.Q. Wang, *J. Catal.* 365 (**2018**) 420-428.
[74] T. Mizugaki, T. Yamakawa, Y. Nagatsu, Z. Maeno, T. Mitsudome, K. Jitsukawa, K. Kaneda, *ACS Sustain. Chem. Eng.* 2 (**2014**) 2243-2247.
[75] D.S. Pisal, G.D. Yadav, *ACS Omega* 4 (**2019**) 1201-1214.
[76] H.H.G. L. E. Schniepp, *J. Am. Chem. Soc.* 68 (**1946**) 1646–1648.
[77] G. W. Huber, J. A. Dumesic, K. J. Barnett, Z. J. Brentzel, U.S. Patent No. 10183904B2 (**2019**).
[78] S. Koso, I. Furikado, A. Shimao, T. Miyazawa, K. Kunimori, K. Tomishige, *Chem. Commun.* (**2009**) 2035-2037.
[79] S. Koso, N. Ueda, Y. Shinmi, K. Okumura, T. Kizuka, K. Tomishige, *J. Catal.* 267 (**2009**) 89-92.
[80] S. Koso, Y. Nakagawa, K. Tomishige, *J. Catal.* 280 (**2011**) 221-229.
[81] S. Koso, H. Watanabe, K. Okumura, Y. Nakagawa, K. Tomishige, *Appl. Catal., B* 111 (**2012**) 27-37.
[82] S. Koso, H. Watanabe, K. Okumura, Y. Nakagawa, K. Tomishige, *J. Phys. Chem. C* 116 (**2012**) 3079-3090.
[83] K. Chen, K. Mori, H. Watanabe, Y. Nakagawa, K. Tomishige, *J. Catal.* 294 (**2012**) 171-183.

[84] Z.Q. Wang, B. Pholjaroen, M.X. Li, W.J. Dong, N. Li, A.Q. Wang, X.D. Wang, Y. Cong, T. Zhang, *J. Energy Chem.* 23 (**2014**) 427-434.

[85] B. Pholjaroen, N. Li, Y.Q. Huang, L. Li, A.Q. Wang, T. Zhang, *Catal. Today* 245 (**2015**) 93-99.

[86] J.C. Lee, Y. Xu, G.W. Huber, *Appl. Catal., B* 140 (**2013**) 98-107.

[87] H.W. Wijaya, T. Sato, H. Tange, T. Hara, N. Ichikuni, S. Shimazu, *Chem. Lett.* 46 (**2017**) 744-746.

[88] H.W. Wijaya, T. Hara, N. Ichikuni, S. Shimazu, *Chem. Lett.* 47 (**2018**) 103-106.

[89] E. Soghrati, C. Kok Poh, Y.H. Du, F. Gao, S. Kawi, A. Borgna, *ChemCatChem* 10 (**2018**) 4652-4664.

[90] E. Soghrati, T.K.C. Ong, C.K. Poh, S. Kawi, A. Borgna, *Appl. Catal., B* 235 (**2018**) 130-142.

[91] B.F. Kuang, Q. Zhang, Y.X. Fang, Y. Bai, S.B. Qin, P. Wu, Y.L. Qin, T.J. Wang, *Ind. Eng. Chem. Res.* 59 (**2020**) 9372-9381.

[92] C. Wang, J.D. Lee, Y.C. Ji, T.M. Onn, J. Luo, C.B. Murray, R.J. Gorte, *Catal. Lett.* 148 (**2018**) 1047-1054.

[93] S.X. Feng, A. Nagao, T. Aihara, H. Miura, T. Shishido, *Catal. Today* 303 (**2018**) 207-212.

[94] M. Chatterjee, H. Kawanami, T. Ishizaka, M. Sato, T. Suzuki, A. Suzuki, *Catal. Sci. Technol.* 1 (**2011**) 1466-1471.

[95] M. Chia, Y.J. Pagan-Torres, D. Hibbitts, Q.H. Tan, H.N. Pham, A.K. Datye, M. Neurock, R.J. Davis, J.A. Dumesic, *J. Am. Chem. Soc.* 133 (**2011**) 12675-12689.

[96] J. Guan, G.M. Peng, Q. Cao, X.D. Mu, *J. Phys. Chem. C* 118 (**2014**) 25555-25566.

[97] K.Y. Chen, S. Koso, T. Kubota, Y. Nakagawa, K. Tomishige, *ChemCatChem* 2 (**2010**) 547-555.

[98] K. Tomishige, Y. Nakagawa, M. Tamura, *Green Chem.* 19 (**2017**) 2876-2924.

[99] X. Hu, S. Kadarwati, S. Wang, Y. Song, M.D.M. Hasan, C.Z. Li, *Fuel Process. Technol.* 137 (**2015**) 212-219.

[100] Q. Xu, X. Hu, L.J. Zhang, K. Sun, Y.W. Shao, Z.R. Gao, Q. Liu, C.Z. Li, *Green Energy Environ.* 6 (**2021**) 138-149.

[101] X. Hu, K. Nango, L. Bao, T.T. Li, M.D.M. Hasan, C.Z. Li, *Green Chem.* 21 (**2019**) 1128-1140.

[102] S.B. Liu, Y. Amada, M. Tamura, Y. Nakagawa, K. Tomishige, *Catal. Sci. Technol.* 4 (**2014**) 2535-2549.

[103] L. Gavilá, A. Lähde, J. Jokiniemi, M. Constanti, F. Medina, E. del Río, D. Tichit, M.G. Alvarez, *ChemCatChem* 11 (**2019**) 4944-4953.

[104] H.W. Wijaya, T. Kojima, T. Hara, N. Ichikuni, S. Shimazu, *ChemCatChem* 9 (**2017**) 2869-2874.

[105] J.Y. Yeh, B.M. Matsagar, S.S. Chen, H.L. Sung, D.C.W. Tsang, Y.P. Li, K.C.W. Wu, *J. Catal.* 390 (**2020**) 46-56.

[106] S. Chen, R. Wojcieszak, F. Dumeignil, E. Marceau, S. Royer, *Chem. Rev.* 118 (**2018**) 11023-11117.

[107] Y. Nakagawa, K. Tomishige, *Catal. Today* (**2012**) 136-143.

[108] K. Tomishige, Y. Nakagawa, M. Tamura, *Green Chem.* 19 (**2017**) 2876-2924.

[109] M. Al-Yusufi, N. Steinfeldt, R. Eckelt, H. Atia, H. Lund, S. Bartling, N. Rockstroh, A. Köckritz, *ACS Sustain. Chem. Eng.* 10 (**2022**) 4954-4968.

[110] J.H. Scofield, *J. Electron Spectrosc. Relat. Phenom.* 8 (**1976**) 129-137.

[111] M. Newville, *J. Synchrotron Radiat.* 8 (**2001**) 322-324.

[112] A.M. Abdel-Mageed, Operando investigations of particle size and support effects during the selective CO methanation over oxide supported Ru nanoparticles in idealized and realistic H_2 feed gases, *Universität Ulm* (**2016**).

[113] A.L. Ankudinov, B. Ravel, J. Rehr, S. Conradson, *Phys. Rev. B* 58 (**1998**) 7565.

[114] D. Koningsberger, B. Mojet, G. Van Dorssen, D. Ramaker, *Top. Catal.* 10 (**2000**) 143-155.

[115] A.S. Al-Fatesh, Y. Arafat, A.A. Ibrahim, H. Atia, A.H. Fakeeha, U. Armbruster, A.E. Abasaeed, F. Frusteri, *Appl. Catal., A* 567 (**2018**) 102-111.

[116] Ehrfeld, https://ehrfeld.com/produkte/mmrs.html. accessed date 02.04.2021.

[117] P. Loos, H. Alex, J. Hassfeld, K. Lovis, J. Platzek, N. Steinfeldt, S. Hubner, *Org. Process Res. Dev.* 20 (**2016**) 452-464.

[118] V.I. Baranenko, V.S. Kirov, *At. Energy* 66 (**1989**) 30-34.

[119] K. Tomishige, H. Yasuda, Y. Yoshida, M. Nurunnabi, B.T. Li, K. Kunimori, *Green Chem.* 6 (**2004**) 206-214.

[120] E. Leino, N. Kumar, P. Maki-Arvela, A. Aho, K. Kordas, A.R. Leino, A. Shchukarev, D.Y. Murzin, J.P. Mikkola, *Mater. Chem. Phys.* 143 (**2013**) 65-75.

[121] I. Prymak, V.N. Kalevaru, S. Wohlrab, A. Martin, *Catal. Sci. Technol.* 5 (2015) 2322-2331.

[122] K. Fajans, *Naturwissenschaften* 11 (**1923**) 165-172.

[123] M.C. Biesinger, B.P. Payne, L.W.M. Lau, A. Gerson, R.S.C. Smart, *Surf. Interface Anal.* 41 (**2009**) 324-332.

[124] M.C. Biesinger, B.P. Payne, A.P. Grosvenor, L.W.M. Lau, A.R. Gerson, R.S. Smart, *Appl. Surf. Sci.* 257 (**2011**) 2717-2730.

[125] B. Mutz, H.W.P. Carvalho, S. Mangold, W. Kleist, J.D. Grunwaldt, *J. Catal.* 327 (**2015**) 48-53.

[126] S. Chavan, J.G. Vitillo, E. Groppo, F. Bonino, C. Lamberti, P.D.C. Dietzel, S. Bordiga, *J. Phys. Chem. C* 113 (**2009**) 3292-3299.

[127] A. Sharma, M. Varshney, H.J. Shin, B.H. Lee, K.H. Chae, S.O. Won, *Mater. Chem. Phys.* 191 (**2017**) 129-144.

[128] H. Wang, J.T. Miller, M. Shakouri, C.Y. Xi, T.P. Wu, H.Y. Zhao, M.C. Akatay, *Catal. Today* 207 (**2013**) 3-12.

[129] W.W. Lin, H.Y. Cheng, J. Ming, Y.C. Yu, F.Y. Zhao, *J. Catal.* 291 (**2012**) 149-154.

[130] S. Jaatinen, R. Karinen, *Top. Catal.* 60 (**2017**) 1473-1481.

[131] R.T. D. Ambrose, *J. Chem. Soc.* (**1963**) 3614-3625.

[132] E. Brunner, Ber. Bunsengesell. *Phys. Chem.* 83 (**1979**) 715-721.

[133] A.K. O. Koch, M. Kant, A. Martin, A. Schöning, U. Armbruster, M. Bartoszek, S. Evert, B. Lange, R. Bienert, U.S. Patent No. 8921617 (**2014**).

[134] B. Zhang, Y.L. Zhu, G.Q. Ding, H.Y. Zheng, Y.W. Li, *Green Chem.* 14 (**2012**) 3402-3409.

[135] J. Tan, Y. Su, K. Gao, J. Cui, Y. Wang, Y. Zhao, *J. Fuel Chem. Technol.* 49 (**2021**) 780-790.

[136] T. Buntara, I. Melian-Cabrera, Q.H. Tan, J.L.G. Fierro, M. Neurock, J.G. de Vries, H.J. Heeres, *Catal. Today* 210 (**2013**) 106-116.

[137] D. Hibbitts, Q.H. Tan, M. Neurock, *J. Catal.* 315 (**2014**) 48-58.

[138] S. Sato, J. Igarashi, Y. Yamada, *Appl. Catal., A* 453 (**2013**) 213-218.

[139] F.Y. Zhang, B. Zhang, X.C. Wang, L. Huang, D.K. Ji, S.S. Du, L. Ma, S.J. Lin, *Catalysts* 8 (**2018**).

[140] J. Zhang, J. Yang, J.Y. Tian, H.L. Liu, X.M. Li, W.G. Fang, X. Hu, C.G. Xia, J. Chen, Z.W. Huang, *New J. Chem.* 45 (**2021**) 4236-4245.

[141] R. Benassi, 2.05 - Furans and their Benzo Derivatives: Structure, in: Comprehensive Heterocyclic Chemistry II, 259-295, *Pergamon* (**1996**).

[142] M.J. Gilkey, B. Xu, *ACS Catal.* 6 (**2016**) 1420-1436.

[143] M.J. Gilkey, P. Panagiotopoulou, A.V. Mironenko, G.R. Jenness, D.G. Vlachos, B.J. Xu, *ACS Catal.* 5 (**2015**) 3988-3994.

[144] A.V. Mironenko, M.J. Gilkey, P. Panagiotopoulou, G. Facas, D.G. Vlachos, B.J. Xu, *J. Phys. Chem. C* 119 (**2015**) 6075-6085.

[145] Y. Amada, Y. Shinmi, S. Koso, T. Kubota, Y. Nakagawa, K. Tomishige, *Appl. Catal., B* 105 (**2011**) 117-127.

7. Appendix

Synthesis of supports

SiO_2 (GelX)

In a 250 ml beaker, a mixture of 69 g distilled water and 69 g tetraethoxysilane (TEOS, 333 mmol) was stirred at room temperature (R.T.), and 0,3 g of conc. HCl was added. After 10 min, the mixture was clear and homogeneous (pH = 2). The solution was stirred at R.T. for additional 1 h. Then the pH value was adjusted to 5-6 by addition of a solution of 5 g ammonium acetate in 10 ml distilled water, and the solution was instantly transferred to an autoclave. Within 1 min, the sol yielded a strong, clear gel. The gel was aged at 70 °C for 16 h. The separated liquid was removed, and 100 ml of diluted ammonia solution (10 g conc. ammonia + 90 g distilled water) was added. Then the gel was aged additionally at 90 °C for 2 days. The gel was dried at R.T. for 1 day and crushed. After drying at 100 °C for 2 h, the gel was calcined at 550°C for 5 h (heating rate 2 K/min).

SiO_2 (SBA-15)

In a 1-L-glass bottle, first 600 g of distilled water and 120 g of concentrated HCl (37 %) were mixed by stirring at room temperature. To this solution, 24 g Pluronic 123* (MW=5800, Aldrich) was added and the mixture was stirred for 30 min until homogenization. Then 48 g TEOS (tetraethoxysilane, 98 %, Alfa Aesar) was added under stirring. The solution was heated to 45 °C during 30 min. The clear solution changed to a white suspension and was stirred at 45°C for 24 h and finally aged at 90 °C for 48 h without stirring. After cooling to R.T., the dispersion was filtered with a glass frit (G3). The solids were re-dispersed twice in 200 g of distilled water and filtered again. The filter cake was dried at room temperature for 24 h, at 120 °C for 4 h and calcined in air with a heating rate of 50 K/h up to 550 °C for 6 h in a muffle oven.

γ-Al_2O_3

In a 250 ml beaker, 80 g of water and 20 g Disperal P2 (particle size of 5 nm), were stirred with a magnetic stirrer at room temperature for 1 hour. Then 10 g Triton X100 (nonionic surfactant) was added and stirring was continued for another 2 h. The gel was dried at R.T. overnight and then at 90 °C for 12 h. The calcination of 10 g of the sample was done in a tubular furnace with a heating rate of 1 K/min in a flow of air (150 ml/min) up to 550 °C, with 3 hour holding time at the applied temperature. The amount of Triton could be varied between 0 and the weight of Disperal, modifying the pore size between 4 and 15 nm, with a surface area of about 300 m^2/g.

Additional characterization and experiments (paragraph 4.1)

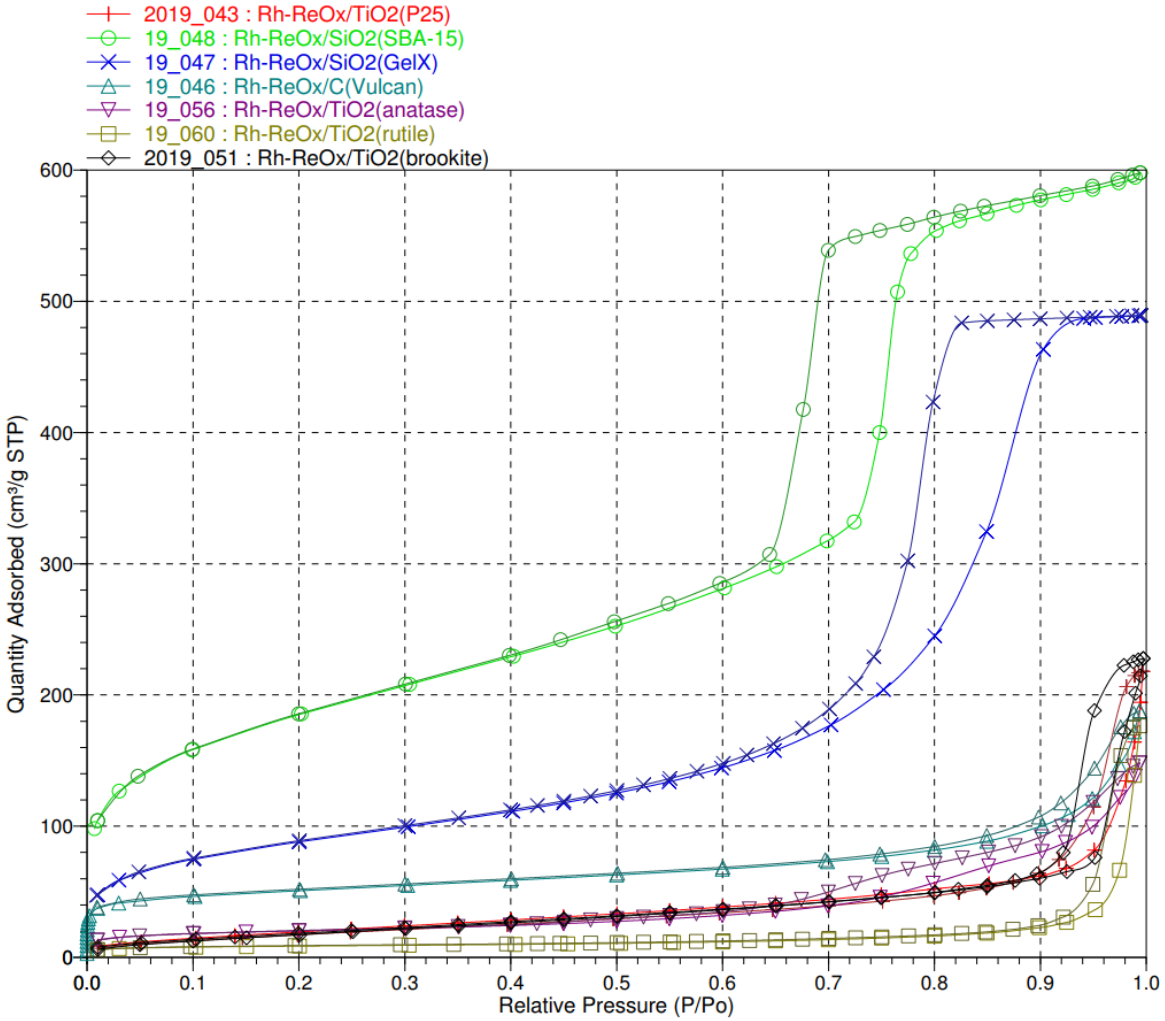

Figure A1. N_2 adsorption-desorption isotherms of Rh-ReO_x on different supports.

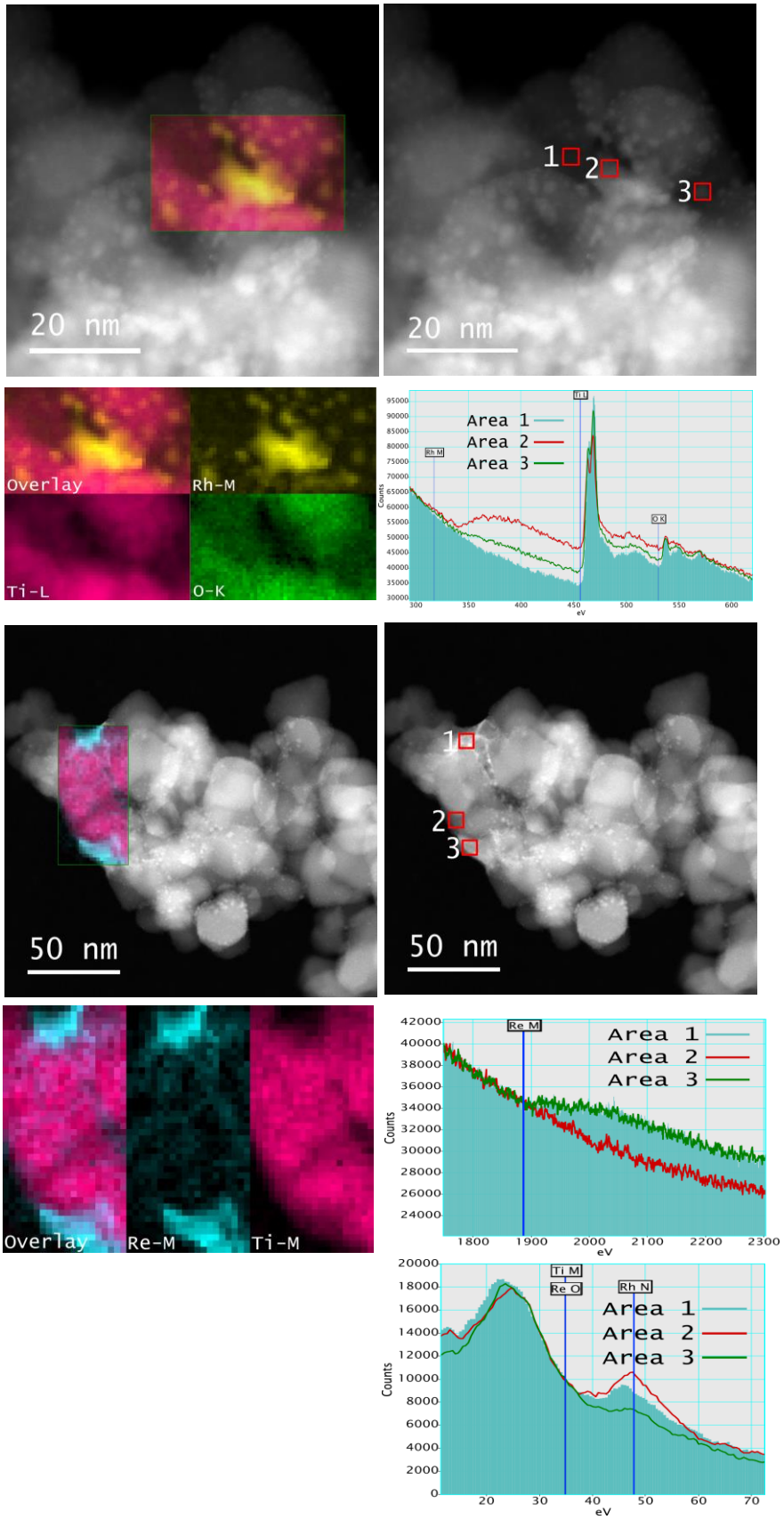

Figure A2. Electron energy loss spectroscopy (EELS) spectra of 2.7Rh-ReO_x/TiO_2 (P25).

Table A1. The influence of metal oxide modifier on the conversion and 1,5-PeD yield over Ir catalysts in hydrogenolysis of THFA.

Entry	Cat on TiO_2 (P25)	Ir (or Ni) loading [wt%]	M:Ir (or Ni) molar ratio	Conv. [%]	Yield [%]				
					1,5-PeD	1,2-PeD	1-PeOH	1-BuOH	Others
1	Ir-ReO_x	3.6	1.33	64.6	45.2	0.0	2.6	0.6	16.3
2	Ir-MoO_x	3.1	0.32	38.4	23.6	0.0	1.7	0.7	12.3
3[a]	Ir-NbO_x	2.6	3.80	15.8	3.3	0.1	0.0	0.2	12.2
4	Ir-WO_x	3.5	0.25	7.4	1.7	0	0.8	0.4	4.5
5	Ni-ReO_x	7.7	0.44	0	0	0	0	0	0
6	Ni-MoO_x	8.1	0.71	0	0	0	0	0	0
7[a]	Ni-NbO_x	12.9	0.37	0	0	0	0	0	0
8	Ni-WO_x	6.8	0.61	0	0	0	0	0	0

Reaction conditions: 5wt% THFA aqueous solution (2 mL), m(cat)= 20 mg, mass ratio (cat:THFA)= 1:5, T= 120 °C, p)H_2)= 8 MPa, t= 24 h. [a] m(cat)= 50 mg, [a]mass ratio (cat:THFA)= 1:2.

Additional characterization of catalysts (paragraph 4.1.1)

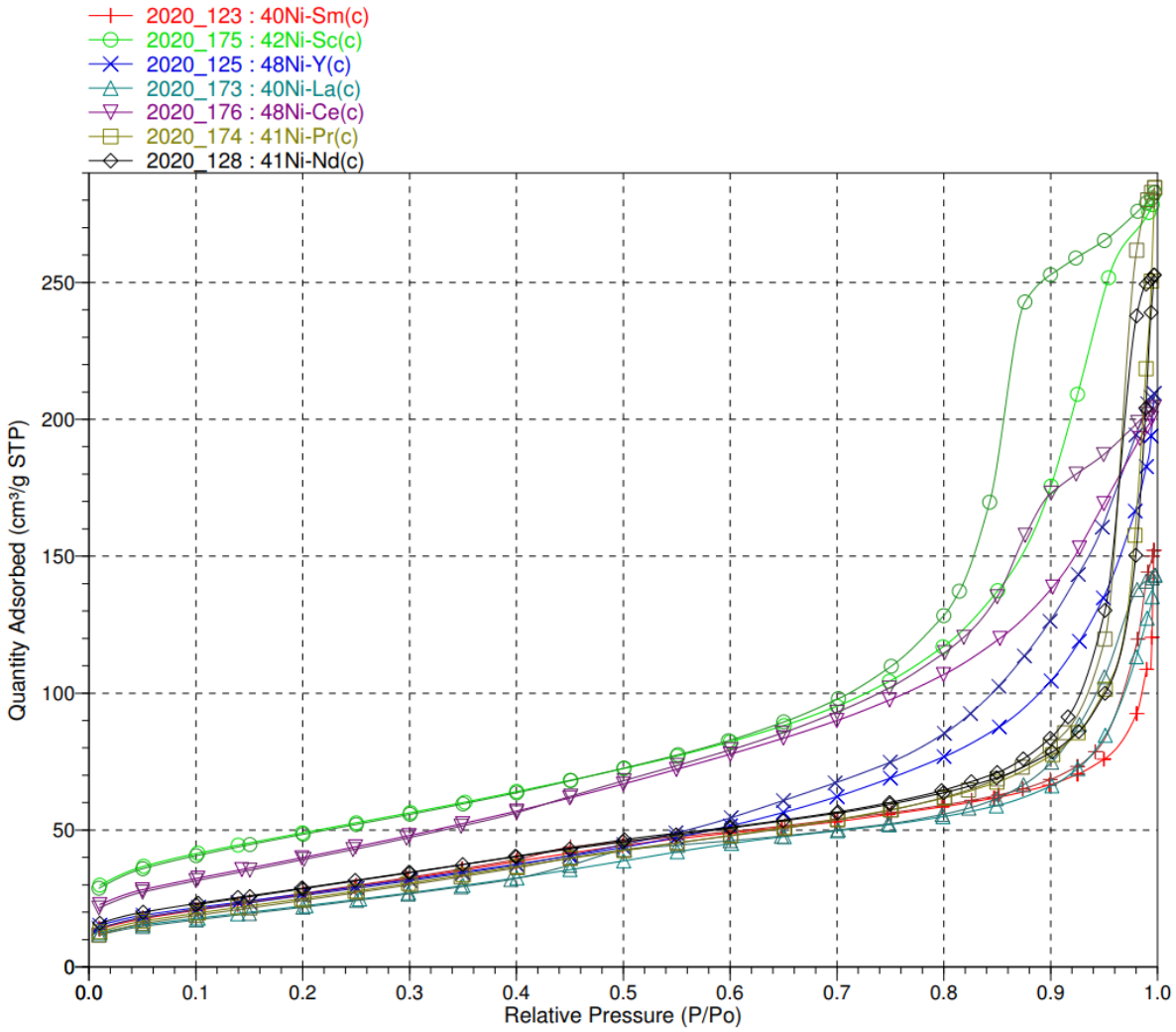

Figure A3. N_2 adsorption-desorption isotherms of Ni on different rare-earth metal supports.

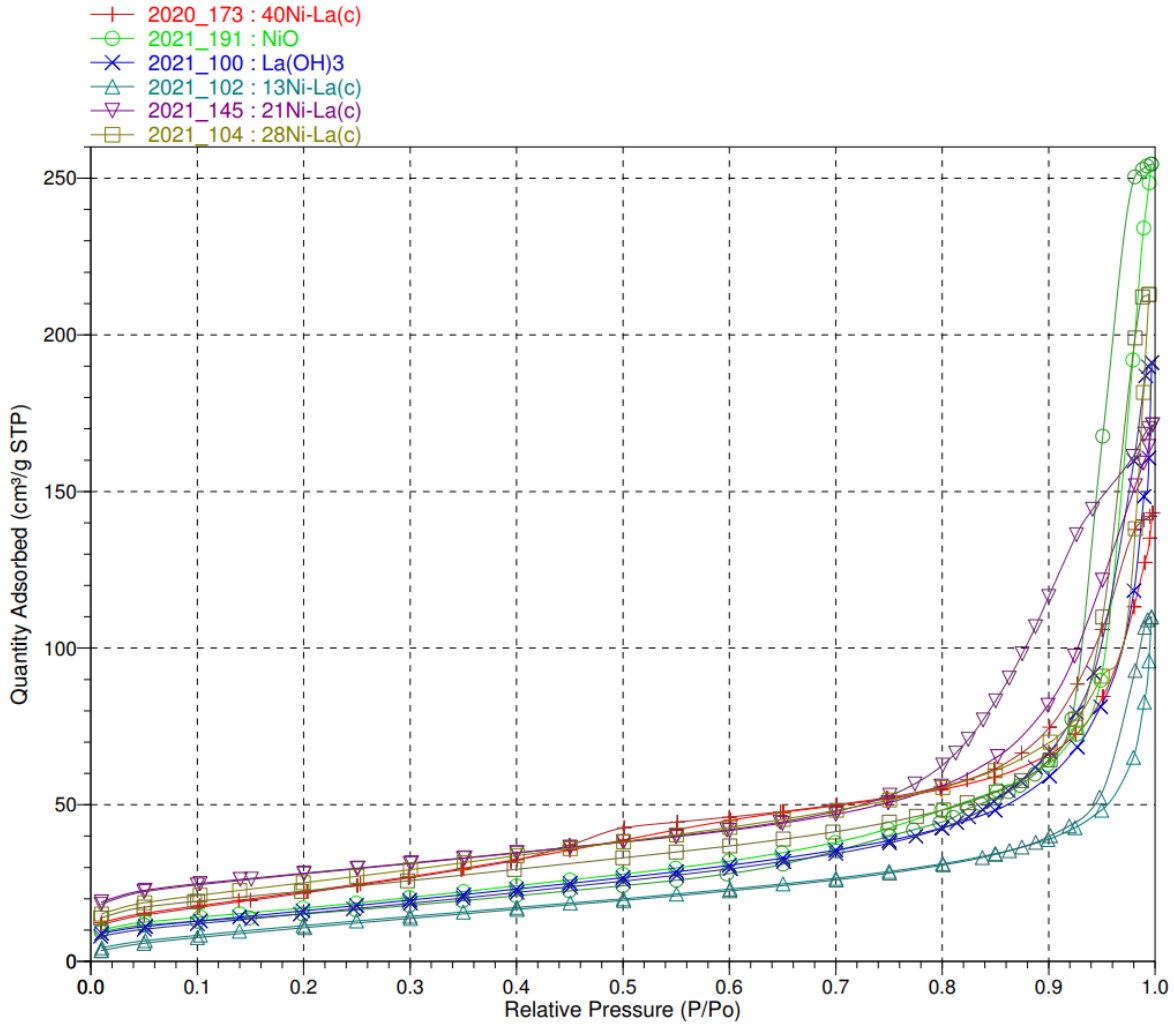

Figure A4. N_2 adsorption-desorption isotherms of NiO, $La(OH)_3$ and Ni-La(C) with different Ni loading.

Table A2. The hydrogen consumption during TPR measurements.

Entry	Catalyst	Molar ratio (Ni/Ln)	H_2 uptake during TPR [μmol/g]		Error ratio [%]
			Calculated	Found	
1	NiO	-	13387	13888	3.6
2	40NiO-La(C)	2.5	6814	7735	11.9
3	41NiO-Pr(C)	2.7	7155	7633	6.3
4	40NiO-Sm(C)	2.8	6814	7240	5.8

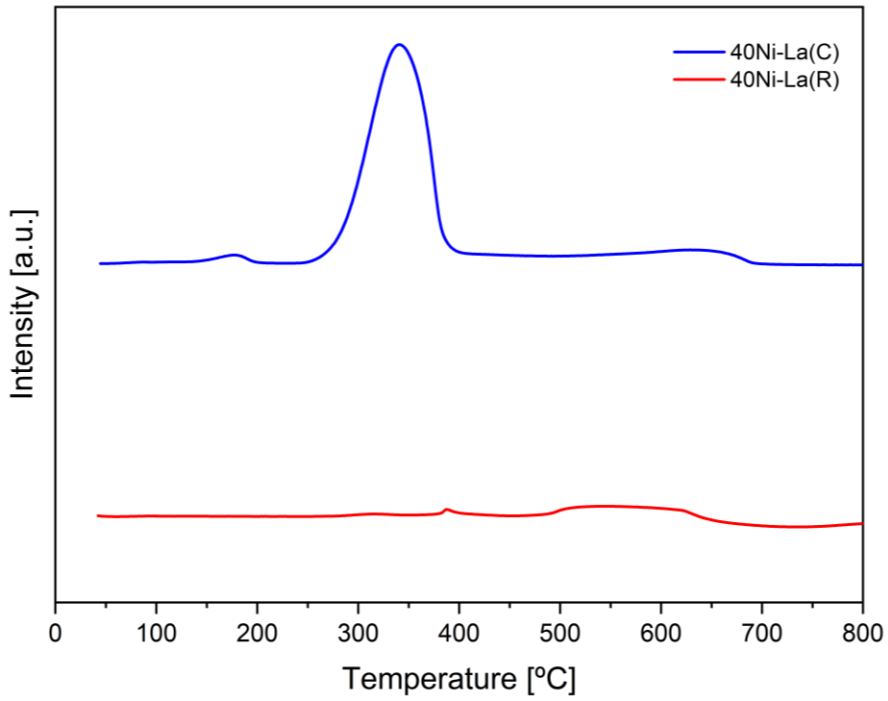

Figure A5. TPR profiles for Ni-La after calcination (C) and Ni-La after reduction (R).

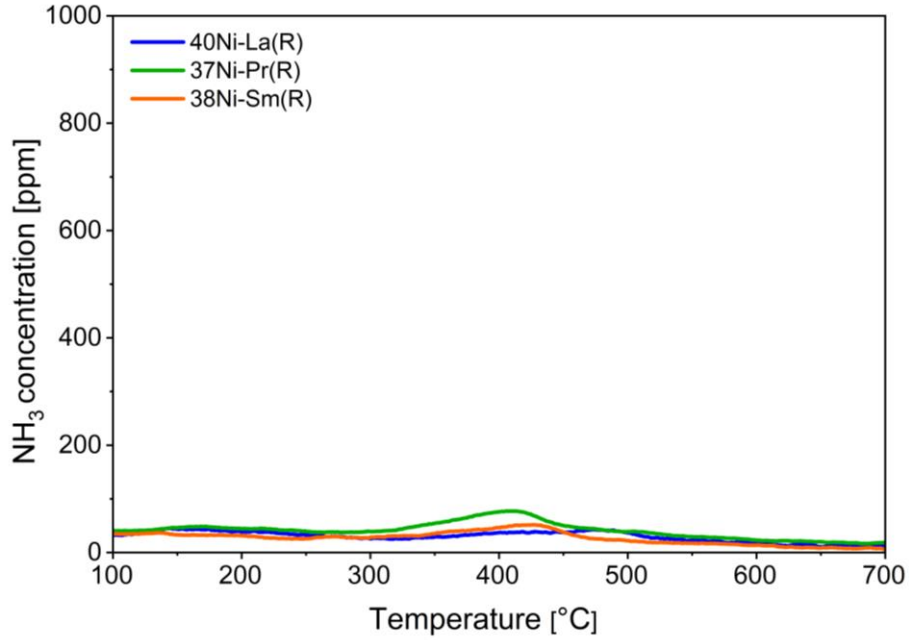

Figure A6. TPD-NH_3 profiles of Ni-Ln(R) (Ln: La, Pr, Sm).

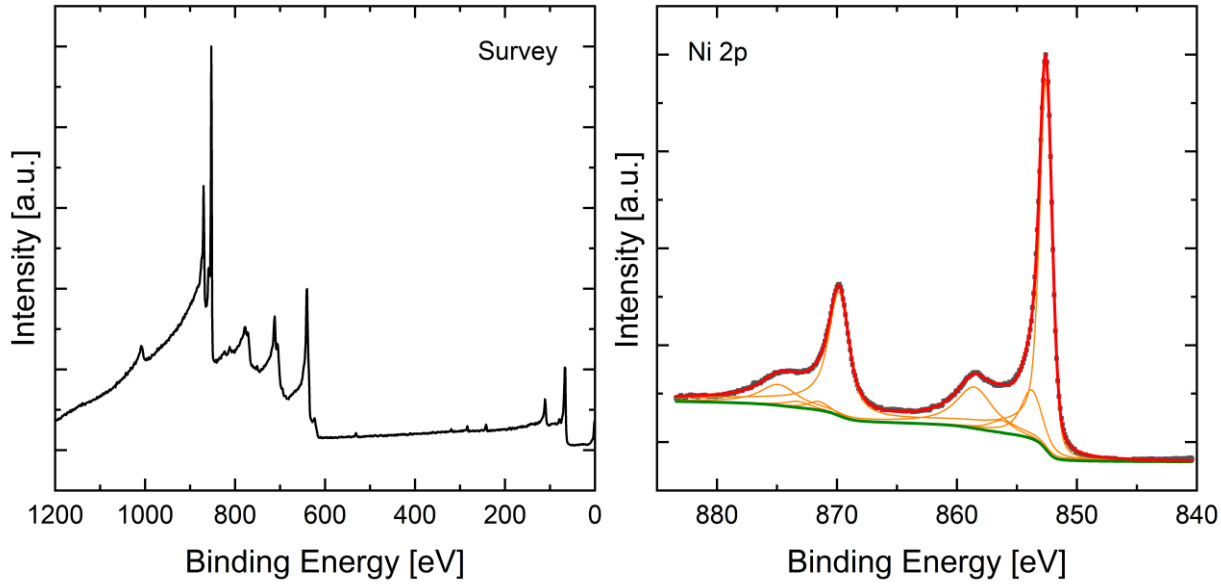

Figure A7. XPS survey and Ni 2p spectra of Ar sputtered Ni foil (3kV. $4*10^{-5}$ mbar. 30 min). The Ni 2p spectra were used to develop a fitting routine for Ni^0 making use of 4 doublets with the two at lower binding energy having a slightly asymmetric peak shape.

Table A3. XPS binding energy values and surface concentration of Ni species in calcined and reduced Ni-Ln (Ln: La, Pr, Sm hydroxide/oxyhydroxide).

		40Ni-La				37Ni-Pr				38Ni-Sm			
		calcined		reduced		calcined		reduced		calcined		reduced	
	Doublet	Binding energy [eV]	rel. conc. [at.%]	Binding energy [eV]	rel. conc. [at.%]	Binding energy [eV]	rel. conc. [at.%]	Binding energy [eV]	rel. conc. [at.%]	Binding energy [eV]	rel. conc. [at.%]	Binding energy [eV]	rel. conc. [at.%]
NiO	1	853.6	3.0	856.8	0.7	853.7	4.5	854.6	1.0	853.5	4.4	855.5	0.2
	2	855.5	13.0	858.7	2.9	855.6	10.8	856.4	2.3	855.4	10.7	857.4	0.5
	3	860.5	7.1	863.7	1.6	860.7	10.1	861.5	2.0	860.5	9.6	862.5	0.4
	4	863.1	8.0	866.4	3.3	863.1	1.2	864.0	0.3	862.8	1.1	864.9	0.1
	5	867.1	3.2	870.1	0.1	867.0	0.4	867.9	0.1	866.9	0.3	868.8	0.0
Ni^0	1			852.5	23.1			852.4	14.5			852.6	21.8
	2			853.5	2.6			853.4	2.2			853.6	3.4
	3			855.3	1.3			855.2	1.3			855.4	2.0
	4			858.5	5.1			858.4	5.5			585.5	8.7
$La(OH)_3$	1	834.5	6.4	835.2	6.4								
	2	838.4	2.6	839.2	4.3								
Degree of reduction Ni^0/Ni(total)				**79%[a]**				**81%**				**97%**	

For quantification of Ni^0 concentration on the surface, a Ni^0 peak profile was deduced from sputter cleaned Ni foil (Figure A7) and combined with the NiO profile from the calcined samples when fitting the spectra of the reduced catalysts. [a] Strong overlap of Ni 2p and La 3d region cause a rather big uncertainty of this value.

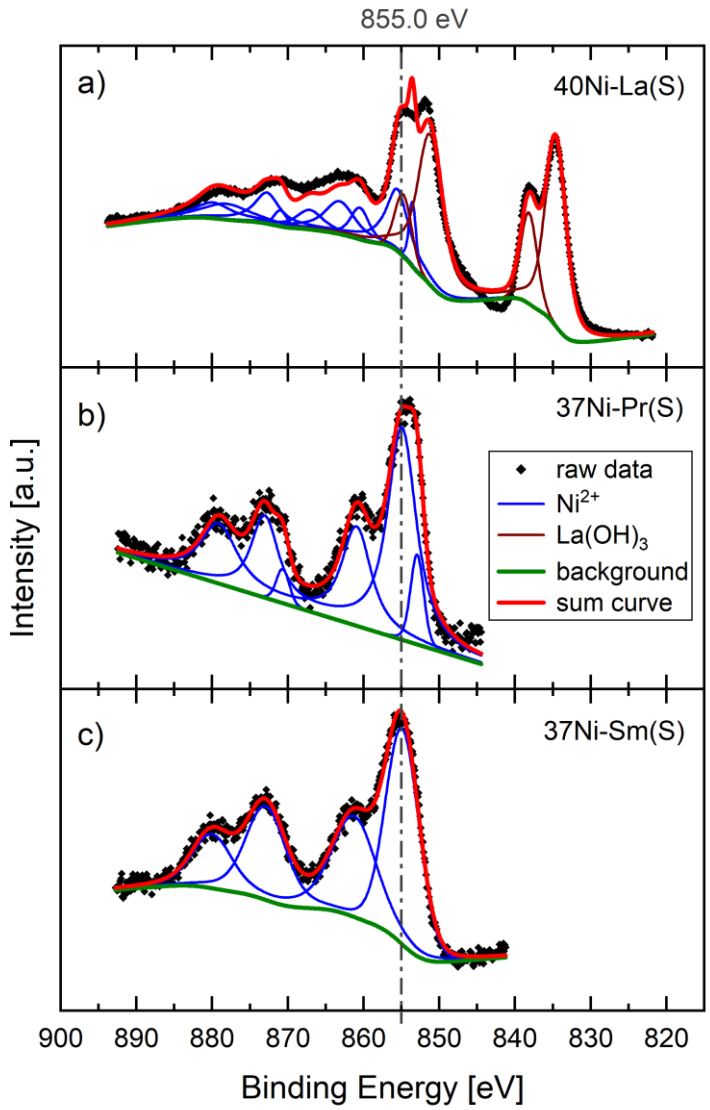

Figure A8. XPS Ni 2p spectra of spent catalysts 40Ni-La(R) (a), 37Ni-Pr(R) (b) and 37Ni-Sm(R) (c).

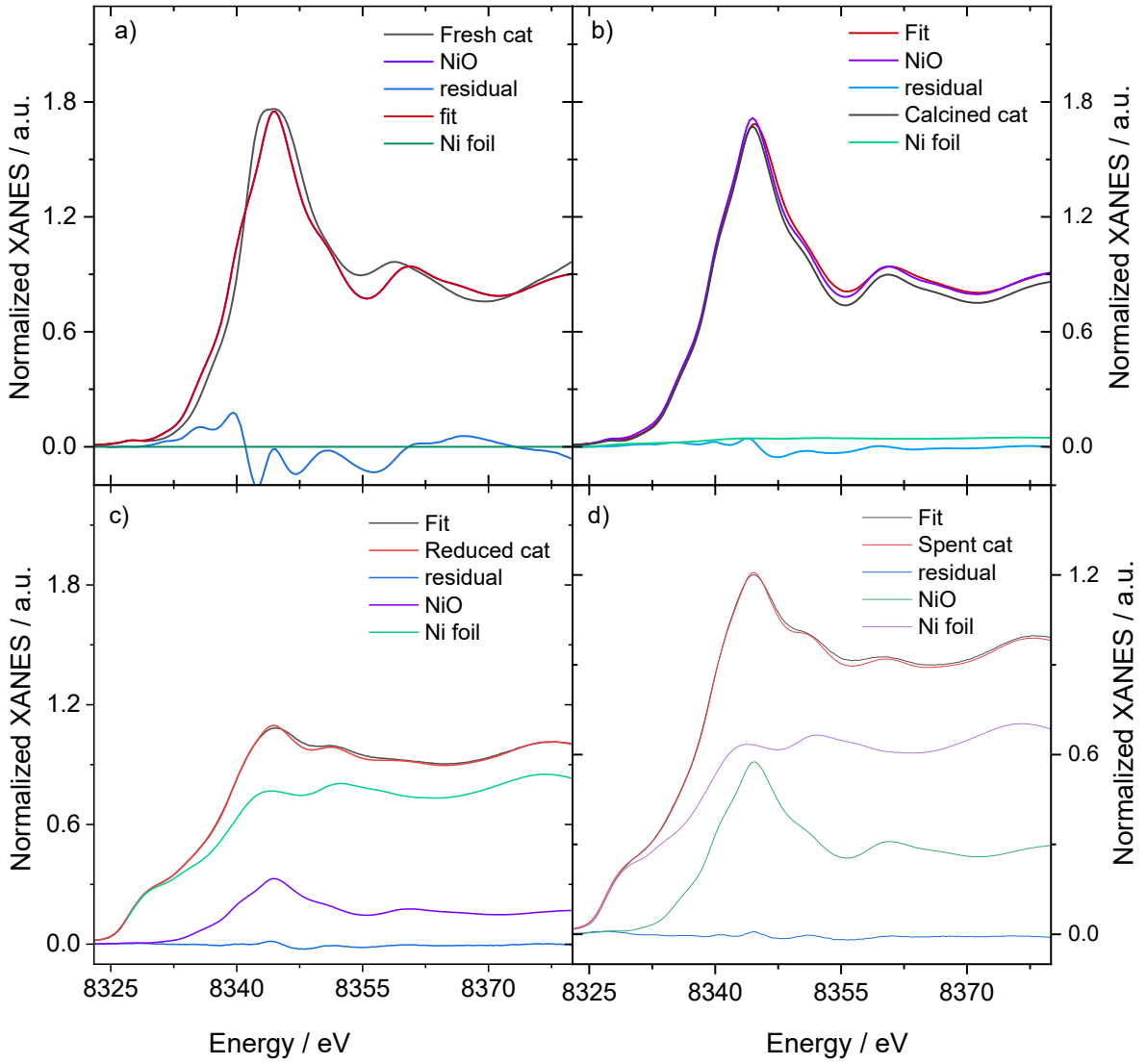

Figure A9. XANES spectra of the 21Ni-La: a) fresh catalyst 21Ni-La(F); b) calcined catalyst 21Ni-La(C); c) reduced catalyst 21Ni-La(R); d) spent catalyst 21Ni-La(S), displayed together with linear combination fit, the reference spectra (NiO and Ni foil) and the residual.

Table A4. EXAFS fit parameters of 21Ni-La before/after pretreatment and reaction.

Sample	Shells	CN[a]	σ^2 [Å^{-2}][b]	R [Å][c]	E_0[d]
21Ni-La(F)	Ni-O	5.7± 0.5	0.00620± 0.00092	2.87± 0.01	2.74 ±0.41
21Ni-La(C)	Ni-O	6.0± 0.5	0.0103 ± 0.0013	2.07± 0.01	-1.25 ±0.46
21Ni-La(R)	Ni-O	2.2 ± 0.5	-0.00585± 0.0015	2.09 ± 0.01	-10.4 ±0.5
	Ni-Ni	7.9 ±1.0	-0.00743±0.001	2.55 ± 0.01	-10.0 ± 0.6
21Ni-La(S)	Ni-O	2.8± 0.5	0.001± 0.005	2.03 ± 0.01	-10.0 ±0.83
	Ni-Ni	7.5 ± 1.0	-0.0070±0.003	2.56 ± 0.01	-15.0 ± 0.33

[a] CN: Ni-Ni, Ni-O first shell coordination number; [b] σ^2 mean square displacement, part of the Debye-Waller factor (DWF: $\exp(-2\sigma^2k^2$; k is wave vector); [c] R: Ni-Ni or Ni-O first shell bond distance; [d] E_0: energy reference parameter.

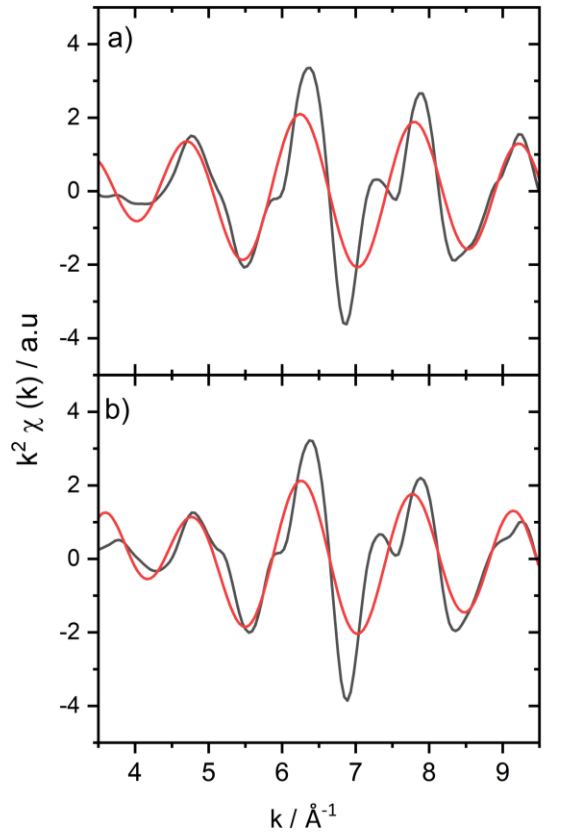

Figure A10. k-2 weighted Chi function of the EXAFS spectra of 21Ni-La(R) (a) and 21Ni-La(S) (b).

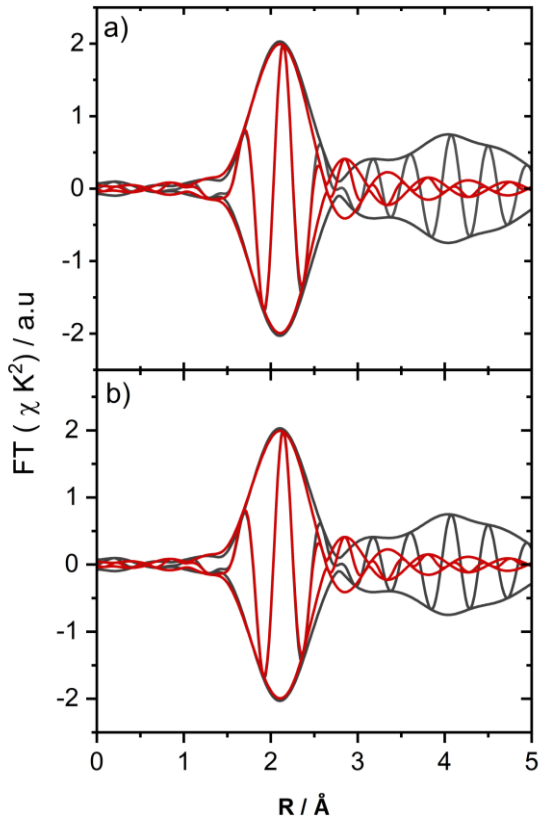

Figure A11. k-2 weighted Fourier transformed EXAFS spectra of 21Ni-La(R) (a) and 21Ni-La(S) (b).

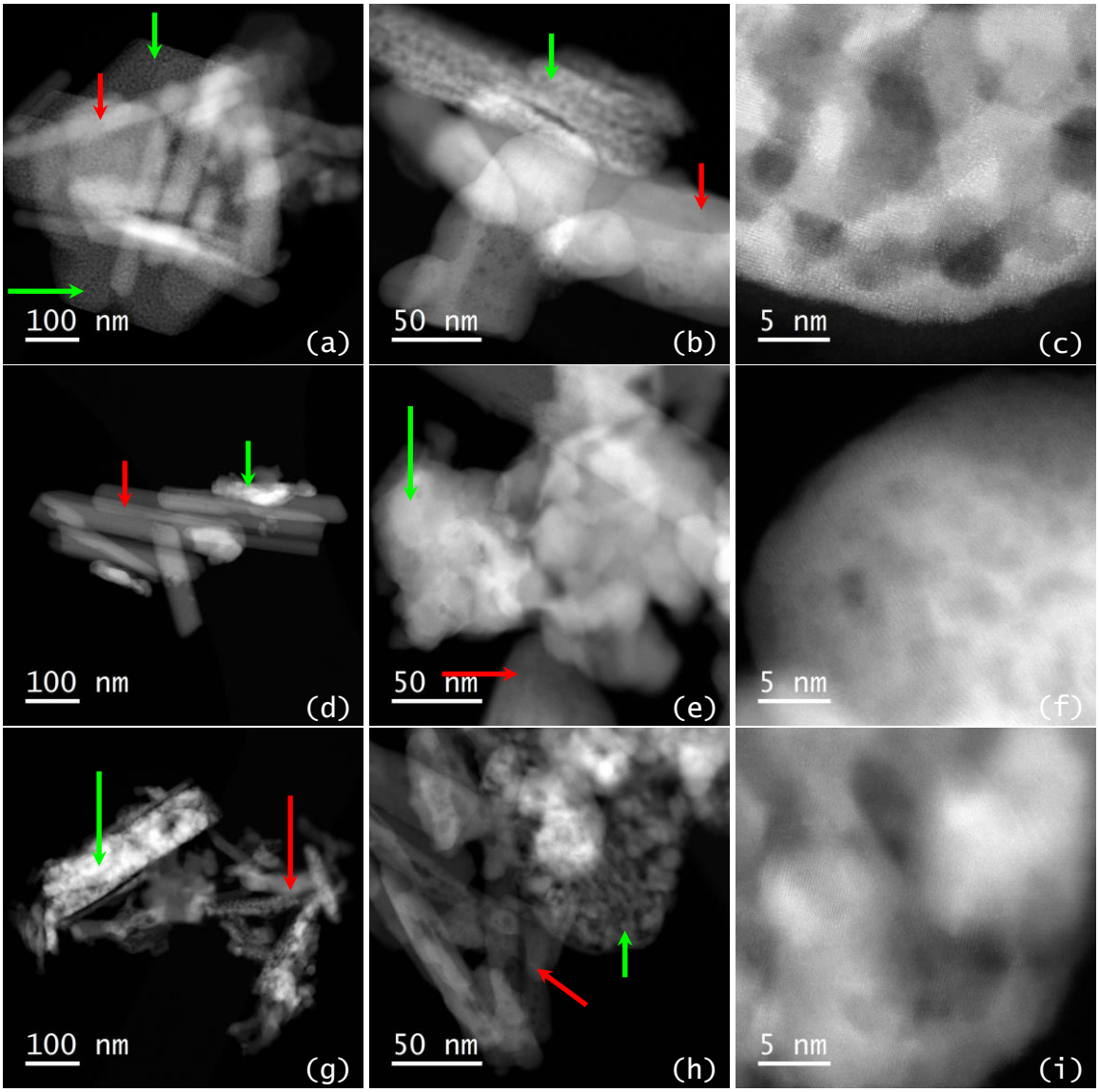

Figure A12. HAADF-STEM images of 40Ni-La(C) (a-c), 40Ni-La(R) (d-f) and 40Ni-La(S) after 386 h TOS (g-i). Ni phase is marked with green arrows, while the La phase is indicated by red arrows.

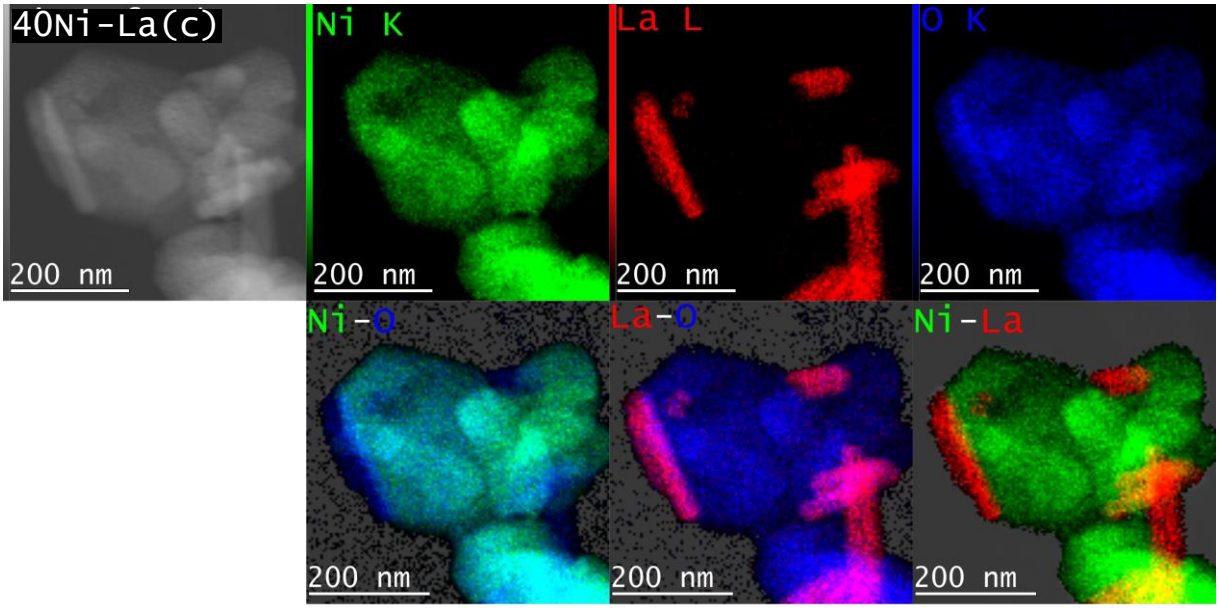

Figure A13. EDX elemental mapping of 40Ni-La(C). In this material, Ni and La are present as NiO and $La(OH)_3$ and form rather independent entities.

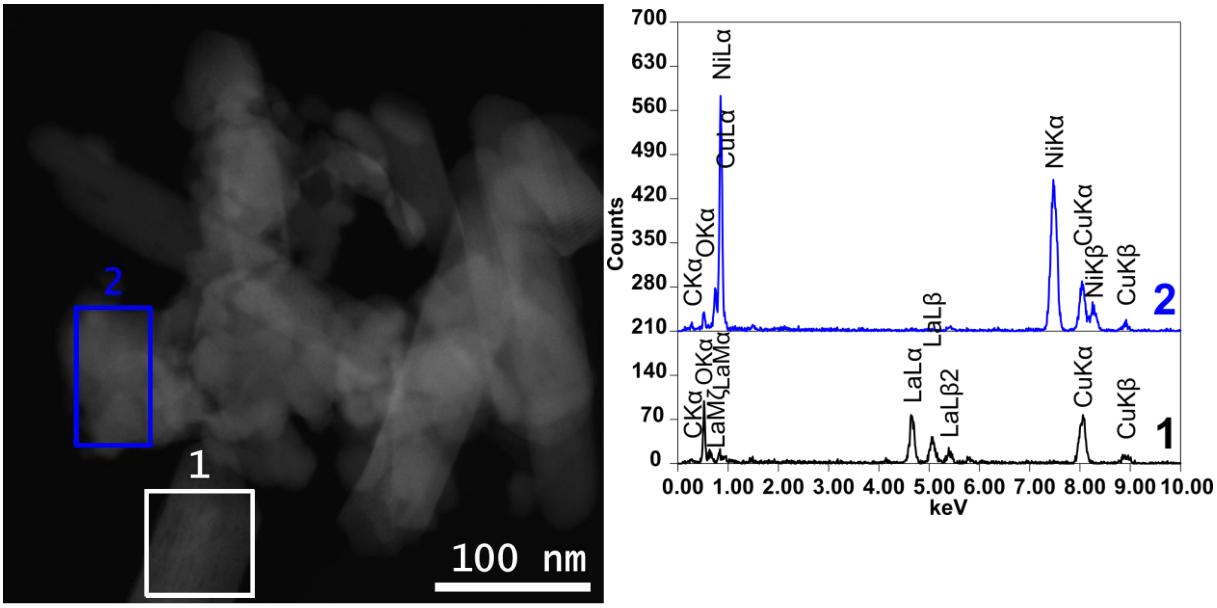

Figure A14. Selected EDX spectra of the marked areas extracted from the mapping of 40Ni-La(R) (Figure 4.16). Area 1 consists of La and oxygen, while Ni and only traces of oxygen are present in the area 2, demonstrating the sufficient reduction of NiO to metallic Ni.

Detailed results of flow experiments (paragraph 4.3.4 and 4.3.5)

Table A5. Summarized results of the stability tests in continuous CTH of THFA in Figure 4.24.

Catalyst	Temperature [°C]	Time [h]	Conversion [%]	Yield [%]		
				1,5-PeD	1-BuOH	Others
40Ni-La(R)	150	2	80	60	8	8
		4	70	59	5	7
		20	89	68	9	12
		22	91	68	9	16
		24	92	67	10	16
		45	94	61	11	23
		48	95	58	11	24
	145	50	90	60	6	25
		68	90	60	6	24
	140	94	85	69	6	21
		120	85	69	4	17
	135	138	75	68	5	12
		144	75	66	5	11
		163	72	67	3	4
		170	72	66	3	5
	140	187	81	68	3	2
		192	84	70	3	3
		209	83	69	5	8
		216	81	68	7	6
		232	80	70	6	7
		240	80	69	5	8
		268	80	70	5	5
		286	82	72	5	7
		303	83	72	6	4
		312	81	71	6	4
		332	85	72	6	5
		337	85	73	6	5
		356	85	72	7	6
		360	86	72	6	6
	150	377	96	60	7	7
		386	95	59	7	7
37Ni-Pr(R)	140	2	63	54	3	6
		21	27	25	1	1
		24	27	25	1	1
		28	22	21	1	0.1
		45	29	27	1	1
		48	32	28	1	3

Table A6. Summarized results of the stability tests in continuous CTH of THFA in Figure 4.25.

Catalyst	Temperature [°C]	Time [h]	Conversion [%]	Yield [%]		
				1,5-PeD	1-BuOH	Others
37Ni-Nd(R)	140	4	40	28	6	2
		20	34	29	2	2
		24	31	27	1	3
	150	26	52	43	3	3
		50	40	37	3	3
		72	41	37	3	4
		90	44	36	3	3
		97	45	37	3	5
	160	98	69	50	11	9
		115	62	42	11	5
		118	61	42	11	8
		138	55	38	9	4
		144	56	37	9	7
		160	50	36	7	5
		168	50	36	7	6
		190	15	11	2	0
38Ni-Sm(R)	140	4	38	36	2	0
	150	20	66	58	4	1
		27	52	48	4	1
		47	60	54	6	1
		50	59	55	6	1
		68	57	53	6	1
	160	75	86	51	21	14
		92	82	47	21	14
		98	81	47	22	13
		118	82	46	23	13
		147	84	45	24	15
		164	82	47	24	12
		188	81	46	22	12

Table A7. Summarized results of 1 g catalyst of 40Ni-La(R) in continuous CTH of THFA in Figure 4.26.

Temperature [°C]	Time [h]	Conversion [%]	Yield [%]		
			1,5-PeD	1-BuOH	Others
140	4	19	18	0.4	0.4
	6	20	16	1	0.4
150	28	43	40	1	2
	50	38	33	1	1
	69	42	37	2	2
	79	43	38	2	2
	102	45	40	2	2
	108	45	39	2	3
	124	43	38	1	2

Detailed results of in situ FTIR experiment (paragraph 4.4.4)

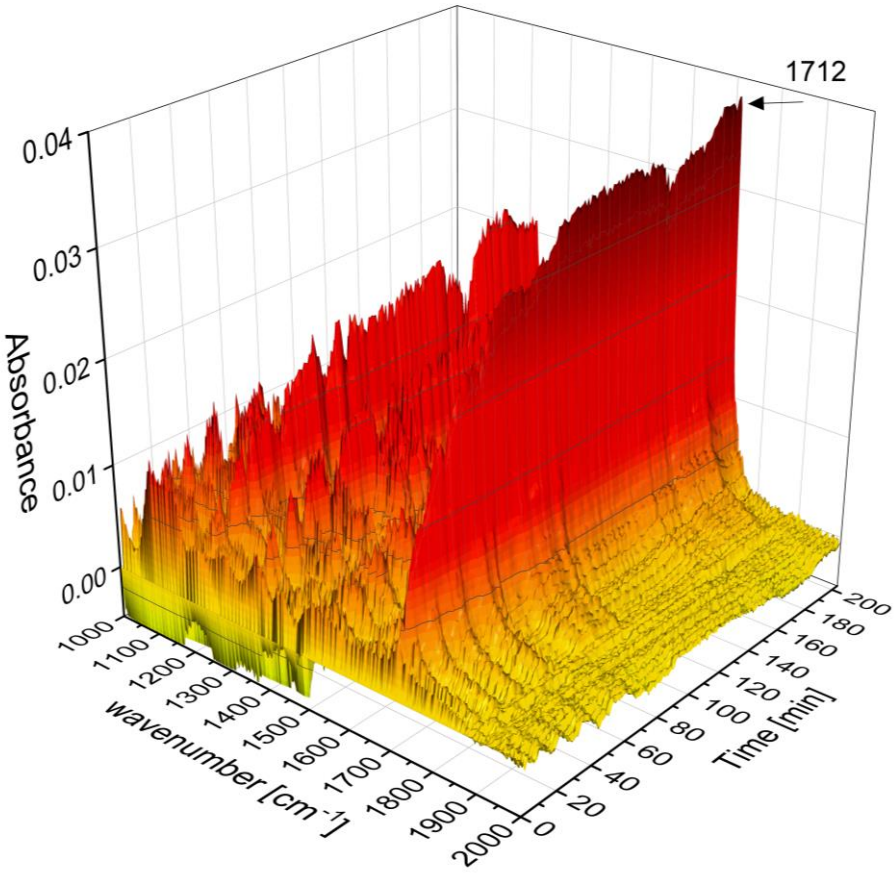

Figure A15. 3D plot of FTIR spectra detecting the acetone formation in the CTH of THFA over 40Ni-La(R) in 2-PrOH. Reaction conditions: c= 1 mmol THFA in 2-PrOH (12 mL), m(cat)= 100 mg, T= 150 °C, p(Ar) = 3 MPa, t= 4h.